



The advanced developments of the Smart Cut™ technology : fabrication of silicon thin wafers & silicon-on-something hetero-structures

Raphaël Meyer

► To cite this version:

Raphaël Meyer. The advanced developments of the Smart Cut™ technology : fabrication of silicon thin wafers & silicon-on-something hetero-structures. Materials. Université de Lyon, 2016. English. NNT : 2016LYSEI033 . tel-01694114

HAL Id: tel-01694114

<https://theses.hal.science/tel-01694114>

Submitted on 26 Jan 2018

HAL is a multi-disciplinary open access archive for the deposit and dissemination of scientific research documents, whether they are published or not. The documents may come from teaching and research institutions in France or abroad, or from public or private research centers.

L'archive ouverte pluridisciplinaire **HAL**, est destinée au dépôt et à la diffusion de documents scientifiques de niveau recherche, publiés ou non, émanant des établissements d'enseignement et de recherche français ou étrangers, des laboratoires publics ou privés.

N°d'ordre NNT : 2016LYSEI033

THESE de DOCTORAT DE L'UNIVERSITE DE LYON

préparée au sein de
l'INSA LYON

Ecole Doctorale N° accréditation
MATERIAUX DE LYON

Spécialité de doctorat : Physique des Matériaux

Soutenue publiquement le 20/04/2016, par :
Raphaël Meyer

The Advanced Developments of the Smart Cut™ Technology: Fabrication of Silicon Thin Wafers & Silicon-On-Something Hetero-structures

Devant le jury composé de :

Bremond, Georges	Professeur/Insa Lyon	Président
Claverie, Alain	Professeur/CNRS	Rapporteur
Tournié, Eric	Professeur/Université Montpellier	Rapporteur
Bruel, Michel	Directeur/Aplinov	Examineur
Zaidat, Kader	Maître de conférence/Grenoble INP	Examineur
Lemiti, Mustapha	Professeur/Insa Lyon	Directeur de thèse
Moriceau, Hubert	Docteur/CEA	Co-encadrant
Kononchuk, Oleg	Docteur/Soitec	Co-encadrant
Rieutord, François	Directeur de recherche/CEA	Invité

Département FEDORA – INSA Lyon - Ecoles Doctorales – Quinquennal 2016-2020

SIGLE	ECOLE DOCTORALE	NOM ET COORDONNEES DU RESPONSABLE
CHIMIE	CHIMIE DE LYON http://www.edchimie-lyon.fr Sec : Renée EL MELHEM Bat Blaise Pascal 3 ^e étage secretariat@edchimie-lyon.fr Insa : R. GOURDON	M. Stéphane DANIELE Institut de Recherches sur la Catalyse et l'Environnement de Lyon IRCELYON-UMR 5256 Equipe CDPA 2 avenue Albert Einstein 69626 Villeurbanne cedex directeur@edchimie-lyon.fr
E.E.A.	ELECTRONIQUE, ELECTROTECHNIQUE, AUTOMATIQUE http://edeea.ec-lyon.fr Sec : M.C. HAVGOUDOUKIAN Ecole-Doctorale.eea@ec-lyon.fr	M. Gérard SCORLETTI Ecole Centrale de Lyon 36 avenue Guy de Collongue 69134 ECULLY Tél : 04.72.18 60.97 Fax : 04 78 43 37 17 Gerard.scorletti@ec-lyon.fr
E2M2	EVOLUTION, ECOSYSTEME, MICROBIOLOGIE, MODELISATION http://e2m2.universite-lyon.fr Sec : Safia AIT CHALAL Bat Darwin - UCB Lyon 1 04.72.43.28.91 Insa : H. CHARLES Safia.ait-chalal@univ-lyon1.fr	Mme Gudrun BORNETTE CNRS UMR 5023 LEHNA Université Claude Bernard Lyon 1 Bât Forel 43 bd du 11 novembre 1918 69622 VILLEURBANNE Cedex Tél : 06.07.53.89.13 e2m2@univ-lyon1.fr
EDISS	INTERDISCIPLINAIRE SCIENCES-SANTÉ http://www.ediss-lyon.fr Sec : Safia AIT CHALAL Hôpital Louis Pradel - Bron 04 72 68 49 09 Insa : M. LAGARDE Safia.ait-chalal@univ-lyon1.fr	Mme Emmanuelle CANET-SOULAS INSERM U1060, CarMeN lab, Univ. Lyon 1 Bâtiment IMBL 11 avenue Jean Capelle INSA de Lyon 696621 Villeurbanne Tél : 04.72.68.49.09 Fax : 04 72 68 49 16 Emmanuelle.canet@univ-lyon1.fr
INFOMATHS	INFORMATIQUE ET MATHEMATIQUES http://infomaths.univ-lyon1.fr Sec : Renée EL MELHEM Bat Blaise Pascal 3 ^e étage infomaths@univ-lyon1.fr	Mme Sylvie CALABRETTO LIRIS – INSA de Lyon Bat Blaise Pascal 7 avenue Jean Capelle 69622 VILLEURBANNE Cedex Tél : 04.72. 43. 80. 46 Fax 04 72 43 16 87 Sylvie.calabretto@insa-lyon.fr
Matériaux	MATERIAUX DE LYON http://ed34.universite-lyon.fr Sec : M. LABOUNE PM : 71.70 -Fax : 87.12 Bat. Saint Exupéry Ed.materiaux@insa-lyon.fr	M. Jean-Yves BUFFIERE INSA de Lyon MATEIS Bâtiment Saint Exupéry 7 avenue Jean Capelle 69621 VILLEURBANNE Cedex Tél : 04.72.43 71.70 Fax 04 72 43 85 28 Ed.materiaux@insa-lyon.fr
MEGA	MECANIQUE, ENERGETIQUE, GENIE CIVIL, ACOUSTIQUE http://mega.universite-lyon.fr Sec : M. LABOUNE PM : 71.70 -Fax : 87.12 Bat. Saint Exupéry mega@insa-lyon.fr	M. Philippe BOISSE INSA de Lyon Laboratoire LAMCOS Bâtiment Jacquard 25 bis avenue Jean Capelle 69621 VILLEURBANNE Cedex Tél : 04.72 .43.71.70 Fax : 04 72 43 72 37 Philippe.boisse@insa-lyon.fr
ScSo	ScSo* http://recherche.univ-lyon2.fr/scso/ Sec : Viviane POLSINELLI Brigitte DUBOIS Insa : J.V. TOUSSAINT viviane.polsinelli@univ-lyon2.fr	Mme Isabelle VON BUELTZINGLOEWEN Université Lyon 2 86 rue Pasteur 69365 LYON Cedex 07 Tél : 04.78.77.23.86 Fax : 04.37.28.04.48

*ScSo : Histoire, Géographie, Aménagement, Urbanisme, Archéologie, Science politique, Sociologie, Anthropologie

« Mais on ne se bat pas dans l'espoir du succès !
Non ! Non, c'est bien plus beau quand c'est inutile ! »
Cyrano de Bergerac, Edmond Rostand.

PREAMBLE

This sentence of Edmond Rostand means a lot to me, as these words do not only signify the quixotic destiny of idealistic people, but also bring a highlighting, despite a bit contradictory, definition on how innovation can be created. Of course, the concept of useful/useless is highly subjective, in the field of innovation like in many others. Sadly, the frontier between these two notions can often be limited by objective criteria, aiming to limit the risk taking. On the other side, investigating a direction that a preliminary analysis would initially estimate as wrong way can bring unexpected results and, into the end, useful applications.

By this preamble, my objective is first to testify my pride to have taken part in this adventure, started from the genius mind of Michel Bruel, to whom, hundreds of people are beholden of their position today. Michel has supported this project by many ways, including certain financial aspects. My undying gratitude to him, for these moments spent trying to convince and, time after time, to go forward.

The second testimony is dedicated to the Soitec Company, which has incarnated the risk taking by supporting this research, despite a difficult context. May I modestly hope that this research, which brought two patents in initially unexpected directions, will show the necessity to pursue in-house and out-of-the box research.

Finally, I wish to commend the humanness of so many people met during this thesis in CEA, in SiMaP, in INSA Lyon, in Solarforce, Applied Materials and in Soitec.

SUMMARY

Ecoles Doctorales	2
PREAMBLE	4
ACKNOWLEDGEMENTS	5
SUMMARY	6
Chapter 1. Introduction.....	13
1. Description of the thesis topics.....	14
1.1. Technological context in microelectronics.....	14
1.2. About SOI and Smart Cut™ technology.....	14
2. Hetero-structure elaboration by laser-assisted Smart Cut™	15
2.1. Description of the process.....	15
3. Why going toward thin wafer of Si?.....	16
3.1. Market of photovoltaics.....	16
3.2. Thin-foils of Si applied to photovoltaics.....	17
4. Ultra-thin chips based on thin Si wafer	18
5. Elaboration of thin foil of single-crystal Si by liquid phase epitaxy on an implanted Si substrate	18
6. Description of the thesis strategy.	20
References.....	22
Chapter 2. State of the art.....	23
1. About Smart Cut™ technology	24
1.1. Historical aspects of Smart Cut™ and applications of SOI.....	24
1.2. Main steps of the Smart Cut™	25
1.3. State of the art of Smart Cut™	26
1.4. Defects generated by the implantation	26
1.5. Formation of the platelets during the annealing	28
1.5.1 Analysis of platelets orientation.....	30
1.6. Formation and coalescence of micro-cracks.....	30
1.7. Energy analysis of the crack propagation in the H implanted Si.....	32
1.8. Splitting kinetics	34
1.9. Morphology of the surface after film separation.....	35
1.10. Energy of the bonding interface.....	36
1.11. Theoretical analysis on the effect of high temperature annealing on Smart Cut™ mechanisms.....	38

2.	Fabrication of planar heterostructures of semiconductors	39
2.1.	Motivations for using planar heterostructures	39
2.2.	Fabrication techniques for the production of planar heterostructures.....	41
2.2.1.	Heteroepitaxy of semiconductors	41
2.2.2	Laser lift-off (LLO)	42
2.2.3	Bonding and etch-back approach.....	42
2.3	Smart Cut™ applied to heterostructures.....	42
2.4	Annealing of an implanted material by laser beam	43
3	Kerf-less production of thin wafer of Si: an alternative approach driven by photovoltaics	45
3.1	Stress-induced lift-off (SLiM-Cut)	45
3.2	Layer transfer based on porous substrates or pore coalescence	46
3.3	Techniques based on ion implantation	47
3.4	Liquid phase epitaxial (LPE) growth of Si from the molten phase	48
3.4.1	Physical principles of solidification.....	48
3.4.2	Kinetics of solidification.....	49
3.4.3	Growth velocity	50
3.4.4	Grain boundary formation	51
3.5	Spreading of liquid Si onto a surface.....	53
3.6	Electromagnetic levitation	54
	Conclusion	56
	References.....	57
Chapter 3.	Design of experiments.....	61
1.	Blistering and splitting study (treated in the Chapter 4).....	62
1.1.	Blistering samples preparation	62
1.2.	Splitting samples preparation	62
1.2.1.	Preparation of the samples	62
1.2.2.	Temperature recording	63
1.3.	Description of the heating system	64
1.4	Characterization facilities	66
1.4.1	Secondary Ion Mass Spectrometry (SIMS)	66
1.4.2	Atomic Force Microscopy (AFM)	66
1.4.3	Optical profilometer	67
1.4.4	Measurement of the bonding energy by double cantilever beam (DCB)	68
2	Laser-assisted Smart Cut™ study (Chapter 5)	69
2.1	Preparation of the blistering samples	69
2.2	Preparation of the samples for the elaboration of hetero-structures.....	69

2.2.1	Implanted Si bonded with sapphire	69
2.3	Description of the laser equipment	70
2.3.1	Excimer ArF ns laser ($\lambda = 193$ nm).....	70
2.3.2	Dynamic Surface Anneal (DSA) laser ($\lambda = 808$ nm)	71
2.3.3	Optical pyrometer	72
2.4	Characterization facilities.....	73
2.4.1	Raman spectroscopy	73
2.4.2	X-Ray Diffraction analysis (XRD)	74
2.4.3	Scanning Acoustic Microscope (SAM)	75
2.4.4	4-point probe measurement.....	75
3	Study growth of silicon from a liquid of Si	77
3.1	Conditions of implantation of samples	77
3.2	Surface preparation before deposition of liquid Si	77
3.3	Description of the benches of liquid Si deposition.....	77
3.3.1	Melting of Si in graphite crucible	77
3.3.2	Basic principles on electromagnetic levitation.....	78
3.3.3	Melting of Si in a self-crucible	80
3.3.4	Melting of Si in an electromagnetic levitator	80
3.4	Characterization facilities	81
3.4.1	Electron Back-Scattered Diffraction (EBSD)	81
3.4.2	High Angle Annular Dark Field (HAADF) and Electron Energy Loss Spectroscopy (EELS)..	83
3.4.3	Photoluminescence (PL)	84
	Conclusion	86
	References.....	87
	Chapter 4. Study of Smart Cut™ at high temperature by conventional furnace	89
1.	Characterization of the heating system	90
1.1.	Heating plate used for the characterization of blistering samples	90
1.2.	Heating system using steel plates for the characterization of splitting.....	91
2.	Kinetics of blistering and splitting	93
2.1.	Blistering kinetics up to 600°C.....	93
3.	Splitting kinetics up to 700°C	96
3.1.1.	96
3.1.2.	Activation energy as function of dose	97
3.1.3.	Analysis of thermal budget of splitting	98
3.1.4.	Characterization of splitting for low dose samples.....	99
3.2.	Kinetics of splitting at the bulk-oxide layer interface up to 950°C.....	101

3.3.	Detachment at the bonding interface.....	103
3.4.	Annealing of different sample geometries implanted at $3.5 \cdot 10^{16} \text{ Hcm}^{-2}$	104
4.	Characterization of H diffusion (Si samples implanted with $3.5 \cdot 10^{16} \text{ Hcm}^{-2}$)	106
4.1.	SIMS characterization (as implanted samples, annealing at 600°C and 850°C for 30 s).....	106
4.1.1.	H concentration in implantation zone.....	106
4.1.2.	H concentration in the thermal oxide	107
5.	Modelling of H diffusion	110
5.1.	Modelling considering the diffusion of free H	110
5.2.	Model of diffusion by de-trapping of H.....	111
5.3.	Comparison between numerical modelling and SIMS for $3.5 \cdot 10^{16} \text{ Hcm}^{-2}$ samples.....	113
6.	Characterization of adhesion energy of bonding interface.....	116
6.1.	Results	116
7.	As-split surface roughness.....	120
7.1.	Roughness as a function of temperature of Si splitting samples implanted with $5.0 \cdot 10^{16} \text{ Hcm}^{-2}$ by AFM characterization.....	120
8.	Model of splitting	121
8.1.	Thermal budget calculation including the out-diffusion.....	121
8.2.	Prediction of the model for higher temperatures.....	123
8.3.	Mechanisms leading to oxide layer transfer and detachment at the bonding interface ...	125
9.	Conclusion of the chapter	126
	References.....	127
	Chapter 5. Application of laser annealing to Smart Cut™	129
1.	Effects of ns laser annealing of bulk implanted Si wafers	130
1.1.	Description of the ns laser annealing setup	130
1.2.	Effect of multi-pulse annealing	131
1.3.	Generation of blisters by multi-pulse ns laser annealing ($1.0 \cdot 10^{17} \text{ Hcm}^{-2}$)	133
2.	Kinetics of splitting by laser annealing (Implanted Si, SOS, SOG)	135
2.1.	Numerical modelling of millisecond laser annealing of the bonded heterostructure	135
2.1.1.	Constitutive equations	135
2.1.2.	Bending of the bonded structure on the laser chuck.....	136
2.1.3.	Optical model	138
2.2.	Application of the numerical modelling to the annealing of implanted structures.....	141
2.2.1.	Comparison with pyrometer characterization	141
2.2.2.	Modelling of the thermal stress within the structure	142
2.2.3.	Modelling of out-diffusion during the laser annealing.....	143
2.3	Design of experiment for the characterization of the splitting kinetics by laser annealing	145

3. Experimental annealing of the Silicon-On-Sapphire samples	146
3.1. Experimental observations.....	146
3.2. Blistering / non blistering domain determination ($4.0 \cdot 10^{16} \text{Hcm}^{-2}$, $5.0 \cdot 10^{16} \text{Hcm}^{-2}$, $1.0 \cdot 10^{17} \text{Hcm}^{-2}$, $1.2 \cdot 10^{17} \text{Hcm}^{-2}$).....	147
3.3. Splitting/non-splitting domain determination SOS ($4.0 \cdot 10^{16} \text{Hcm}^{-2}$, $5.0 \cdot 10^{16} \text{Hcm}^{-2}$, $1.0 \cdot 10^{17} \text{Hcm}^{-2}$, $1.2 \cdot 10^{17} \text{Hcm}^{-2}$).....	150
4. Splitting/non-splitting domain determination for SOG samples ($4.0 \cdot 10^{16} \text{Hcm}^{-2}$, $5.0 \cdot 10^{16} \text{Hcm}^{-2}$, $1.0 \cdot 10^{17} \text{Hcm}^{-2}$, $1.2 \cdot 10^{17} \text{Hcm}^{-2}$)	152
4.1. General observations	152
4.1.1. Inhomogeneity of annealing	152
4.1.2. Fracture of samples of Glass bonded with Si	153
4.2. Characterization of splitting	155
4.3. Validation of the splitting model.....	156
4.3.1. Thermal budget calculations	156
4.3.2. Unified model of splitting over the overall temperature range.....	159
5. Characterization of the films elaborated by laser-assisted Smart Cut™	160
5.1.1. Best-in-class result.....	160
5.1.2. Analysis of the patterns formed by the transferred layers	161
5.1.3. Bow of the structure after splitting.....	162
5.1.4. Stress analysis by Raman.....	164
5.1.5. Model for the formation of marbles	166
5.2. Roughness of SOS and SOG films by laser annealing and comparison with furnace annealing	167
5.2.1. Roughness of SOS films	167
5.2.2. Surface analysis of the SOG films	168
5.3. 4-probe measurement (SOG)	170
6. Conclusion of chapter.....	171
References.....	172
Chapter 6. Deposition of liquid Si on Si substrate.....	173
1. Modelling of Si liquid crystallization.....	174
1.1. Model description	174
1.2. Numerical study of solidification of the liquid silicon by Comsol Multiphysics®	175
1.2.1. Thermal profile during the solidification of a film of liquid Si.....	175
1.2.2. Thermal profile of the solidification of droplet of liquid Si	176
1.2.3. Numerical calculation of the temperature within the implanted zone during the solidification of liquid Si	178
1.2.4. Thermal budget of splitting.....	179

2. Liquid Si dropped on a rotating substrate (collaboration with Solarforce company).....	181
2.1. General considerations	181
2.1.1. Deposition on a rotating substrate from a graphite crucible.....	181
2.1.2. Deposition rate of the silicon through orifice in the crucible	182
2.1.3. Spreading of the liquid film on the rotating substrate.....	182
2.2. Experimental observations.....	183
2.2.1. Film thickness characterization	183
2.2.2. Generated stress in the substrate	186
2.2.3. Thickness of the layer detached by Smart Cut™	186
2.2.4. Characterization of the surface of the donor wafer by AFM	187
2.2.5. Backside of the droplets detached by Smart Cut™	187
2.3. Film characterization	188
2.3.1. EBSD cartography of sample deposited onto a non-implanted substrate.....	188
2.3.2. HR-TEM imaging at the interface between the substrate and the droplet	190
2.3.3. Deposition onto an implanted substrate	191
2.3.4. Interface between the implanted substrate	191
2.3.5. Grains study in the droplet after detachment by Smart Cut™	192
3. Deposition of liquid Si by use of a self-aligned crucible (collaboration with SiMaP laboratory)	194
3.1. Preliminary observations.....	194
3.1.1. Spreading of the liquid on the substrate.....	194
3.1.2. Adhesion between the substrate and the deposited films	196
3.1.3. Formation of SiO ₂ layer at the vicinity of the solidified films	197
3.1.4. Blistering analysis	198
3.2. EBSD cartography of sample deposited on an implanted substrate.....	199
4. Deposition of liquid Si by electromagnetic levitation (collaboration with SiMaP laboratory)	201
4.1. Summary of the experimental conditions.....	201
4.2. General observations of the deposited films	202
4.3. Detachment by Smart Cut™	202
4.4. EBSD characterizations.....	203
4.4.1. EBSD cartography of samples deposited on a non-implanted substrate.....	203
4.4.2. EBSD cartography of a sample deposited on an implanted substrate.....	204
4.5. High Angle Annular Dark Field (HAADF) analysis at the interface between the film and the substrate.....	205
5. Photoluminescence analysis	206
6. Comparative study between the graphite and the self-aligned crucible.....	208

6.1.1. Summary of the experimental conditions.....	208
7. Roadmap for future developments.....	210
8. Conclusion of the chapter	211
References.....	212
Conclusion of the thesis	213
Kinetics of Smart Cut™ at high temperature.....	213
Smart Cut™ assisted by laser beam annealing.....	213
Fabrication of Si foils by LPE onto an implanted substrate.....	214
About the thesis strategy	214
Conferences, publications and patents.....	215
Résumé de la thèse en français.....	216
Folio administratif	250

Chapter I: Introduction

Abstract: Wafers of Si are as the starting brick for a wide variety of devices and systems in electronics, photovoltaics and, more and more, in medicine. Working with thinner wafers allows to both reduce the cost, and to possibly form a bendable device. The process proposed here offers an innovative way to elaborate thin wafers of Si, by depositing of liquid Si upon an implanted Si substrate, in order to induce an epitaxial growth as a first step, and a detachment of the resulting film by Smart Cut™ as a second step, by leveraging the heat diffusion subsequent to the crystallization. The applications choice is highly versatile, e.g. for solar panels or for flexible electronics. Indeed, the mainstream photovoltaics based on silicon (Si) reaches a plateau in terms of efficiency improvement. Thus, the development of new functionalities, such as bendability of the device appears as a good strategy for solar panels producers. On the other hand, the market of devices allowing the internet of things is about to explode, and requires cheap and ubiquitous electronic devices. The present work relies on two main study subjects: the kinetics of detachment by Smart Cut™ at high temperature and the crystallization of Si in the defined conditions of the process. Finally, hetero-structure such as Si-On-Glass and Si-On-Sapphire are fabricated for the first time by laser-assisted Smart Cut™, exploiting the comprehension of the kinetics of films detachment at high temperature.

1. Description of the thesis topic

1.1. Personal views of the societal context for both microelectronics and photovoltaics

The amount of manpower by industrial product has been continuously decreasing since the second industrial revolution by the exceptional progress realized in terms of industrialization. Thus, under Fourastié's principle, the industrial cost follows the same tendency of continuous decreasing [1]. As a consequence, the improvement of the technological content appears as the main innovation leverage to keep added value of industrial products constant or higher. This process has been tremendously accelerated by the conversion to market society of the large majority of worldwide countries after the fall of the communist bloc.

Microelectronics is probably the most emblematic industrial sector illustrating this reality. The very famous Moore's law perfectly illustrates the underlying necessity of continuous improvement of the calculation power, in order to maintain profits in this very competitive market. Into parallel with the increasing of the calculation power, the majors of microelectronics are developing new fields of applications with the internet of things (IoT). These devices aim to bring an ubiquitous intelligence to daily products, in order to reduce risk, to improve the user experience and to allow a control over a multitude of objects. Different societal challenges such as the aging of the society, the reduction of energy consumption or the supply of food for 9.6 billion of people in 2050 can be partially solved by the use of IoT. Obviously, other fields of IoT applications can be considered as less useful for the common well-being.

The photovoltaics (PV) industry is facing another industrial context, as the cost per Watt peak has violently decreased in the past years, by the strong development of industrial capacity in China. This cost reduction is helping a lot the development of worldwide PV capacity and can be positively considered, apart the impact on the western PV industries and the environmental impact in China. The future of PV industry will be driven by the development of new functionality, such as flexibility of the panels or the development of energy storage, which is the missing brick on the electrical grids.

It remains that the raw material depletion as well as the reduction of industrial emissions will bring growing constraints over the development of the new generation of products for both microelectronics and PV industry. Therefore, innovative and frugal processes will be necessary in order to maintain the industrial roadmaps previously mentioned. This thesis aims to participate to this effort of developing alternative approaches in both microelectronics and PV.

1.2. Technological context in microelectronics

Most of microelectronics production starts on Si, whether the starting material is a bulk Si wafer or a wafer of Silicon-On-Insulator (SOI). Since the 70's, the Moore's law has driven the scaling down of the transistors, with exponential progresses in devices performance [1] and a continuous cost decreasing. The industrial roadmap resulting from this law basically imposes a scaling factor of 0.7 of the dimensions of the integrated circuit every 2 years. Nevertheless, the exceptional development of the mobile applications has recently complicated this straight paving. Indeed, the necessity of multitask components on a smaller and smaller device, with the constraint of the energy consumption, has led to integrate several functions on the same chip, such as radiofrequency, sensors, actuators (non-digital content) and of course the computational capacity and memory (digital content). The so-called More-than-Moore approach (illustrated on Fig. 1) pushes to the limit material science, circuit design and process development [2].

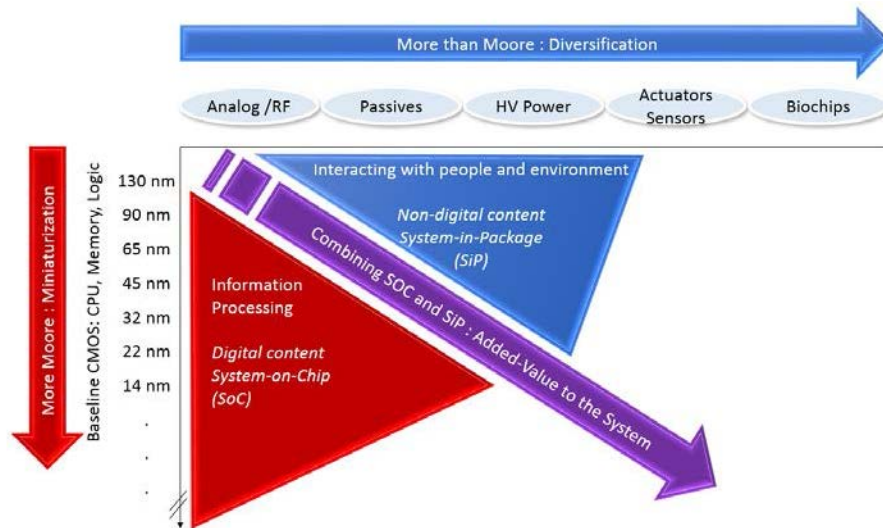


Figure 1: The combination of digital and non-digital content adds to the classical Moore's law the need of functionality diversification: the More-than-Moore's approach [2].

As a consequence, a huge pressure is imposed on the research facilities and on the industrial ecosystems to accelerate the development of any bricks allowing a performance step, among which, the substrate. This starting brick appears as the central trunk for many alternative approaches in microelectronics, such as fully-depleted Silicon-On-Insulator (FD-SOI) technology [3, 4] or for the development of electronic-photonic integrated circuits on Silicon-On-Sapphire (SOS) [5].

1.3. About SOI and Smart Cut™ technology

Both materials are part of Soitec portfolio of products, but only FD-SOI substrates are produced by the flagship technology of Soitec, the Smart Cut™ process. This elegant way of transferring a layer of semiconductor upon another is based on ionic implantation, wafer bonding and layer splitting induced by a thermal annealing, as illustrated on Fig. 2. It allows to report, with an extreme control of the thickness and a low material damaging, layers as thin as a ten of nanometers [6].

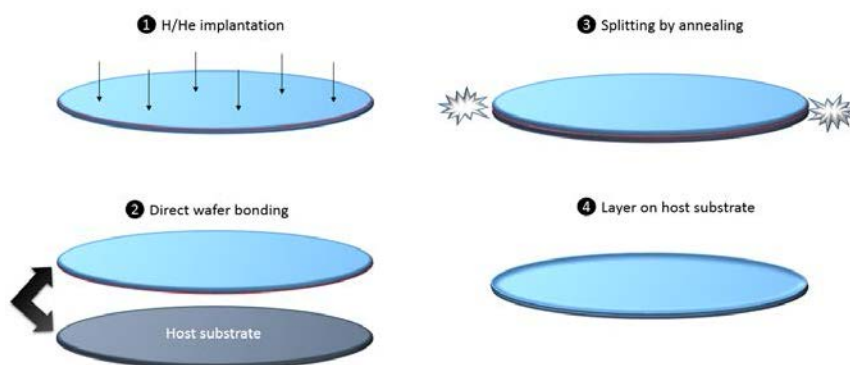


Figure 2: Main steps of the Smart Cut™ process.

This process has become the industrial standard for the production of SOI wafer. On the other side, this technique is still emerging for the fabrication of hetero-structures such as SOS (or III-V material on Silicon), because of the difficulty to anneal two materials of different nature, bonded together. Indeed, the coefficient of thermal expansion (CTE) varies with the material, and can lead to the damaging or

to the breakage of a bonding of two different materials when annealing it. Due to this difficulty to implement the film transfer by Smart Cut™, that kind of hetero-structures is usually fabricated by bonding the two materials together, followed by a chemical-mechanical polishing (CMP) to thin the upper wafer up to required thickness layer [7]. The resulting substrate is called bonded-SOS (bSOS). The main part of the wafer is obviously lost during the CMP step. Additionally, this relatively slow process when applied to an important thickness removal, is uneasy to apply for large wafer diameters for thickness uniformity matters [8]. This brings us to the first object of study of this thesis, i.e. to develop an alternative annealing approach to enlarge the Smart Cut™ domain to hetero-structures like SOS or Silicon-On-Glass (SOG).

2. Hetero-structure elaboration by laser-assisted Smart Cut™

2.1. Description of the process

As explained earlier, the main issue to proceed to the splitting of the bonded structure is the full-plate annealing, due to the CTE difference. Thus, it is proposed to apply an ultrashort-time annealing at high temperature, on a limited area of the implanted material, with a limited side-heating of the second material bonded with. The solution can be found by using a laser-beam, of a defined wavelength, in order to have a beam absorption limited to the implanted material. The annealing of the entire plate can be realized by a scanning a limited area at once, as illustrated on Fig. 3. Thus, with the proper conditions of annealing, the layer splitting by Smart Cut™ can theoretically be thermally induced without breakage of the plates. The required weak thermal diffusion within the bonded structure requires an ultra-short time annealing, what implies to anneal the implanted structure at much higher temperature than the classical conditions of Smart Cut™, as we will see in the next chapter.

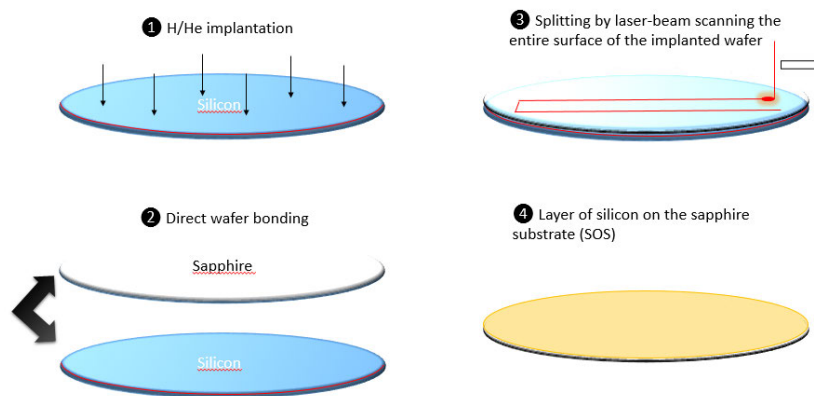


Figure 3: Main steps of the Smart Cut™ assisted by laser-beam annealing. Nota bene: the brownish yellow color indeed corresponds to a layer of SOS of a thickness inferior to 1 μm .

Considering a fast scanning of the laser beam, the process is much faster compared to the bSOS approach. Additionally, the initially implanted Si wafer can be reused for another cycle, as it is the case in the Smart Cut™ process. We will go back a bit later on the different aspects to investigate in order to put into practice this first process.

3. Why going toward thin wafer of Si?

3.1. Market of photovoltaics

As anyone knows, most of European producers of solar panels are facing difficult times, due to the continuous deflation of the cost per watt peak (€/Wp) driven by the development of major Chinese and Taiwanese producers. The decreasing of the governmental incentives has been an additional factor of bankruptcy for many European factories [10]. In this technological struggle, important efforts of research are put on replacing bulk Si by alternative structures and materials, like thin-films (mainly Si, Cd-Te, CIGS and amorphous-Si), heterojunction dye sensitized or organic cells. This wide variety of material is illustrated in the Table 1. Despite important progresses of the competing technologies, cells based on bulk Si still present conversion efficiency superior to most others. It is worth noting than most of the research groups present in Table 1 are either from Japan or Western countries.

Table.1. Summary of the confirmed cell and submodule efficiencies for the main solar cell technologies [11].

Classification	Efficiency [%]	Test center (date)	Description
Silicon			
Si (crystalline)	25.6 ± 0.5	AIST (2/14)	Panasonic HIT, rear-junction
Si (multicrystalline)	20.4 ± 0.5	NREL (5/04)	FhG-ISE
Si (thin film transfer)	20.1 ± 0.4	NREL (10/12)	Solexel (43 µm thick)
Si (thin film minimodule)	10.5 ± 0.3	FhG-ISE (8/07)	CSG Solar (<2 µm on glass)
III-V Cells			
GaAs (thin film)	20.5 ± 0.6	NREL (5/12)	Alta Devices
GaAs (multicrystalline)	18.7 ± 0.6	NREL (11/95)	RTI, Ge substrates
InP (crystalline)	19.6 ± 0.4	NREL (4/90)	Spire, epitaxial
Thin film chalcogenide			
CIGS (cell)	20.5 ± 0.6	NREL (5/14)	Solibro, on glass
CIGS (mini-module)	18.7 ± 0.6	FhG-ISE (9/13)	Solibro, four serial cells
CdTe (cell)	19.6 ± 0.4	Newport (6/13)	GE Global research
Amorphous/microcrystalline Si			
Si (amorphous)	10.1 ± 0.3	NREL (7/09)	Oerlikon Solar Lab
Si (microcrystalline)	11.0 ± 0.3	AIST (1/14)	AIST
Dye-sensitized	11.9 ± 0.4	AIST (9/12)	Sharp
Organic			
Organic thin film	10.7 ± 0.3	AIST (10/12)	Mitsubishi chemical
Organic (minimodule)	9.1 ± 0.3	AIST (2/14)	Toshiba (four series cells)
Organic (submodule)	6.8 ± 0.3	AIST (10/12)	Toshiba (15 series cells)
Multijunction devices			
GaInP/GaAs//GaInAsP/GaInAs	44.7	FhG-ISE (01/14)	Soitec, FhG-ISE, CEA Leti [20]
InGaP/GaAs/InGaAs	37.9	AIST (2/13)	Sharp
a-Si/nc-Si/nc-Si (thin film)	13.4	NREL (7/12)	LG Electronics

This good balance between conversion efficiency and industrial maturity of Si probably explains why the market share of Si has never been that high (i.e. considering thin film, monocrystalline-Si and multi-crystalline-Si) as shown on Fig. 4 over a historically high market of photovoltaics.

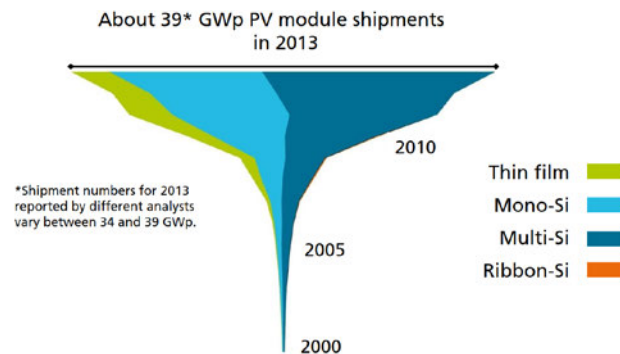


Figure 4: Global annual photovoltaics production by technology [10].

3.2. Thin-foils of Si applied to photovoltaics

Considering this domination of bulk Si as the starting material, an incremental approach has been investigated in the late 2000's: the thin-foil silicon solar cells [13]. The driving concept consists in reducing the thickness of the active material to the optimum of light absorption. Therefore, thin-foils solar cells use less than 100 μm of thickness (e.g. the world record has been established with a 60 μm cell [12]), compared to the 180 μm of classical Si bulk cells obtained by multiple wafer sawing (MWS) [13]. Additionally, this technology possibly allows to form flexible panels, like the S-Tile of Solixel (Fig. 5), which can facilitate the building integration of the panels. Thus, this technology combines the advantage of the thin-film technology (such as a-S), drastically reducing the use of active material, and the bulk technology with high conversion efficiency.



Figure 5: Illustration of the S-Tile solar panels of Solixel (© 2015 Solixel).

4. Ultra-thin chips based on thin Si wafer

The use of Si films of similar thickness is already running for the industrial production of microsystems, such as for Micro-Electromechanical Systems (MEMS). The MEMS thin membranes are machined or etched within a wafer of regular thickness (500 μm to 1000 μm) with microelectronics derived processes [14]. Similarly, a thinning of microelectronics chips can be realized at the end of the process, when specific form factor or power dissipation are required [15]. Thus, an alternative option for both MEMS and chips can be to start from a Si wafer, having the required thickness (from 75 μm to 300 μm) [TW 06]. The Fig. 6 gives some examples of applications of ultra-thin chips.

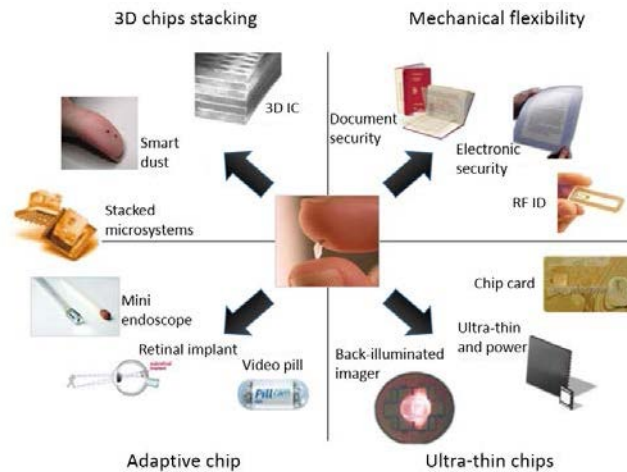


Figure 6: Illustration of the driving applications for the development of ultra-thin chips [15].

5. Elaboration of thin foil of single-crystal Si by liquid phase epitaxy on an implanted Si substrate

In this thesis, we propose an innovative approach to fabricate the Si foils for both mentioned fields of applications (i.e. microelectronics and photovoltaics). This process, described in Fig. 7 relies on the spreading of a film of liquid Si (above the melting point of Si, $T_m = 1410\text{ }^\circ\text{C}$) upon an implanted Si substrate. It is worth noting that the low viscosity of liquid Si can help the spreading to form a film of the thickness required for the desired applications (i.e. inferior to 100 μm). The Si substrate acts as a seed layer, all over the surface of the film, in order to facilitate a liquid phase epitaxial growth (LPE). Simultaneously to this solidification, an important amount of heat diffuses toward the implanted zone due to the very high latent heat of Si ($L_{Si} = 1926\text{ kJ/kg}$). Thus, the thermal mechanism of defects formation can be activated, possibly up to the splitting of the upper part of the implanted substrate, with the deposited film upon. The so-formed Si foil is detached from the substrate that can be reused for another cycle.

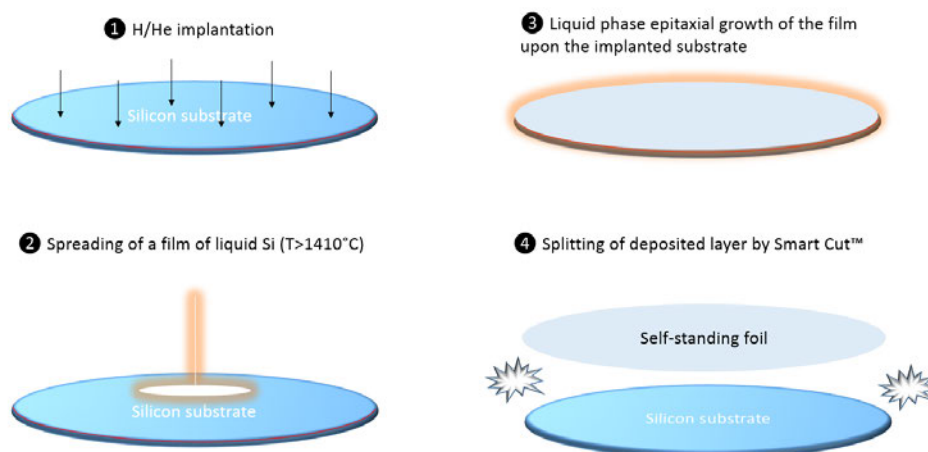


Figure 7: Description of the main steps of the proposed process to form foil of single-crystal Si.

6. Description of the thesis strategy.

As the main goal of the thesis is to explore the feasibility of alternative uses of Smart Cut™ background (i.e. the annealing of an implanted material into contact with another one), the experimental routine will require a wide variety of samples and characterizations. Of course, this will sometimes imply a more qualitative approach instead of a conclusive one. A constant exists between the two processes presented above, in a sense where they both consider an annealing of the implanted substrate at much higher temperature than the industrial process of Smart Cut™ usually does (i.e. $T < 600\text{ °C}$). As a consequence, the first step of the study will be to extend the comprehension of Smart Cut™ in these conditions of high temperature. This will be developed in the first experimental chapter (Chapter IV).

Therefore, the characterization of the splitting kinetics is established by use of a rapid and well-controlled annealing tool. The range of temperature starts with conditions from the literature (typically up to 500 °C) and goes up to the maximum measurable by direct observation of the splitting itself (i.e. up to 700 °C). Based on this characterization, a model is proposed to explain the experimental observations. This model relies on the behavior of the implanted species when increasing the temperature of splitting annealing. In particular, it is observed that particular conditions of annealing lead to a reduction of the implanted dose. This reduction affects the kinetics, and can be identified by various experimental observations. Different characterizations are brought to support the model. Finally, numerical calculations are run to establish predictive assumptions for higher temperature of annealing (up to the melting point of Si, $T_m = 1410\text{ °C}$). Later on in the work, these predictions are completed by the characterization of splitting by laser annealing (i.e. in a much higher temperature range of $900\text{--}1300\text{ °C}$).

Once establishing a characterization and a predictive model for the splitting kinetics, the two processes introduced by this thesis are separately investigated (Chapter V and Chapter VI). However, the experimental modus operandi are similar, starting first by modelling, in order to define a tight design of experiment. It is worth noting that without these comprehensive steps, the limited equipment time would have rendered the investigation impossible. Indeed, the samples preparation has required the use of a set of completely different equipment (lasers, three different chambers of LPE), what has limited the experiment time by machine. After this predictive work being established, the processes are investigated by applying the resulting design of experiments. Finally, the samples are characterized regarding the requisites of the final application, in order to have a qualitative comprehension of the different physical parameters involved.

Thus, the process of splitting by laser-beam annealing is first investigated with numerical calculations, in order to determine the loss of implanted species, mentioned earlier. Then, implanted substrates without bonding with other wafers are annealed by laser-beam, to prove the possibility to form blisters, which are considered as a preliminary condition for the splitting of an equivalent sample after bonding with an acceptor wafer. After this preliminary work, different conditions of annealing (i.e. in terms of time and temperature) are applied on two different types of samples (Si bonded with sapphire and Si bonded with glass) in order to determine a splitting kinetics. The experimental results of splitting conditions are then combined to numerical modelling of the laser annealing (providing an exact signal of temperature as a function of time) in order to establish a splitting model. Finally, the samples are characterized on several parameters important for the industrial applications.

The same strategy is applied for the exploration of the second process, of elaboration of Si foils. The modelling part first proposes the solidification of different types of films of liquid Si upon a cold Si substrate. Then, the splitting model established earlier in the study is applied with the calculated thermal diffusion resulting from the solidification of the film. The main objective is to validate that the solidification of a solid layer into contact with the implanted substrate is formed early in the process, in order to offer the possibility of layer detachment by Smart Cut™ splitting. Then, the experimental part of deposition of liquid Si onto different types of substrates (with and without ionic implantation) is realized by help of different epitaxy benches. Different types of characterization are realized in order to evaluate the crystalline properties of the Si foils. Finally, a roadmap for the next development steps is proposed.

References

- [1] **E. Cohen**, La prospérité du vice, Une introduction (inquiète) à l'économie, Albin Michel, 2009.
- [2] "More-than-Moore" ITRS White paper, editors: W Arden, M. Brillouët, P. Cogez, M. Graef, B. Huizing, R. Mahnkopf, p. 8.
- [3] **M. Ekman, K. Persson, G. Grimvall**, Lattice dynamics and thermodynamic properties of the β -Sn phase in Si, *Phys. Rev. B*, vol. 62, no. 22, pp. 14784-14789, 2000.
- [4] **S. P. Pandey, A. Dayal, S. Khandelwal, S. Akashe**, Multiple-gate Silicon on Insulator (SOI) MOSFETs: device design and analysis, *Proc. of the IEEE*, pp. 1-6, 2013.
- [5] **K. Bourdelle**, Engineered substrates for advanced CMOS technology nodes and More-than-Moore applications, in Functional nanomaterials and devices for electronics, sensors and energy harvesting, editors : Alexei Nazarov, Francis Balestra, Valeriya Kilchytska, Denis Flandre, pp. 12-20, 2014.
- [6] **T. Baehr-Jones**, A. Spott, R. Ilic, A. Spott, B. Penkov, W. Asher, M. Hochberg, Silicon-on-sapphire integrated waveguides for the mid-infrared, *Opt. Expr.*, vol. 18, no. 12, pp. 12127-12135, 2010.
- [7] **P. E. Acosta-Alba, O. Kononchuk, G. Riou, C. Moulin, C. Bertrand-Giuliani, A. Claverie**, Mutli-scale thickness and roughness characterization of thin Silicon-on-Insulator films, *ECS J. of Sol. St. Sc. and Tech.*, vol. 2, no. 9, pp. 357-361, 2013.
- [8] **M. R. Oliver**, Chemical-Mechanical Planarization of semiconductor materials, editor: M. R. Oliver, pp. 5-12, 2004.
- [9] **B. T. Jonker, Y. D. Park, B. R. Bennett, H. D. Cheong, G. Kioseoglou, A. Petrou**, Robust electrical spin injection into a semiconductor heterostructure, *Phys. Rev. B*, vol. 62, no. 12, pp. 8180-8183, 2000.
- [10] Photovoltaics report, Fraunhofer Institute for Solar Energy Systems ISE, pp. 1-42, 2014.
- [11] **M. A. Green, K. Emery, Y. Hishikawa, W. Warta, E. D. Dunlop**, Solar cell efficiency tables (version 44), *Prog. in Photov.: Res. and Appl.*, vol. 22, pp. 701-710, 2014.
- [12] **F. Dimroth et al.**, Wafer bonded four-junction GaInP/GaAs//GaInAsP/GaInAs concentrator solar cells with 44.7% efficiency, *Prog. in Photov.: Res. and Appl.*, vol. 22, pp. 277-282, 2014.
- [13] **F. Dross, J. Poortmans**, Crystalline thin-foil silicon solar cells: where crystalline quality meets thin-film processing, IMEC Energy, pp. 1-15, 2012.
- [14] **F. Ayazi, K. Najafi**, High aspect-ratio combined poly and single-crystal silicon (HARPSS) MEMS technology, *J. of Micro. Syst.*, vol. 9, no. 3, pp. 288-294, 2000.
- [15] **J. N. Burghartz, W. Appel, C. Harendt, H. Rempp, H. Richter, M. Zimmermann**, Ultra-thin chips and related applications, a new paradigm in silicon technology, conference publication in *Solid. St. Dev. Res. C*, pp. 29-36, 2009.

Chapter 2. State of the art

As we have noted in the introduction chapter, three distinct experimental works based on the layer separation of an implanted Si wafer (namely the Smart Cut™ technology) are treated in the thesis:

- the kinetics of splitting of an implanted Si for temperature in the range 450-700°C (Chapter 4)
- the use of a laser beam to induce the layer separation in an implanted Si wafer for the production of thin-film heterostructures (Chapter 5).
- the deposition of liquid Si upon an implanted Si wafer in order to form a Si foil by laser separation subsequent to the liquid Si crystallization (Chapter 6)

This chapter aims to summarize the main results of previous studies in the different addressed fields.

First, the main knowledge from the Smart Cut™ will be introduced in order to facilitate the understanding of the phenomena involved in the response of an implanted Si at elevated temperature.

Then, the existing technologies for the fabrication of thin-films heterostructures will be summarized before introducing the challenges of applying the Smart Cut™ approach in this field.

Finally, different processes for the production of thin wafers of Si and their main results will be presented.

1. About Smart Cut™ technology

Smart Cut™ technology has been widely studied for temperature annealing inferior to 500°C, where the current industrial processes are found [1]. The layer splitting is the final step of a complex mechanism of defect growth and coalescence involving diffusion process, and both surface energy and stress minimization.

Nevertheless, the splitting kinetics and the involved mechanisms is not fully understood for temperature in the range 500-700°C, mainly for experimental issues. Several physical parameters are affected by temperature, such as the diffusion coefficient of the implanted species or the stability of the defects.

Our objective here will be to introduce the industrial context of the Smart Cut™, before summarizing the main scientific knowledge brought by 20 years of research.

1.1. Historical aspects of Smart Cut™ and applications of SOI

The Smart Cut™ process has emerged in the beginning of the 90's in CEA Leti, motivated by the development of alternative routes for the fabrication of silicon on insulator (SOI) substrates [1]. This structure consists of a thin film of single-crystal Si separated from a bulk wafer by an insulator layer, or laying on insulator wafer. The resulting stacking has initially found applications in military, spatial and nuclear fields, as it provides a structure resistant to ionizing radiations, such as X-ray or γ radiations [2]. Nevertheless, the development of SOI-based technologies relies today on consumer applications in the field of microelectronics and telecommunication with the appearance of the fully-depleted SOI (FD-SOI) [3] and the high-resistivity SOI (HR-SOI) [4]. Indeed, thanks to the insulating layer, SOI-based components offer a lower power dissipation and a higher flexibility in the circuit design, compared to components based on bulk Si [5].

Different approaches have been considered for the fabrication of SOI substrates, among them the separation by implantation of oxygen (SIMOX). In this process, the insulating layer is formed by the implantation of oxygen ions into the Si wafer, followed by a step of annealing at high temperature (1250-1405 °C). Another approach uses the bonding and thinning, for instance the bonded and etched-back SOI (BE-SOI) [2]. The last process is still running at the industrial scale for the production of thin substrates, such as silicon on sapphire substrate (SOS), as we will see in the paragraph 2 of this chapter [6].

The inspiration of the Smart Cut™ came out with the observation of the materials constituting the nuclear reactors, under α irradiation. Indeed, the projection of light atoms, such as He, at high energy and dose, had been observed to induce blistering and flakes formation inside the reactor chamber. The combined effect of the excess vacancies generated by the high energies of the gaseous species and of the migration of the implanted species into these voids was proposed to help the formation of flat cavities into the material [7]. Nevertheless the resulting partial surface exfoliation was considered as an undesirable side-effect before the idea of Michel Brueel. Brueel proposed to bond a so-called "stiffener layer" into contact with the implanted surface, in order to help the lateral development of the cavities up to the layer splitting, parallel to the surface [1]. As we will see in what is following, this splitting step is the starting point of the Smart Cut™, as well as the one of the main topic of interest of this study.

1.2. Main steps of the Smart Cut™

In addition to the layer splitting step, different other steps are combined to produce a SOI wafer, as summarized on Fig. 1. The process starts with the formation of the insulating layer, in most case made of SiO₂ upon the so-called “donor wafer” (wafer A). This layer, whose thickness can vary between 10 nm and 1.5 µm, will become the buried oxide layer of the SOI structure [8]. This step is usually realized by thermal oxidation of Si in wet atmosphere, typically at 1000 °C. Deposition of oxide by chemical vapor deposition (CVD) or plasma-enhanced CVD (PECVD), despite more rarely considered, can also be used for this step [9]. In another configuration, the oxide is located upon the “acceptor wafer” (wafer B). This other configuration is called “inversed-bonding”, and will be of interest in this work, as we will see later.

After forming the oxide layer, an ion implantation of H for instance (or H then He) is realized in the donor wafer. Usually inferior to 200 keV, the implantation energy defines the depth of the mean ion projected range (R_p) and of the separation plane. The depth varies as a function of the final applications, typically between 100 nm (for FD-SOI structures) and 1.5 µm (for power applications) [10].

The implanted face is then bonded to the acceptor wafer, by direct bonding. The surface preparation before bonding can include chemical cleaning, chemical mechanical polishing (CMP) or plasma treatment.

The structure is then annealed, usually in a batch-annealing equipment, in order to weaken the implantation zone, up to its separation. Thus, the upper part of the donor wafer is transferred onto the acceptor one, what forms the SOI structure. The donor wafer can be “refreshed” (i.e. prepared for another cycle) up to several times.

Finally, the SOI wafer can be annealed, to remove the remaining implanted species and to strengthen the structure, and chemically etched and/or polished, in order to lower the surface roughness.

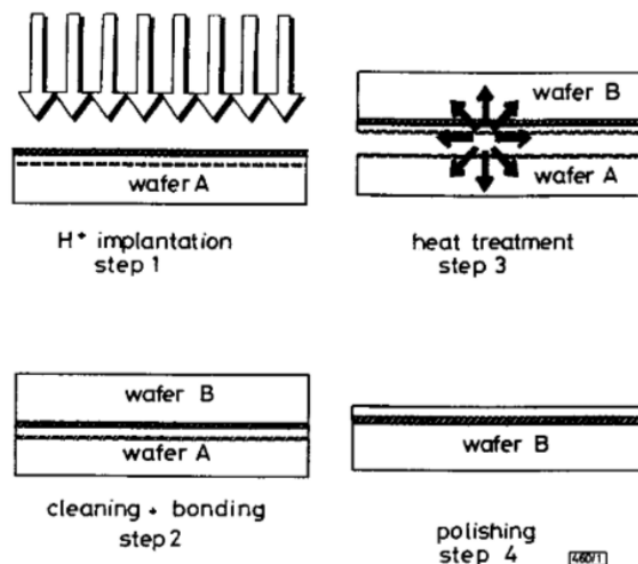


Figure 1: Principle of the Smart Cut™, as described by M. Bruel [1].

1.3. State of the art of Smart Cut™

The theory of Smart Cut™ has been constantly extended by several teams around the world. Despite some points of comprehension remain controversial, the splitting mechanism starting with the appearance of the early defects (platelets) up to the fracture is relatively well established and the research in that field has mainly been confined to the process with temperature below to 600 °C.

We will introduce step by step the theoretical aspects that will be useful for the analysis and for the comprehension of the kinetics of Smart Cut™, in the temperature range of the two processes we will investigate, i.e. for temperature superior to 1000 °C. It is worth noting that we will focus for the rest of the thesis on structure of silicon implanted with H only. It is worth noting that Smart Cut™ is also demonstrated with other materials, like Ge or III-V materials [11, 12]. We will go back on this point in the next part of the chapter.

1.4. Defects generated by the implantation

The ion implantation introduces atomic species which can precipitate in the gaseous state at a certain depth in the material. Interestingly, the choice of ionic species is very limited mainly for two reasons. The first imposes these species to form a gas during the annealing, to create cracks into the bulk material. As the second reason, they must induce a limited damaging during the implantation. Indeed, as the ions are strongly accelerated under an electric field before being introduced in the target material, light atoms (like H or He) will tend to slow down by electronic stopping, with a reduced amount of generated defects. Heavy atoms will tend to be stopped by nuclear stopping, by predominantly colliding with the target nuclei, what creates more damages [13].

The ion distribution follows a Gaussian distribution, see on Fig. 2, with R_p depending on the implantation energy. At the same time, matrix atoms are displaced and a significant amount of native defects, such as vacancies and self-interstitials, are created. The in-depth distribution is not located at the same depth compared to the ion profile (see on Fig. 2).

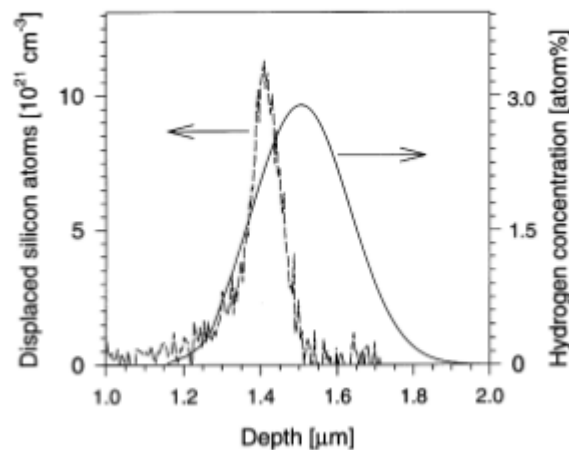


Figure 2: In-depth distribution of the implanted hydrogen (by Elastic Recoil Detection Analysis, ERDA) and the displaced Si atoms concentration as a function of sample depth (by Rutherford Back-Scattering, RBS) for Si sample implanted with $5.0 \cdot 10^{16} \text{ Hcm}^{-2}$ at 175 keV [14].

Different characterization tools, such as Raman or Fourier Transform Infrared spectroscopy (FTIR) show that implanted H is trapped by defects in Si. Atomic configuration of the defects and their relative concentrations vary with the implanted dose, as illustrated on Fig. 3. Furthermore, the implantation

dose has a strong influence on the kinetics of layer separation (splitting). On Fig. 3, the dose $1.0 \cdot 10^{16} \text{ Hcm}^{-2}$ and $2.0 \cdot 10^{16} \text{ Hcm}^{-2}$ are not sufficient to observe the splitting after thermal annealing (subthreshold dose), whereas $6.0 \cdot 10^{16} \text{ Hcm}^{-2}$ and $7.0 \cdot 10^{16} \text{ Hcm}^{-2}$ are. Among the variety of defects, we can distinguish the lower-frequency broad band (LF), below 2050 cm^{-1} , which is associated with multi-vacancies, denoted $V_n H_m$, with $m \leq n$. This type of defects is associated with highly disordered area of the implanted material. The higher-frequency (HF), superior to 2050 cm^{-1} , corresponds to single-vacancy defects, namely VH_n with $n = 2-4$, or to H-terminated internal surfaces $\text{Si}(100):\text{H}$ [15].

For subthreshold doses, the signal from the LF region is significantly larger than that from the HF region. On the other side, the HF modes and particularly the $\text{Si}(100):\text{H}$ mode are dominant for higher doses..

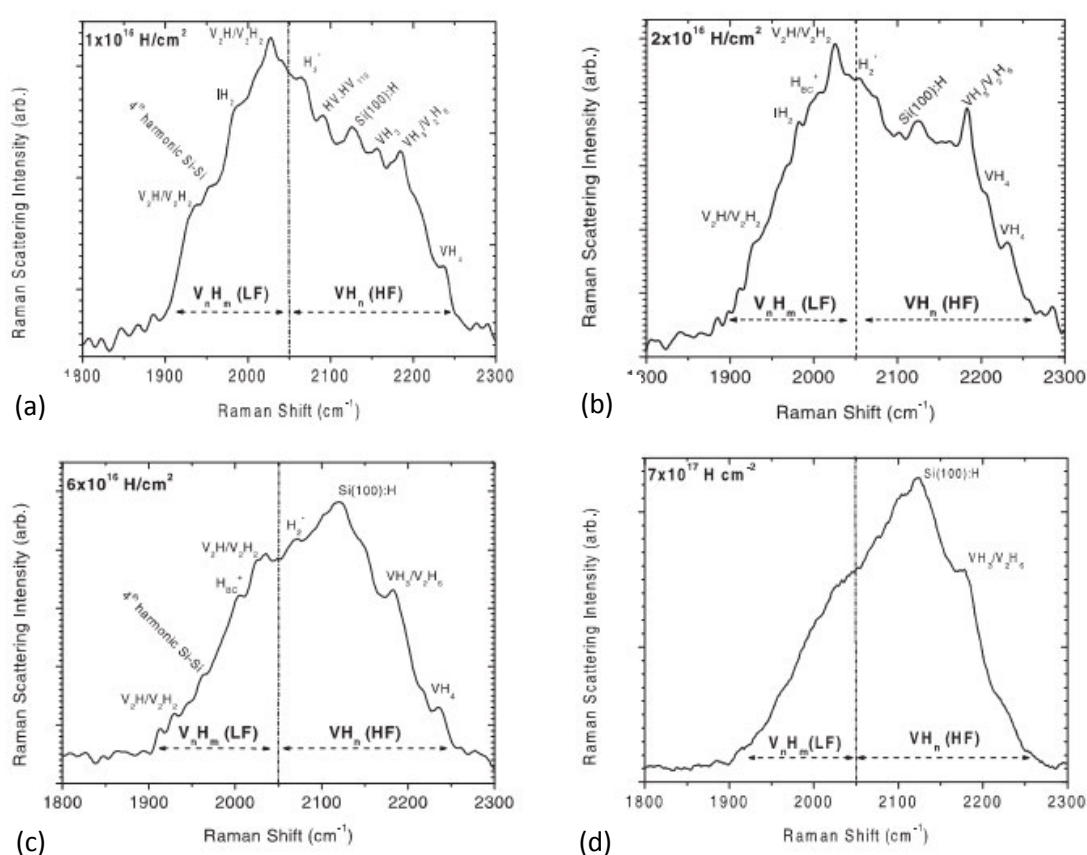


Figure 3: Spectra of Raman scattering intensity for implantation energy of 10 keV and doses of (a) $1.0 \cdot 10^{16} \text{ Hcm}^{-2}$, (b) $2.0 \cdot 10^{16} \text{ Hcm}^{-2}$, (c) $6.0 \cdot 10^{16} \text{ Hcm}^{-2}$ and (d) $7.0 \cdot 10^{16} \text{ Hcm}^{-2}$ [15].

1.5. Formation of the platelets during the annealing

During the annealing, a very specific type of structures can progressively be observed by Transmission Electron Microscope (TEM) at the maximum of the implanted zone (i.e. 200 nm around R_p): the platelet. These defects have a cylindrical shape with a diameter between 10 nm and 30 nm and a height of 1 or 2 atomic planes [16]. They are oriented along the crystallographic axis of Si, i.e. for (100) substrates, most of platelets are oriented parallel to the surface, in (100) plane, as figured on Fig. 4. However, platelets in {111} planes can also be observed depending the implantation conditions

Platelets have been shown to be filled with H atoms, either involved in Si-H (chemically bonded) or in H-H (gaseous). The evolution of the concentration of H has been studied with FTIR or SIMS characterizations, showing a decreasing of the concentration of H with annealing time. As, both FTIR and SIMS methods only detect H bonded with the matrix, and not the molecular H_2 , this decreasing has logically been put into relation with the formation of gaseous H_2 [5].

It is worth noting that the platelet formation is very specific to implanted Si, and is related to the chemistry of H within Si. Indeed, in metals, the little affinity between H and the lattice limits the formation of high-pressure pockets that eventually lead to blistering [17]. In that case, the spherical shape of defects is very different from the 2D shape of platelets.

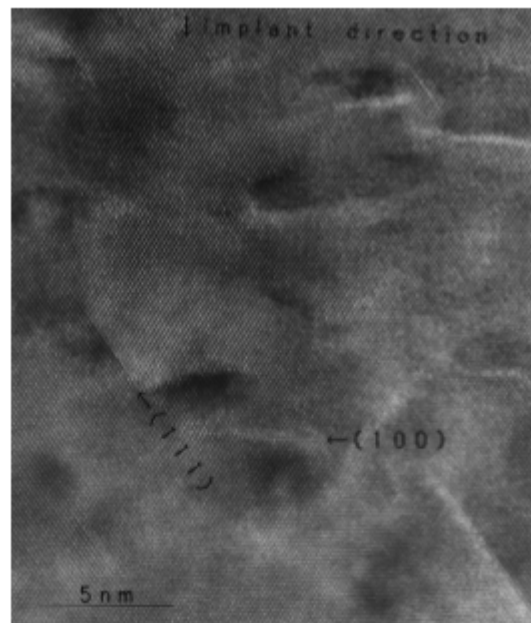


Figure 4: Bright field image by cross-sectional transmission electron microscopy (XTEM) of the damaged layer in Si implanted with $8 \cdot 10^{16} \text{ Hcm}^{-2}$ at 80 keV. The high resolution image was taken along [110] [18].

The population of platelets progressively increases during the annealing, as illustrated on Fig. 5. The growth kinetics has been widely studied by TEM, in order to identify the driving mechanism.

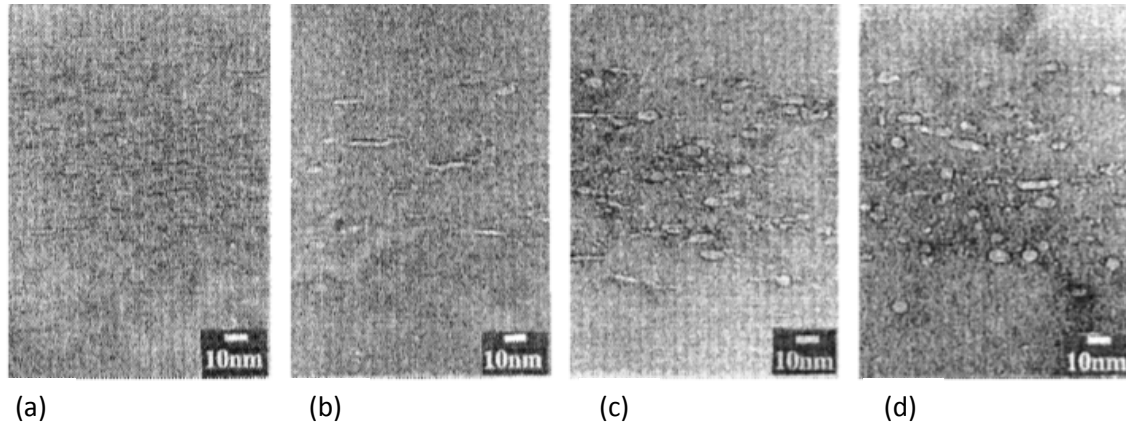
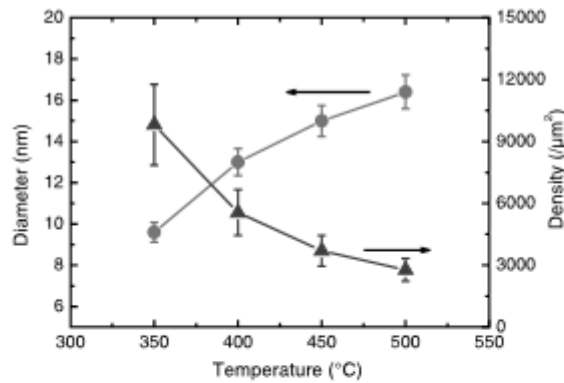


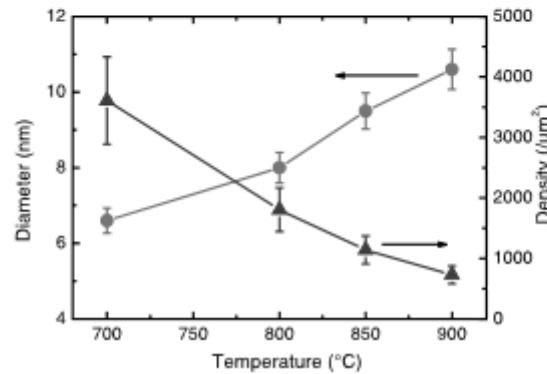
Figure 5: Transmission electron microscopy (TEM) images of defects created after (a) as-implanted state with implantation conditions of $3.0 \times 10^{16} \text{ Hcm}^{-2}$ at 61 keV, (b) after an annealing of 30 min at 500°C (c) 1 h at 500°C and (d) 10 h at 500°C [19].

Thus, it was observed that after the nucleation step in the early stages of the annealing, the density of platelets decreases, whereas their mean size increases, as reported on Fig. 6. This competitive growth is related to the Ostwald ripening, where the reduction of the surface energy is the driving force. Thus, inter-diffusion of H between the platelets will tend to promote the bigger objects [16].

The driving force for this mechanism is the reduction of the formation energy consecutive to the size increase of the cavities. In the meantime, while the overall elastic energy decreases in the layer, the strain locally increases around the projected range of the protons, as the annealing proceeds [5].



(a)



(b)

Figure 6: Variations with temperature of the platelets density and mean size for $t = 1 \text{ h } 30 \text{ min}$ annealing (a), variations with temperature of the spherical cavities, density and mean size for $t = 30 \text{ min}$ annealing for Si samples implanted with $3.0 \times 10^{16} \text{ Hcm}^{-2}$ at 61 keV [19] (b).

1.5.1. Analysis of platelets orientation

As we have seen earlier, the H implantation is responsible of the formation of numerous defects in the Si matrix. It also induces an important out-of-plane strain (ϵ_{zz}) and a bi-axial compressive stress (σ_{xx} and σ_{yy}) as illustrated on Fig. 7 [20].

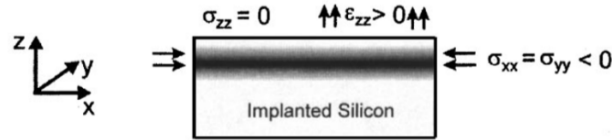


Figure 7: Schematic representation of the out-of-plane strain and in-plane stress within the implanted material.

Johnson has developed an analysis based on the total free energy change before nucleation of a platelet (supersaturated state) and after nucleation of a platelet of a diameter R and thickness t (platelet state). His analysis shows that platelets, defined by their Burger vector b_n develop preferentially parallel to the surface. Indeed, non-aligned platelets would see their development limited by the compressive stress present in the implantation zone [20].

1.6. Formation and coalescence of micro-cracks

During later stages of annealing, much bigger objects appear (of μm size): the micro-cracks. Based on the observation of the coalescence of platelets it has been proposed that namely the platelets are responsible for the initiation of the micro-cracks [1, 5, 21]. Other studies assess that the nucleation of micro-cracks remain unclear [22]. Later on, the micro-cracks follow an Ostwald ripening process, similarly to platelets. However, coalescence involving crack propagation is observed later in the annealing (Fig. 8), with an increase of the surface covered by the cracks as illustrated on Fig. 9 (a).

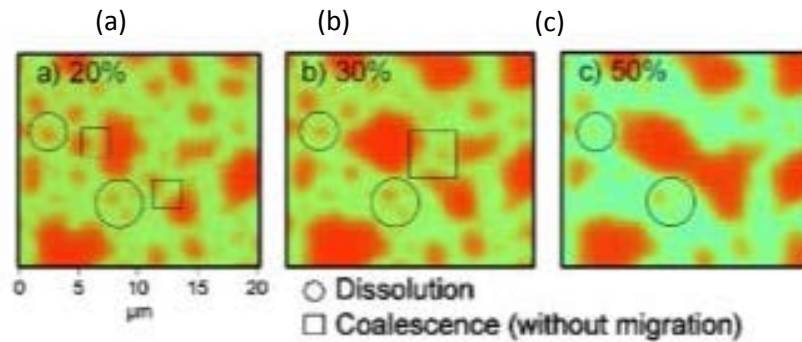


Figure 8: Images by optical profilometer of the buried micro-cracks after an annealing at 350°C of (a) 20%, (b) 30% and (c) 50% of the thermal budget of splitting. The images illustrate the dissolution of cracks by Ostwald ripening and the coalescence mechanism [2].

An interesting analysis of the opening of the damaged interface has allowed to measure (by mass spectrometry) the amount of gaseous H_2 present within the cracks as a function of annealing time. It clearly shows a continuous increase of the H_2 collected by the growing micro-cracks during the annealing [22] (Fig. 9).

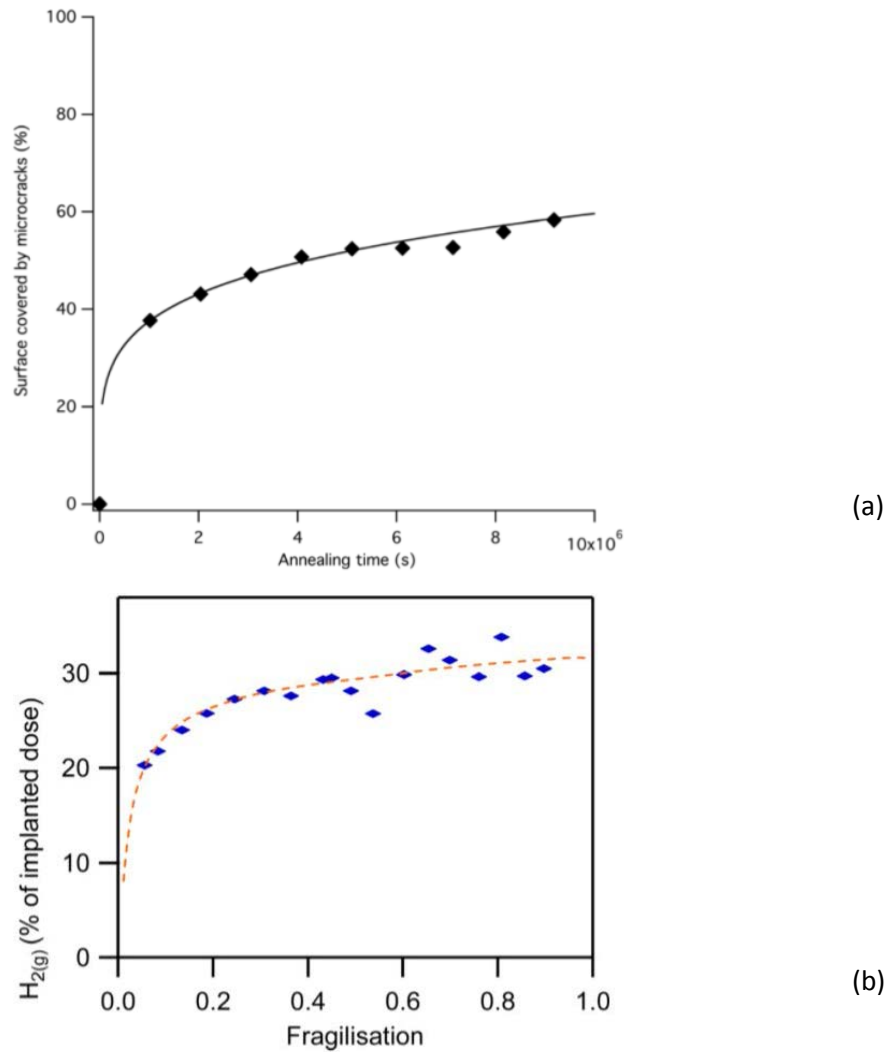


Figure 9: (a) Fraction of surface area covered by micro-cracks as observed by optical microscopy and (b) amount of gaseous H_2 released during the splitting measured by mass spectrometry [22].

Based on this observation, a model of the growth of micro-cracks has been proposed. Indeed, the amount of gaseous H_2 appears to be proportional to the area covered by micro-cracks. It suggests that the growth of micro-cracks is fed by the vertical pumping of H, as illustrated on Fig. 10.

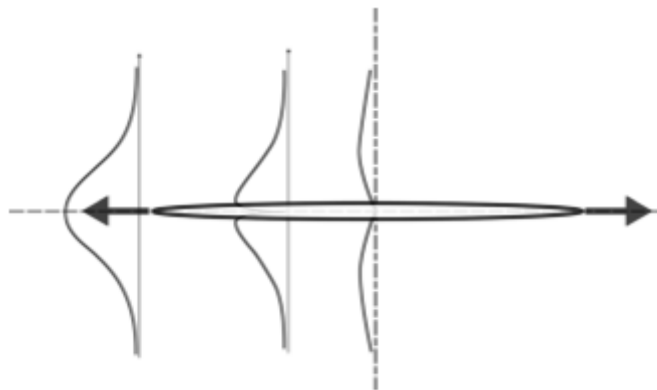


Figure 10: Schematic representation of the development of micro-cracks by vertical pumping [22].

The consequence of the development of cracks is a continuous pumping of H, to fill the platelets, in the early stage of annealing, and then the cracks, up to the layer splitting. As a consequence, this pumping leads to continuous decreasing of the H signal detected by FTIR or SIMS (as illustrated on Fig. 11.) due to its conversion into gaseous H₂ which is not detected by SIMS.

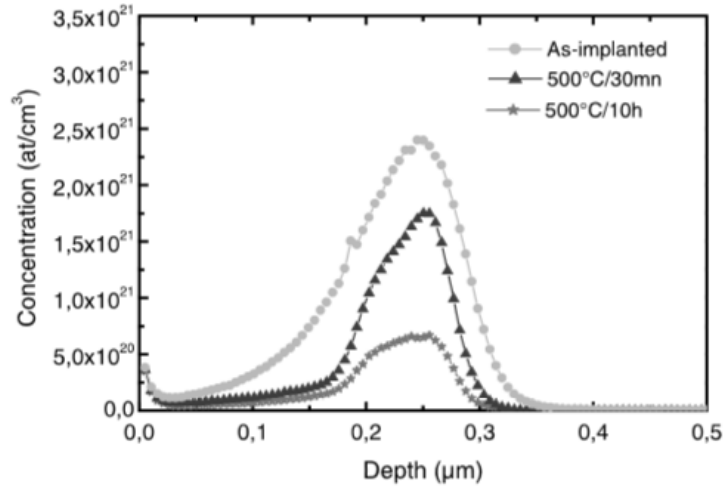


Figure 11: Evolution of the H profiles by secondary ions mass spectrometry (SIMS) as a function of annealing time [19].

1.7. Energy analysis of the crack propagation in the H implanted Si

Earlier in the literature, Freund has proposed a model of the crack opening, based on the Griffith analysis of the opening of fracture front. The criterion for the crack growth is the reduction of total mechanical energy of the system, i.e. the amount of mechanical energy released by the crack enlargement compared to the surface energy of the two newly created surfaces [24].

Freund considers a crack geometry as proposed on Fig. 12, in an elastic material with μ and ν the shear modulus and the Poisson ratio.

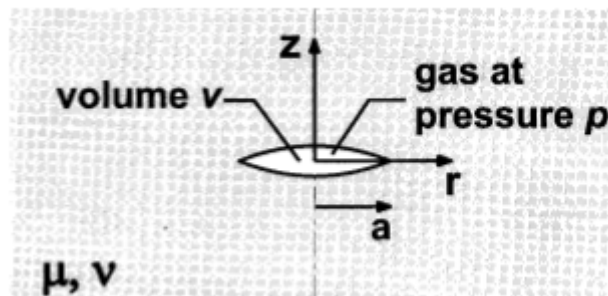


Figure 12: Schematic representation of the cross-section of a lenticular crack [24].

Postulating no internal pressure (p) in the cavity, the crack is closed and the material unstressed. As a consequence of p increasing, the cavity is opened and the crack faces symmetrically follow a vertical displacement u_z defined as following:

$$u_z = \pm a \frac{p}{\mu} \frac{2(1-\nu)}{\pi} \sqrt{1 - r^2/a^2}$$

The volume of the cavity for a given pressure and crack size is given by the integration of u_z over the crack area:

$$v(p, a) = \frac{8}{3}(1 - \nu)a^3p/\mu$$

The total mechanical energy of the system for a given pressure, $\Omega(p, a)$, is the elastic strain energy of the material plus the energy of the applied pressure loading on the crack faces. Integrating p over the crack surface area, we obtain:

$$\Omega(p, a) = -\frac{4}{3}(1 - \nu)p^2a^3/\mu$$

Considering a constant surface energy per surface unit γ , the total surface energy $\Gamma(a) = 2\gamma\pi a^2$. Finally, applying the Griffith criterion, of equilibrium between the evolution of mechanical energy of the system and the surface energy, we can deduce:

$$\left(\frac{\partial}{\partial a}(\Omega + \Gamma)\right)_p = 0 \rightarrow \frac{p}{\mu} = \sqrt{\frac{\pi}{1 - \nu} \frac{\gamma}{a\mu}}$$

Thus, the pressure required for the crack growth decreases as the crack size increases. From this equation, the use the law of ideal gas ($pv = nk_B T$, with T the absolute temperature and k the Boltzmann constant) yields:

$$\frac{8}{3}(1 - \nu)p^2/\mu^2 = nk_B T/\mu a^3$$

And by substitution of p/μ by the equilibrium equation, we obtain as the equilibrium size of the cracks:

$$\frac{8}{3}\pi a^2\gamma = nk_B T$$

This equation can be applied to the case of hydrogen implantation with a dose of J atoms per unit area. Taking a single crack within implanted material and considering that this crack incorporates all the implanted H over the crack area, it appears that for a crack of area πa^2 , the amount of H incorporated available to drive the crack is equal to $n = J\pi a^2$. It finally yields to a very useful relation describing the minimum implantation dose J_{min} , in order to have the splitting fracture:

$$J_{min} = \frac{8}{3} \frac{\gamma}{k_B T}$$

Experimental studies have shown that the minimum dose given by the above relation is slightly underestimated as a part of the implanted H remains chemically bonded to the Si matrix [22, 24]. Additionally, this ideal case only considers one single fracture, whereas the development of cracks during annealing will lead them to interact, and potentially to block their development between each other [8].

At this stage of cracks interaction, Penot has proposed a complementary model, based on Irvine theory, in order to determine a criterion of the cracks coalescence [8]. It relies on the stress intensity factor at the crack tip K_I . Thus, the coalescence occurs when K_I is higher than the toughness of the material K_{IC} :

$$K_I \geq K_{IC}$$

1.8. Splitting kinetics

Now, we will focus on a more macroscopic approach, looking at the kinetics of the splitting, i.e. the annealing time necessary to the splitting for a given annealing temperature and a given implantation. Lagahe has characterized this kinetics for different implantation doses, illustrated on Fig. 13 in the form of an Arrhenius plot [25].

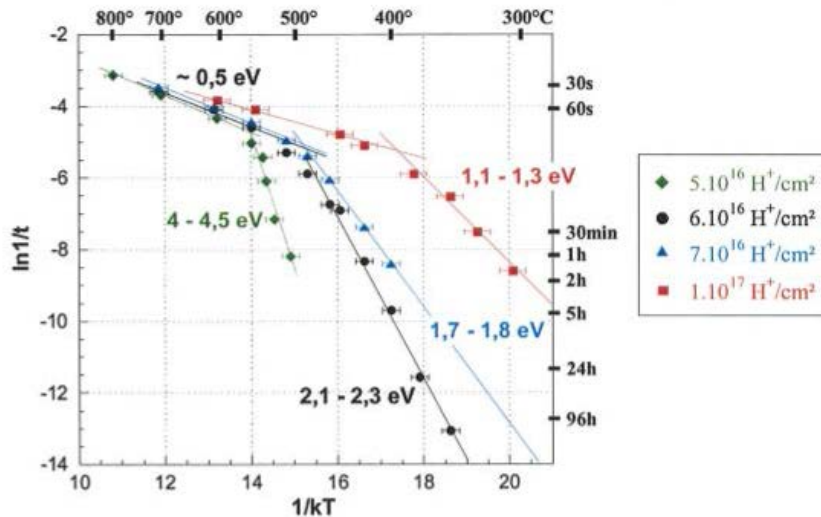


Figure 13: Kinetics of splitting as a function of the dose of implanted H [25].

This plot, despite being very “famous” in the Smart Cut™ literature, includes several elements whose comprehension is still controversial. First of all, the relation between the activation energy of splitting and the implantation dose is still not well explained. Early works [1], have put this variation into relation with the variation of the defect profile in the implanted material, as reported on Fig. 3. Penot has proposed that the change of activation energy originates from a pseudo Arrhenius relation, as following [8]:

$$E_{eff} = E_a + \frac{16\gamma}{3n}$$

The first term corresponds to the activation energy of hydrogen diffusion, to allow the competitive growth and the exchange of H between defects. The second term corresponds to the environment around the crack, i.e. the amount of H available for the crack growth. This analysis has been recently published [22].

Another discussion aspect about the splitting kinetics relates to the presence of two distinct regions: a low-temperature part, where activation energy varies with implantation dose, and a high-temperature part, with a convergence of this activation energy to 0.5 eV. The mechanisms driving to such behavior remain unclear. Lagahe proposed that a decomposition of the hydrogenated defects above a certain temperature, would lead the splitting process to be limited by the diffusion of free H, which activation energy is 0.49 eV [25]. This explanation will be further discussed in the first experimental part of this thesis.

In spite of the lack of solid theoretical explanation the work of Lagahe has introduced most of the concepts and tools on Smart Cut™ characterization, including the notion of thermal budget of splitting, that we will use later in the first experimental chapter.

1.9. Morphology of the surface after film separation

Another important practical aspect of the splitting process is the roughness of the two surfaces created by the splitting fracture. As SOI wafers are used as starting substrates for a wide variety of microelectronic applications, the surface roughness is a key parameter defining SOI quality. As it has been explained in several publications, and especially by the work of Penot, the surface roughness is directly defined by the growth, coalescence and propagation of cracks within the implanted material [8].

The Fig. 14 gives an illustration of the process of crack propagation and how it defines the surface roughness. In this particular case, the fracture path between two distinct micro-cracks forms a step that leads to particular roughness structure of the film after separation.

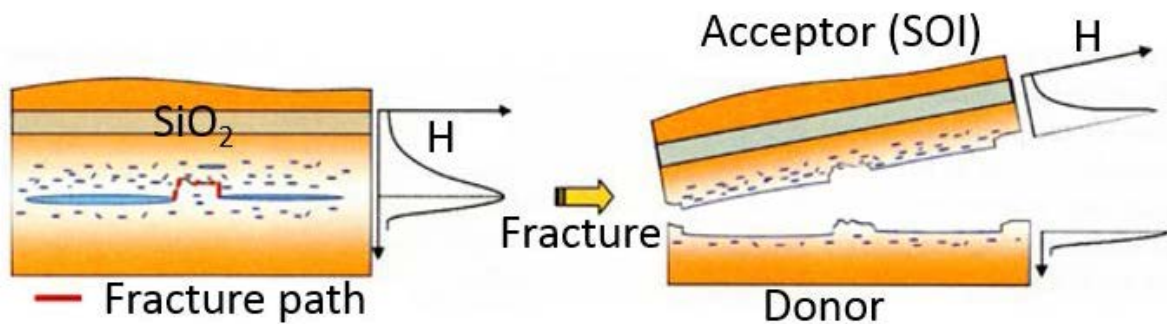


Figure 14: Schematic representation of the fracture propagation and how it participates the surface roughness of the transferred film [8].

Additional parameter affecting surface roughness is the implantation dose. It has been observed that the roughness decreases strongly with the implantation dose, as illustrated by the atomic force microscopy (AFM) images on Fig. 15. Indeed, it has been shown that high dose H-ion implantation weakens the implantation zone [26], what in return, facilitates the crack propagation with a subsequent reduction of the roughness. This observation can be put into relation with the density of platelets increasing with the implantation dose [18].

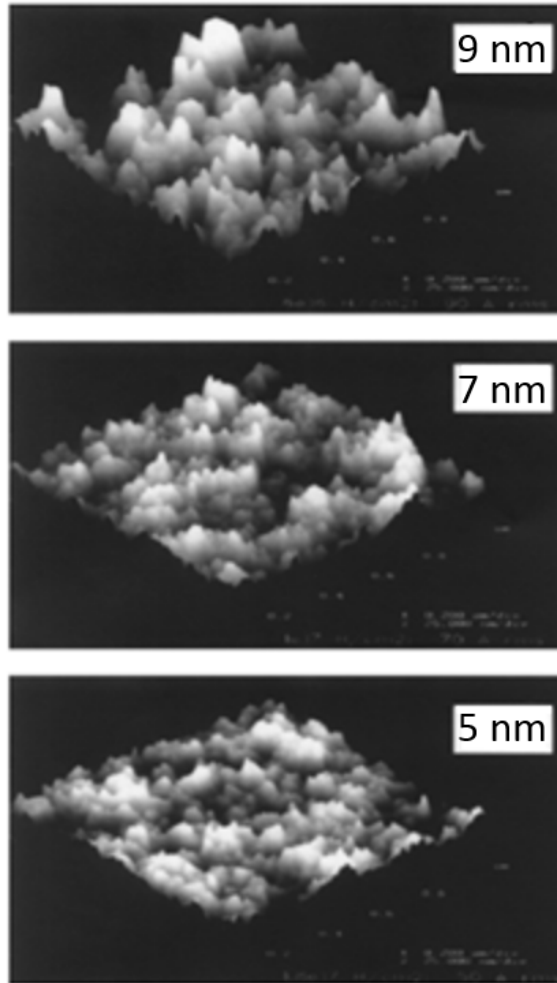


Figure 15: Surface roughness measured by AFM over $15 \mu\text{m} \times 15 \mu\text{m}$ regions for exfoliated samples implanted at 75 keV with $6.0 \times 10^{16} \text{ Hcm}^{-2}$ (top), $1.0 \times 10^{17} \text{ Hcm}^{-2}$ (middle) and $1.8 \times 10^{18} \text{ Hcm}^{-2}$ (bottom) [17].

1.10. Energy of the bonding interface

The process of direct bonding of two particle-free surfaces of Si/SiO₂ has been largely studied, and now relies on a relatively large consensus. We will restrain our description to hydrophilic bonding (i.e. to surfaces covered of native oxide, Si_{nox}, or thermal oxide, Si_{ox} being put into contact). After putting into intimate contact the two surfaces, weak physical interactions, such as H bonds formation, brings the force necessary to join the wafers and expel the gaseous species [27]. The propagation of the bonding front usually is a rather fast process (a few seconds) and can be observed by an infrared (IR) camera, as represented on Fig. 16.

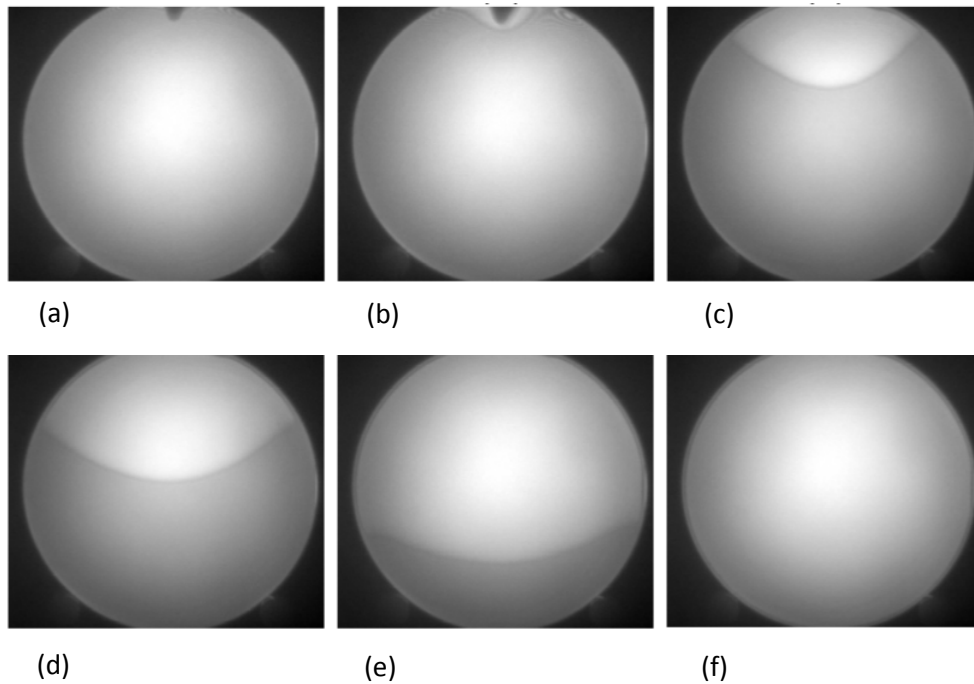


Figure 16: Propagation of the bonding front observed by IR camera [28].

After the initial closure of the interface, a reinforcement annealing is usually realized. The kinetics of reinforcement has been studied and can follow different chemical reactions according to the temperature of annealing. Thus, below $T = 150^{\circ}\text{C}$, the reaction is driven by the formation of siloxane bonds at the wafer surface at the contact points [29], as illustrated on Fig. 17:

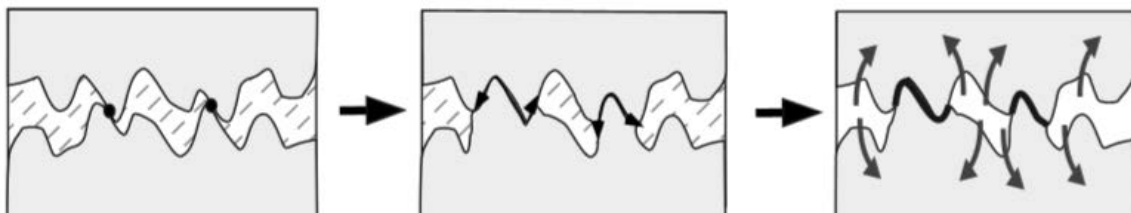
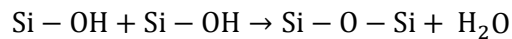
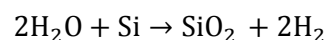
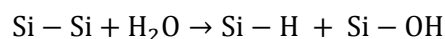


Figure 17: Schematic representation of the extension of contact points, leading eventually to Si oxidation [29].

The water produced by the silanol condensation is added to the water trapped during the interface closure. In case of Si_{nox} bonded with Si_{ox} or Si_{nox} bonded Si_{nox} , water has been proved to react with Si to form additional oxide, under the following reaction:



The reaction of silanol condensation is progressively competed at higher temperature by a second reaction:



, which leads to the disappearing of the water at the interface and formation of additional oxide layers. The evolution of the bonding energy as a function of the annealing temperature has been studied by double cantilever beam method, by introducing a razor blade at the bonding interface. The results for SiO₂-SiO₂ and SiO₂-Si bonding, after the stop of the blade and 1 hour after, are summarized on Fig. 18 [30].

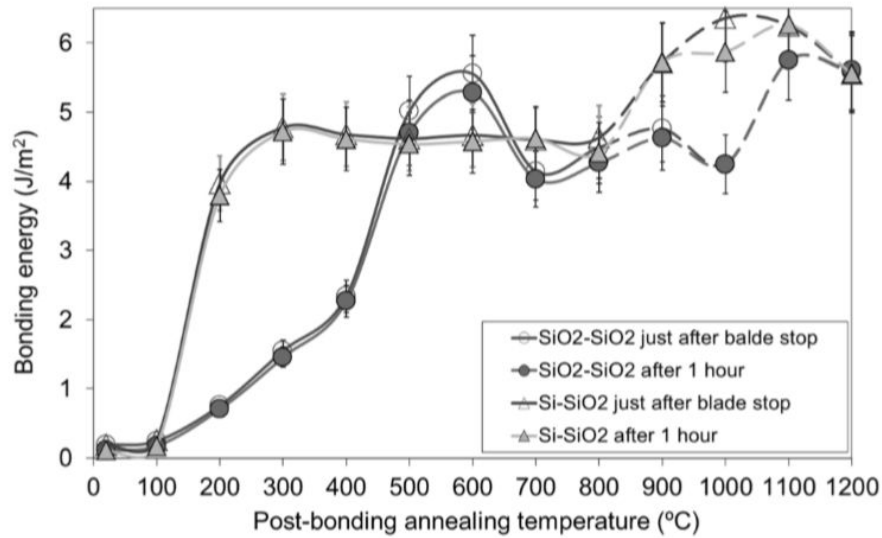


Figure 18: Evolution of the bonding energy measured by razor blade insertion, as a function of the annealing temperature [30].

1.11. Theoretical analysis on the effect of high temperature annealing on Smart Cut™ mechanisms

It has been postulated that an annealing temperature superior to 700°C promotes the out-diffusion of H, out of the implantation zone, possibly caused by the decomposition of H-related defects, disabling the growth of the 2D shape platelets which finally affects negatively the fracture possibility [19, 31]. On the contrary, it has been observed that the temperature stability of the defects within implanted Si increases with the temperature ramp rate [32]. Thus, the annealing of an implanted substrate by rapid thermal annealing (RTA) or laser, i.e. with high ramp rate, should preserve the defects stability.

Elsewhere, an increasing of annealing temperature enhances the out-of-plane tensile stress ε_{zz} within the implantation zone, what contrariwise promotes the formation of lenticular platelets with a positive effect on the fracture propagation [33, 34]. Additionally, a higher temperature annealing is supposed to enhance the probability of agglomeration of H and H₂ in a reduced number of internal (vacancy-derived) traps. [17].

Finally, as a room-temperature brittle material, Si follows a brittle-to-ductile transition, whose temperature T_c varies between 550°C and 600°C [35]. As the dislocations motion is rendered much easier above this temperature, the fracture stress should be significantly reduced by plastic deformation, affecting negatively the possibility of splitting for H-implanted material. Nevertheless, two elements tend to invalidate the role of such a transition. First, T_c in Si increases with the strain rate [35], the last being itself a function of the temperature ramp-rate, which, as explained earlier, increases with the annealing temperature. Thus, this aspect will not be investigated in this work.

2. Fabrication of planar heterostructures of semiconductors

Heterostructures are of industrial interest, as they can combine different types of distinct properties. Different approaches exist, either relying on the deposition of one material upon another or by assembling the two materials together.

2.1. Motivations for using planar heterostructures

Hetero-structure is a generic term in semiconductors which defines a stack of several materials lying on each other, with heterogeneous characteristics in terms of structural and electronic properties. Obviously, SOI is a perfect example of heterostructure. The complementarity of the layers forming the heterostructure allows optimizing the performance of the final devices built on the structures. On the other side, the production of such structure can be rendered difficult due to mismatch in thermal expansion coefficients which could lead to prohibitive stress levels during thermal processing of such structures, as illustrated on Fig. 18. Additionally, the reactivity of the species can lead to the formation of a non-desired third alloy at the interface between two layers.

It is worth noting that we will focus ignore the quantum well or the nanowire structures.

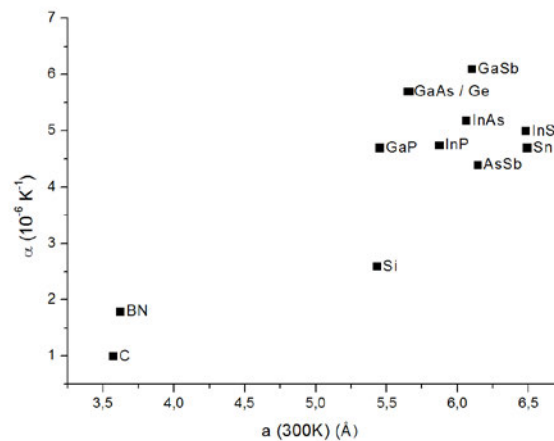


Figure 18: Coefficients of thermal expansion as a function of the lattice constant for semiconductors at room temperature [37].

Those layered heterostructures find industrial applications for instance in microelectronics and in photovoltaics. In the latter case, we consider heterojunction cells, where the optical absorption is optimized by combining materials having a desired absorption in a defined part of the light spectrum. Thus, the superposition of the different layers tremendously improves the yield of the total cell compared to each layer being separately taken, as illustrated on Fig. 19. The different layers are usually made of compounds of III-V elements, such as In, Ga, As, P, or N [38].

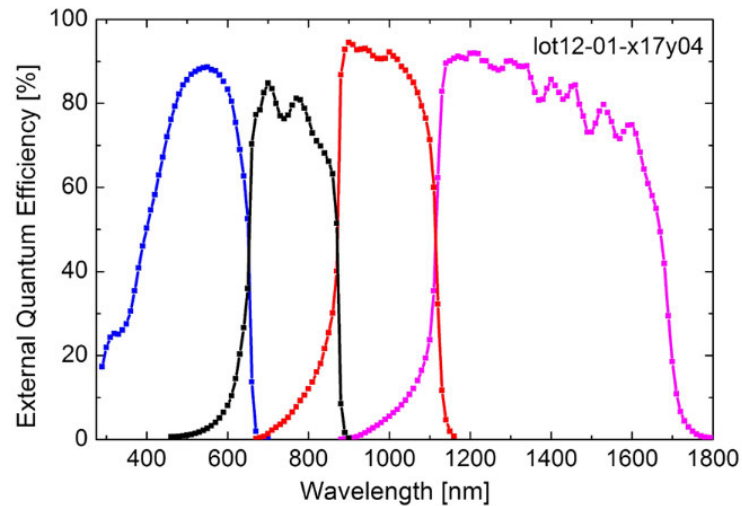


Figure 19: Absolute quantum efficiency of the four-junction GaInP/GaAs//GaInAsP/GaInAs solar cell [38].

In microelectronics, the same beneficial effect of planar heterostructures can be used to combine the specific properties from one layer (e.g. high mobility) with the properties of a second one (e.g. high electrical resistivity, good heat conduction, high refractive index etc.). Thus, apart SOI, which already is a standard heterostructure, materials such as III-V components and Ge can be used as the channel material for the fabrication of NMOS and PMOS transistors on Si substrates, respectively [39]. Additionally, structures with strained-SOI layer (sSOI), constituted by a layer of strained Si in a tensile state on an insulator layer, which provides a higher mobility compared to bulk Si [40]. Finally, more exotic structures such as lithium niobate on Insulator (LNOI) or lithium tantalate on insulator (LTOI) have been investigated for optical waveguides and resonators [41, 42].

A last type of planar heterostructures will focus our attention in this thesis work. It consists of a layer of Si transferred on a transparent substrate, such as glass (forming a Silicon-On-Glass wafer, SOG), quartz (SOQ) or sapphire wafer (SOS). It is worth noting that the particular properties of those alternative substrates (such as resistivity and optical properties), compared to the SiO_2 of the buried layer of SOI, offer better characteristics than SOI for some applications. In particular, SOS substrates are employed for RF systems, where the very high resistivity of sapphire reduces the RF signal losses as well as generation of parasitic harmonics [39]. SOS can also be used to produce performing waveguides, as figured on Fig. 20, due to the low refractive index of sapphire, which limits the leakage [43]. SOG can be used as a starting material for the fabrication of microelectromechanical systems (MEMS) [44]. SOQ has also been studied as a material for microwave applications [45].

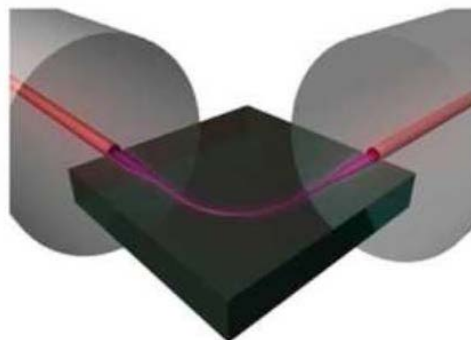


Figure 20: Schematic representation of a waveguide made of SOS [43]

After listing the various applications of planar heterostructures, particularly (SOS and SOG), we will review the state of the art of the fabrication techniques, both based on deposition techniques, and on bonding of two wafers of different types.

2.2. Fabrication techniques for the production of planar heterostructures

2.2.1. Heteroepitaxy of semiconductors

The heteroepitaxy consists in the growth of a single-crystal of one semiconductor on another single crystal wafer, acting as a substrate. This method offers the possibility to grow films of materials which are not available in the form of a wafer of desired diameter. The starting substrates for heteroepitaxial growth are quite limited, Si, GaAs, InP, 6H-SiC, 4H-SiC and sapphire being the most commonly used., They are required to be of a good crystalline quality and reasonably low cost [37].

The principal limitations of heteroepitaxy mainly originate from three factors, linked to the nature of the deposited film and the substrate. First, the lattice mismatch between the film and the substrate promotes the formation of misfit dislocations. Second, chemical reactions between the reactants and the substrate can contaminate the film, possibly leading to non-desired doping. Finally, the difference of structural characteristics, such as CTE and the Young's modulus, can affect the integrity of the structure during the cooling after the deposition step [46]. In addition, the surface of the substrate as well as the conditions of deposition can drastically affect the properties of the film. [37].

Heteroepitaxy can use traditional techniques like chemical vapor deposition (CVD) as well as more complex techniques like molecular beam epitaxy (MBE) or metalorganic vapor phase epitaxy (MOVPE), e.g. for heterojunction solar cells [38]. Atomic layer deposition (ALD) is the most recent method for the deposition of exotic layers for the most advanced microelectronics structures [47]. Finally, many approaches consider the deposition of a so-called "buffer layer" between the epitaxial layer and the substrate, in order to reduce the effects of the lattice constant mismatch between two layers [12].

SOS wafers were initially produced by heteroepitaxy, and can be a good example of the difficulties of using this method [43]. Indeed, Si (face centered cubic structure of diamond) and sapphire (rhombohedral crystal structure) presents significant lattice mismatch, see on Table 1. Additionally, chemical reactions between Si and Al_2O_3 may release Al atoms into the Si layer, which modifies the doping level of Si. Finally, the difference of thermal expansion coefficients between Si and sapphire causes structural damages to the heterostructure [46].

Table 1. Physical properties of Si and sapphire [46]

Parameters	Si	Sapphire ($\alpha - Al_2O_3$)
Crystal structure	Face-centered cubic	Rhombohedral (hexagonal)
Unit cell dimension (Å)	$a = 5.4301$	$a = 4.758, c = 12.991$
Density (g cm ⁻³)	2.33	3.98
Melting point (°C)	1412	2030
Thermal conductivity (W cm ⁻¹ °C ⁻¹)	1.3	0.25
Thermal expansion coefficient (°C ⁻¹)	$3.59 * 10^{-6}$	$8.4 * 10^{-6}$

2.2.2. Laser lift-off (LLO)

LLO approaches have been developed in order to separate the film from its substrate after deposition. Indeed the choice of a substrate deals mainly with its ability to form a film of a good quality and not necessarily with the specifications of the final device. As an example, LLO approaches have been widely studied for the fabrication of GaN layers to support the development of the blue light-emitting diodes (LED) [48]. In this example, sapphire is a good candidate as a substrate, by offering high-temperature stability and similar crystal symmetry with III-nitrides such as GaN. Nevertheless, host substrates of Si or GaAs would offer better characteristics, in terms of electrical or thermal properties and easier microsystem integration [48].

The procedure of LLO begins by the deposition of the layer of interest (e.g. a few μm of GaN) onto a substrate such as sapphire. Additional layers can be deposited during this step, like charge injection metallic layers. The system is then bonded to the final host-substrate, this step being usually realized by metallic bonding. Finally, the initial substrate is detached by the interfacial decomposition of the deposited layer, by laser irradiation through the substrate. The decomposition can be followed by a thermal or a mechanical detachment.

2.2.3. Bonding and etch-back approach

Because of the difficulties of heteroepitaxy, an alternative approach has been developed, due to the progress of the chemical-mechanical polishing: the bonding and etch-back SOI (BE-SOI) process [49]. It consists in bonding a silicon wafer with a sapphire and removing the major part of the Si wafer hereafter [6]. The same method can be applied to heterostructures like SOQ [39] or III-V materials [38]. The main advantage of this method is to avoid the step of growth of one material upon another. Additionally, it allows producing wafers with high degree of thickness uniformity as well as low surface roughness. Obviously, the inherent limitation of this approach is the loss of the majority of the wafer, which can be a severe economic limitation for some candidates (such as III-V materials). Furthermore, the steps of etching and polishing are rather slow, as they can generally imply single wafer equipment. For these reasons, the Smart Cut™ approach has been investigated as an alternative process for the production of other than SOI heterostructures.

2.3. Smart Cut™ applied to heterostructures

A few years after the first publication on Smart Cut™ [1], the team of Bruel has demonstrated the possibility to transfer thin layers of GaAs on Si by ionic implantation, wafer bonding and separation annealing [12]. The conditions of implantation, such as implantation dose and energy have an influence on the kinetics of appearance of platelets and micro-cracks, similarly to the case of implantation in Si. As an example, the Fig. 21 reports the blistering energy in GaAs co-implanted with H and He. Similarly to implanted Si, the conditions of implantation influence the kinetics.

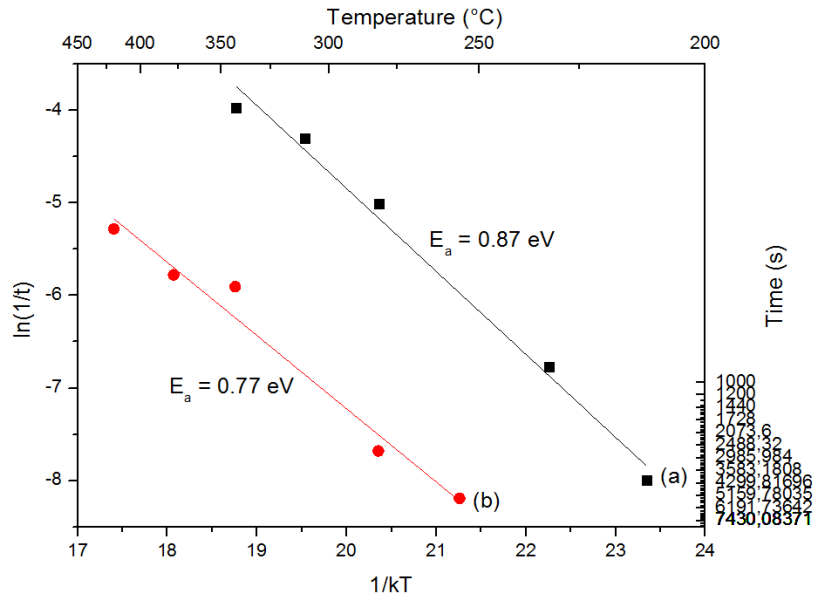


Figure 21: Activation energy of blistering in GaAs co-implanted with He first and then H. Co-implantation of He⁺ 5*10¹⁵ cm⁻² at 105 keV followed by (a) 2*10¹⁶ Hcm⁻² at 160 keV and (b) 3*10¹⁶ Hcm⁻² at 160 keV [12].

Despite successfully applied for some heterostructures, the Smart Cut™ technology still has limited use in production due to the difficulties associated with the difference of thermal expansion of the materials. Although recently different improvements of Smart Cut™ were developed to reduce thermal mismatch stress in heterostructures, such as the use of co-implantation in order to reduce the temperature of splitting annealing [12] or bonding the two different materials at elevated temperatures [50].

As already mentioned in the introduction of this work, the difficulty of application of Smart Cut™ for heterostructures for large diameter wafers is our motivation for exploring alternative routes, such as considering local and short time annealing utilizing laser beam.

2.4. Annealing of an implanted material by laser beam

A wide literature exists on the dopant activation by laser annealing after doping implantation of Si. The main advantage of this approach consists in avoiding the unwanted diffusion of dopants by the significant reduction of the annealing time [51]. Additionally, laser annealing can be considered for the relaxation of a stress in implanted structure, and especially to remove the defects generated by the implantation [53]. Indeed, the implantation of heavy atoms such Sb can induce the formation of a highly-disordered structure in Si, and even can lead to the creation of an amorphous layer [53].

It is interesting to notice that studies have investigated desorption of H in H implanted Si by nanosecond laser annealing [54]. In this case, the laser beam was utilized to reach high temperature (up to 1500K) with fast thermal ramps. The presence of blisters is observed in some annealing conditions. This demonstration of blistering of an implanted surface usually denotes the possibility of full layer splitting, after bonding with a stiffener layer. Nonetheless, to our knowledge, the Smart Cut™ utilizing the splitting annealing of the implanted material by laser has only been investigated for the integration of LiNbO₃ on Si by a team of Caltech [55]. This very innovative approach was motivated by

the difficulty of realization of the heterostructure by conventional Smart Cut™ due the high CTE mismatch.

The process is illustrated on Fig. 22 and starts by a co-implantation of H and He of the LiNbO₃ wafer. The implanted face is then bonded to a Si wafer. Finally, the splitting annealing is proceeded by scanning the LiNbO₃ wafer by a CO₂ laser of high power (100 MWm⁻²), whose wavelength (10.6 μm) allows an efficient enough absorption in LiNbO₃ and a high transmission in Si. The very close vicinity between the implanted face and the surface of the heated Si (a few hundreds of nm) allows the absorbed heat to diffuse to the implanted zone. The resulting development of cracks leads to the detachment of the superficial layer of LiNbO₃ and to the transfer of this layer on the Si wafer.

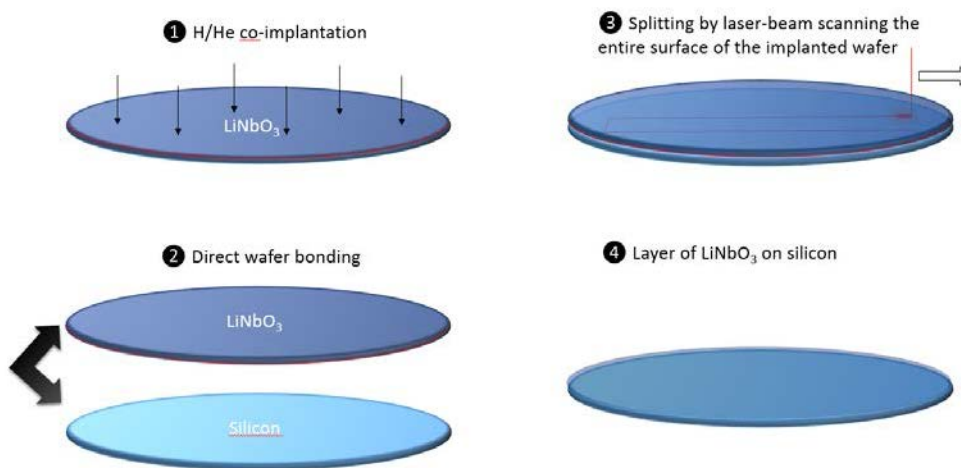
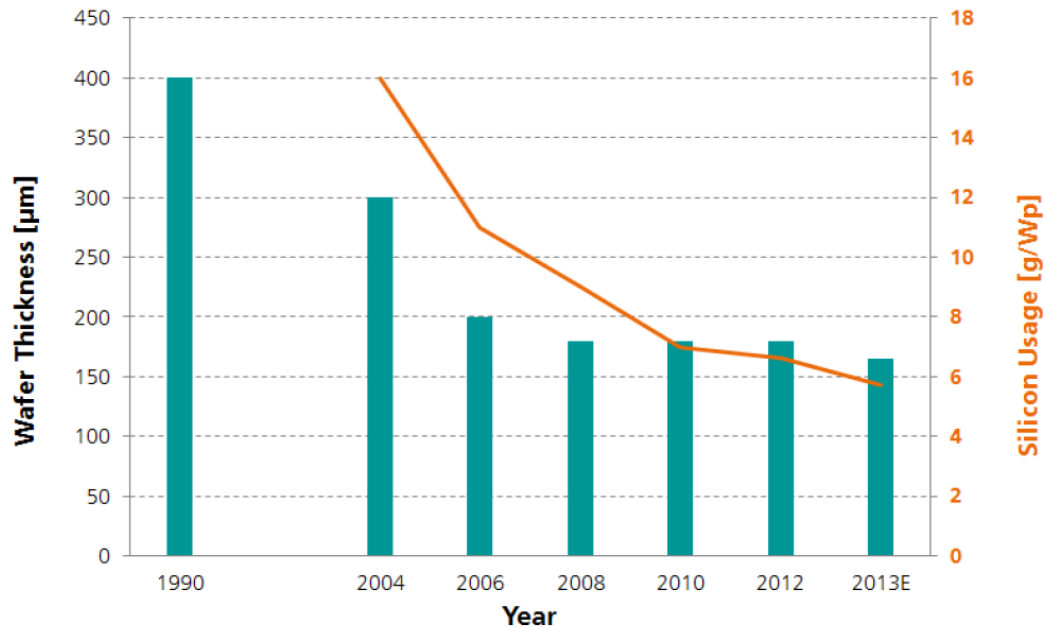


Figure 22: Schematic representation of the process of layer transfer of LiNbO₃ on Si by laser beam annealing [55].

This study has successfully demonstrated the possibility of transfer of single-crystal domain of LiNbO₃ (6 mm²) on 100 mm diameter wafers. We will explore this alternative way of producing planar heterostructures and extend both the choice of material (glass and sapphire) and transferred surface (wafer up to 200 mm diameter).

3. Kerf-less production of thin wafer of Si : an alternative approach driven by photovoltaics

As already exposed in the introductive part on photovoltaics, the reduction of use of Si for the active layer of the solar cell is one of the major axis of development since the 90' [56], as plotted on Fig. 23.



Data: until 2012: EU PV Technology Platform Strategic Research Agenda, for 2012: c-Si Roadmap ITRPV; 2013: Estimation. Graph: PSE AG 2013

Figure 23: Evolution of the wafer thickness as well as the Si usage for the production of photovoltaic cells [56].

Apart the 'traditional' approach which relies on the optimization of sawing step, various breakthrough technologies have been proposed by different teams, mostly European, avoiding the sawing step. These alternative approaches are called 'kerf-free' methods [57]. Among them, we can distinguish different categories: the stress induction, the use of porous structures and the ionic implantation [57]. The common points of these methods rely on the creation of a separation plane within a Si ingot or substrate. It is worth noting that none of them has entered the industrial scale. Rapid decrease of the price of Si solar cells fabricated by MWS has hampered the introduction of alternative approaches so far.

3.1 Stress-induced lift-off (SLiM-Cut)

This approach has been introduced by the team in IMEC and is depicted on Fig. 24 [57]. It consists in high temperature deposition on a bare c-Si of a layer of a material with a CTE largely different from that of Si (e.g. Al and/or Ag screen-printing pastes). During the cooling of the assembly, this stress-inducing layer transfers large stress to the Si substrate, which leads to the spallation of the thin Si layer, as defined by the stress field within Si. Thus, the conditions (thickness of the deposited layer, temperature of deposition etc.) are optimized to control a smooth crack path propagating within a depth of 50 μm.

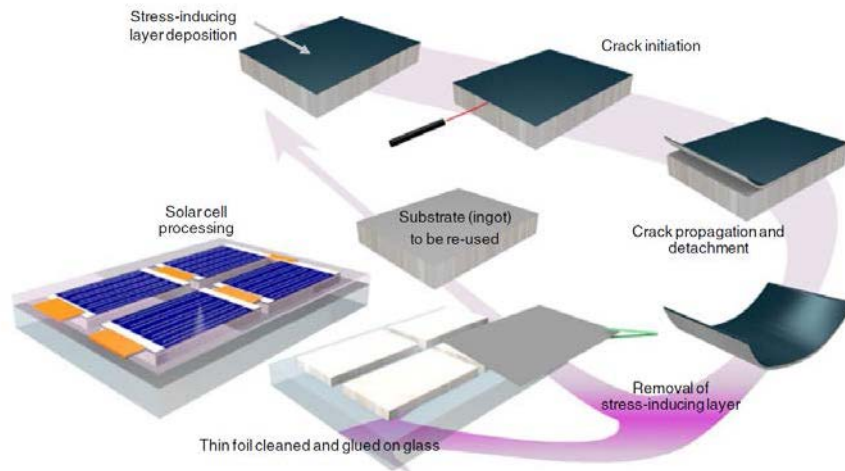


Figure 24: Schematic description of the SiM-Cut process [57].

It has been identified that a temperature deposition lower than the ductile-to-brittle transition of Si helps reducing the generated dislocations, that act as carrier recombination centers and reduces the carrier lifetime. The best conversion efficiency achieved by this process demonstrated a value of 10.0 % [57].

3.2 Layer transfer based on porous substrates or pore coalescence

Another approach, which has been largely studied by several research groups such as IMEC or IPE in Stuttgart, proposes to create a porous layer within a c-Si substrate and to deposit a thin foil of Si by epitaxial growth (Fig. 25) [57-59]. The process starts by an anodic porosification of the host Si substrate, e.g. by electrochemical etching in HF. A high temperature annealing step in hydrogen atmosphere leads to the rearrangement of the system of pores and yields the formation of buried layer of large cavities. The foil of single crystalline Si (up to several tens of μm) is then deposited by CVD upon the substrate. Different steps of the device fabrication can be realized with the layer still attached to the substrate. Finally, a glass superstrate is glued to the processed foil and mechanical force detaches the thin film. Using this process, the team of IPE has realized a cell with 17.0 % efficiency based on a 50 μm Si foil [58].

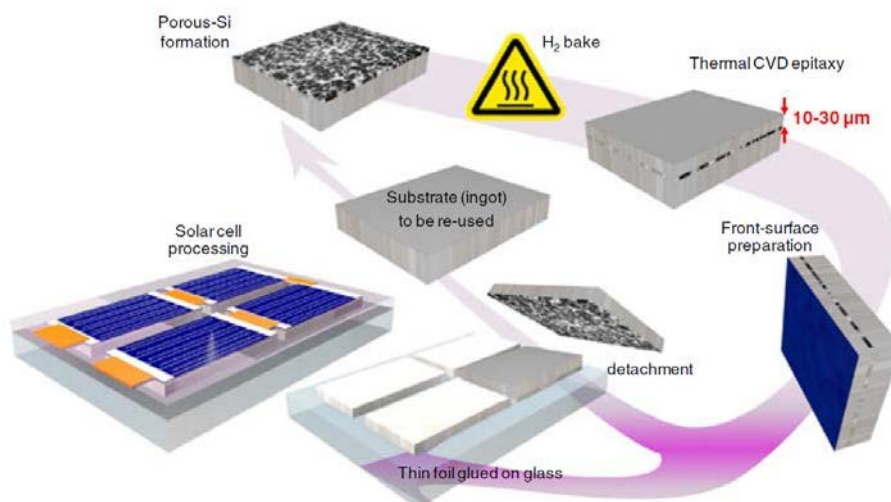


Figure 25: Schematic principle of a process of layer transfer using a weak layer of porous Si [57].

3.3 Techniques based on ion implantation

The last method we propose to focus on relies on a step of implantation of light ions in order to induce a separation layer, very similar to Smart Cut™. At one side, the CNRS-CERI has proposed deep implantation directly in Si donor wafer by utilizing MeV beam of H ions [60]. Thus, R_p of the implantation zone can reach up to several tens of μm in depth. As already mentioned in the first part of this chapter, the thickness implanted Si is sufficient to act as a stiffener layer to produce self-supporting Si foils. Thus, by an appropriate annealing (e.g. 700°C during 10 min [61]), the process of defect development involved in the Smart Cut™ can be implemented. The Fig. 26 gives an illustration of an exfoliated film after implantation at 3 MeV with a dose of $1.0 \times 10^{17} \text{ Hcm}^{-2}$. Despite interesting, this approach is limited by the cost of such MeV implantation and by the lack of equipment available.

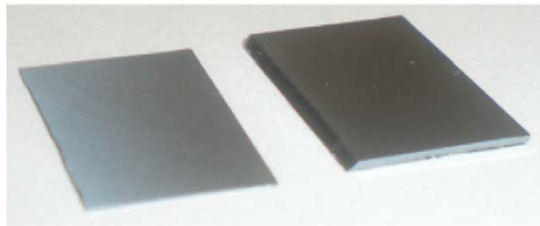


Figure 26: Exfoliated film (left) and remaining substrate (right) after implantation of $1 \times 10^{17} \text{ Hcm}^{-2}$ at 3 MeV and subsequent annealing at 700°C [61].

The last approach is the closest from the process we will explore in this work: it combines an ionic implantation, with conditions of implantation similar to the Smart Cut™ (i.e. a much lower implantation energy compared to the high-energy implantation presented above), and a step of deposition of the Si foil. This process has been proposed in CEA-Leti in 2003, and is described on Fig. 27 [62]. After the implantation step, a Si film is deposited by CVD on the implanted face of the substrate. The film is then separated by a splitting annealing. This process is limited by the possibility to deposit good quality CVD films at a temperature low enough to not activate the separation process within the implanted substrate.

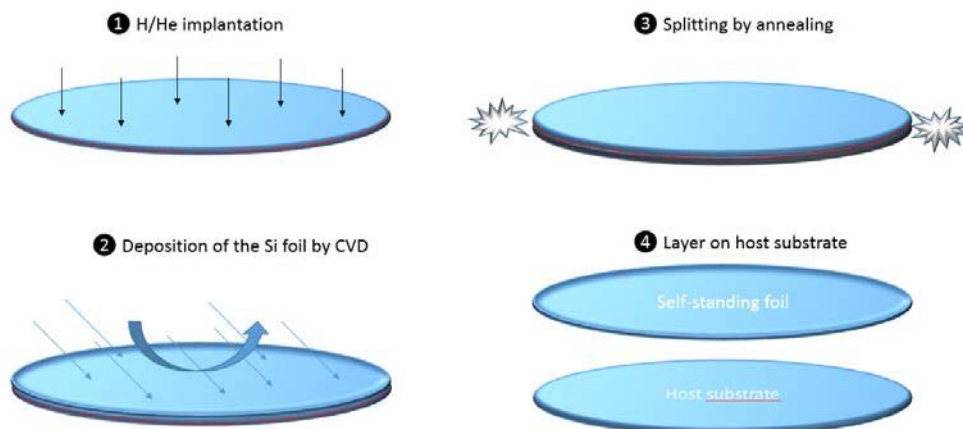


Figure 27: Schematic description of the steps of fabrication of Si foil by CVD deposition upon an implanted substrate.

3.4 Liquid phase epitaxial (LPE) growth of Si from the molten phase

The step of epitaxial growth is the last step for the production of single crystal Si ingots (or Si films by LPE technology). We will not describe the numerous steps, previous to the epitaxial growth, necessary to reduce and purify Si in order to transform pure silica (SiO_2) into microelectronic or photovoltaic grade Si. Nevertheless, it is fundamental to keep in mind that the processes involved in this transformation are extremely greedy in both energy and chemical products. This is an additional argument for the development of frugal approaches for the production of Si films, reducing the losses of material, and particularly, the kerf-less methods reviewed hereinabove.

Most research in the field of LPE currently aims to optimize the macro- and microstructure of the Si ingots, in terms of grains size, orientation and boundaries, as well as reducing dislocation and impurity density. Indeed, the presence of these different types of defects badly affects the performance of the final devices.

We will first introduce general principles of crystal growth before describing different processes of LPE. The second part will put focus on LPE based on Si liquid impinging a Si substrate (dropping-type LPE), which will be used in the process of producing of Si foil proposed in the thesis.

3.4.1 Physical principles of solidification

The LPE consists in forming a crystalline phase from a liquid phase, by controlling the different parameters involved in the transformation (temperature, pressure, concentration) and with help of a seed layer, somewhere into contact with the liquid. The phase diagram, as illustrated on Fig. 28, defines the phase transformation of Si as a function of temperature and pressure, at the thermodynamic equilibrium of the system.

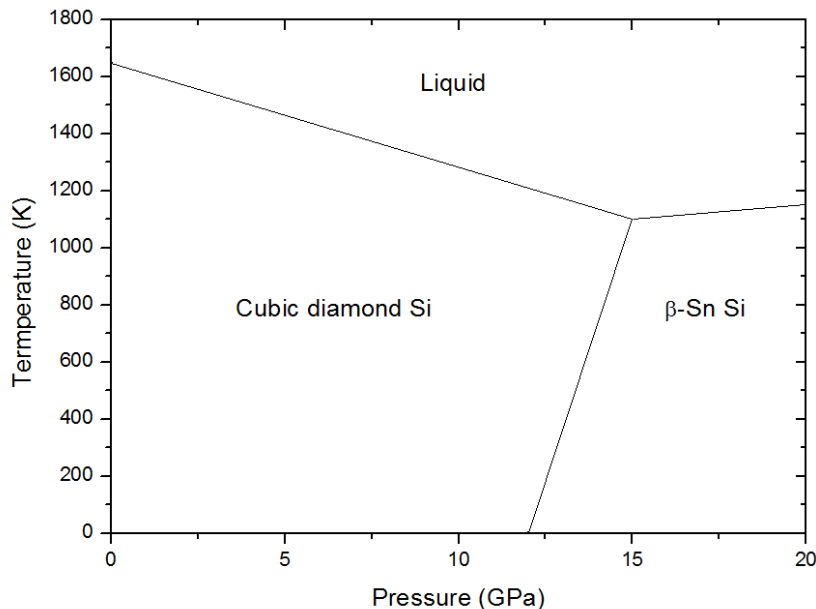


Figure 28: Phase diagram of Si [63].

3.4.2 Kinetics of solidification

The phase diagram only gives very limited information on the state of a system after crystallization. Indeed, the crystallization of Si into contact with a seed layer can follow different kinetics. Thus, it has been shown that the generation of crystal defects, such as dislocations, twin boundaries and impurities segregation is related to the morphology of the crystal-melt interface. As an example, the Fig. 29 shows the Si (100) crystal-melt interface whose growth velocity is equal to $162 \mu\text{m/s}$. The front of solidification, that is initially planar, progressively switches to zigzag facets. This effect that is not observed for lower growth velocity is explained by a wavelike perturbation, progressively amplified, that deforms the interface [64].

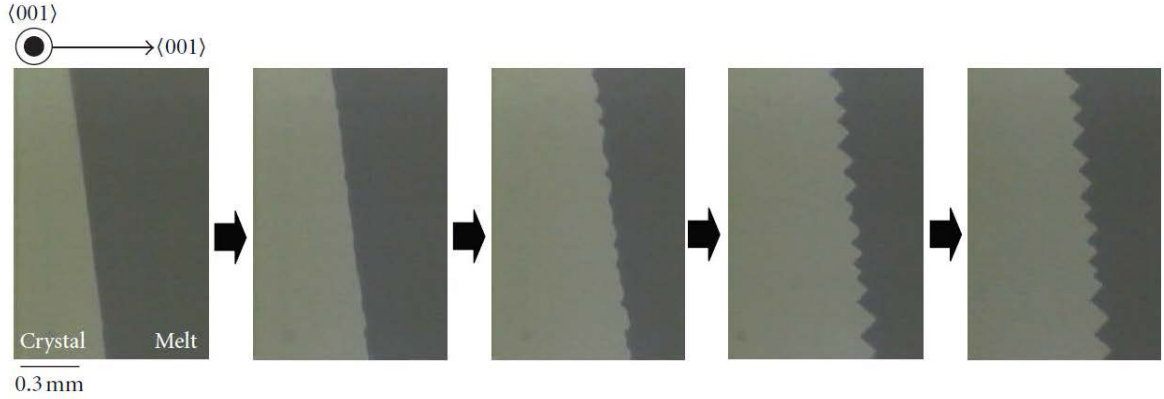


Figure 29: Morphological transformation of Si (100) crystal-melt interface moving at $162 \mu\text{m/s}$ [64].

In this example of the zigzagged solidification front cited earlier, it is considered that the crystal-melt interface becomes unstable when the temperature gradient at the interface is negative along the growth direction. This thermal gradient evolves as a function of the growth velocity, V as illustrated on Fig. 30, where the thermal gradient switches from positive to negative values for $V > 150 \mu\text{m/s}$. It is worth noting that the high latent heat of Si, ($l_{\text{Si}} = 1926 \text{ J/g}$) helps keeping high the temperature at the crystal-melt interface, what emphasizes the sensitiveness to the growth velocity V .

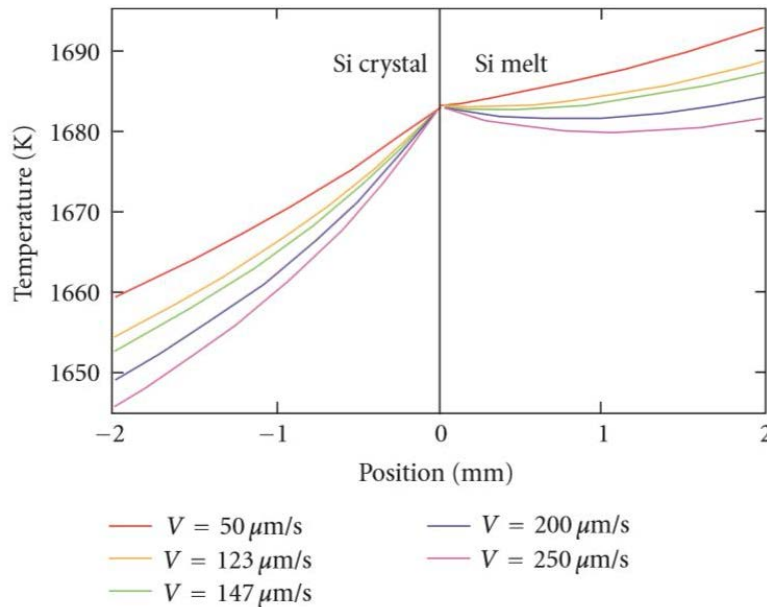


Figure 30: Temperature profile at the crystal-melt interface as a function of the growth velocity V [64]. The thermal gradient in the Si melt changes from positive to negative as V increases.

Thus the solidification front can be rough, faceted or with dendrites according to the solidification velocity V [65]. The α coefficient of Jackson defines the transitions from a rough interface of solidification to a smooth faceted interface. This coefficient is defined by the following relation:

$$\alpha = \frac{\eta}{Z} \frac{l}{k_b T_m}$$

where η is the number of atoms being adjacent to the atom at the interface, Z is the total number of neighboring atoms in the crystal, l is the latent heat (in $\text{J}\cdot\text{mol}^{-1}\cdot\text{K}^{-1}$) and T_m is the melting temperature. When $\alpha < 2$, the crystal-melt interface is rough, whereas facets are observed for $\alpha > 2$, forming a smooth interface [66].

The Table 2 reports the main parameters into relation with α of the main crystallographic planes in Si. Thus, the {111} planes present the lowest surface energy and require the incorporation of 3 ad-atoms to form a seed. The α of {111} is equal to 2.71, which corresponds to a smooth interface. On the other side, {100} only requires the incorporation of 1 ad-atom to create a seed upon an existing plane, what gives a rough interface according Jackson α parameter.

Table 2. Main parameters defining the low index interfaces of Si [67].

Plane	α	Interface	Ad-atom	Surface energy [Jm^{-2}]
{111}	2.71	smooth	3	1.15
{110}	1.80	rough	2	1.41
{100}	0.90	rough	1	1.99

3.4.3 Growth velocity

As we have seen previously, the growth velocity is a key parameter in the microstructure of the material after solidification. Beatty et al. have put it into relation with the undercooling ΔT for the growth of {111} and {100} planes, i.e. the lowering of temperature of a liquid from its solidification point, without forming a solid phase.

As an example, the growth velocity of {100} planes, $v_{\{100\}}$, is defined as following [65]:

$$v_{\{100\}} = 0.12 \Delta T \text{ (in m/s)}$$

It has been observed that there are 3 distinct morphological domains (I, II, III), as illustrated on Fig. 31 varying with according to the growth velocity [65]:

- Zone I ($\Delta T < 100\text{K}$): the microstructure is faceted with a low index between the different planes, with the presence of twins.
- Zone II ($100\text{K} < \Delta T < 210\text{K}$): faceted dendrites appear, with a tetragonal symmetry. The microstructure gets finer, but the dendrites are still ordered.
- Zone III ($\Delta T > 210\text{K}$): disordered dendrites are observed and the size of grains decreases.

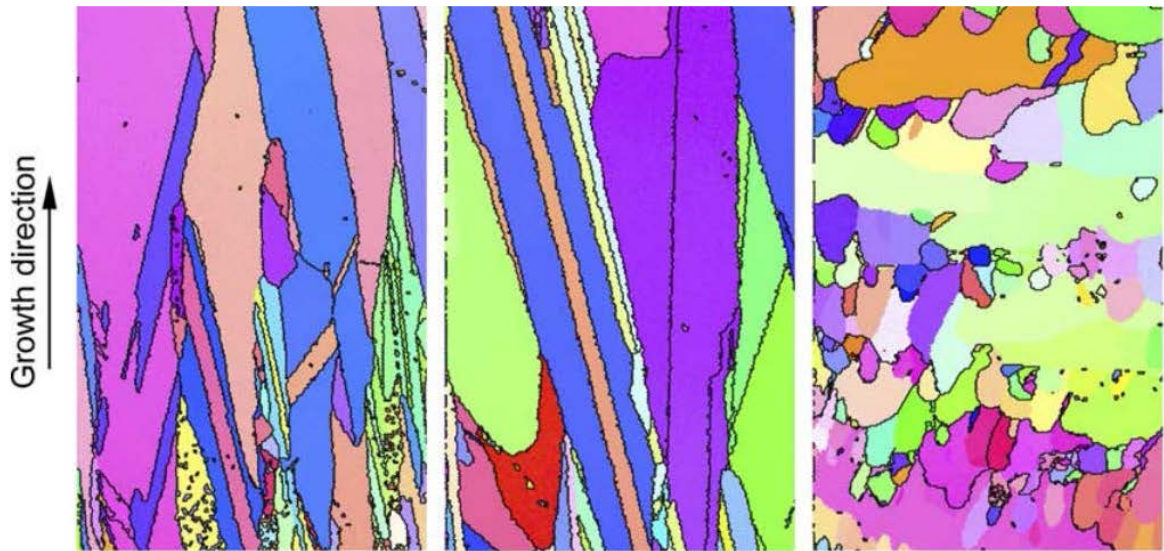


Figure 31: Electron Backscattered diffraction Pattern (EBSP) orientation map of cross-section at the bottom/center for initial undercooling of (a) 14K, (b) 117K, (c) 237K. The directions parallel to the growth direction indicated by the arrow are colored [68].

3.4.4 Grain boundary formation

The structure of grain boundaries is a major subject of interest, as it governs mechanical, optical and electrical properties of the material. Some types of grain boundaries affect negatively the conversion efficiency of the Si solar cell, like coincidence site lattice (CSL) boundaries or random grain boundaries. Fig. 32 shows the crystal growth behavior when two grains converge during the crystallization process. Here, two different grains grow along $\langle 111 \rangle$ direction, up to the formation of a grain boundary. The color contrast shown on the electron backscattered diffraction pattern (EBSD) image illustrates the crystallographic orientation. A $(111) \Sigma 3$ grain boundary, shown by a red line is formed where $\{111\}$ facet planes impinge on each other, i.e. the two lattices have a relation through three rotation angles, and the boundary plane is defined by a unit vector [69]. On the other side, Fig. 32 also shows at the bottom of the EBSD image a random grain boundary, represented by a black line, meaning the absence of relation between the two grains into contact with each other.

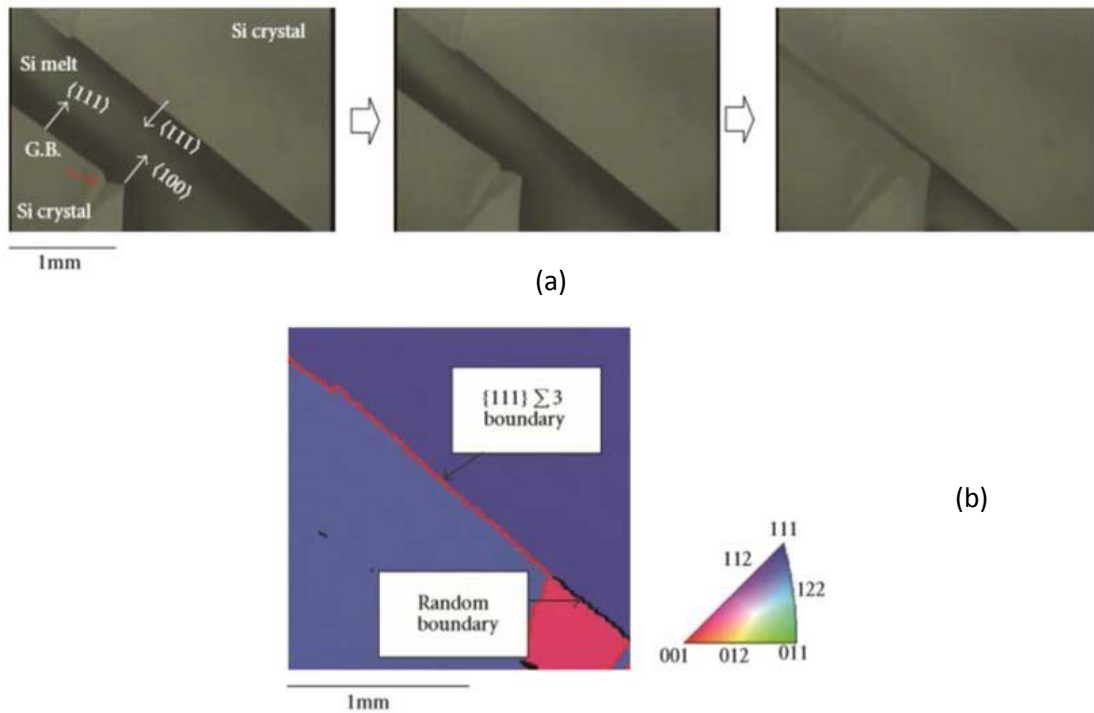


Figure 32: Growth behavior of two Si crystals when they meet during crystallization. In the underlying crystal, the shapes of the growing interface are different on both sides of the grain boundary indicated by the arrow (a), Results of EBSD analysis of region observed in (a), (b). The orientation vertical to the grain boundary is shown in color using the inverse pole figure triangle. The grain boundary is also shown in color in accordance with the grain characteristics [64].

The Fig. 33 illustrates the growth behavior of the two crystals with zigzag faceted interface. Contrary to the previous case, the sharp corners of the growing grains are progressively disappearing and a random boundary is formed.

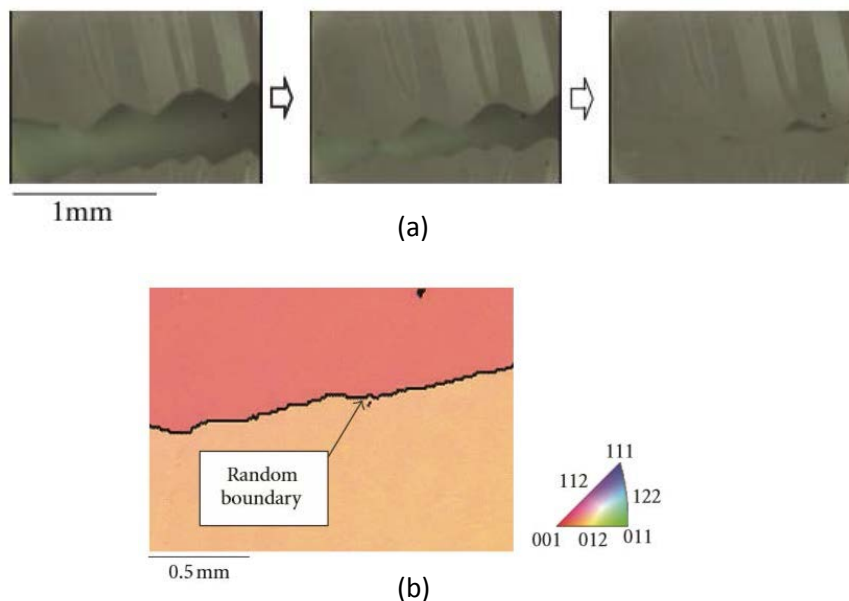


Figure 33: Growth behavior of two Si crystals with zigzag-faceted interfaces (a), detail of an EBSD image of the sample shown in a) [64] (b).

3.5 Spreading of liquid Si onto a surface

As the process we will explore in the thesis relies on the spreading of Si onto a substrate, it is now important to review the studies that have been done in that field. Such rapid solidification processes have been studied in detail, particularly in Japan, e.g. by the team of Fujiwara and Nakajima [64, 70] and by the team of Kuribayashi [71].

Different types of LPE equipment have been considered, usually consisting in releasing droplets of Si onto a Si wafer. One of the key factors is generally the control of the contamination of the liquid during the melting step, originating from both the crucible and the atmosphere. To avoid possible contamination experimental setup utilizing a quartz crucible to contain the liquid, has been proposed as illustrated on Fig. 34. The spreading of the liquid is then realized by dipping the Si substrate directly into the crucible.

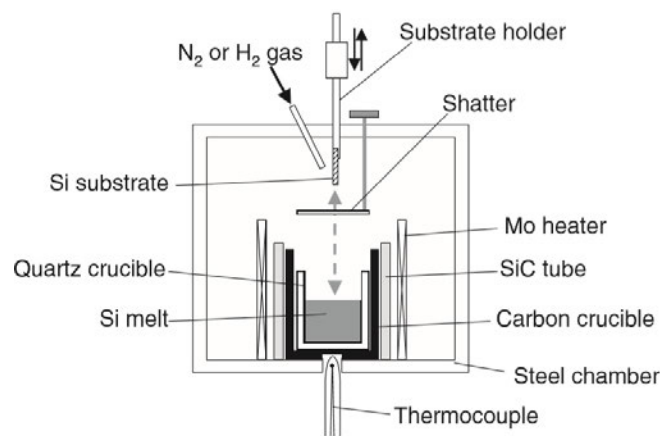


Figure 34: Schematic representation of the dipping-type LPE apparatus [72].

Typical results are presented in Fig. 35, showing that small area epitaxial growth is possible, as illustrated by the EBSD contrast [72]. One of the key parameters highlighted by the authors is the initial temperature of the melt before introduction of the substrate, as well as the cooling rate of the system. The demonstration of the possibility of epitaxial growth considering deposition conditions far from the equilibrium, such as in the Czochralski process, is one important justification of the process being proposed in this thesis.

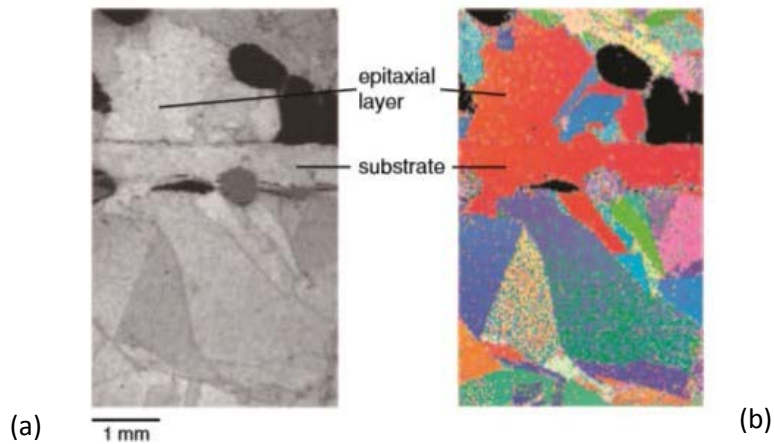


Figure 35: SEM image of the cross-section of the Si substrate (a), Si epitaxial layers and Si polycrystal, EBSD image of the same cross-section [72] (b).

3.6 Electromagnetic levitation

In order, to address the question of the contamination of the liquid, apparatus using the electromagnetic levitation have been developed, as presented on Fig. 36. Thus, the initial undercooling of the Si droplet can be controlled because of the absence of crucible contamination. The droplet is levitated in between copper coils and the pre-heating is realized through a laser heating, in order to generate a sufficient amount of carriers within Si to induce enough coupling with the electromagnetic field.

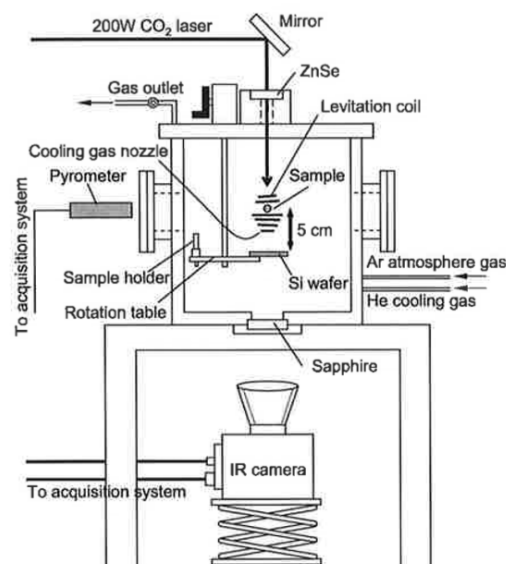
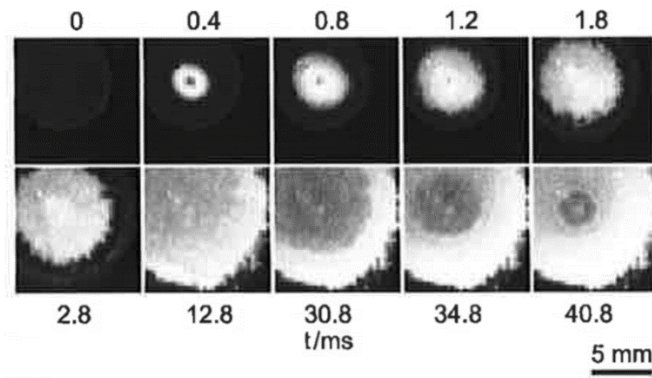


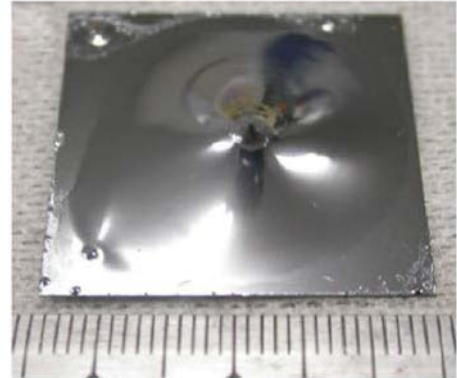
Figure 36: Schematic representation of the electromagnetic levitator with the thermal imaging system [71].

The spreading of liquid onto Si substrate has been studied in this type of equipment, by releasing droplets in different conditions of undercooling. The Fig. 37 (a) shows the evolution of the staggering of the droplet by thermal imaging from below the substrate, as illustrated on the Fig. 36. The most interesting aspect is the possibility of a good spreading of the droplet onto Si substrate, as illustrated

on the Fig. 37 (b), helped by the low viscosity of liquid Si ($\mu_{Si} = 0.75 \text{ mPa}\cdot\text{s}$ to compare with $\mu_{water} = 1 \text{ mPa}\cdot\text{s}$).



(a)



(b)

Figure 37: (a) Thermal images of the spreading of a droplet impinging onto a Si substrate, with an initial undercooling of 48K [71], (b) image of a solidified droplet after spreading [70].

Conclusion

In this chapter, we have seen the main physical aspects regarding the layer separation of implanted Si, and the possible effects of a temperature annealing higher than reported in the different studies. Thus the literature of Smart Cut™ despite being very wide, is mainly focused on the industrial conditions of process (i.e. for annealing temperature lower than 500°C). The chapter 4 will start from this knowledge in order to build a model for the splitting kinetics at higher temperature.

Different approaches have been developed for the production of heterostructures, in order to overcome the difficulties of forming a thin-film of a material upon another, of a different type (in terms of lattice parameter, chemical species etc.). The Smart Cut™ can be applied for heterostructures (e.g. LiNbO₃) , by proceeding to a local annealing by laser. This background paves the way for the study of the chapter 5, aiming to explore the possibility to apply this approach to fabricate Si on Sapphire and Si on Glass.

The use of thin wafers of Si is an interesting approach for the cost reduction of PV panels. On the other hand, it brings a potential of new electronic devices. Several research groups have developed different processes for the creation of Si wafers or Si foils. The main issue for these processes is the slicing step or separation step of the wafer/foil. The layer separation by Smart Cut™ using liquid Si deposition for the production of Si foils will be investigated in the Chapter 6.

References

- [1] **M. Bruel**, Silicon on insulator material technology, *Electr. Letters*, vol. 31, p. 1201, 1995.
- [2] **S. Cristoloveanu, S. Li**, Electrical characterization of silicon-on-insulator materials and devices, 1995.
- [3] **M. A. Pavanello, J. A. Martino, V. Dessard, D. Flandre**, Analog performance and application of graded-channel fully depleted SOI MOSFETs, *Sol. Stat. Electr.*, vol. 44, pp. 1219-1222, 2000.
- [4] **J.-P. Raskin**, SOI technology: an opportunity for RF designers?, *J. of Telec. And Info. Tech.*, Invited paper, 2004.
- [5] **J. Grisolia, G. Ben Assayag, A. Claverie, B. Aspar, C. Lagahe, L. Lanaab**, *Appl. Phys. Lett.*, vol. 76, No. 7, pp. 852-854, 2000.
- [6] **K. K. Bourdelle**, Engineered Substrates for Advanced CMOS Technology Nodes and More-Than-Moore Applications. in Functional Nanomaterials and Devices for Electronics, Sensors and Energy Harvesting. Engineering Materials, *Springer*, pp. 3-5, 2014.
- [7] **F. C. Frank**, The equilibrium shape of gas-filled voids in a solid, *J. of Nucl. Mat.*, vol. 48, pp. 199-200, 1973.
- [8] **J. D. Penot**, Fragilisation et dynamique de rupture du silicium implanté, Thèse de l'Université de Grenoble, 2010.
- [9] **F. Maseeh, S. M. Gelston, S. D. Senturia**, Mechanical properties of microelectronics thin films : silicon dioxide (SiO₂), *VLSI Publications*, Massachusetts Institute of Technology, VLSI Memp No. 89-575, 1989.
- [10] **P. E. Acosta-Alba, O. Kononchuk, G. Riou, C. Moulin, C. Bertrand-Giuliani, A. Claverie**, Multi-Scale Thickness and Roughness Characterization of Thin Silicon-On-Insulator Films, *ECS J. of Sol. State Sc. And Techn.*, vol. 2, No. 9, pp. 357-361, 2013.
- [11] **Q.-Y. Tong, U. M. Gösele**, Wafer Bonding and Layer Splitting for Microsystems, *Adv. Mat.*, vol. 11, No. 17, 1999.
- [12] **I. Radu, I. Szafraniak, R. Scholz, M. Alexe, U. Gösele**, Low-temperature layer splitting of (100) GaAs by He+H coimplantation and direct wafer bonding, *Appl. Phys. Lett.*, vol. 82, No. 15, 2003.
- [13] **C. Moulet, M. S. Goorsky**, Lattice strain measurement in hydrogen implanted materials for layer transfer processes. in Ion Implantation, *Prof. Mark Goorsky (Ed.)*, 2012.
- [14] **T. Höchbauer, A. Misra, R. Verda, Y. Zheng, S. S. Lau, J. W. Mayer, M. Nastasi**, The influence of ion-implantation damage on hydrogen-induced ion-cut, *Nucl. Instr. and Met. In Phys. Res. B*, No. 175-177, pp. 169-175, 2001.
- [15] **O. Moutanabbir, B. Terreault, M. Chicoine, F. Schiettekatte**, The fluence effect in hydrogen-ion cleaving of silicon at the sub-100-nm scale, *Appl. Phys. A*, vol. 80, pp. 1455-1462, 2005.
- [16] **B. Aspar et al.**, The generic nature of the Smart-Cut™ process for thin film transfer, *J. of Electr. Mat.*, vol. 30, No. 7, pp. 834-840, 2001.
- [17] **Y.J. Chabal, M.K. Weldon, Y. Caudano, B.B. Stefanov, K. Raghavachari**, Spectroscopic studies of H-decorated interstitials and vacancies in thin-film silicon exfoliation, *Phys. B*, No. 273-274, pp. 152-163, 1999.
- [18] **H. Iwata, M. Takagi, Y. Tokuda, T. Imura**, Analysis of platelet distribution in H ion-implanted silicon, *J. of Crys. Grow.*, vol. 210, pp. 94-97, 2000.
- [19] **J. Grisolia, F. Cristiano, G. Ben Assayad, A. Claverie**, Kinetic aspects of the growth of platelets and voids in H implanted Si, *Nucl. Instr. and Meth. in Phys. Res. B*, vol. 178, pp. 160-164, 2001.
- [20] **M. Nastasi, T. Höchbauer, J.-K. Lee, A. Misra, J. P. Hirth et al.**, Nucleation and growth of platelets in hydrogen-ion-implanted silicon, *Appl. Phys. Lett.*, vol. 86, pp. 154102-1-3, 2005.
- [21] **T. Höchbauer, A. Misra, R. Verda, Y. Zheng, S. S. Lau, J. W. Mayer, M. Nastasi**, The influence of ion-implantation damage on hydrogen-induced ion-cut, *Nucl. Instr. and Meth. in Phys. Res. B*, vol. 175-177, pp. 169-175, 2001.

- [22] **J.-D. Penot, D. Massy, F. Rieutord, F. Mazen, S. Reboh, F. Madeira, L. Capello, D. Landru, O. Kononchuk**, Development of micro-cracks in hydrogen-implanted silicon substrates, *J. of Appl. Phys.*, vol. 114, pp. 123513-1-6, 2013.
- [23] **S. Personnic, K. K. Bourdelle, F. Letertre, A. Tauzin, N. Cherkashin, A. Claverie, R. Fortunier, and H. Klocker**, Impact of the transient formation of molecular hydrogen on the microcrack nucleation and evolution in H-implanted Si (001), *J. of Appl. Phys.*, vol. 103, pp. 023508-1-9, 2008.
- [24] **L. B. Freund**, A lower bound on implant density to induce wafer splitting in forming compliant substrate structures, *Appl. Phys. Lett.*, vol. 70, pp. 3519-3521, 1997.
- [25] **C. Lagahe**, Etude de la fracture impliquée dans le procédé Smart Cut™ application au matériau SOI, Thèse de l'INPG, 2000.
- [26] **T. Höchbauer, A. Misra, M. Nastasi, K. Henttinen, T. Suni, I. Suni, S. S. Lau, W. Ensiger**, Comparison of thermally and mechanically induced Si layer transfer in hydrogen-implanted Si wafers, *Nucl. Instr. and Meth. in Phys. Res. B*, vol. 216, pp. 257-263, 2004.
- [27] **M. K. Weldon, Y. J. Chabal, D. R. Hamann, S. B. Christman, E. E. Chaban, and L. C. Feldman**, Physics and chemistry of silicon wafer bonding investigated by infrared absorption spectroscopy, *J. of Vac. Sc. & Tech. B*, vol. 14, pp. 3095-3106, 1996.
- [28] **C. Ventosa**, Etude des mécanismes mis en jeu dans le collage direct de surfaces hydrophiles, Thèse de doctorat de l'Université Joseph Fourier, 2009.
- [29] **C. Ventosa, F. Rieutord, L. Libralesso, C. Morales, F. Fournel, and H. Moriceau**, Hydrophilic low-temperature direct wafer bonding, *J. of Appl. Phys.* vol. 104, pp. 123524-1-6, 2008.
- [30] **F. Fournel, L. Continni, C. Morales, J. Da Fonseca, H. Moriceau et al.**, Measurement of bonding energy in an anhydrous nitrogen atmosphere and its application to silicon direct bonding technology, *J. of Appl. Phys.* vol. 111, pp. 104907-1-7, 2012.
- [31] **F.-X. Darras, N. Cherkashin, F. Cristiano, O. Kononchuk, L. Capello, A. Claverie**, Quantification of the number of Si interstitials formed by hydrogen implantation in silicon using boron marker layers, *Nucl. Instr. and Meth. in Phys. Res. B*, vol. 327, pp. 29-32, 2014.
- [32] **E. Romano, G. F. Cerofolini, D. Narducci, F. Corni, S. Frabboni, G. Ottaviani, R. Tonini**, Evidence of H₂ at high pressure in the silicon nanocavities after dipping in HF solution, *Surf. Sc.*, vol. 603, pp. 2188-2192, 2009.
- [33] **S. Reboh, A. A. D. de Mattos, F. Schaurich, P. F. P. Fichtner, M. F. Beaufort, J. F. Barbot**, The mechanisms of surface exfoliation in H and He implanted Si crystals, *Scr. Mater.*, vol. 65, pp. 1045-1048, 2011.
- [34] **B. Gu, H.-Y. Liu, Y.-W. Mai, X.-Q. Feng, S.-W. Yu**, Fracture mechanisms analysis of the effects of temperature and material mismatch on the Smart-Cut™ technology, *Eng. Fract. Mech.*, vol. 75, pp. 4996-5006, 2008.
- [35] **J. Samuels, S. G. Roberts, E. B. Hirsch**, The Brittle-to-Ductile Transition in Silicon, *Mat. Sc. and Eng. A*, vol. 105-106, pp. 29-46, 1987.
- [36] **S. To, H. Wang, E. V. Jelenkovic**, Enhancement of the machinability of silicon by hydrogen ion, implantation for ultra-precision micro-cutting, *Int. J. of Mach. Tools and Manu.*, vol. pp. 50-55, 2013.
- [37] **J. E. Ayers**, Heteroepitaxy of semiconductors. Theory, growth and characterization. CRC Press. Taylor Francis Group. pp. 1-15, 2007.
- [38] **F. Dimroth et al**, Wafer bonded four-junction GaInP/GaAs//GaInAsP/GaInAs concentrator solar cells with 44.7% efficiency, *Progr. In Photov.: Res. and Appl.* vol. 20, pp. 277-282, 2014.
- [39] **M. R. Oliver**, Chemical-mechanical planarization of semiconductor materials, Material Sciences, Springer, pp. 5-15, 2004.
- [40] **F. Andrieu, O. Weber, T. Ernst, O. Faynot, S. Deleonibus**, Strain and channel engineering for fully depleted SOI mosfets toward the 32 nm technology node, *Microel. Eng.*, vol. 84, No. 9-10, pp. 2047-2053, 2007.

- [41] **S. Diziain, R. Geiss, M. Steinert, C. Schmidt, W.-K. Chang, S. Fasold, D. Füssel, Y.-H. Chen, T. Pertsch**, Self-suspended micro-resonators patterned in Z-cut lithium niobate membranes, *Opt. Mat. Exp.*, vol. 5, No.9, pp. 2081-2089, 2015.
- [42] **M. Pijolat, C. Deguet, C. Billard, D. Mercier, A. Reinhardt, M. Aïd, S. Ballandras, E. Defay**, Bias-controlled electrostrictive longitudinal resonance in X-cut lithium niobate thin films resonator, *Appl. Phys. Lett.*, vol. 98, 2032902-1-3, 2011.
- [43] **T. Baehr-Jones, A. Spott, R. Ilic, A. Spott, B. Penkov, W. Asher, M. Hochberg**, Silicon-on-sapphire integrated waveguides for the mid-infrared, *Opt. Expr.*, vol. 18, No. 12, 12117-12135, 2010.
- [44] **E. Sagioglu Topalli, K. Topalli, S. Emre Alper, T. Serin, and T. Akin**, Pirani vacuum gauges using silicon-on-glass and dissolved-wafer processes for the characterization of MEMS vacuum packaging, *IEEE Sens. Journ.*, vol. 9, No. 3, 2009.
- [45] **Q. Y. Tong, U. Gösele, T. Martini, M. Reiche**, Ultrathin single-crystalline silicon on quartz (SOQ) by 150°C wafer bonding, *Sens. And Actuat. A*, vol. 48, pp. 117-123, 1995.
- [46] **G. W. Cullen, C. C. Wang**, Heteroepitaxial semiconductors for electronic devices, Springer Science + Business Media, LLC, 1978.
- [47] **Y. Liu, M. Xu, J. Heo, P. D. Ye, R. G. Gordon**, Heteroepitaxy of single-crystal LaLuO₃ on GaAs(111)A by atomic layer deposition, *Appl. Phys. Lett.*, vol. 97, pp. 162910-1-3.
- [48] **W. S. Wong, T. Sands, N. W. Cheung, M. Kneissl, D. P. Bour, P. Mei, L. T. Romano, N. M. Johnson**, In_x Ga_{1-x}N light emitting diodes on Si substrates fabricated by Pd-In metal bonding and laser lift-off, *Appl. Phys. Lett.*, vol. 77, No.18, pp. 2822-2824, 2000.
- [49] **J. B. Lasky, S. R. Stiffler, F. R. White, J. R. Abernathy**, Silicon-on-insulator (SOI) by bonding and etch-back, Conference publication published in *Electron Devices Meeting*, vol. 31, pp. 684-687, 1985.
- [50] **R. E. Belford, S. Sood**, Surface activation using remote plasma for silicon to quartz wafer bonding, *Microsyst. Techn.*, vol. 15, pp. 407-412, 2009.
- [51] **A. Colin**, Etude des couplages radiatifs et thermiques et des modifications physico-chimiques engendrées par un recuit laser milliseconde sur la grille polysilicium de la technologie CMOS 45 nm, Thèse de doctorat de l'Université de Strasbourg, 2010.
- [52] **G. D. Ivlev, E. I. Gatzkevich, R. M. Bayazitov, R. I. Batalov, I. B. Khaibullin**, Dynamics of photo-ionization, heating and crystallization of implanted silicon during laser annealing, *Nucl. Instr. and Meth. In Phys. Res. B*, vol. 257, pp. 208-211, 2007.
- [53] **D. Klingera, J. Auleytnera, D. Zymierskaa,*, L. Nowickib**, Nanostructure of near-surface Si layers formed by implantation and pulsed laser annealing, *J. of All. And Comp.*, vol. 362, pp. 282-286, 2004.
- [54] **R. Boivin and B. Terreault**, Desorption and other effects of pulsed laser annealing of hydrogen implanted silicon, *J. of Appl. Phys.*, vol. 73, 1943-1951, 1993.
- [55] **Y.-B. Park, B. Min, K. J. Vahala, H. A. Atwate**, Integration of single-crystal LiNbO₃ thin film on silicon by laser irradiation and ion implantation-induced layer transfer, *Adv. Mat.*, vol. 18, pp. 1533-1536, 2006.
- [56] Photovoltaics report, Fraunhofer Institute For Solar Energy System ISE, 2014.
- [57] **F. Dross et al**, Crystalline thin-foil silicon solar cells: where crystalline quality meets thin-film processing, *Prog. In Photov.: Res. And Appl.*, vol. 20, pp. 770-784, 2012.
- [58] **M. Reuter, W. Brendle, O. Tobail, J. H. Werner**, 50mm thin solar cells with 17.0% efficiency, *Sol. Energ. Mat. & Sol. Cells*, vol. 93, pp. 704-706, 2009.
- [59] **H. Assaf, E. Ntsoenzok**, Transfer of thin silicon layers by MeV hydrogen implantation, *Nucl. Instr. and Meth. in Phys. Res.*, vol. 240, pp. 183-187, 2005.
- [60] **S. Amtablian**, Du transfert de film minces de silicium monocristallin vers un procédé cellule à faible budget thermique, Thèse de doctorat de l'Insa de Lyon, 2008.
- [61] **C. Braley, F. Mazen, A. Tauzin, F. Rieutord, C. Deguet, E. Ntsoenzok**, Si exfoliation by MeV proton implantation, *Nucl. Instr. and Meth. in Phys. Res.*, vol. 277, pp. 93-97, 2012.

- [62] **A. Beaumont**, Adaptation du procédé de fragilisation par faisceau d'ions pour la réalisation de couches minces de silicium monocristallin application au photovoltaïque, Thèse de doctorat de l'Insa de Lyon, 2003.
- [63] **M. Ekman, K. Persson, G. Grimvall**, Lattice dynamics and thermodynamic properties of the β -Sn phase in Si, *Phys. Rev. B*, vol. 62, No. 22, pp. 14784-14789, 2000.
- [64] **K. Fujiwara**, Crystal growth behaviors of silicon during melt growth processes, *Int. J. of Photoen.* vol. 2012, pp. 1-16, 2011.
- [65] **M. Beaudhuin**, Etude expérimentale et numérique de la précipitation d'impuretés et de la formation des grans dans le silicium photovoltaïque, Thèse de doctorat de l'Institut Polytechnique de Grenoble, 2009.
- [66] **K. A. Jackson**, Constitutional supercooling surface roughening, in 50 years progress in crystal growth, R. S. Feigelson (Ed.), Elsevier, pp. 69-80, 2004.
- [67] **K. Nagashio, K. Kuribayashi**, Growth mechanism of Si from undercooled melts, *Space Utiliz. Res.*, vol. 21, pp. 9-12, 2005.
- [68] **K. Nagashio, H. Murarata, K. Kuribayashi**, Spreading and solidification behavior of molten Si droplets impinging on substrates, *Act. Mat.*, vol. 52, pp. 5295-5301, 2004.
- [69] **T. DUffar, A. Nadri**, On the twinning occurrence in in bulk semiconductor crystal growth, *Script. Mat.*, vol. 62, pp. 955-960, 2010.
- [70] **Z. Mei, K. Kutsukake, H. Kodama, N. Usami, K. Fujiwara, Y. Nose, K. Nakajima**, Influence of growth temperature and cooling rate on the growth of Si epitaxial layer by dropping-type liquid phase epitaxy from the pure Si melt, *J. of Cryst. Grow.*, vol. 310, pp. 5248-5251, 2008.
- [71] **K. Nozaki, K. Nagashio, K. Kuibayashi**, In-situ observation of solidification behaviour from undercooled α -Fe₂Si₅ melt using an electromagnetic levitator, *Rev. Adv. Mater. Sci.*, vol. 18, pp. 439-443, 2008.
- [72] **K. Nakajima, K. Fujwara, Y. Nose, N. Usami**, Liquid phase epitaxial growth of Si layers on Si thin substrates from Si pure melts under near-equilibrium conditions, *Jap. J. of Appl. Phys.*, vol. 44, No. 7A, pp. 5092-5095, 2005.

Chapter 3. Design of experiments

The Smart Cut™ splitting is acoustically detected for defined conditions of implantation and rapid thermal annealing. The sample splitting time is the final step of complex maturations of defects, involving diffusion processes and fracture mechanisms. Its comprehension requires to be supported by characterizations of species diffusion (SIMS, ERDA) and adequate modelling. The splitting conditions influence properties of the resulting films, such as film roughness that are characterized by AFM and optical profilometer. Elsewhere, the subsequent effect of rapid thermal annealing on the structure of bonded wafers is studied by measurement of adhesion energy by Maszara razor blade method.

Smart Cut™ by laser annealing is demonstrated for temperature superior to 900°C and up to 1300°C. Samples consist here of standalone implanted Si wafers and of implanted Si wafers bonded with transparent wafers (glass and sapphire). Temperature signal within the sample is recorded during the annealing by a pyrometer. The transferred films are characterized by optical microscopy, optical and mechanical profilometer and acoustic microscopy, AFM, Raman and XRD. Finally, the resistivity of the films of SOG is characterized by 4-probe measurement method.

In the last part of the work, the deposition of liquid Si is proceeding by dropping-type liquid phase epitaxy method on implanted and non-implanted Si substrates. The deposition and cooling of Si droplet is observed by thermal camera and ultra-rapid camera. The microstructure of the deposited films is characterized by SEM, EBSD and Raman. On the other hand the electrical properties of the resulting films are determined by photoluminescence.

1. Blistering and splitting study (treated in the Chapter 4)

As a reminder, the blistering is the phenomenon of blisters apparition of an implanted material, standing alone, subsequent and depending on a thermal annealing. The splitting is the layer separation of an implanted material bonded with an acceptor material, similarly depending on the thermal annealing.

The specifications for this study have been driven by characterizing the splitting kinetics for temperatures as high as possible, with a good control on the reached temperature as a function of time.

We have seen that the splitting kinetics depends on the implantation dose, in a way that the required thermal budget (i.e. the temperature-time) is higher for a lower implantation dose (Fig. II.13). Thus, we propose to establish implantation conditions starting from “under-doses” up to regular doses in order to cover the longest splitting duration for any temperature annealing. On the other hand, as the time for splitting exponentially decreases with the increase of temperature annealing, the thermal ramp is required to be as fast as possible from low temperature (300°C). Finally, we have seen in the previous chapter that the annealing duration is within a range from the second to several minutes.

1.1 Blistering samples preparation

A short study of blistering kinetics characterization has been first realized as a preliminary work. Three conditions of implantation are proposed, as summarized in table 1, from low dose ($3.0 \cdot 10^{16}$ Hcm⁻²) to high dose ($1.0 \cdot 10^{17}$ Hcm⁻²).

Table 1. Conditions of implantation

Imp. dose (Hcm ⁻²)	$3.0 \cdot 10^{16}$	$5.0 \cdot 10^{16}$	$1.0 \cdot 10^{17}$
32 keV	X	X	X

1.2 Splitting samples preparation

As already exposed in the introduction, this work will only consider implantation of H alone (and not H/He co-implantation) in order to simplify the comprehension of the experimental results. Similarly, the other steps of the preparation of samples (cleaning, bonding, etc.) will be taken as standard as possible, i.e. corresponding to the well-established state of the art of the Smart Cut™ literature.

1.2.1 Preparation of the samples

The splitting samples start with wafers of p-type (100) Si of standard microelectronics quality (the so-called “monitor” wafers), grown by the Czochralski (CZ) process. The splitting samples follow different preparation steps:

- The ionic implantation of H in the donor wafer, with energy from 32 keV to 60 keV, corresponding to a transferred thickness of ~ 400 nm and ~ 650 nm. The implantation dose is varied according to the table 2.

Table 2. Conditions of implantation

Imp. dose (Hcm ⁻²)	3.0*10 ¹⁶	3.5*10 ¹⁶	4.0*10 ¹⁶	4.5*10 ¹⁶	5.0*10 ¹⁶	8.0*10 ¹⁶	1.0*10 ¹⁷
32 keV	X	X	X	X	X	X	X
60 keV		X	X	X	X		

- The formation of the buried oxide (thickness of 145 nm) on the acceptor wafer by thermal oxidation in a wet atmosphere. This step is realized in a batch annealing furnace where several tens of wafers can be treated at once.
- The cleaning before bonding is realized in a bench, with a RCA solution (whose name originates from the Radio Corporation of America where the process had been invented) [1]. It aims to remove the organic contaminants as well as the particles on the surfaces of both acceptor and donor wafers.
- The plasma activation in air plasma equipment, aiming to enhance the hydrophilic properties of the surfaces of acceptor and donor wafers and to increase the bonding energy of the bonded system.
- The bonding of the acceptor and of the donor wafer is realized in automated bonding [equipment].
- The cleaving is finally realized manually with a diamond tip, in order to have samples of 1 cm*1 cm.

1.2.2 Temperature recording

The samples implanted with 60 keV have been patterned in order to allow the introduction of a thermocouple at the interface of bonding. Thus, the surface of the donor wafer has been machined using cutting equipment, i.e. using a cutting blade into rotation. The process of preparation of samples has been slightly modified including a step of thermal oxidation of the donor wafer before implantation, see on Fig.1:

- Thermal oxidation of the acceptor wafer, as before (step ①).
- Ionic implantation similarly as before (step ②).
- Machining of trenches of 300 µm * 300 µm dimension in the implanted surface of the donor wafers (step ③).
- Removal of the oxide layer of the donor wafers, in order to remove the surface damages due to the machining step (step ④).
- Cleaning and bonding similarly than before (step ⑤).

- Slicing of 1 cm * 1 cm samples and manual thermocouple introduction (step 6).

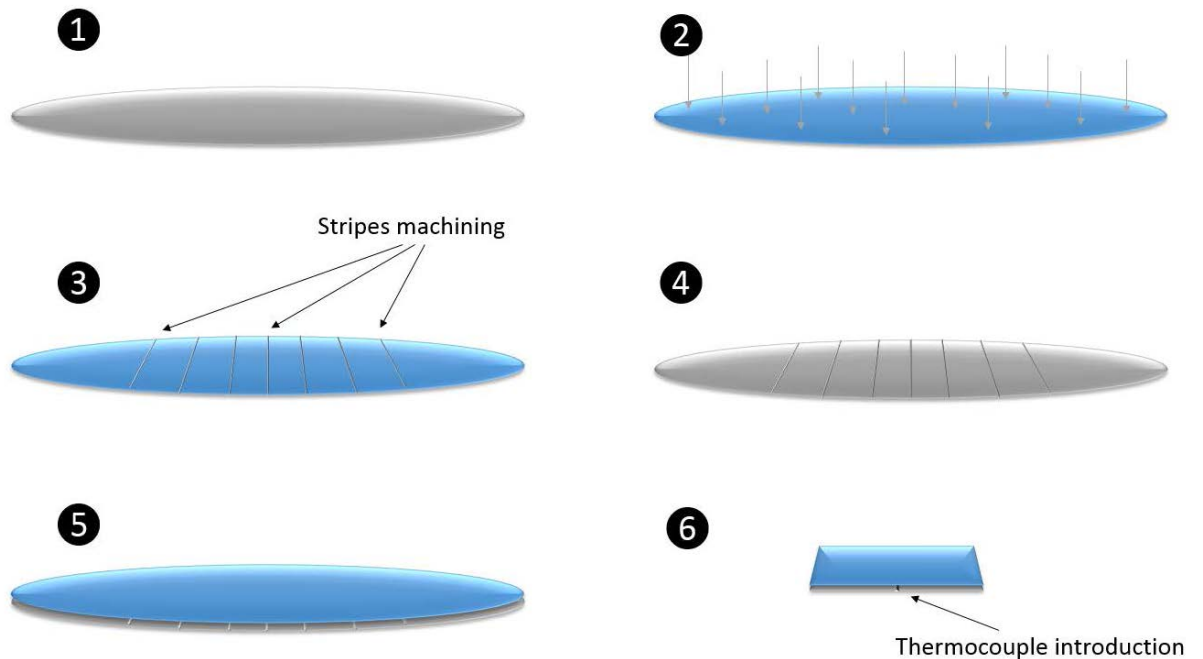


Figure 1: Schematic representation of the preparation of splitting samples for the in-situ recording of temperature.

1.3 Description of the heating system

Different annealing equipment could have been setup for the study of blistering and splitting:

-*Convection furnace*: such equipment was employed in the previous studies for the splitting annealing [2]. The heating occurs mainly by thermal convection and eventually by radiation but, these modes are too slow for the requirements of this study.

-*Rapid Thermal Annealing (RTA)*: this type of furnace, that can also be called “flash-annealing”, is a relatively common annealing equipment in a clean room, as it allows to reach very high temperature ($> 1100\text{ }^{\circ}\text{C}$) with very fast thermal ramp (e.g. 100 K/s). This heating relies on optical absorption by the wafer of a light beam emitted by lamps that can be of different types and spectral temperatures, like tungsten-halogen lamp (3300 K), long-arc noble gas discharge lamp (6200 K) or continuous resistivity heated bell jar (1700 K) [3]. The control of temperature is realized by an optical pyrometer, with a very good precision. Although very attractive, this process presents some drawbacks. Indeed, a semiconductor such as Si at room temperature, has a rather poor optical absorption on this optical spectrum. For that reason, Si wafers are usually pre-heated at $400\text{--}600^{\circ}\text{C}$, in order to generate enough free carriers to enhance the optical absorption [3]. Additionally, the temperature measurement is usually realized with an optical pyrometer, whose temperature detection starts from $600\text{--}700^{\circ}\text{C}$.

-*Laser annealing*: the laser is very attractive as it allows to emit almost instantaneously a beam of a tremendous energy density (up to GW/m^2 [4]). Additionally, there are many different types of technologies emitting on a large range of wavelengths from deep UV to far IR, what allows to optimize

the absorption in particular regions of a sample only. This aspect will be usefully employed for the study of laser-assisted splitting of heterostructures in Chapter 5. Nevertheless, the laser annealing will not be considered for the study of “traditional” splitting of Chapter 4. Indeed, the required annealing duration excludes the use of a laser to cover a range from the second to several minutes.

-Heating by thermal conduction: in this configuration the sample is placed directly on a heating plate. Thus, the heating occurs mainly by thermal conduction, what is the fastest option, as the Si has a good thermal conductivity.

For the study of blisters formation, the heating plate stands below an optical microscope as illustrated on Fig. 2. The observation of blisters formation is done by direct observation with the optical microscope.

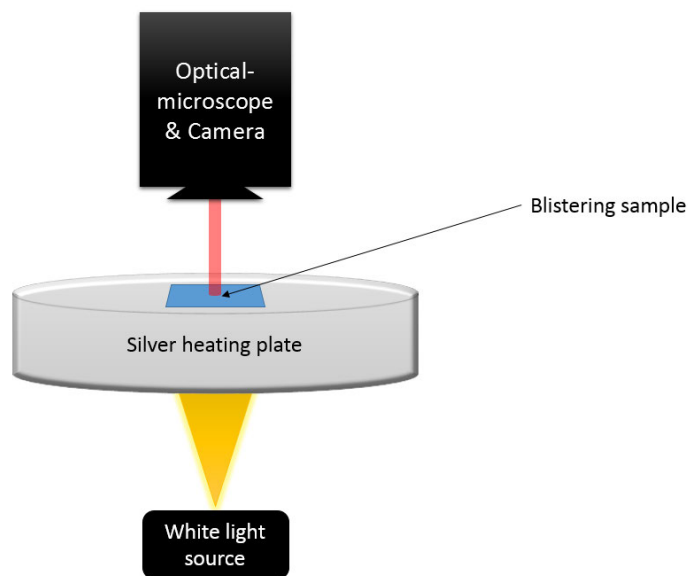


Figure 2: Schematic representation of the heating plate for the blistering samples.

The heating equipment proposed for the study of splitting at high temperature has been developed in house and considers two plates of steel placed in a furnace. The splitting sample is placed in between after heating the plates at the reference temperature. Moreover, the temperature recording is realized in situ, by help of a thermocouple, as shown on Fig. 1 in the step ⑥.

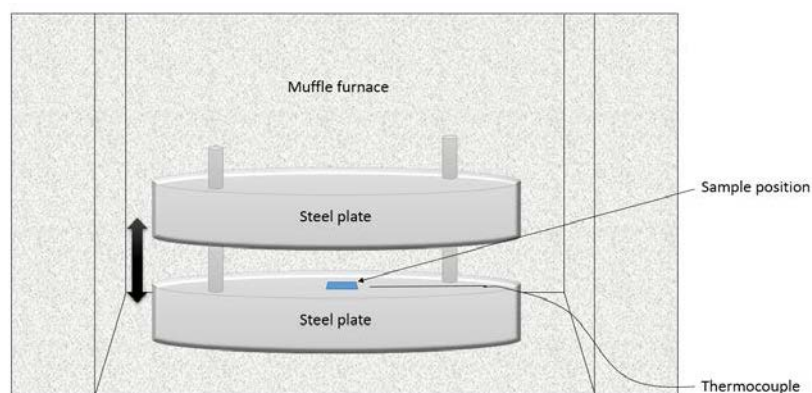


Figure 3: Schematic representation of the furnace developed for the study of splitting at high temperature.

1.4 Characterization facilities

1.4.1 Secondary Ion Mass Spectrometry (SIMS)

The SIMS technique, combined here with Time of Flight measurement (ToF-SIMS) allows to determine the composition at the surface of a sample by analyzing the secondary ions ejected by the bombardment of the sample surface by primary ions, as illustrated on Fig. 4. A second ions beam can be used to etch the surface, possibly atomic layer by atomic layer, what allows to establish a composition profile in depth, with a sub-nm resolution. It is possible to detect any element (including H and its isotopes), what render SIMS very attractive for our study of H implantation [5].

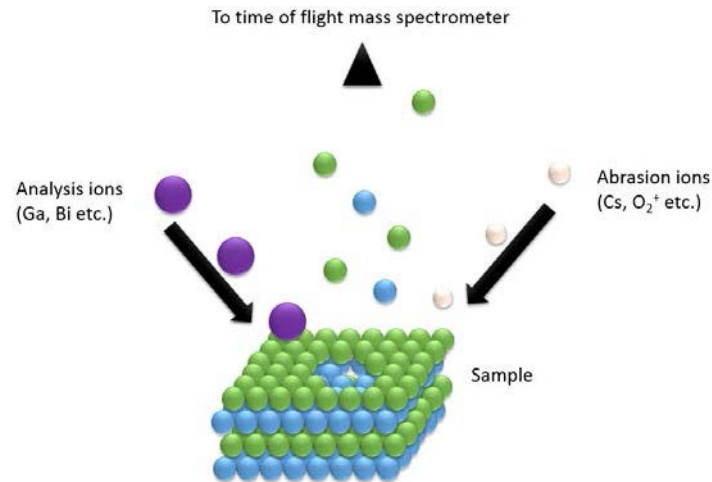


Figure 4: Schematic principle of the ToF-SIMS.

The physical principle relies on the inelastic collision of the primary analysis ions (whose energy is from 100 eV to 20 keV) with the surface of the sample, what induces the pulverization of the lattice atoms. Part of these atoms are ionized and accelerated under a precise energy in the analyzer of time of flight. This extraction energy is proportional to the kinetics energy of ions, fixed by:

$$E = \frac{1}{2}mv^2$$

, where m corresponds to the mass and v to the velocity of the extracted atoms. Thus, by measuring the time necessary to cross the analyzer (proportional to v), it is possible to extract the mass of these atoms [5].

1.4.2 Atomic Force Microscopy (AFM)

AFM is a very common characterization tool that allows to produce 3D profiles of a surface down to the subnanometer scale. AFM can image almost anything, from hard to soft surfaces, in the air, in liquids and in vacuum [6]. The image is constructed by measuring the surface height for each pixel using a solid force probe. The AFM probe consists in a tip, usually made of Si or SiC, placed at the extremity of a cantilever, which bends upward or downward according to the surface morphology. As the bending is extremely weak, it is indirectly measured by the reflection of a laser upon the surface of the cantilever (see on Fig. 5).

The surface is scanned by the probe being into continuous contact (contact mode) or into intermittent contact (tapping mode), either by the displacement of the probe or by that of the sample. The image can reach a sub-nanometer resolution in height and a nanometer resolution horizontally, for dimensions of image comprised between $1\ \mu\text{m} \times 1\ \mu\text{m}$ and $100\ \mu\text{m} \times 100\ \mu\text{m}$.

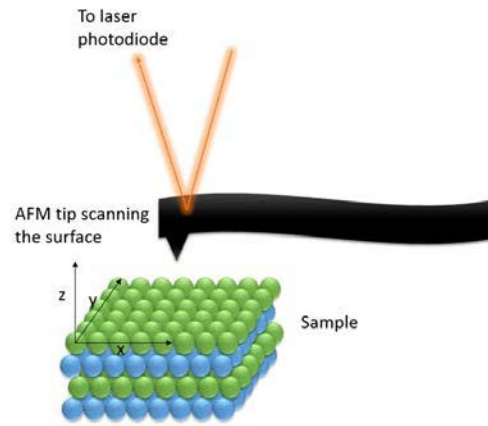


Figure 5: Schematic representation of the AFM working principle.

Different statistics can be extracted from an AFM image, such as peak-to-valley distances, the root mean square roughness (RMS) or the Fourier transform, in order to identify periodic patterns upon a surface [6].

1.4.3 Optical profilometer

The optical profilometer brings another method to study the morphology of a surface. It uses the principle of the optical interferometry to extract the height profile from an image obtained by an optical microscope. The incident beam is split into two beams inside the interferometer: the first is directed on a mirror, forming the reference signal whereas the second beam is direct on the sample surface (see on Fig. 6). The two beams combined together form interference fringes due to the difference of optical paths. After the acquisition with a detector, these fringes can be treated to extract the height of each digitized pixel [7].

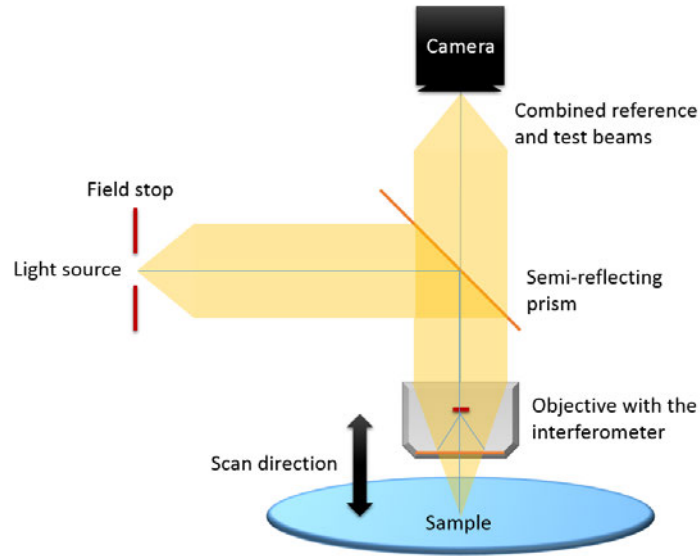


Figure 6: Schematic representation of the optical profilometer.

1.4.4 Measurement of the bonding energy by double cantilever beam (DCB)

The bonding energy of a system of two wafers can be determined by the insertion of a blade at the interface of bonding, as proposed by Maszara [8]. It induces the propagation of an opening front over a distance L , corresponding to the unbounded area (see on Fig. 7).

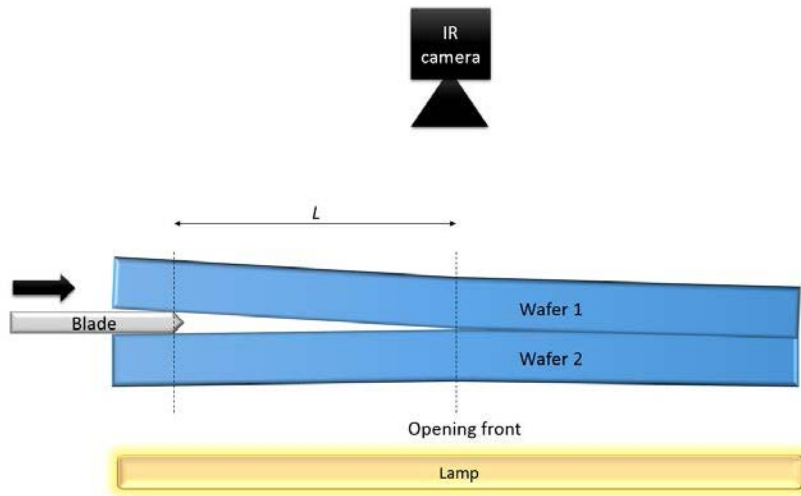


Figure 7: Schematic representation of the DCB approach to characterize the bonding energy.

This distance can be put into relation with the bonding energy, $E_{bonding}$ and the elastic deformation of the plates due to the blade insertion for 2 individual wafers, as following:

$$E_{bonding} = \frac{3}{32} \frac{E * t^3 * y}{L^4}$$

, where E is the Young modulus of Si, t is the thickness of wafer and y the thickness of the blade.

2 Laser-assisted Smart Cut™ study (Chapter 5)

After studying the splitting of implanted Si in a furnace equipment (i.e. with an annealing temperature inferior to 700°C), the chapter 5 proposes to consider a splitting annealing realized by a laser beam. Therefore, the temperature range of splitting annealing is considerably enhanced (up to 1300°C) in order to cover the temperatures that can be reached by the implanted Si during the step of liquid phase epitaxial growth upon an implanted Si (treated in Chapter 6).

Three objectives pave the way for this study:

- The demonstration of the possibility of blistering/splitting in implanted Si by laser annealing.
- The characterization of the splitting kinetics for temperature going possibly up to the melting point of Si.
- A prospective work on the industrial applications for the process of laser-assisted Smart Cut™ for the elaboration of heterostructures.

In spite of the fact that the kinetics of Smart Cut™ has never been investigated over the temperature range considered here (potentially up to the melting of Si, $T_m = 1414^\circ\text{C}$), it is possible to establish a “domain of high probability” in terms of temperature-annealing duration, based on literature. This procedure will be presented in the chapter 5.

2.1 Preparation of the blistering samples

The part of the study dealing with the blistering being just a preliminary part, only one sample has been prepared, with high dose conditions of implantation (i.e. $1.0 \cdot 10^{17} \text{ Hcm}^{-2}$ with an implantation energy of 32 keV). This condition has been chosen in order to facilitate the formation of defects following the annealing.

2.2 Preparation of the samples for the elaboration of hetero-structures

2.2.1 Implanted Si bonded with sapphire

The first part of the study of laser-assisted splitting considers systems made of implanted Si wafer (of 100 mm of diameter) bonded with C-type sapphire of the same diameter. The sequence of preparation of the samples is as following:

- The formation of the buried oxide (thickness of 400 nm) on the Si donor wafer by thermal oxidation in a wet atmosphere.
- The deposition of 200 nm of Si oxide on the sapphire surface by PE-CVD followed by a densification annealing. This oxide facilitates the bonding with the implanted Si.
- The ionic implantation of H in the donor wafer, with energy of 76 keV, corresponding to a transferred thickness of ~800 nm. The implantation dose is varied, according to the Table 3, over a large range of implantation doses, from low dose to high dose, mainly for experimental reasons. Indeed, the time available on the equipment being limited to a few days, it was necessary to consider a large panel of results.

Table 3. Conditions of implantation of the hetero-structure samples

Imp. dose (Hcm ⁻²)	Low dose	Normal dose		High dose	
Si bonded with sapphire (diameter 100 mm)	4.0*10 ¹⁶ 76 keV	5.0*10 ¹⁶ 76 keV	6.0*10 ¹⁶ 76 keV	1.0*10 ¹⁷ 76 keV	1.2*10 ¹⁷ 76 keV

- The cleaning before bonding is realized in a bench, with a RCA solution.
- The bonding of the sapphire and of the implanted Si wafer is realized manually on a bonding bench.

The second part of the study of laser-assisted splitting considers samples composed of implanted Si wafer (of 200 mm of diameter) bonded with Eagle® glass (made by Corning) of the same diameter. The samples are prepared according to the following procedure:

- The formation of the buried oxide (thickness of 400 nm) on the Si donor wafer by thermal oxidation in a wet atmosphere. (NB: the deposition of oxide on the glass wafer is not necessary in this configuration).
- The ionic implantation of H in the donor wafer, with energy of 76 keV, corresponding to a transferred thickness of ~800 nm. The implantation dose is varied, according to the Table 4, over a large range of implantation doses, from low dose to high dose, mainly for experimental reasons.

Table 4. Conditions of implantation of the hetero-structure samples

Imp. dose (Hcm ⁻²)	Low dose	Normal dose	High dose
Si bonded with Eagle glass (diameter 200 mm)	4.0*10 ¹⁶ 76 keV	5.0*10 ¹⁶ 76 keV	1.0*10 ¹⁷ 76 keV

- The cleaning before bonding is realized in a bench, with a RCA solution.
- The bonding of the sapphire and of the implanted Si wafer is realized manually on a bonding bench.

2.3 Description of the laser equipment

Two different lasers were considered for this study, the first aiming to fulfil a preliminary study of blistering of implanted Si, the second being devoted to a splitting characterization.

2.3.1 Excimer ArF ns laser ($\lambda = 193$ nm)

The first laser considered in the study is an ArF excimer laser, with a wavelength of 193 nm. This type of laser proposes fluencies up to 1 J/cm², pulse duration of 20 ns with a repetition rate up to 100 Hz. It can treat spots of limited size (up to 1x1 mm²) and is usually employed for ablation or lift-off processes, thanks the very high density of energy available. Into particular Si has been studied under these process conditions, e.g. for the fabrication of porous Si or nanometer-sized Si [9]. The wavelength of 193 nm

gives a very low absorption length of ~ 1 nm [10], what helps to the formation of non-equilibrium conditions near the surface and finally to the ablation phenomenon [11].

It is worth noting that the equipment considered here has no temperature recording equipment, such as the pyrometer included in the diode laser presented hereafter. Thus, the conditions of annealing will be defined here by a fluency of pulses, with a fixed duration of 20 ns, and a number of pulse repetitions, up to 20 000 times. The configuration of the laser treatment is illustrated by the fig. 8. In this particular configuration, the sample is displaced by the chuck movements and the laser head is fixed.

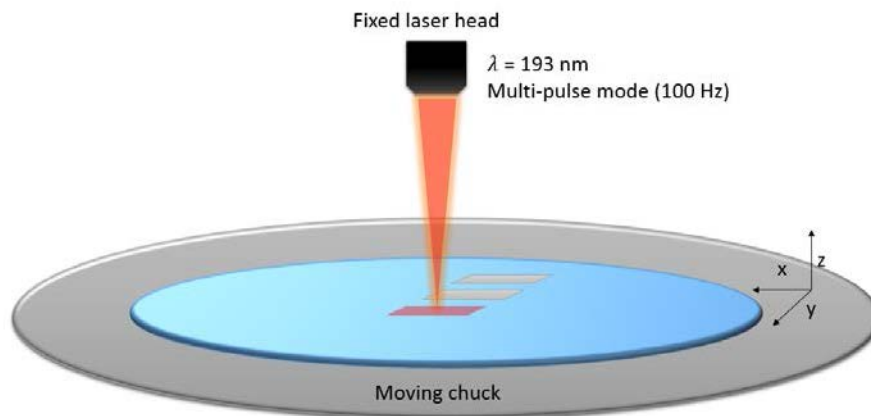


Figure 8: Schematic representation of the annealing of the sample by excimer the ns-laser.

2.3.2 Dynamic Surface Anneal (DSA) laser ($\lambda = 808$ nm)

The DSA is an equipment of continuous laser produced by Applied Materials (see Fig. 9). Its head is composed of an ensemble of 14 diodes of 100 W each, emitting at a wavelength of 808 nm. The laser head scans the material to anneal, with a scanning speed from 75 to 300 mm/s, equivalent to residence time of 1 ms to respectively 0.25 ms, as reported on Table 5. The laser spot presents a width of 11.5 mm with a length of 75 μ m.

The sample is placed on a heating chuck, in order to pre-heat the sample and enhance the laser absorption. In our configuration, the sample will be kept at a temperature of 300°C, in order to minimize the thermal activation of the splitting mechanisms within the implantation zone.

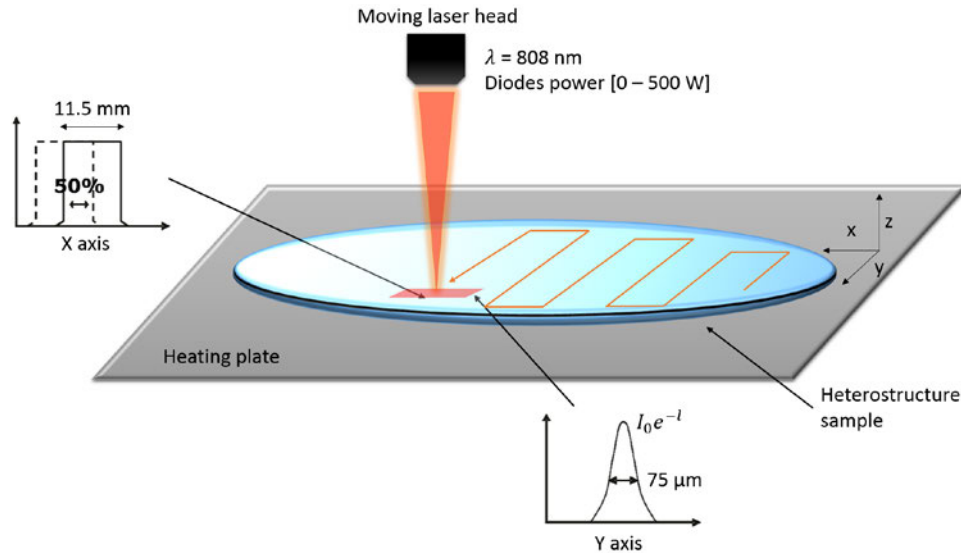


Figure 9: Schematic representation of the sample annealing by ms laser.

Table 5. Main characteristics of the DSA laser

Parameters	Low dose
Wavelength	808 nm
Scanning speed	75 – 300 mm/s
Corresponding residence time	1 – 0.25 ms
Temperature of chuck	300°C

2.3.3 Optical pyrometer

A pyrometer is coupled with the DSA laser head, and allows to record in situ the temperature at the surface of the sample (with a frequency of 100 Hz). The pyrometer employed here considers a wavelength $\lambda = 1020$ nm and a spot of analysis of 12×1 mm², which is a bit larger than the laser spot but does not modify the collected signal corresponding to the maximum temperature.

The signal of temperature is related to the Planck law, describing the emission of black body as a function of the temperature. It can be obtained with the following formula:

$$T_c = \frac{0.014388}{\lambda \ln \left(\frac{S_f \cdot \varepsilon \cdot 3.74 \cdot 10^{-16}}{\lambda^5 \cdot R_p} \right) + 1}$$

where R_p is the collected photo-current, ε is the emissivity of the material, S_f is a constant depending on the pyrometer, that is calibrated by determination of the melting point of the material (i.e. Si in this case) [4].

2.4 Characterization facilities

The characterization tools aims to bring understanding elements on the response of the implanted material during the laser annealing. Thus, the physical properties of the film after laser-assisted exfoliation are evaluated (remaining stress with Raman and strain of the crystal by XRD) as well as the homogeneity of laser heating (with SAM). Into addition, the electrical properties of the films are characterized by 4-probe measurements.

2.4.1 Raman spectroscopy

The Raman spectroscopy is a non-destructive characterization tool relying on the light-material interactions. The Raman diffusion is an inelastic process in which an incident photon creates or annihilates one or several phonons (the quasi particle corresponding to a quantum of vibrations within a crystalline network), with a change in its energy over a precise range.

We can distinguish two types of Raman diffusion as illustrated on the Fig. 10: the Stokes Raman diffusion, where the incident photon diffuses with a frequency ν_d and creates a phonon (frequency ν_{vib}), and the anti-Stokes Raman diffusion, where a phonon (frequency ν_{vib}) is annihilated during the diffusion of the Raman photon (frequency ν_d).

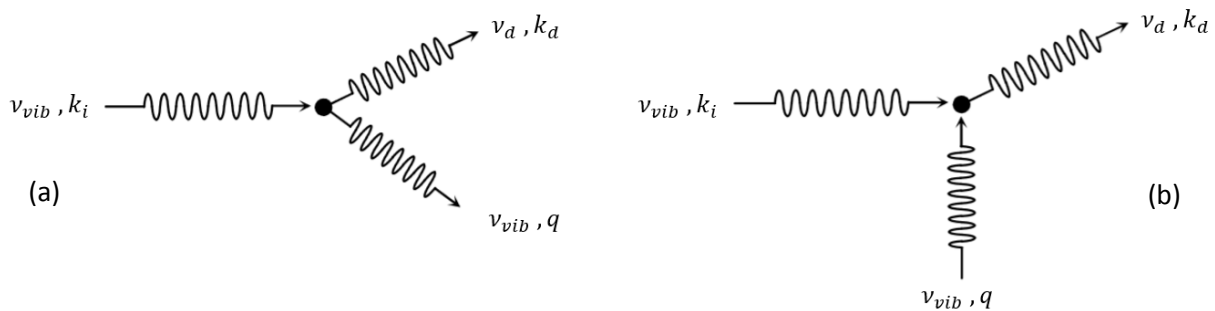


Figure 10: Process of Raman diffusion Stokes (a), anti-Stokes (b).

Thus, the Raman spectrum includes two symmetric parts, as illustrated on Fig. 11.

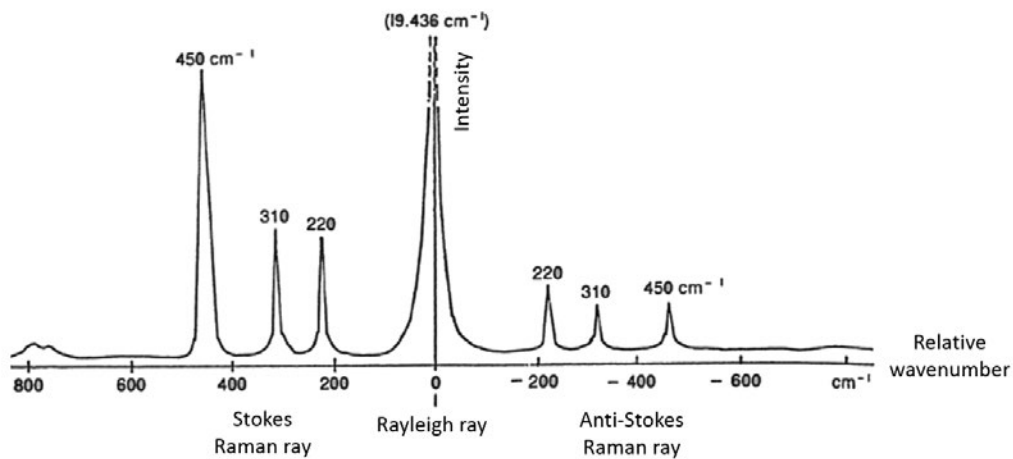


Figure 11: Illustration of a Raman spectrum [12].

As the vibrational states directly depends on the chemical bonds of the crystal, the analysis of this spectrum allows to determine the composition as well as the structure of a crystalline material.

In very basic terms, a Raman tool is composed of a laser beam source (typically He-Ne of $\lambda = 632.8$ nm), a series of optics, a spectrometer and acquisition electronics.

2.4.2 X-Ray Diffraction analysis (XRD)

Similarly to Raman, the XRD analysis relies on light-material interactions that can be observed in the organized lattice of a crystal interacting with X-ray beam. Indeed, two processes might occur, the first being the absorption of the beam by the core electrons of the electronic cloud and the ejection of a photoelectron [13]. This process is used in the X-ray photoelectron spectroscopy (XPS) and will not be considered here. The second process is the scattering of the X-ray by the crystal. As the wavelength range of X-rays is of the same order of magnitude than the interatomic distance in a crystal, the diffused signal will show constructive, alternatively destructive, interferences. These combined interferences form a diffraction pattern that forms the starting point of the analysis [7].

The Fig. 12 illustrates the interaction of an incident X-ray beam with a family of inter-reticular planes, designated by the Miller indices (h, k, l) .

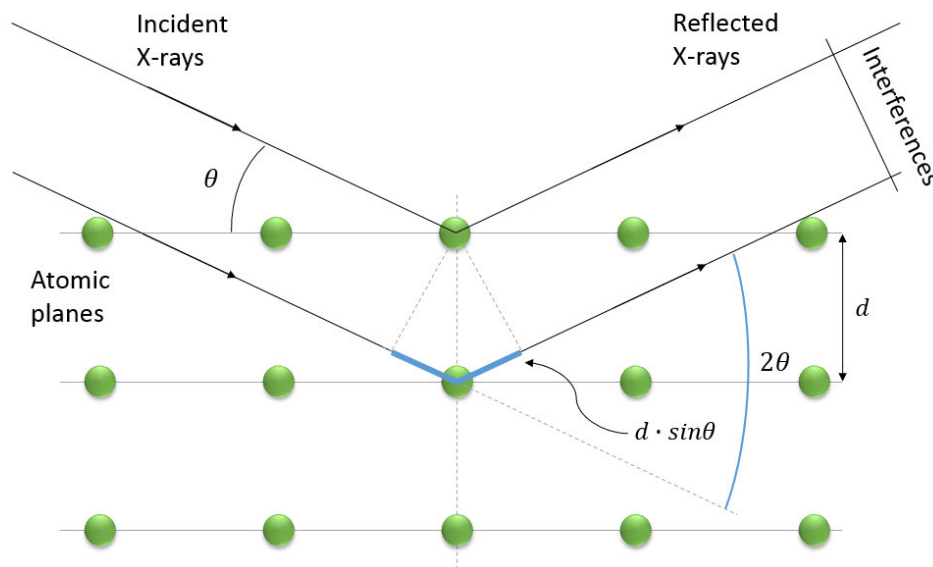


Figure 12: Schematic representation of the x-ray diffraction by a family of (h, k, l) planes of a crystal lattice.

The pics of diffraction, which corresponds to the constructive interferences, are defined by the Bragg's law, i.e. when the difference of optical path is a multiple of the wavelength:

$$2d \cdot \sin\theta = n\lambda$$

Thus, the analysis of the diffraction pattern as a function of the angle of incidence gives information on the lattice parameters and on the possible vertical deformation of the crystal [7].

2.4.3 Scanning Acoustic Microscope (SAM)

The acoustic microscope offers a very performing tool for the analysis of multilayered material. It uses the property of acoustic waves to cross easily materials over thicknesses that can reach several mm, independently of their optical absorption properties. The acquisition procedure consists in sending an acoustic wave in a sample by passing through a coupling fluid (typically water), and in measuring the time of flight of the reflected or scattered sound by a transducer, as illustrated on Fig. 13.

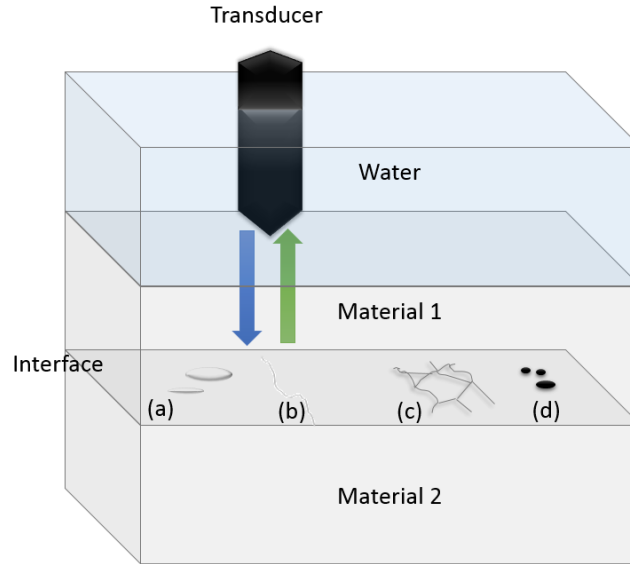


Figure 13: Schematic representation of the principle of the SAM, delamination at the interface (a), crack (b), grain boundaries (c), inclusions (d).

Under the right positioning of the surface, the reflection R at the interface between two materials (including the interface between a material and the coupling fluid), is defined by:

$$R = \frac{Z_2 - Z_1}{Z_2 + Z_1}$$

, where $Z_i = \rho_i v_i$ are the acoustic impedances (ρ is the mass density, v the sound velocity) [3]. Thus, by knowing the composition of a multilayered material, it is possible to detect at the interface of focus any defects such as delamination, crack, inclusion, etc. The image is formed by scanning the bonded structure that requires wafers to be flat and reasonably smooth.

2.4.4 4-point probe measurement

The 4-point probe measurement characterizes the resistivity of a semiconductor, for both bulk and thin film state. The method considers 4 metallic tips, equally spaced at the surface of the sample, as illustrated on Fig. 14. The two outer probes are used to supply a current, whereas the two inner probes measure the voltage in between, to determine the material resistivity.

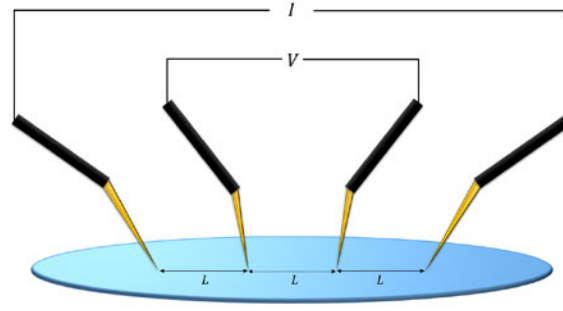


Figure 14: Schematic representation of the 4-point probe measurement method.

For bulk material, if it can be assumed that the point spacing L is very small compared to the thickness of the semiconductor ($L \ll t$). In this case, we consider that the current is emitted as spherical at the probe. The bulk resistivity is defined as following [15]:

$$\rho = 2\pi L \left(\frac{V}{I} \right)$$

For thin film material, what corresponds to our samples, we have the inverse situation (i.e. $L \gg t$) and the current has a ring shape and the sheet resistivity R_s can be expressed as following [15]:

$$R_s = \frac{\pi}{\ln 2} \left(\frac{V}{I} \right)$$

and

$$\rho = \frac{\pi t}{\ln 2} \left(\frac{V}{I} \right)$$

It is worth noting that the samples of Si on Glass or Si on Sapphire could not be characterized by pseudo-MOSFET characterization because of the too high resistivity of the host substrate (for both sapphire and glass).

3 Study growth of silicon from a liquid of Si

We will finish this chapter by presenting the equipment and characterization tools necessary for the study of liquid phase epitaxy onto an implanted Si.

This study has consisted of two distinctive parts, considering two benches of deposition of liquid silicon. This state of affairs has been imposed by the winding-up of the first industrial partner before the end of the initial design of experiments.

Despite considering different equipment, both studies lie on similar approaches. The first essays of deposition of liquid Si are on non-implanted samples, to study the coupling with the surface and the possibility of epitaxial growth. As a second step, the deposition is realized on implanted substrates, to investigate the possibility of detachment of a Si foil hereafter the solidification.

3.1 Conditions of implantation of samples

Three conditions of implantation have been considered as summarized in table 6, with the highest implantation energy available from the implanter (E500 from Varian). This energy of 160 keV gives R_p of 1.8 μm and is chosen in order to seclude as much as possible the splitting zone and the solidification zone.

Table 6. Conditions of samples implantation

Imp. dose (Hcm^{-2})	Non-implanted	$5.0 \cdot 10^{16}$	$1.0 \cdot 10^{17}$
160 keV	X	X	X

3.2 Surface preparation before deposition of liquid Si

The procedure to clean the surface aims to remove as much as possible any traces of oxides or organic contaminants. It includes the following steps:

- Formation of 145 nm of thermal oxide (before the implantation step) in order to form a sacrificial layer
- Oxide removal with hydrofluoric acid (30 % HF solution)
- Deionized water rinsing
- Ethanol rinsing
- Drying with Isopropyl alcohol (IPA) in Ar
- Introduction in the deposition chamber

3.3 Description of the benches of liquid Si deposition

3.3.1 Melting of Si in graphite crucible

The first equipment of LPE (Liquid Phase Epitaxy) considers a crucible of graphite surrounded by electromagnetic induction coils as the source of liquid Si, as illustrated on Fig. 15. The electromagnetic field induces electric fields within the graphite that warms up as a result of the Joule effect. A load of

20 – 100 gr of Si is then heating by convection and radiation up to the melting point, the temperature being recorded by an optical pyrometer. The release of liquid Si is controlled by an inlet of Ar allowing to create an overpressure within the crucible. The last has a buzzard of 0.6 mm of diameter by which the flow of liquid Si is released above the sample surface, the last being into rotation. The sample is placed at the bottom of a steel chamber in over-pressure of Ar, with an exhaust placed at the top of the chamber. Thus, as Ar is denser than most of the air components (in particular O₂, CO₂ and H₂O), this configuration allows to remove the contaminants quite efficiently in a very simple way.

It is worth noting that the use of a graphite crucible is a priori an important source of carbon contamination for the liquid Si. Except this aspect, the proposed configuration is very interesting, as it theoretically allows to form thin layers of Si on a relatively large surface.

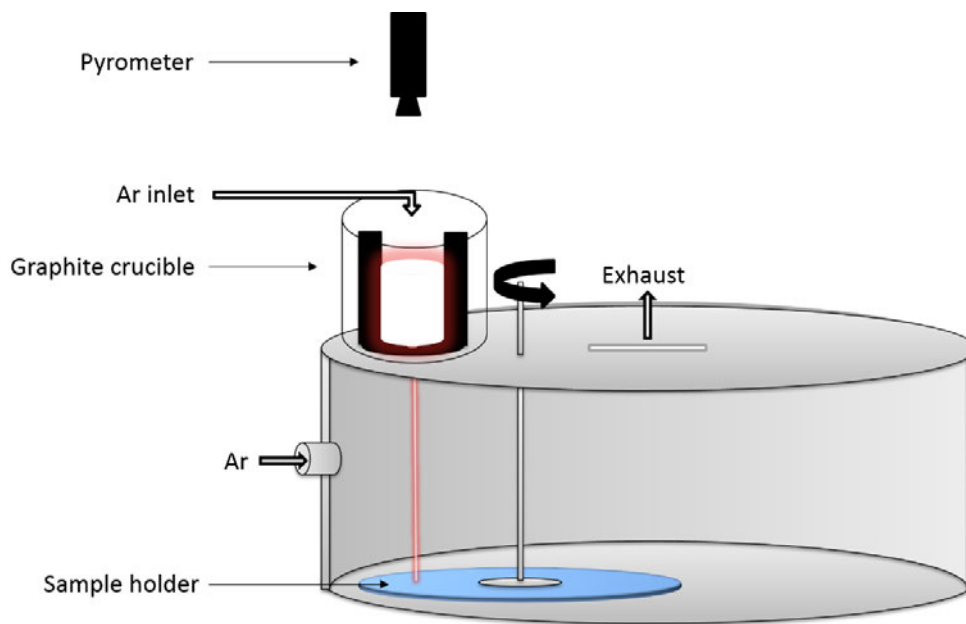


Figure 15: Schematic representation of the equipment of LPE using a graphite crucible as the liquid Si source.

3.3.2 Basic principles on electromagnetic levitation

The electromagnetic levitation consists in compensating the gravitation by electromagnetic force, rendering possible the levitation of a metallic or semiconducting material. The sample to levitate is placed in magnetic cavity produced by a levitation coil combined with a contra-coil connected to a high-frequency generator (typically a few hundreds of kHz) [16].

The underlying equation of the electromagnetic levitation is the Maxwell-Faraday equation, linking the rotational of the electric field $\nabla \wedge E$ and the time derivative of the magnetic field B :

$$\nabla \wedge E = - \frac{\partial B}{\partial t}$$

Thus, considering a conic inducer composed of a series of copper whorls, as illustrated on Fig. 16, the appliance of an alternative current passing through induces an alternative magnetic field. The Lentz

law indicates that the primary current induces an opposite sign currents within the conducting system, what participate in the heat generation by Joule effect [16]. Considering a continuous charge distribution, the electromagnetic force F applied on a charged particle (of charge q and instantaneous speed V_q) of the sample into levitation is defined as following:

$$F = qE + qV_q \wedge B$$

Thus, the induced currents create a centripetal force maintaining the sample within the electromagnetic cavity.

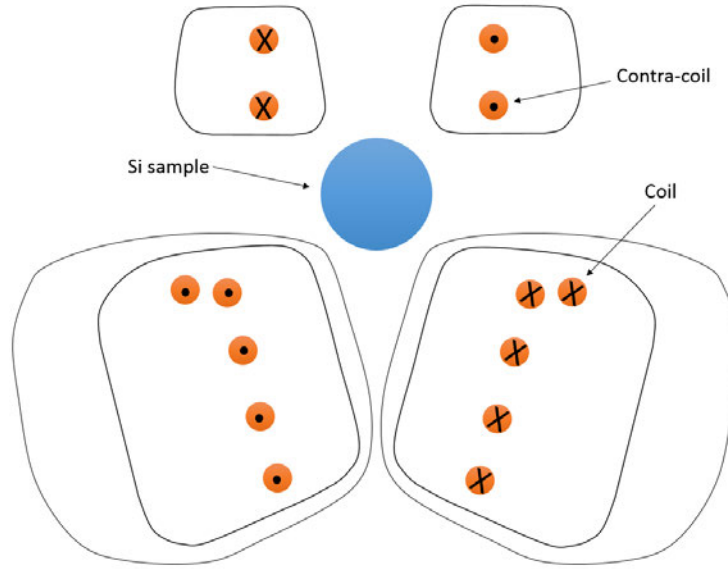


Figure 16: Schematic representation of the levitation coil. The electromagnetic field resulting from the alternative current passing in the coils allows the creation of the electromagnetic force F compensating the gravity.

The main parameters involved in the levitation are summarized in the so-called skin depth δ :

$$\delta = \sqrt{\frac{\rho}{\mu_1 \pi f}}$$

, where f is the frequency of the current, μ_1 is the magnetic permittivity of the sample and ρ is the electrical resistivity. It roughly determines the width in which the induced current is concentrated. Obviously, this parameter must be much small than the sample dimensions in order to have an efficient heating. Thus, in case of a semiconducting material such as Si, the electromagnetic coupling required either an important doping of Si or to pre-heat the sample. The last strategy is employed for the two geometries employed in this study.

3.3.3 Melting of Si in a self-crucible

The first equipment based on the principles exposed earlier is composed of a cylindrical inducer, with a capacity of 20 – 100 gr, placed at the top of a steel chamber under controlled atmosphere (primary vacuum, Ar etc.) as illustrated on Fig. 17. The temperature of the melt is measured by a dual wavelength pyrometer placed above. The preheating of the Si load is realized by a ring of graphite placed above it, without any contact with load for both solid and liquid states. The sample is placed below the inducer, with a variable angle of inclination and the dropping of the liquid Si is controlled by stopping the current generator.

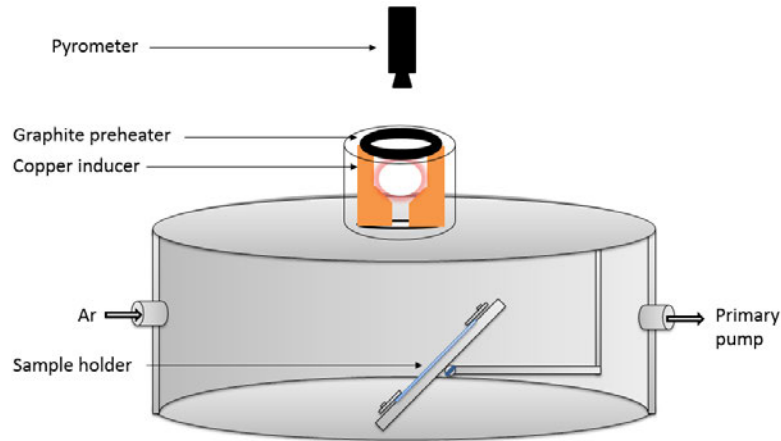


Figure 17: Schematic representation of the liquid Si deposition chamber, using a self-crucible of liquid Si as the source.

3.3.4 Melting of Si in an electromagnetic levitator

The second configuration is composed of an electromagnetic levitator in a quartz chamber, as illustrated on Fig. 18. The chamber can be placed under secondary vacuum with a turbomolecular and an ionic pump.

The Si load to melt is much lower in this configuration (up to 10 gr) and the preheating is realized by a cane composed of graphite embedded in a quartz tube. The cane can be slid vertically, in order to put the sample into levitation after the pre-heating phase. The substrate to be covered by liquid Si is positioned onto a holder that can be rotated to place the substrate below the liquid droplet. Similarly to the first configuration, the release of the droplet is controlled by stopping the current generator.

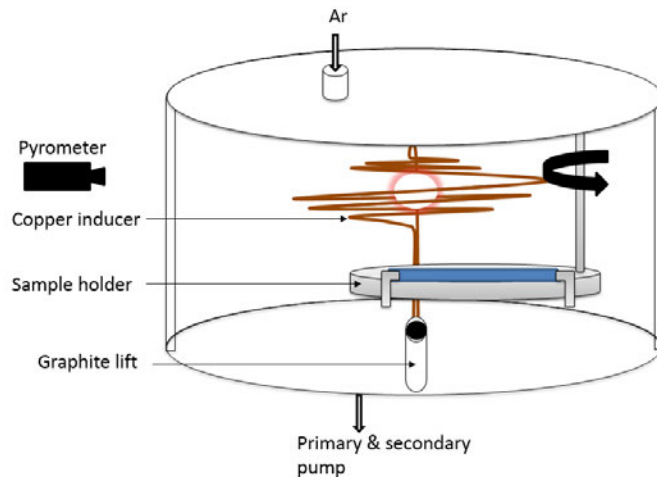


Figure 18: Schematic representation of the equipment of electromagnetic levitation considering a levitating droplet of liquid Si as the source of liquid.

3.4 Characterization facilities

Different characterization tools are employed in this study, in order to determine the potential of the process proposed here, in terms of crystalline quality and optical properties of the film.

3.4.1 Electron Back-Scattered Diffraction (EBSD)

EBSD is the main characterization method that has been considered for the study of the samples of Si deposited by LPE. EBSD allows to identify the orientation of crystalline grains on an image obtained by Scanning Electron Microscopy (SEM). Thus, it provides a powerful tool for the analysis of the epitaxial growth, after deposition and possibly detachment from the surface.

The EBSD detector is usually combined to a SEM equipment and collects the electrons after their back-scattering on a tilted sample (typically with an angle of 65-75°), as figured on Fig. 19. The crystal structure at the point of incidence diffracts the electron beam according to the Bragg's law, already exposed earlier. As a result, each lattice plane generates 2 diffraction cones forming the so-called Kikuchi lines on the phosphor screen of the detector. The obtained figures form the Electron Backscattered Pattern (EBSP).

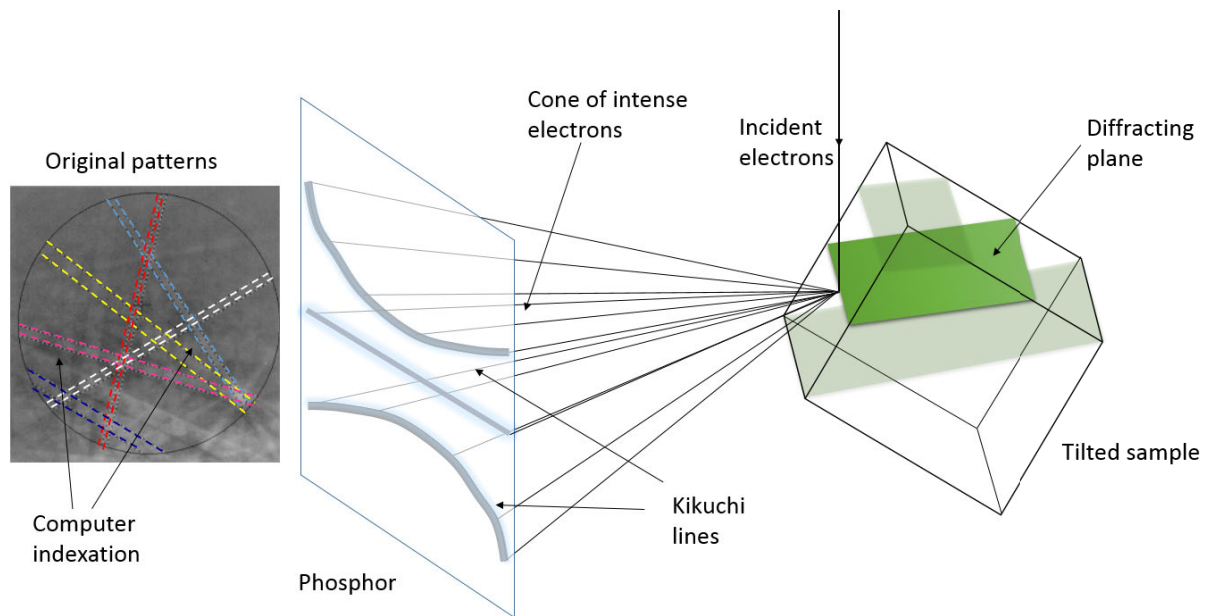


Figure 19: Schematic representation of the scattering of electrons by a tilted crystalline sample. The computer indexation of the Kikuchi lines allows to extract different parameters on a crystal structure (orientation grains, interplanar distance, etc.)

The acquisition procedure consists in acquiring the EBSD over a defined area of the sample, with spatial steps depending on the required resolution. Each diffraction pattern is then indexed by a computing system, according to the user inputs (crystal symmetry, lattice parameters, etc.). Thus, each Kikuchi bands can be used to determine the orientation of the structure, as illustrated on Fig. 20. Finally, a contrast of colour is applied on the SEM image, which gives the coloured image of the EBSD contrast.

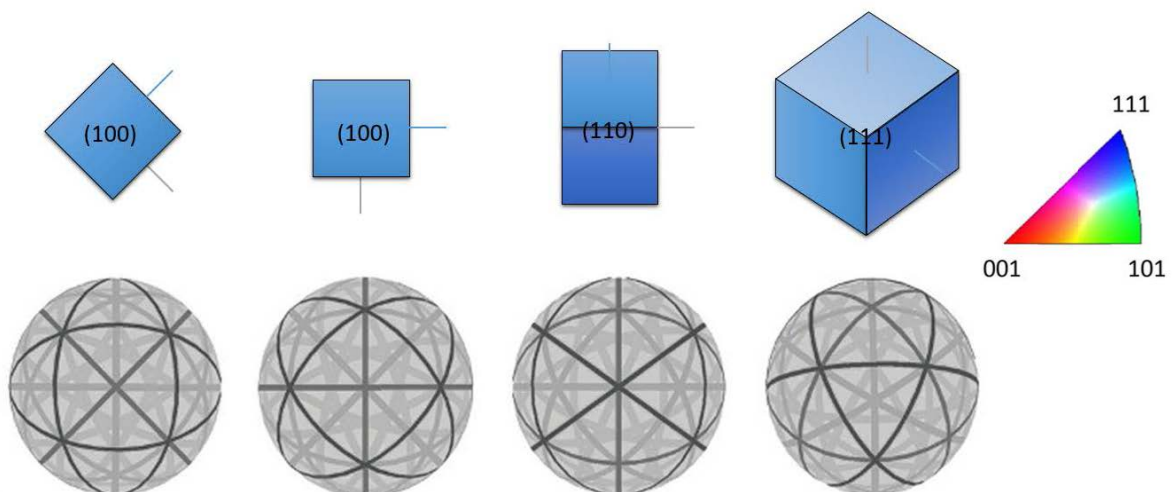


Figure 20: The different diffraction patterns obtained for different orientations of a cubic structure. A contrast of colour is then attributed to each analysis point.

3.4.2 High Angle Annular Dark Field (HAADF) and Electron Energy Loss Spectroscopy (EELS)

The HAADF is a specific imaging mode of the Scanning Transmission Electron Microscope (STEM), which is particularly suitable for the characterization of partially crystalline to highly crystalline materials, as illustrated on Fig. 21 [18]. The main advantage of this mode is to avoid the diffraction effects of the bright-field imaging mode (BF). Thus, a better contrast is obtained when observing nanostructured objects [18].

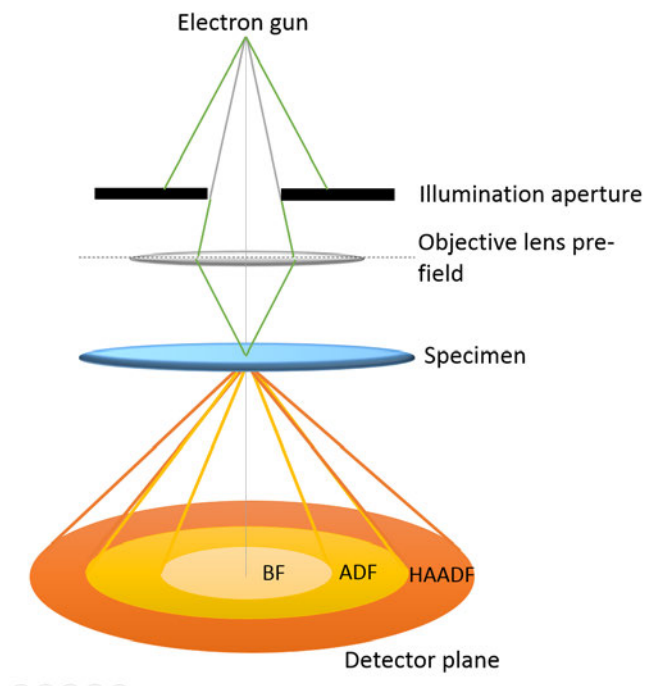


Fig. 21: Schematic representation of the imaging modes in STEM.

The EELS technique brings a chemical contrast to a TEM image (e.g. obtained by HAADF imaging mode). The principle relies on the measurement of the energy loss of electrons after having brought them into the conduction band by inelastic interactions (see on Fig. 22). The identification of the different peaks of energy loss allows to determine the chemical elements into presence in a quantitative way.

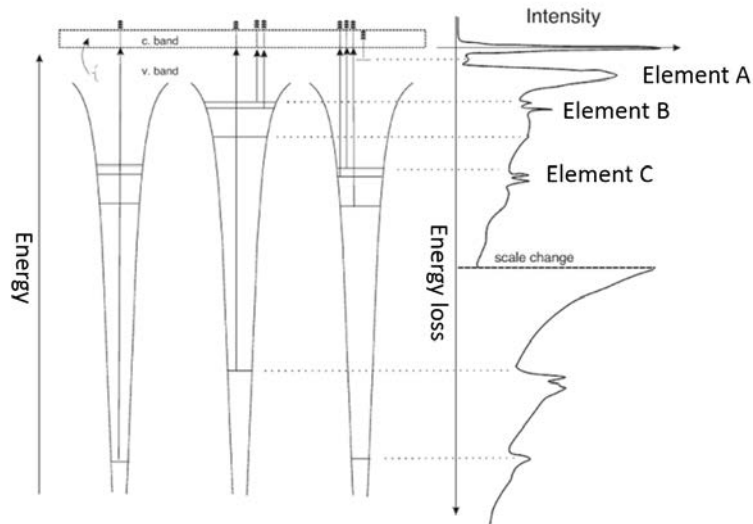


Fig. 22: Schematic representation of the EELS principle and example of EELS spectrum.

3.4.3 Photoluminescence (PL)

The principle of PL relies on the light emission as a relaxation process after the absorption of photons by a material. PL is a very common tool for the optical characterization of a material, in terms of quantum efficiency, presence of midgap defects, etc. The characterization bench is composed of an excitation source, such as a laser or a Xe lamp, a sample holder, a series of optics and a monochromator with a detector, as illustrated on Fig. 23.

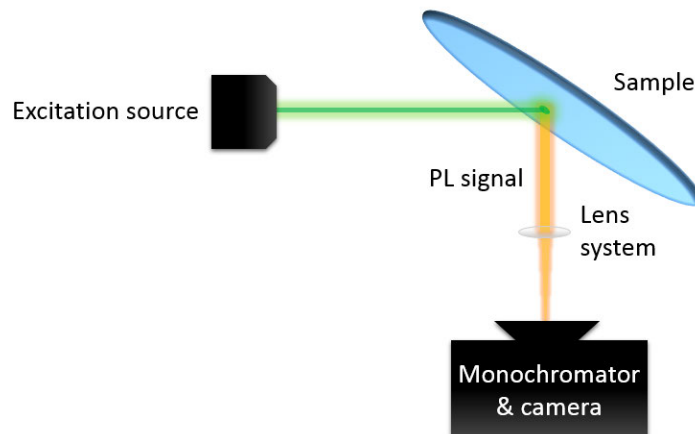


Figure 23: Schematic representation of the PL characterization bench.

An example of PV spectra for a sample of poly-Si wafer is given in Fig. 24, showing different peaks corresponding to different types of dislocation.

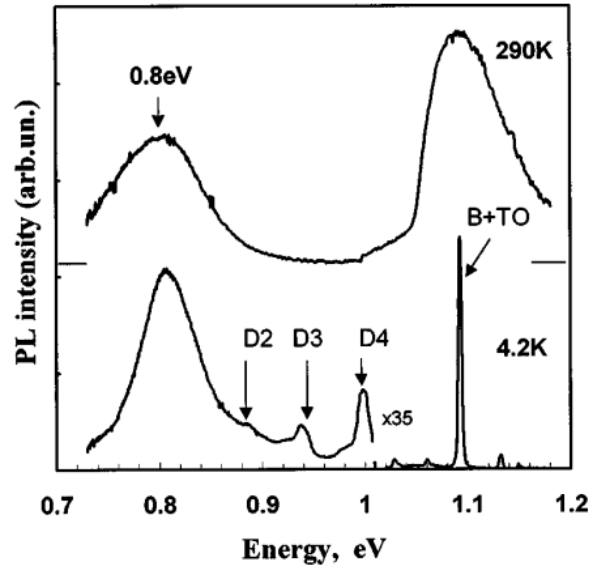


Figure 24: PL spectra of a poly-Si wafer. The PL excitation was performed with a 800 nm wavelength laser illumination at a power of 100 Wcm^{-2} . Different dislocation lines D2, D3 and D4 can be observed on the spectrum measured at 4.2K [17].

Conclusion

The study of blistering and splitting of implanted Si (presented in the chapter 4) relies on the use of heating equipment with fast thermal ramping. Additionally, we propose a specially-dedicated preparation protocol in order to insert thermocouple directly inside the splitting sample. Thus, the thermal history leading to the splitting can be recorded to investigate various different splitting kinetics.

Different characterizations are proposed to study the process of H diffusion during the splitting annealing (SIMS) as well as its effect on the interface energy (DCB). Finally, tools (AFM and optical profilometry) are proposed for the characterization of the surface topology of the samples after splitting.

The second part of this chapter presents different laser tools for the annealing of blistering and splitting of implanted Si. The samples considered here are heterostructures made of an implanted Si bonded with glass or sapphire wafers. Different characterization tools are considered to study the homogeneity of the laser annealing (SAM), the remaining stress within the structure (Raman) and the electrical properties of the samples after splitting (4-probe measurement).

Finally, the last part of this chapter presents on different benches of LPE, using a graphite crucible or a self-crucible. The morphology of the solidified films is characterized by EBSD and HAADF analysis and PL is considered to compare the optical properties of the films obtained by LPE with a reference Si substrate.

References

- [1] **Q. Wang et al.**, Efficient heterojunction solar cells on *p*-type crystal silicon wafers, *Appl. Phys. Lett.*, vol. 96, pp. 1-3, 2010.
- [2] **M. Bruel, B. Aspar, H. Moriceau, E. Jalaguier, C. Lagahe**, Single-crystal semiconductor delamination and transfer through hydrogen implantation, *Electroch. Soc. Proc.*, vol. 99-1, pp. 203-213, 1999.
- [3] **R. B. Fair**, Rapid thermal processing, Science and Technology, Accademic Press, 1993.
- [4] **A. Colin**, Etude des couplages radiatifs et thermiques et des modifications physico-chimiques engendrés par un recuit laser milliseconde sur la grille polysilicium de la technologie CMOS 45 nm, Thèse de doctorat de l'Université de Strasbourg, 2010.
- [5] **Y. Leng**, Materials characterization. Introduction to microscopic and spectroscopic methods. John Wiley & Sons, 2008.
- [6] **G. Haugstad**, Atomic Force Microscopy. Understanding basic modes and advanced applications. John Wiley & Sons, 2012.
- [7] **J. D. Penot**, Fragilisation et dynamique de rupture du silicium implanté, Thèse de l'Université de Grenoble, 2010.
- [8] **F. Fournel, L. Continni, C. Morales, J. Da Fonseca, H. Moriceau, F. Rieutord, A. Barthelemy, I. Radu**, Measurement of bonding energy in an anhydrous nitrogen atmosphere and its application to silicon direct bonding technology, *J. of Appl. Phys.*, vol. 111, pp. 1-7, 2012.
- [9] **Y. Yamada, T. Orii, I. Umezu, S. Takeyama, T. Yoshida**, Optical properties of silicon nanocrystallites prepared by excimer laser ablation in inert gas. *Jpn. J. Appl. Phys.*, vol. 35, pp. 1361-1365, 1996.
- [10] **M. A. Green, M. J. Keevers**, Optical properties of intrinsic silicon at 300 K, *Prog. In Photo.: Res. and Appl.*, vol. 3, pp. 1968-192, 1995.
- [11] **J. Dück, N. Lastzka, S. Steinlechner, R. Schnabel, K. Danzmann**, Absorption measurement in silicon, Institute for Gravitational Physics, Leibniz Universität Hannover and Max Planck Institute for Gravitational Physics (Albert Einstein Institute) Hannover, pp. 1-23.
- [12] **R. Hammoum**, Etude par spectroscopie Raman de la structure des domaines périodiquement polarisés dans le niobate de lithium (PPLN). Thèse de doctorat de l'Université de Metz, 2008.
- [13] **B. E. Warren**, X-Ray diffraction, Dover Publications, 1990.
- [14] **K. Raum, K. V. Jenderka, A. Klemenz, J. Brandt**, Multilayer analysis: quantitative scanning acoustic microscopy for tissue characterization at a microscopic scale, *IEEE Trans. on Ultr., Ferro., and Fred. Contr.*, vol ; 50, No. 5, pp. 507-516 2003.
- [15] **L. B. Valdes**, Resistivity measurements on germanium for transistors, *Proc. of the I-R-E*, pp. 420-427, 1954.
- [16] **M. Beaudhuin**, Etude expérimentale et numérique de la précipitation d'impuretés et de la formation des grains dans le silicium photoovoltaïque, Thèse de doctorat de l'INP, 2009.
- [17] **Y. Koshka, S. Ostapenko, S. Mac Hugo, I. Tarasov**, Scanning room-temperature photoluminescence in polycrystalline silicon, *Appl. Phys. Lett.*, vol. 74, no. 11, pp. 1555-1557, 1999.
- [18] **C. Kübel, A. Voigt, R. Schoenmakers, M. Otten, D. Su, T.-C. Lee, A. Carlsson, J. Bradley**, Recent advances in electron tomography: TEM and HAADF-STEM tomography for materials science and semiconductor applications, *Microsc. Microanal.*, vol. 11, pp. 378-400, 2005.

Chapter 4. Study of Smart Cut™ at high temperature by conventional furnace

This chapter aims to study the kinetics of Smart Cut™ at high temperature for implanted Si. The splitting at high temperature is involved in both processes introduced in the introduction, i.e. the laser-assisted Smart Cut™ and the LPE onto an implanted Si. The two processes involve fast thermal ramps and high temperatures. Thus, we will first focus our attention on the response of the implanted material under such annealing conditions.

The implantation of Si with light ions (such as H and/or He), as well as the formation of defects into relation with the annealing conditions have been widely studied, as we have seen in the chapter 2. Nevertheless, some aspects remain controversial, such as the behavior of implanted H and the kinetics of splitting at high temperature. This part will bring further results in order to build a coherent model putting into relation macroscopic observations (splitting kinetics, bonding energy of the system of bonded wafers), microscopic characterizations (such as the migration of H as a function of annealing conditions) and numerical calculations.

At first, we will characterize the heating system considered for the annealing of samples. Then, a preliminary analysis will be presented by the characterization of the blister growth in an implanted Si standing alone. As a third step, the splitting of samples implanted with different doses will be characterized by help of a specially-dedicated heating equipment. Based on the various observations, different hypothesis of splitting will be investigated, with support of numerical modelling. Finally, some extrapolation analysis will be proposed on the behavior of the implanted samples at even higher temperature (i.e. in the temperature range encountered in the two processes of the thesis).

1. Characterization of the heating system

As the control of annealing temperature is a key aspect in order to have trustful observations, this chapter will start by characterizing the different heating apparatus.

As a reminder from chapter 3, two configurations of heating furnace are proposed:

- a heating plate placed under an optical microscope for the analysis of blister growth
- an ensemble of sliding steel plates placed in a furnace

1.1. Heating plate used for the characterization of blistering samples

The blistering as a function of annealing conditions is realized by help of a heating plate placed below an optical microscope (see on Fig. 1 (a)).

The heating plate is characterized by a sample where a thermocouple is introduced. The time to reach 95% of the temperature of the heating plate is plotted on Fig. 1 (b). It can be observed a quite high standard deviation, due to experimental conditions. In the considered range of annealing temperature (400-600°C), the mean value of thermal ramping is 54.7°C/s.

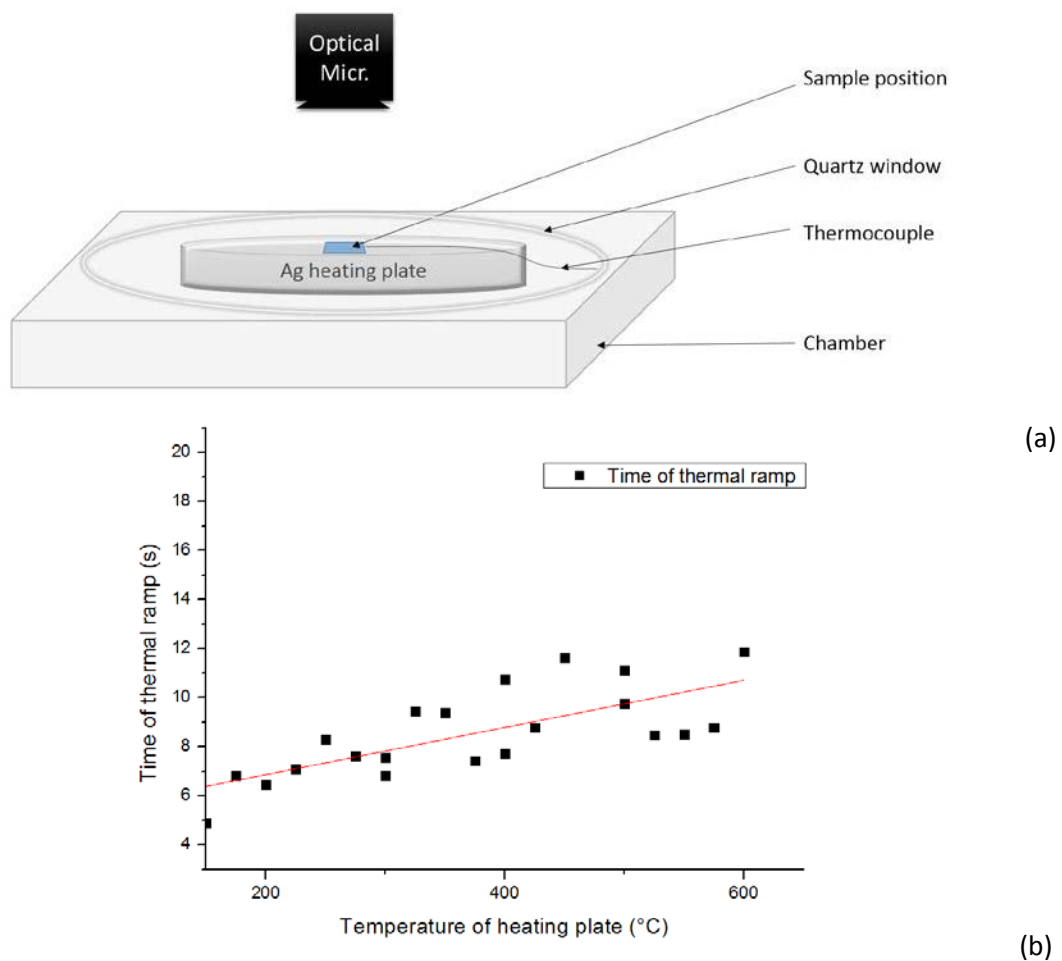


Figure 1: Schematic representation of the heating system for the characterization of blistering (a), time of thermal ramp of the blistering samples as a function of annealing temperature (b).

1.2. Heating system using steel plates for the characterization of splitting

The second equipment characterized here is dedicated to the splitting characterization of samples composed of an implanted wafer bonded with an acceptor wafer, see on Fig. 2 (a). As a reminder from chapter 3, a thermocouple is placed in between the two wafers in order to record the temperature in situ during the splitting annealing (Fig. 2 (b)).

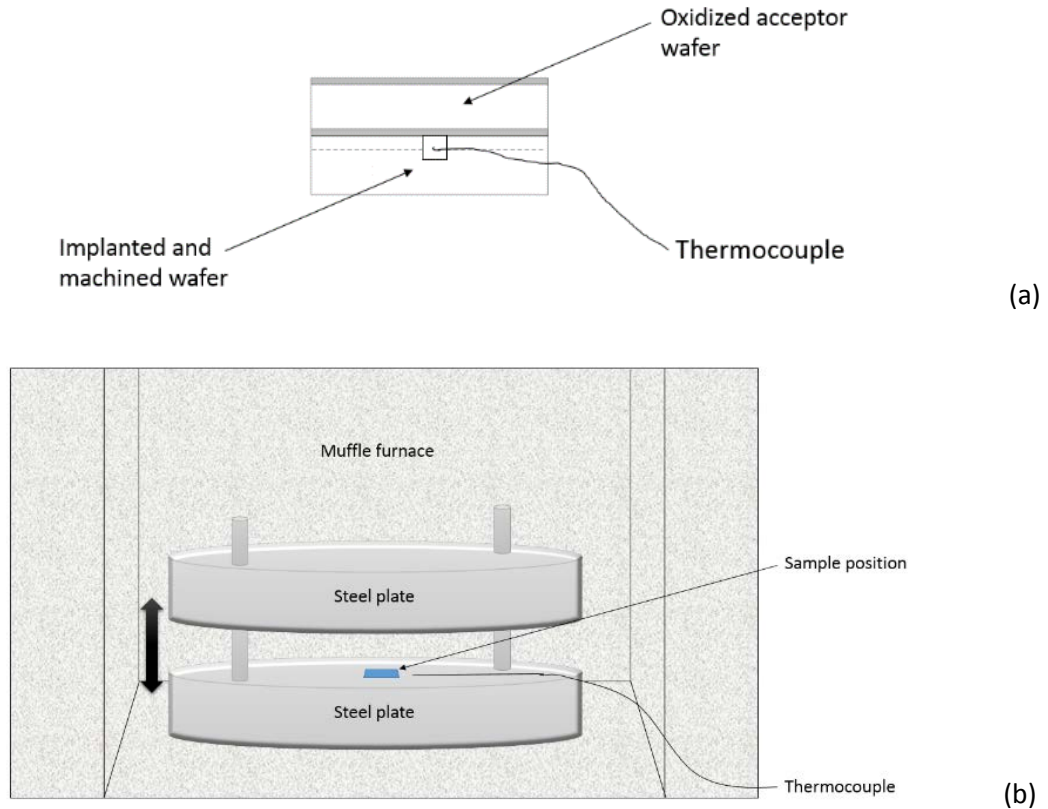
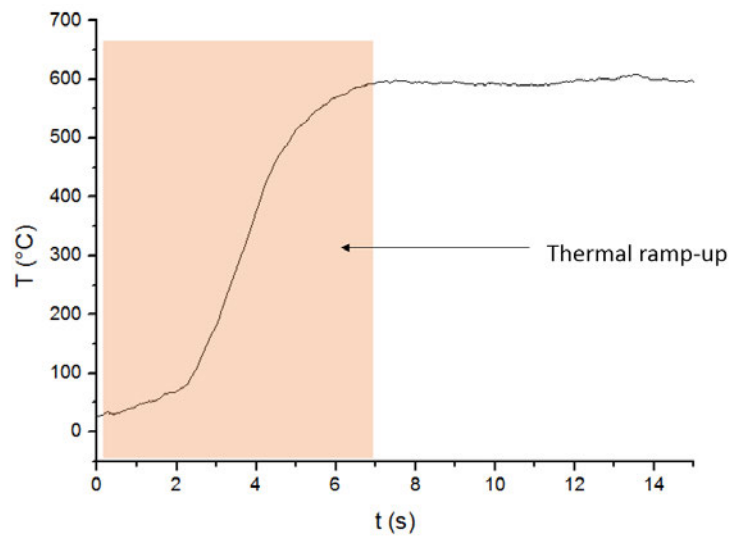
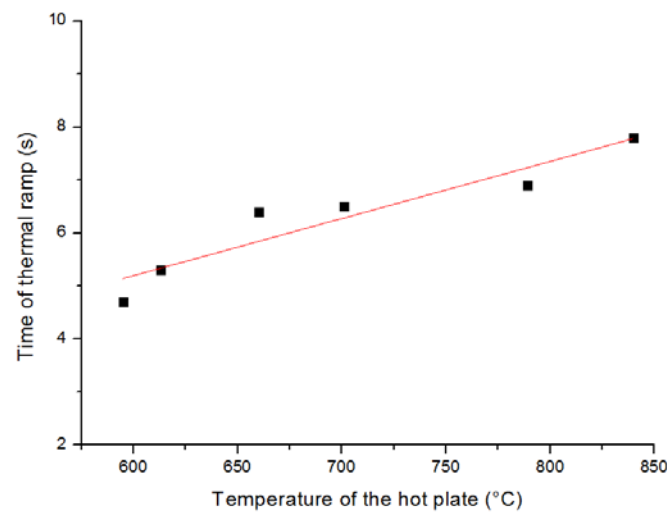


Figure 2: Schematic representation of the splitting sample including a thermocouple (a), and of the heating apparatus for the splitting characterization (b).

The Fig. 3 (a) gives the temperature profile after putting the sample into contact with the hot plates at 600°C, the thermal contact being established at $t = 0$ s. The thermal ramping is plotted as a function of temperature on Fig. 3 (b). The system returns a thermal ramp of 82.8°C/s, i.e. a much higher value than the previous equipment.



(a)



(b)

Figure 3: Temperature profile within the implantation zone during the thermal ramp with the steel plates at 600°C (a), time of thermal ramp within the implantation zone for the steel plates (b).

The Table 1 summarizes the speed of thermal ramping for the different heating configuration.

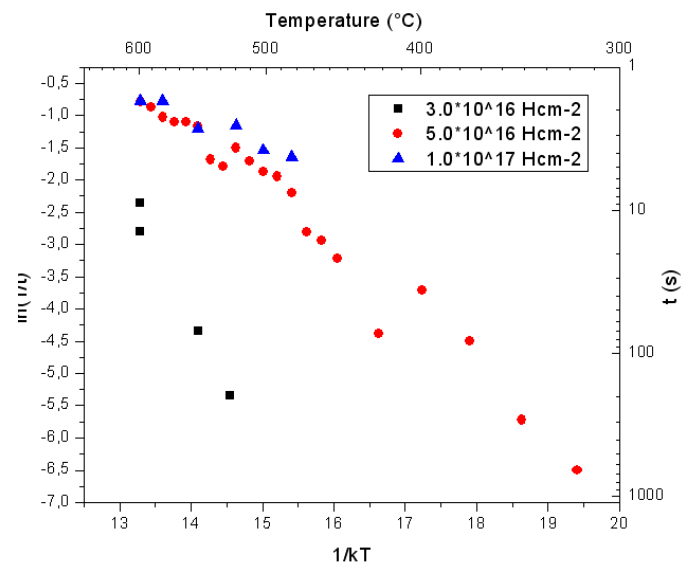
Table 1. Summary of the thermal ramping as a function of the heating equipment.

Heating configuration	Thermal ramping ($^{\circ}\text{C s}^{-1}$)
Heating plate	54.7
Steel plates	82.8

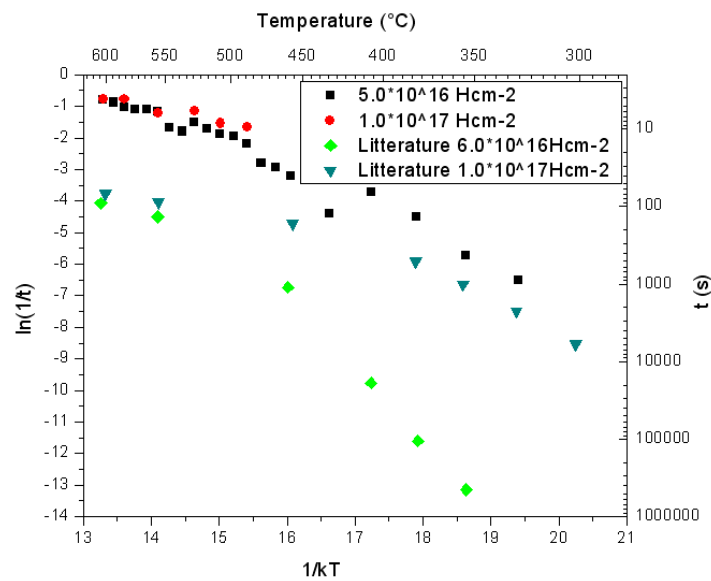
2. Kinetics of blistering and splitting

2.1. Blistering kinetics up to 600°C

The blistering kinetics is characterized for Si samples implanted with $3.0 \cdot 10^{16} \text{ Hcm}^{-2}$, $5.0 \cdot 10^{16} \text{ Hcm}^{-2}$ and $1.0 \cdot 10^{17} \text{ Hcm}^{-2}$ with help of the heating plate. The results are plotted on Fig. 4 (a). The slope of curve for temperature up to 500°C is coherent with the literature as shown on Fig. 4 (b) [1, 2]. The difference in annealing times with literature can be explained by the different implantation energy (76 keV) as well as by the different implanter equipment considered in this study. It is worth noting that the observation of the first blisters, which defines the blistering time, is around 10 times faster than the splitting time. This fact has already be mentioned in literature and can be explained by the fact that blister growth occurs during the crack coalescence process, leading afterwards to the splitting. It is worth noting that the blistering time as a function of temperature deviates from the straight line above 550°C. Moreover, it is worth noting that the time of blistering gets closer from the thermal ramp time, which is a source of artifact. Thus, it is not possible to trust these results above 550°C.



(a)



(b)

Figure 4: Blistering time as a function of temperature for $3.0 \cdot 10^{16} \text{ Hcm}^{-2}$, $5.0 \cdot 10^{16} \text{ Hcm}^{-2}$ and $1.0 \cdot 10^{17} \text{ Hcm}^{-2}$ (a), comparison between experimental results for $5.0 \cdot 10^{16} \text{ Hcm}^{-2}$ and $1.0 \cdot 10^{17} \text{ Hcm}^{-2}$ and literature [2] (b).

Fig. 5 shows images of blisters for different doses of implantation and after 600°C annealing. As expressed on Fig. 6, the blisters density increases, whereas the mean diameter decreases with both implantation dose. Such a behavior can be explained by the fact that both parameters lead to a higher amount of H available for the platelets nucleation.

In addition, the out-of-plane stress which is a driving force for the platelets nucleation increases with implantation dose [3]. As a result, the nucleation rate of platelets increases. The platelets distribution defines those of microcracks, themselves leading to blisters at the end of the blistering annealing. Thus, the increasing of annealing temperature leads to an increasing of blisters density.

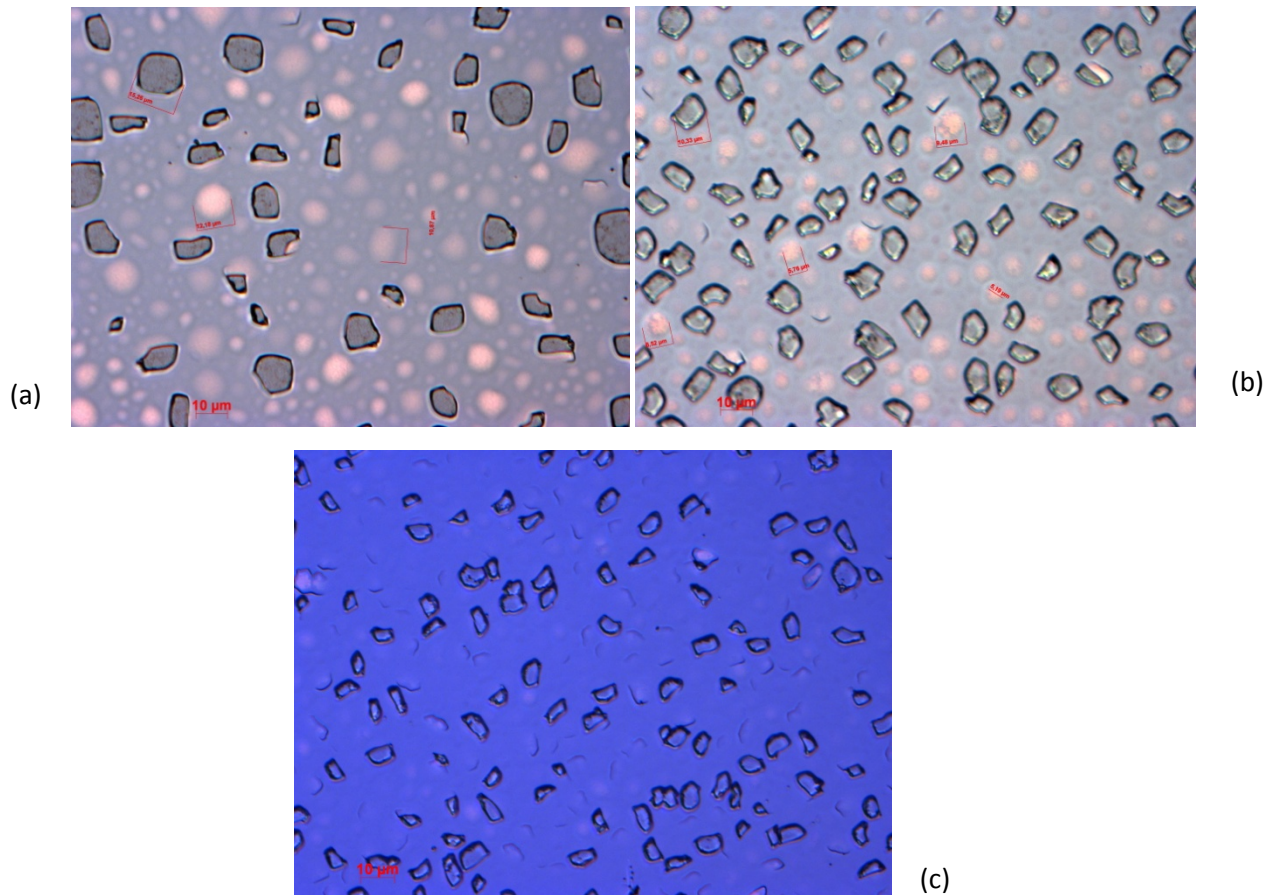


Figure 5: Microscope images (x50) of blisters with $3.0 \times 10^{16} \text{ Hcm}^{-2}$ samples (a), $5.0 \times 10^{16} \text{ Hcm}^{-2}$ samples (b) and $1.0 \times 10^{17} \text{ Hcm}^{-2}$ samples (c), after annealing at 600°C on the heating plate. The annealing is stopped at the observation of the first blisters explosions.

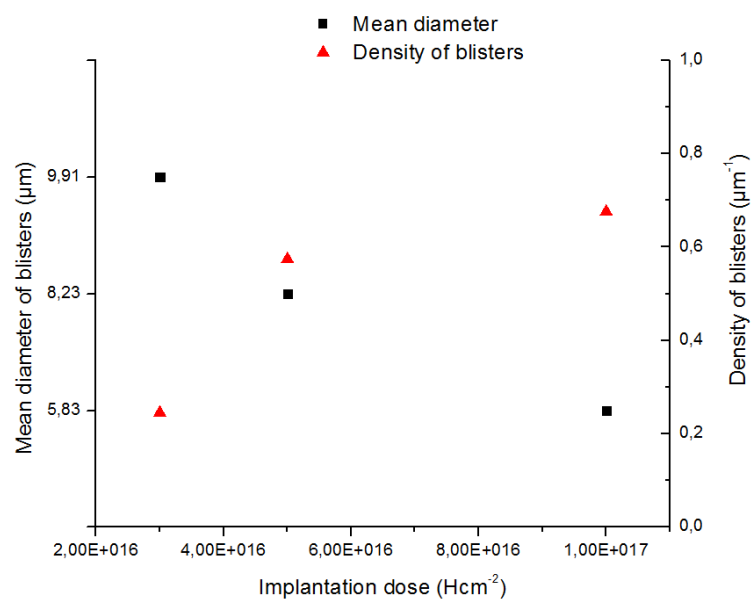


Figure 6: Mean diameter and density of blisters after annealing at 600°C for different implantation doses.

3. Splitting kinetics up to 700°C

3.1.1. Splitting kinetics and comparison with literature

The splitting has been characterized using the steel plate. The Fig. 7 (a) gives an Arrhenius plot of the splitting time as a function of annealing temperature up to 700°C for samples implanted with $4.5 \cdot 10^{16} \text{ Hcm}^{-2}$ - $1.0 \cdot 10^{17} \text{ Hcm}^{-2}$, above wherein the splitting time becomes too short for to be reliably characterized. As it has been noticed in previous studies, two different Arrhenius regimes can be distinguished. For temperature lower than 550°C, the splitting kinetics follows a linear regime with activation energy depending on the implantation dose reported on Fig. 7 (a).

On the other hand, the splitting kinetics deviates from the straight line above 550°C. It can be observed that this deviation occurs progressively in our case, whereas two distinct domains are reported in literature (see on Fig. 7 (b)), what had suggested a change in the Arrhenius regime [4]. It is also observed that the transition temperature, between the linear regime and the elbowed curve, varies as a function of the dose (e.g. $\sim 530^\circ\text{C}$ for $1.0 \cdot 10^{17} \text{ Hcm}^{-2}$ samples and $\sim 600^\circ\text{C}$ for $5.0 \cdot 10^{16} \text{ Hcm}^{-2}$ samples).

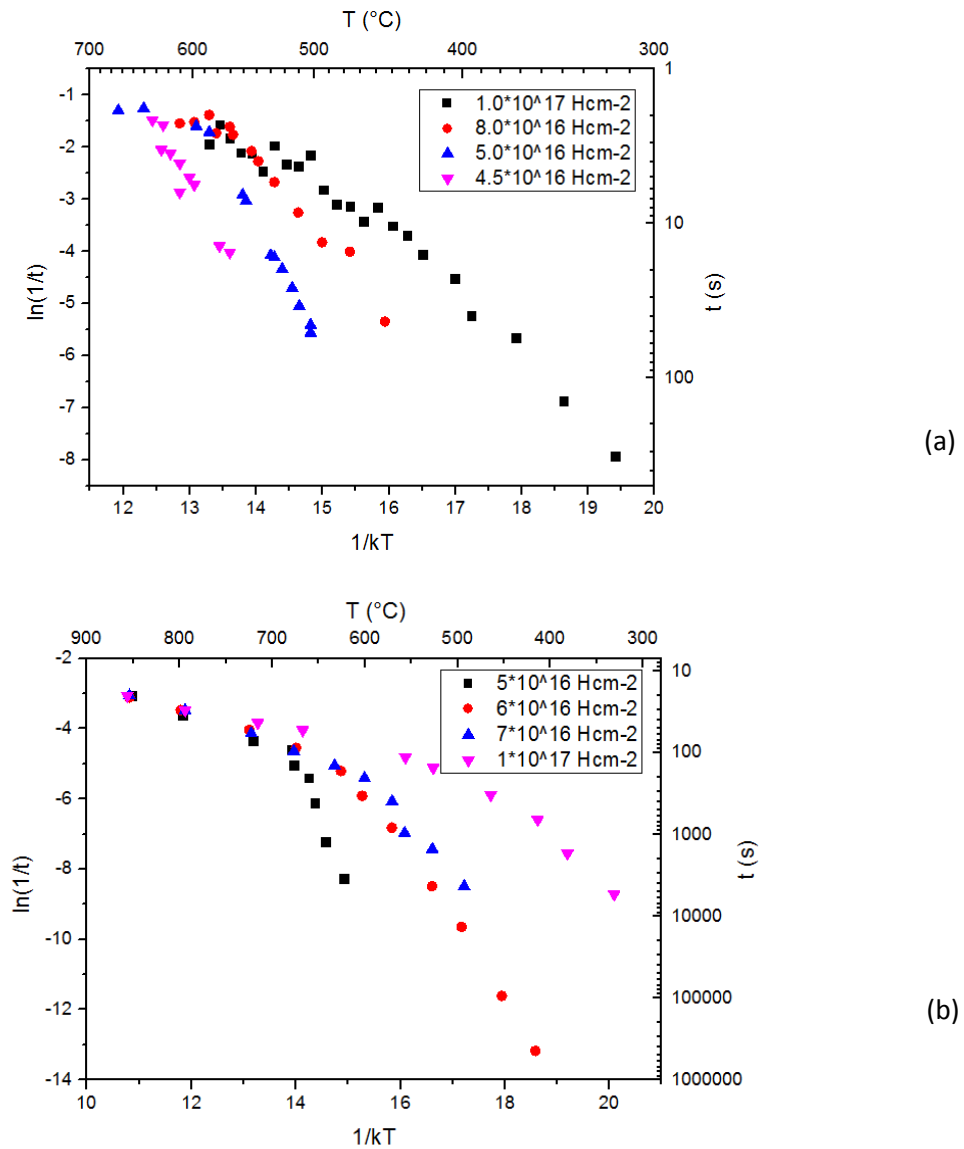


Figure 7: Splitting time τ as a function of temperature (a), splitting time τ as a function of temperature in literature [4] (b).

The literature explains the change of activation energy around 600°C by the decomposition of the implantation defects [4, 5]. After the decomposition of those defects, the diffusive process is proposed to be ruled by the diffusion of free H (i.e. with a diffusion activation energy $E_a = 0.49 \text{ eV}$). As a matter of fact, the Arrhenius plot from Lagahe [2] suggests activation energy close to 0.5 eV, as shown in Fig. 7 (b).

Nevertheless, it appears that the transition between the 2 Arrhenius regime occurs with a spitting time comparable to the time of thermalization of the annealing equipment used in those study. This puts the question of the reported data.

In order to establish a model of spitting, we will calculated the thermal budget of spitting in the paragraph 7.

3.1.2. Activation energy as function of dose

The splitting activation energy is determined from the plot of splitting of the Fig. 7 (a) (i.e. the slope of the curve at low temperature) and compared to literature [2] on Fig. 8. The overall activation of splitting is decreasing with the implantation dose, as observed in literature, except for $4.5 \cdot 10^{16} \text{ Hcm}^{-2}$. It is worth noting that the activation energy with our splitting samples implanted at 60 keV is slightly lower than measured in literature. Indeed, the implantation equipment can introduce uncertainty in the dose.

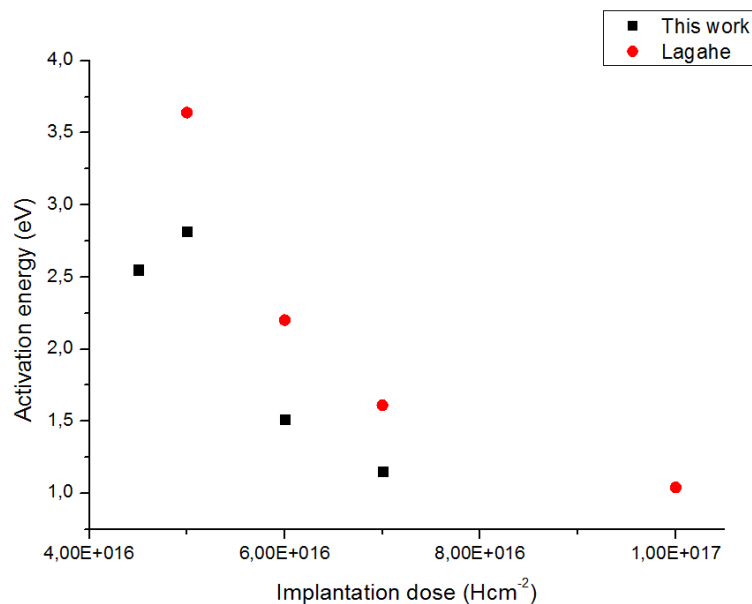


Figure 8: Activation energy of splitting as a function of the dose characterized in this study compared with literature [2].

Additionally, it can be observed that the splitting doesn't occur for temperatures below 580°C in those samples. Indeed, for temperature lower than 580°C, the available dose of H is too small to satisfy the Freund's criterion describing the minimum implantation dose for splitting J_{min} as a function of temperature [8]. This dose have been already introduced in the state of the art part:

$$J_{min} = \frac{8}{3} \frac{\gamma}{k_B T}$$

with γ being the surface energy at R_p of the implantation zone. We will come back to this relation a bit further.

3.1.3. Analysis of thermal budget of splitting

In order to overcome the limitation of the comparatively high duration of thermal ramp compared to the splitting annealing, we introduce here the function σ_T of the normalized thermal budget:

$$\sigma_T = \int \frac{1}{\tau(T(t))} dt$$

where τ is the characteristic time of splitting as defined by the hypothesis of Arrhenius regime to compare with the Arrhenius plot representation, expressed by:

$$\tau = \tau_0 * \exp\left(\frac{-E_a}{k_B T(t)}\right)$$

with τ_0 being the pre-exponential factor. $T(t)$ is recorded by the in-situ thermocouple during the annealing. We will focus on the $5.0 \cdot 10^{16} \text{ Hcm}^{-2}$ splitting samples, in order to compare two hypothesis of splitting scenarios.

The first hypothesis considers two Arrhenius regimes as proposed in literature [2], with a low temperature regime, whose activation energy is defined by the implantation dose (i.e. $E_a = 2.815 \text{ eV}$ for $5.0 \cdot 10^{16} \text{ Hcm}^{-2}$), and a high temperature regime defined by the diffusion of atomic hydrogen ($E_a = 0.49 \text{ eV}$).

The second hypothesis postulates a single regime for any temperature, defined by the implantation dose ($E_a = 2.815 \text{ eV}$ for $5.0 \cdot 10^{16} \text{ Hcm}^{-2}$).

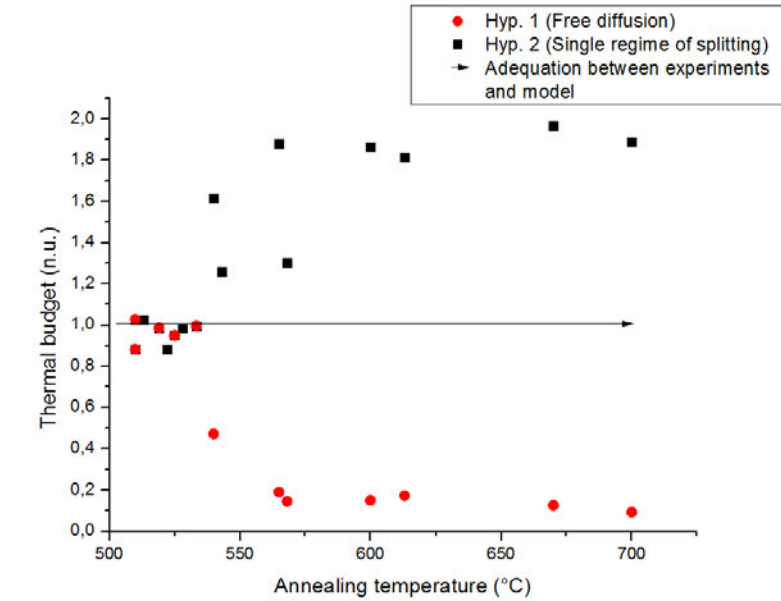


Figure 9: Thermal budget calculation using the in-situ temperature signal for $5.0 \cdot 10^{16} \text{ Hcm}^{-2}$ splitting samples.

The plot of the normalized thermal budget σ_T allows to represent the experimental data of the splitting time as a function of time under different regime hypotheses. Thus, a value of σ_T equal to 1 means that the regime hypothesis fits the true splitting kinetics. A value of σ_T superior to 1 implies that the regime hypothesis is faster than the splitting kinetics (and slower in case of a value of σ_T inferior to 1).

The Fig. 9 shows that the first hypothesis cannot explain the data above 600°C, with a plateau at ~ 0.15 , what invalidates a second regime for high temperature annealing. On the other hand, the second hypothesis of a linear regime of splitting kinetics gives a progressive drift of σ_T above 550°C, to reach a plateau at $\sigma_T=1.9$. This drift is caused by a progressive increasing of the annealing time compared to the Arrhenius regime defined by the implantation dose. Thus, it is possible to assess that none of these hypotheses is correct, and that another, relying on another physical mechanism must be identified.

3.1.4. Characterization of splitting for low dose samples

Experimentally it has been observed that no splitting occurs below 575°C for $4.5 \cdot 10^{16} \text{ Hcm}^{-2}$ samples (Fig. 10) and below 725°C for $4.0 \cdot 10^{16} \text{ Hcm}^{-2}$ samples, in case of the implantation energy of 60 keV whatever the annealing time. For 4.0 sample the splitting kinetics is comparable with temperature ramp time, thus rendering the extraction of activation energy highly unreliable.

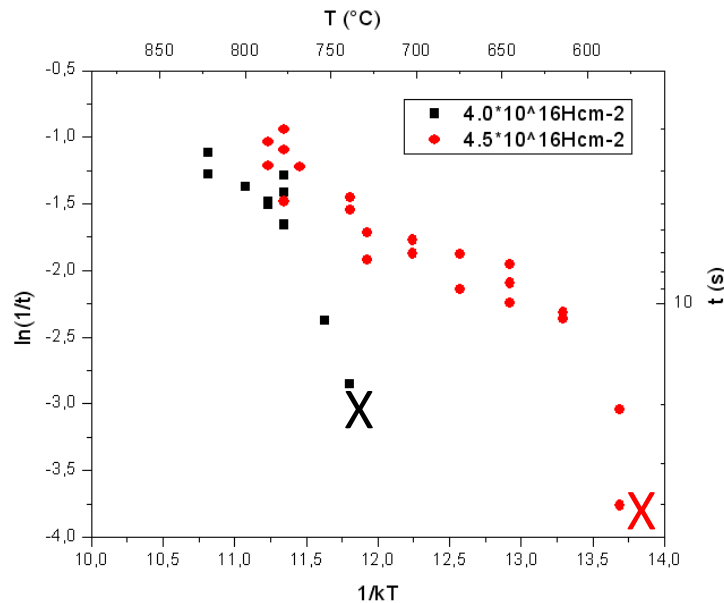


Figure. 10: Splitting time as a function of temperature for $4.0 \cdot 10^{16} \text{ Hcm}^{-2}$ and $4.5 \cdot 10^{16} \text{ Hcm}^{-2}$.

It is worth noting that the thermal ramping speed affects the possibility of splitting. Thus, considering a classical annealing, i.e. with the thermal ramp of the furnace equipment (i.e. below 1°C/s), no splitting can be observed. This observation means the presence of a competing mechanism, affecting negatively the defect growth leading to splitting.

We can propose that this mechanism responsible for ramp rate dependence is the out-diffusion of hydrogen towards the bonding interface. Indeed, the dose necessary for the splitting J_{min} is defined by the Freund's relation (already mentioned in section 3.1.2):

$$J_{min} = \frac{3}{8} * \gamma * k_B T$$

Thus, if the thermal ramp affects the possibility of splitting (for a same annealing temperature T), it implies that the available dose J_{min} is reduced during the thermal ramp (as well as during the annealing itself). This dose reduction can only be explained by an out-diffusion process.

It is possible to calculate the surface energy within the implantation zone, γ , using the minimal splitting temperature, for the two considered doses J_{min} . Indeed, the Freund's formula defines γ as following:

$$\gamma = \frac{3}{8} * J_{min} * k_B T$$

Both minimal doses of splitting returns a γ value close to 1 Jm⁻² see Table 2, which is fully coherent with the value proposed in literature [8].

Table 2. Summary of the minimum temperature of splitting as a function of implantation dose and of the corresponding surface energy.

Implantation Dose (Hcm ⁻²)	Minimum Temperature for Splitting (°C)	Surface Energy (J/m ²)
4.0*10 ¹⁶	725	1.03
4.5*10 ¹⁶	575	0.99

Finally, using this surface energy, it is possible to calculate the minimum temperature of splitting T_{min} for even lower implantation dose, keeping in mind that the reduction of H dose is a limiting factor for the splitting, as we have seen earlier. Using the mean value of γ of 1.01 J/m² obtained from the Table 2, we obtain:

$$T_{min} = \frac{8}{3} * \frac{\gamma}{J_{min} k_B}$$

The results are plotted on Fig. 11.

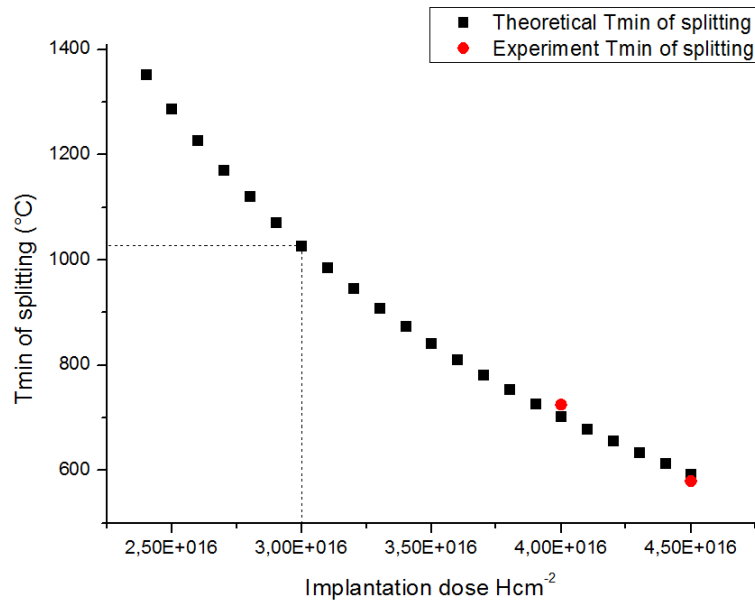


Figure 11: Minimum temperature T_{min} of splitting as a function of the implantation dose, with a $\gamma = 1.01$ J/m².

For our lowest dose sample of splitting (i.e. $3.0 \cdot 10^{16} \text{ Hcm}^{-2}$), it can theoretically be postulated that the splitting is possible (with an annealing temperature superior to 1030°C). Indeed, blisters are observed for this dose (see on Fig. 5 (a)) at annealing at 600°C ., and the possibility of blistering of a standing alone implanted wafer is considered as one of the necessary conditions for the splitting of an equivalent bonded structure [5].

Considering the Fig. 11, it is theoretically possible to have splitting for samples implanted with $3.5 \cdot 10^{16} \text{ Hcm}^{-2}$ for temperature annealing superior to 830°C . Nevertheless, the splitting of the implanted zone has not been observed in this temperature domain. Surprisingly, a non-expected phenomenon is observed with the $3.5 \cdot 10^{16} \text{ Hcm}^{-2}$ samples. This particular splitting occurs at the interface between the oxide interface and the Si substrate of the acceptor wafer, instead that at the R_p of the implanted zone. It will be studied in the next paragraph.

3.2. Kinetics of splitting at the bulk-oxide layer interface up to 950°C

This different splitting observed for samples implanted with $3.5 \cdot 10^{16} \text{ Hcm}^{-2}$ is illustrated on Fig. 12. Thus, the interface that splits is the interface between the thermally grown oxide layer and the rest of the non-implanted wafer. The surface after separation is clear from any defects (such as blisters).

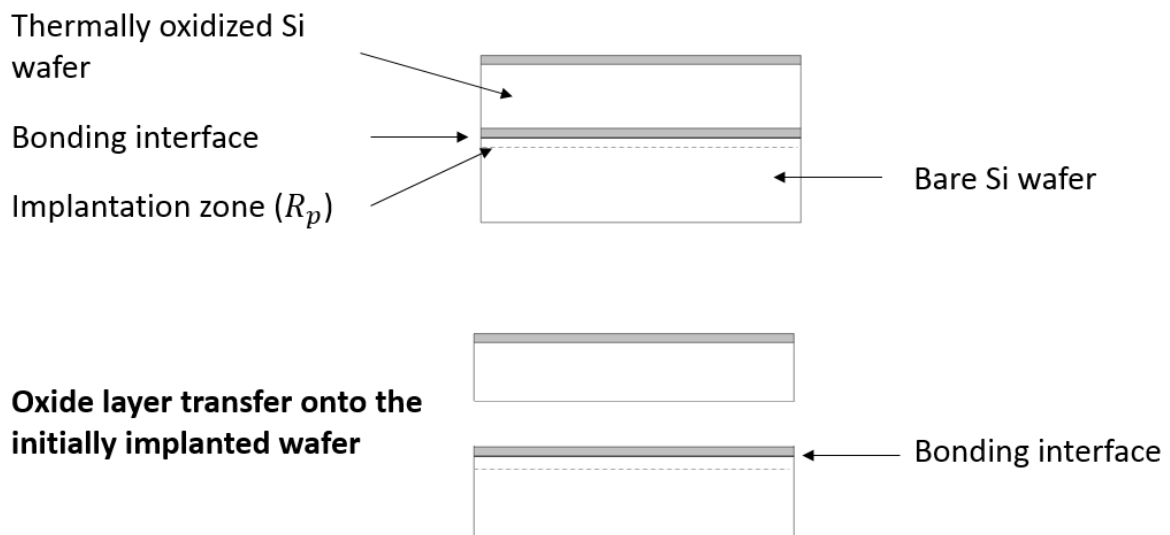


Figure 12: Illustration of the oxide layer transfer mechanism. The thermally grown oxide layer bonded to the surface of the implanted wafer separates at the thermal oxide/bulk interface.

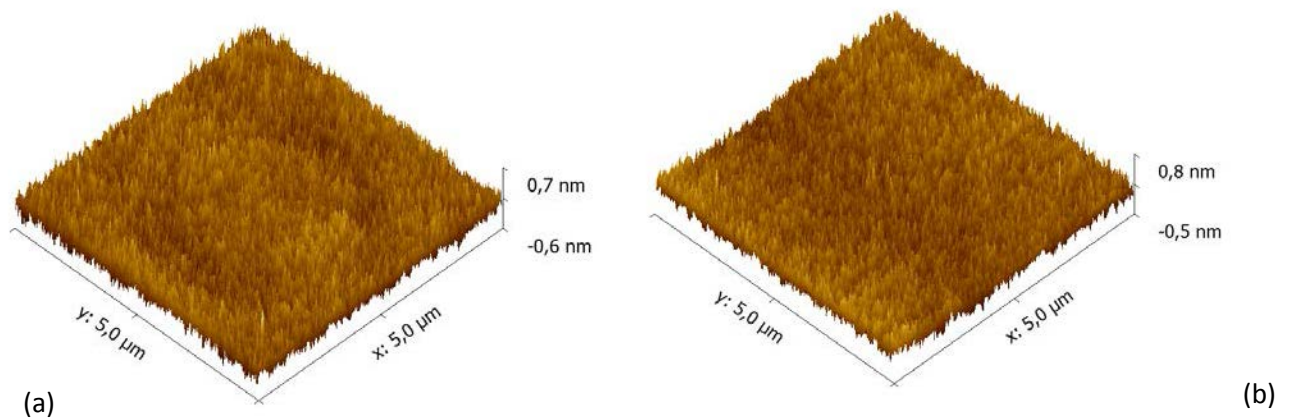


Figure 13: AFM images of the transferred oxide layer at 900°C (a) and of the donor wafer, initially oxidized (b).

This absence of micro-crack formation is confirmed by the AFM measurements performed at the surface of the top i.e. initially implanted wafer, after annealing at 900°C. They show a very low roughness (see Fig. 13 and summarized in Table 3) for both transferred oxide layer and for the donor wafer (i.e. the thermally oxidized wafer), after transfer.

Table 3. RMS roughness of the transferred layer of thermal oxide and of the donor wafer after transfer

Type of layer	RMS roughness [nm]
Transferred oxide layer	0.12
Negative wafer after transfer	0.11

The obtained RMS value of roughness (close to 1\AA) is very similar to the roughness of the starting bare wafer as well as the roughness of the interface of the thermal oxide in our samples. It is much lower than the roughness after a splitting within the implanted zone (see Fig. 13). Such a low roughness can be explained by a very narrow layer separation within the interface between the oxide layer and the rest of the bulk, whereas the separation in case of regular splitting occurs over a zone of $\sim 100\text{ nm}$ of depth in the implanted wafer [7].

It is worth noting that the oxide transfer also follows an Arrhenius law, with activation energy of 2.8 eV, what is very comparable to the splitting activation energy for $5.0 \cdot 10^{16}\text{ Hcm}^{-2}$. Additionally, as can be seen on Fig. 14, the time for oxide separation (for $3.5 \cdot 10^{16}\text{ Hcm}^{-2}$) is comprised between 20 s and 40 s. Thus, the time for transfer being longer than the thermal ramping, the characterization of the kinetics is reliable.

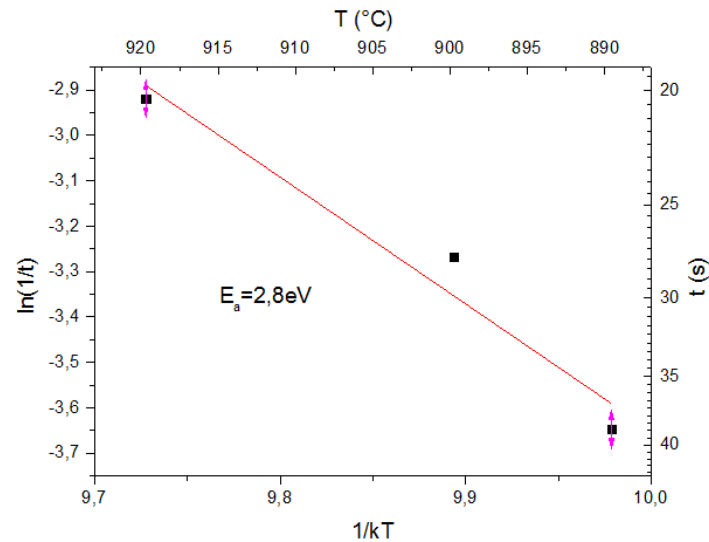


Figure 14: Time of oxide layer transfer as a function of annealing temperature for $3.5 \cdot 10^{16} \text{ Hcm}^{-2}$. The activation energy corresponds to the slope of the curve under form of Arrhenius graph.

3.3. Detachment at the bonding interface

Even more surprising than the oxide layer transfer, another phenomenon is observed for $4.0 \cdot 10^{16} \text{ Hcm}^{-2}$ samples above 840°C as plotted in Fig. 15. It consists in a separation at the bonding interface between the implanted sample and the oxidized wafer, after a duration very similar to the oxide film transfer (i.e. a comparatively longer time compared to the splitting time for the same $4.0 \cdot 10^{16} \text{ Hcm}^{-2}$ samples at high temperature).

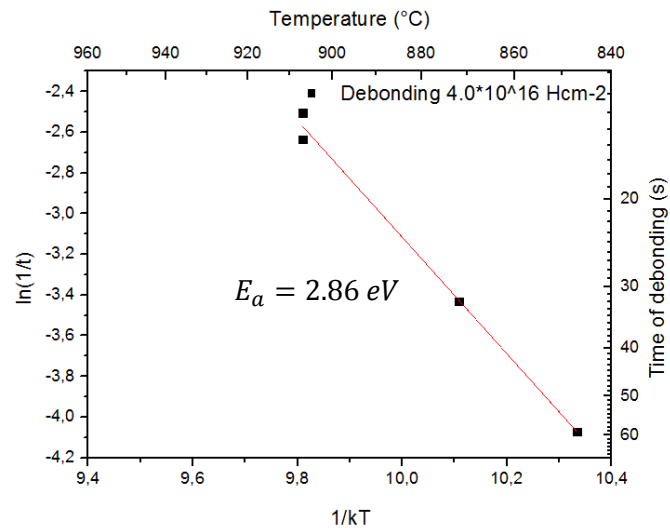


Figure 15: Time of debonding as a function of annealing temperature above 840°C for $4.0 \cdot 10^{16} \text{ Hcm}^{-2}$. The activation energy corresponds to the slope of the curve under form of Arrhenius graph.

The Fig. 16 makes the comparison between the oxide transfer and the detachment at the bonding interface. The kinetics appear as really close from each other, what suggests that similar processes run simultaneously with a competition driven by the implantation dose.

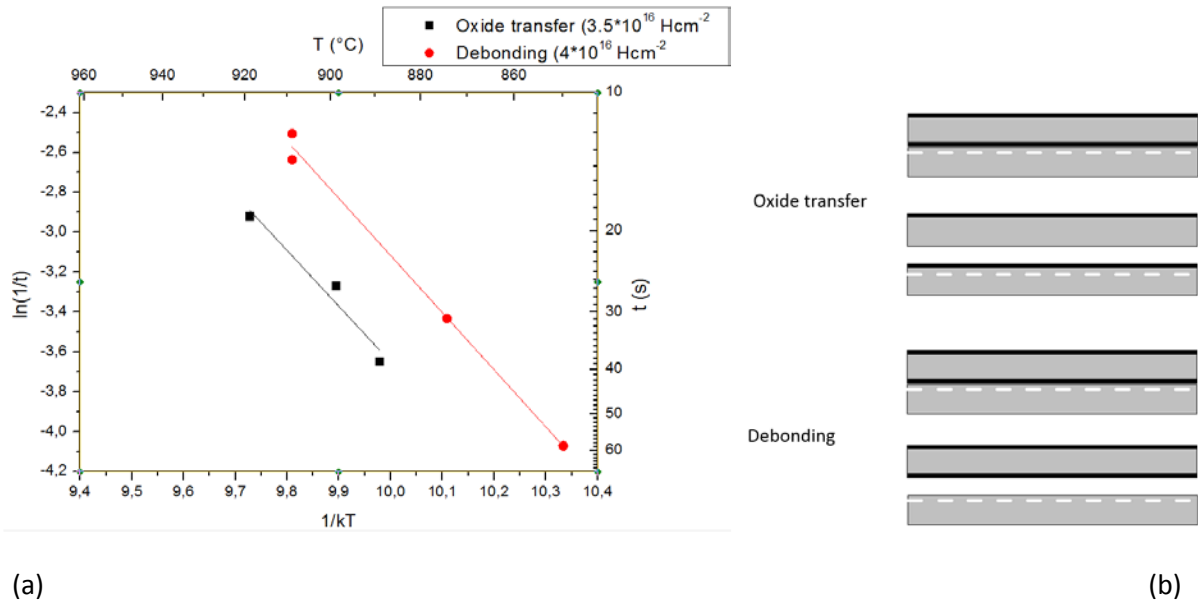


Figure 16: Comparison between oxide transfer for $3.5 \cdot 10^{16} \text{ Hcm}^{-2}$ samples and detachment at the bonding interface (without splitting) for $4.0 \cdot 10^{16} \text{ Hcm}^{-2}$ samples.

The difference between these two processes, implying different interfaces of detachment, will be discussed in paragraph IV 7.3.

3.4. Annealing of different sample geometries implanted at $3.5 \cdot 10^{16} \text{ Hcm}^{-2}$

In order to bring additional elements of understanding, we have prepared different geometries of samples, implanted with the same conditions, i.e. $3.5 \cdot 10^{16} \text{ Hcm}^{-2}$ at 60 keV, or having a similar bonding configuration, as illustrated on Fig. 17. The thermal oxide have a thickness of 145nm with the same fabrication conditions than the splitting samples.

First, we consider a similar structure consisting of an oxidized wafer with an implantation ($3.5 \cdot 10^{16} \text{ Hcm}^{-2}$ at 60 keV) through the oxide, bonded with a bulk Si wafer (Fig. 17 (b)). This structure, very similar to the reference structure of the splitting samples differs by the position of the implantation zone. It is worth noting that the configuration remains stable, even with the maximum annealing temperature of 1100°C .

Then, similar bonded structures were prepared without implantation, with an oxidized wafer bonded with a bulk wafer (Fig. 17 (c)) and a structure with two oxidized wafer bonded together (Fig. 17 (d)). Finally, an SOI wafer (composed of 200 nm of Si onto 145 nm of oxide) is implanted ($3.5 \cdot 10^{16} \text{ Hcm}^{-2}$ at 60 keV) through the buried oxide and bonded with a non-implanted Si wafer (Fig. 17 (e)). None of these

structures (i.e. (b) to (e)) induce a layer separation even after an annealing temperature at the up to 1100°C.

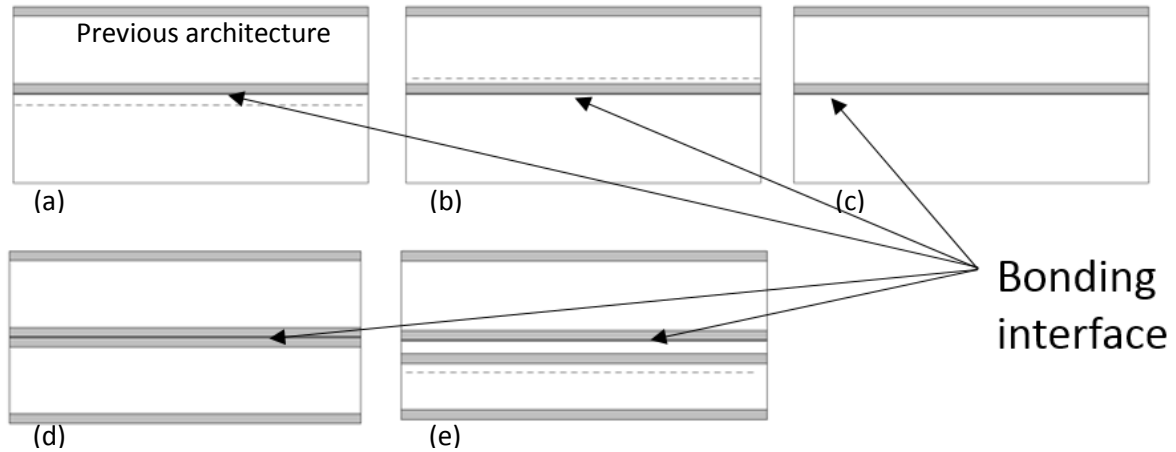


Figure 17: Schematic of the various configurations of samples. The dashed lines correspond to the location of H implanted with a dose of $3.5 \cdot 10^{16} \text{ Hcm}^{-2}$ at 60 keV.

As an intermediate conclusion, it is possible to conclude that H plays a role in the oxide separation, as no separation occurs without H implantation (Fig. 17 (c) and (d)). It means that the H has to out-diffuse from the implantation zone to migrate to the oxide interface. On the other hand, it appears that if H is implanted through the thermal oxide, no layer separation occurs (Fig. 17 (b) and (e)). We can postulate that the implantation modifies the structure of thermal oxide layer, and its interface with Si.

We will go back to this mechanism of oxide layer transfer and of debonding after studying the migration of H during the splitting annealing in paragraph 7.3.

4. Characterization of H diffusion (Si samples implanted with $3.5 \cdot 10^{16} \text{ Hcm}^{-2}$)

From the evolution of the splitting kinetics above 550°C - 600°C and the oxide film transfer, it appears that a mechanism of out-diffusion of H takes place within the implanted material. Thus, it is necessary to focus on the evolution of H concentration during annealing, within the implantation zone and at the oxide interfaces.

4.1. SIMS characterization (as implanted samples, annealing at 600°C and 850°C for 30 s)

We propose to focus first on SIMS analysis of the bonded structures with $3.5 \cdot 10^{16} \text{ Hcm}^{-2}$ implantation. The details of these measurements were given in the chapter xxx.. These samples allow an annealing of duration of 30 s without splitting, long enough to neglect the effect of the thermal ramp. On the other hand, this implantation dose is considered as sufficient for the nucleation of platelets in implanted Si, which is necessary for the splitting, as already mentioned. Thus, it is possible to study the mechanisms involved in splitting kinetics with the samples annealed at 600°C , and oxide layer transfer phenomenon with the samples annealed at 850°C .

4.1.1. H concentration in implantation zone

The first observation concerns the implantation zone itself on Fig. 18. As already mentioned, the implantation peak shows a narrowing instead of a flattening [7]. The last effect would have been the consequence of a diffusive process. Literature explains the narrowing and the reduction of the implantation peak maximum by the formation of molecular H_2 , undetectable by SIMS. This gaseous H_2 , whose existence has been proved in literature, fills the platelets. Additionally, an amount of typically 30 % of the total implanted dose is released during the splitting [7].

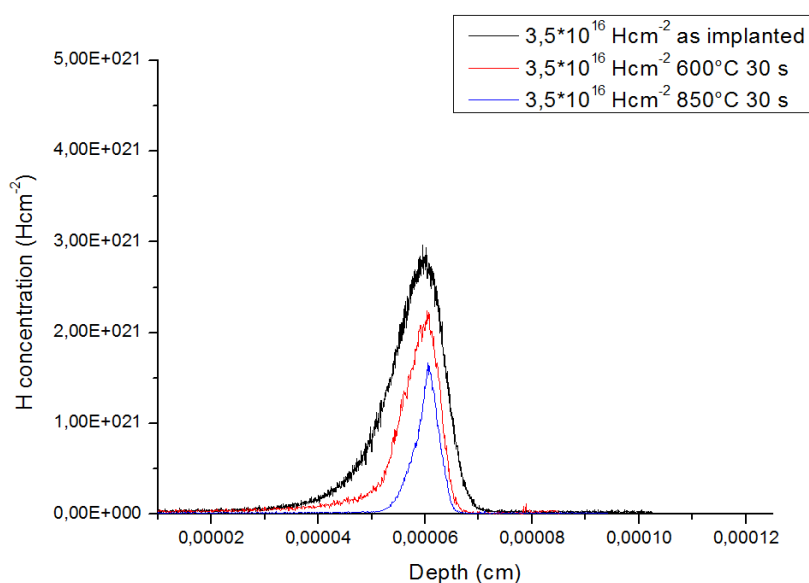


Figure 18: Evolution of the concentration of H within the implantation zone for $3.5 \cdot 10^{16} \text{ Hcm}^{-2}$ as a function of annealing conditions by SIMS analysis.

It can be seen that a significant signal of H remains, even after annealing at 850°C, where previous studies show no H is detected after 90 s at 850°C (i.e. with a longer annealing duration at the same temperature) [6] or even above only 700°C with very close implantation conditions, i.e. $3.0 \cdot 10^{16} \text{ Hcm}^{-2}$ and 61 keV [5]. Our results support the fact the splitting should be still possible for much higher temperatures than studied in this chapter, and invalidates a complete decomposition of hydrogenated defects.

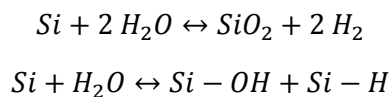
The integrals of the SIMS profiles are summarized in Table 4, showing that around 50 % has disappeared after 30 s at 600°C. It is worth noting that the SIMS analysis only detects H bonded with the Si matrix and not gaseous H_2 that fills the platelets. Thus, at this stage there is no possibility to distinguish the out-diffused H from the gaseous H_2 that stays within the implanted zone, in a more stable state than after implantation. To complete the study of the diffusion process of H during annealing, the evolution of H within the thermal oxide will be studied.

Table 4. Integral of the signal of H by SIMS for $3.5 \cdot 10^{16} \text{ Hcm}^{-2}$ samples within the implanted zone.

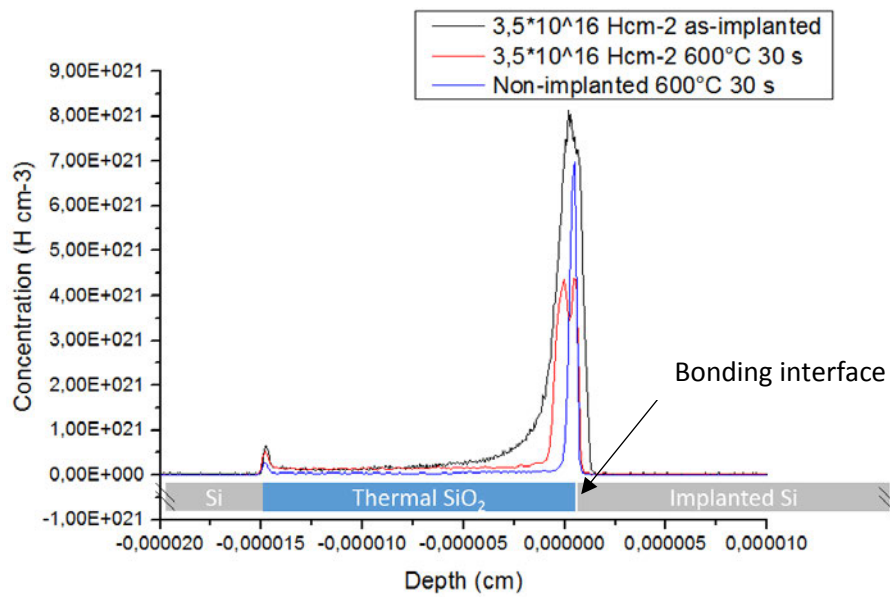
Annealing conditions (Temperature, duration)	Integral of H signal (Hcm^{-2})	Fraction of H lost compared to as-implanted samples (%)
As-implanted	$3.82 \cdot 10^{16}$	-
600°C 30 s	$2.11 \cdot 10^{16}$	49
850°C 30 s	$9.45 \cdot 10^{15}$	82

4.1.2. H concentration in the thermal oxide

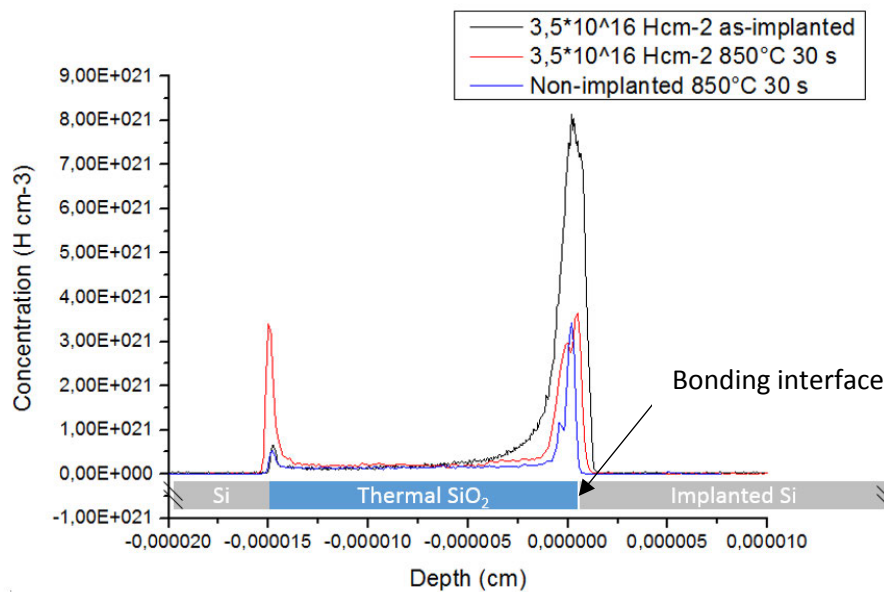
It appears that the oxide interfaces acts as a trap for H, and especially at the bonding interface, as can be observed in Fig. 19. Thus, we propose to study the evolution of the concentration of H within the oxide in order to quantify the mechanism of hydrogen out-diffusion out of the implantation zone. On the other hand, it is well known that the direct bonding of two hydrophilic wafers encloses 2-3 monolayers of water at the bonding interface. The bonding process implies the decomposition of this water, by formation of silanols (Si-OH) and siloxanes (Si-O-Si) bonds [9] following two chemical reactions:



The first reaction is supposed to be prevalent at high temperature annealing, whereas the second occurs mostly below 500°C [10]. These reactions results in a generation of either gaseous H_2 or H bonded with Si. As the resulting H does not originate from the diffusive process out of the implantation zone described above, it is necessary to compare the concentration of H inside the 145nm of the oxide interface between implanted and non-implanted sample. Therefore, it is possible to calculate the dose of out-diffused H by subtracting the concentration of H between implanted and non-implanted samples.



(a)



(b)

Figure 19: Comparison of the H present at oxide bonding interface between samples as-implanted with a dose of $3.5 \cdot 10^{16} \text{ Hcm}^{-2}$, samples implanted with a dose of $3.5 \cdot 10^{16} \text{ Hcm}^{-2}$ and non-implanted after annealing at 600°C during 30 s (a), samples as-implanted with a dose of $3.5 \cdot 10^{16} \text{ Hcm}^{-2}$, samples implanted with a dose of $3.5 \cdot 10^{16} \text{ Hcm}^{-2}$ and non-implanted after annealing at 850°C during 30 s (b).

First, the SIMS analysis shows that the H initially present within the oxide, i.e. without annealing, represents a dose of H, equal to $1.58 \cdot 10^{16} \text{ Hcm}^{-2}$, which is almost half of the implantation dose for these samples. This H results from the process of thermal oxidation that occurs in a steam atmosphere (H_2O) plus a contribution from the water present at the bonding interface. The difference between non-annealed and annealed sample can be explained by the formation of H_2 at the bonding interface. As a reminder, H_2 cannot be detected by SIMS which explains the lower signal.

As summarized in Table 5, the subtraction between non-implanted and implanted samples gives $3.7 \cdot 10^{15} \text{ Hcm}^{-2}$ after an annealing of 30 s at 600°C . This loss represents 9.8 % of the total implanted H and reduces the available dose for splitting. After 30s at 850°C , the same subtraction between implanted and non-implanted samples gives a higher value equals to $4.7 \cdot 10^{15} \text{ Hcm}^{-2}$ or 12.4 % of the initial dose. It is worth mentioning that out-diffusion of H from implanted samples was observed earlier [11] by thermal desorption spectroscopy (TDS), although at lower temperatures. This study showed a peak of desorption of H at 430°C , for $8 \cdot 10^{16} \text{ Hcm}^{-2}$ samples implanted at 30 keV [11].

Additionally, our SIMS data show that the maximum concentration reached at the bonding interface, as well as at the thermal oxide interface after annealing at 850°C , is comparable to the maximum concentration in the implantation peak, as characterized by SIMS on Fig. 19. The H present in the oxide can find different contributions: the thermal oxidation in steam atmosphere, the bonding water decomposition and the out-diffusion of H out of the implanted zone during the annealing.

Table 5. Integral of the signal of H by SIMS within the oxide layer for $3.5 \cdot 10^{16} \text{ Hcm}^{-2}$ samples and non-implanted samples (data from Fig. 19).

NB: the integral is calculated considering the thermal oxide and the bonding interface

Annealing conditions (Temperature, duration)	Integral of H signal for $3.5 \cdot 10^{16} \text{ Hcm}^{-2}$ samples (Hcm^{-2})	Integral of H signal for non-implanted samples (Hcm^{-2})	Out-diffused H from the implantation zone (Hcm^{-2})	Ratio of out-diffused H over the initial implantation dose (%)
Non-annealed	$1.58 \cdot 10^{16}$	-	-	-
600°C 30 s	$7.68 \cdot 10^{15}$	$3.95 \cdot 10^{15}$	$3.72 \cdot 10^{15}$	9.8
850°C 30 s	$9.33 \cdot 10^{15}$	$4.61 \cdot 10^{15}$	$4.72 \cdot 10^{15}$	12.4

From this study, it is possible to assess that the total amount of H present in the oxide after annealing at 850°C is equal to $2.05 \cdot 10^{16} \text{ Hcm}^{-2}$ (i.e. the combination of the H initially present in oxide, $1.58 \cdot 10^{16} \text{ Hcm}^{-2}$ with the out-diffused H during the annealing $4.72 \cdot 10^{15} \text{ Hcm}^{-2}$).

Thus, considering the Freund's criterion of J_{min} :

$$J_{min} = \frac{8}{3} \frac{\gamma}{k_B T}$$

, already introduced, the minimum temperature of splitting for this equivalent dose of H should be 1260°C . As we observe the oxide transfer above 880°C only, it is not possible to affirm that the oxide layer transfer is caused by a splitting mechanism similar to defect growth within the implantation zone. Nonetheless, it appears that the presence of this high amount of H in the oxide helps the film separation in the damaged zone of the thermal oxide interface.

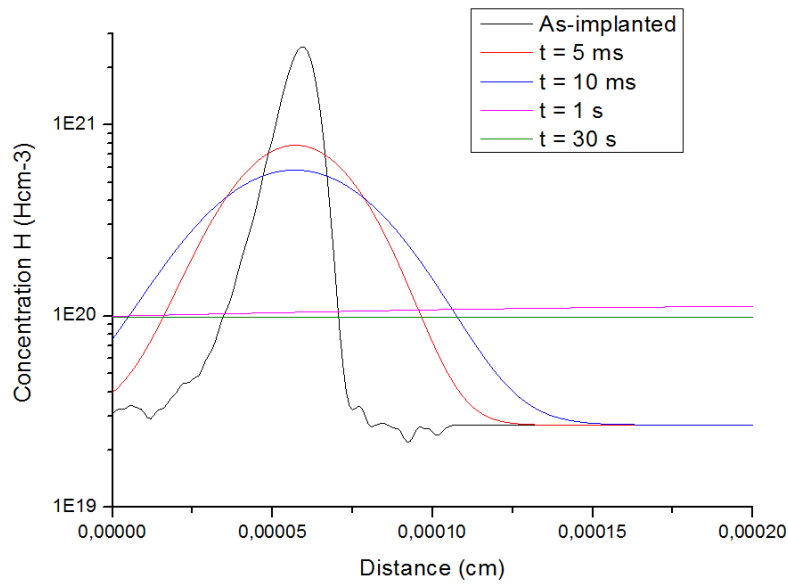
5. Modelling of H diffusion

5.1. Modelling considering the diffusion of free H

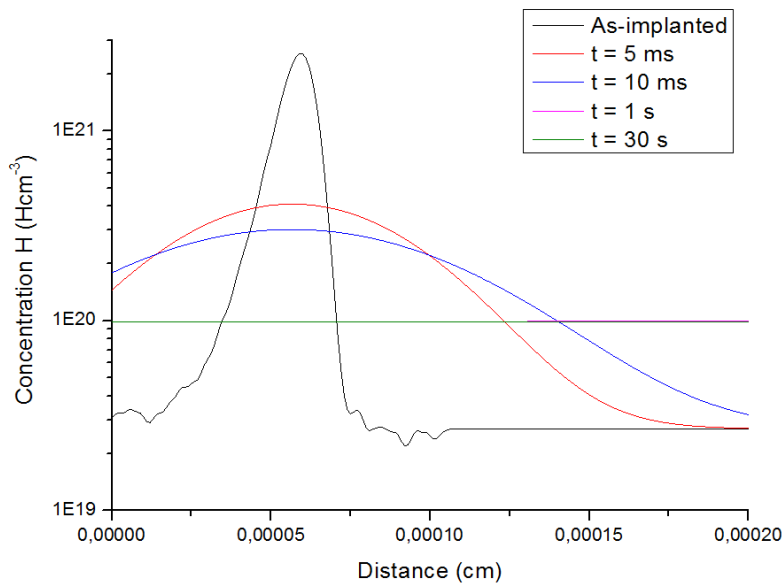
We propose first to consider the hypothesis of diffusion of free H of which the coefficient diffusion is D_H within the material [17].

$$D_H = 2 * 10^{-4} * \exp\left(\frac{-0.49 \text{ eV}}{kT}\right) \text{ in cm}^2\text{s}^{-1}$$

Despite, this hypothesis has been proved to be invalid for low temperature annealing (e.g. equal to 400°C [7]), it is necessary to verify the invalidity of this model in the high temperature domain ($T > 500^\circ\text{C}$), considered here for splitting annealing. The results are present in Fig. 20 for the two conditions of annealing considered in the SIMS analysis previously.



(a)



(b)

Figure 20: Calculated profiles of concentration of H by considering the coefficient of diffusion of free H for an annealing at 600°C (a), and 850°C (b).

It appears that the profiles obtained by modelling are far from the experimental results characterized by SIMS. Indeed, no H signal remains after only 1 s of annealing, which is opposite to SIMS results for annealing at both 600°C and 850°C.

In addition, the two calculated profiles show a flattening of H concentration with time, which is characteristic of a purely diffusive process without interaction with defects. This behavior is not observed, as illustrated on Fig. 18, where the concentration profiles show a thinning with time. As a consequence, another process of diffusion is running within the implanted material, with dependence on both the concentration of H and the coefficient diffusion of free H.

5.2. Model of diffusion by de-trapping of H

As mentioned in the chapter 2, the implanted zone is a highly damaged material, where H is trapped. A study considering desorption of H by pulsed laser annealing, proposes that the activation energy of de-trapping is comprised in the range 1.5-3 eV and a majority of results around 2 eV [12]. The activation energy depends on the implantation dose, as does the defect repartition.

It has been observed that implanted H forms a wide variety of defects, such as Si(100):H or V_nH_m type defects [13]. It is also observed that the signal corresponding to Si(100):H strongly decreases after annealing (typically in the range of 470°C-550°C, the annealing duration is not mentioned), whereas the signal corresponding to VH_2 or V_2H_6 remains relatively constant [13, 14]. This decreasing is very clear on the Raman spectra as characterized by Moutanabbir et al. [13] and shown in the chapter 2 Fig. 3.

This effect is explained by the dissolution of defects of low formation energy followed by the migration of the consequently released H to V_nH_m defects, like V_2H_6 , in order to form platelets (i.e. with the formation of H_2). Such diffusive process within a trapping material is ruled by the following equation:

$$D_H = D_0 \left(\frac{n_{bond}}{n_{free}} \right) \exp \left(\frac{E_B - E_a}{k_B T} \right) [15]$$

, where $D_0 = 2 * 10^{-4} \text{ cm}^2 \text{ s}^{-1}$ is a pre-factor giving the diffusion rate at infinite temperature, $\frac{n_{bond}}{n_{free}}$ is the ratio between bonded and free H concentration and $E_B = 1.95 \text{ eV}$ is the binding energy of the trap corresponding to Si(100):H [16] and $E_a = 0.49 \text{ eV}$ the activation energy of H_{BC} diffusion, considered as free H [17].

The bonding energy is taken from the desorption of H in undoped a-Si:H with a H concentration exceeding 10% [16]. Indeed, we assume that the Si implanted with a high dose of H shows a similar defects structure compared to a-Si:H, i.e. with a large amount of hydrogenated defects.

The repartition of H as a function of concentration has been proposed by ab-initio calculations, which are summarized on Fig. 21 [18].

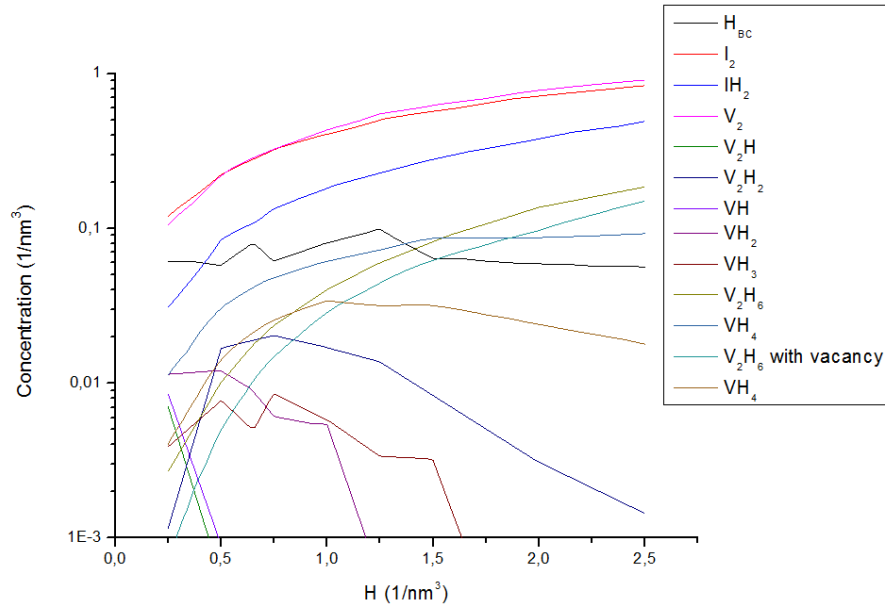


Figure 21: Simulated concentration of different types of hydrogenated complexes as a function of H, by ab-initio calculations at RT. Reproduced from [18].

The ratio H_{BC} (considered as H in a free state) over the rest of the other defects gives the n_{bond}/n_{free} , plotted on Fig. 22. These ab-initio calculations are done at room temperature, which is relatively close to the conditions of implantation temperature. As the defects are formed at room temperature during the implantation step, these calculations offer an appropriate estimation of the defects repartition, confirmed by Raman spectra [13].

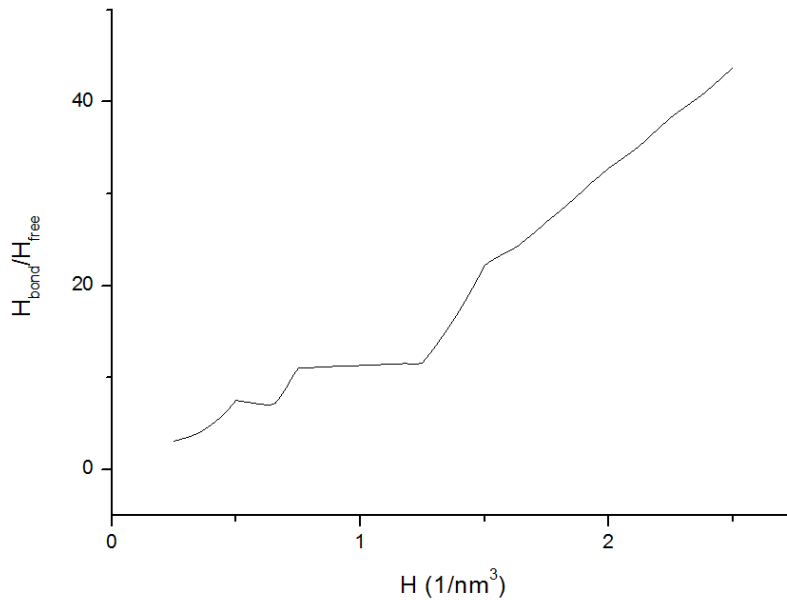


Figure 22: Ratio between bonded H atoms and free H atoms calculated by ab-initio calculations.

The resulting diffusion coefficient gives $E_D = 1.46\text{eV}$ and $D_0 \left(\frac{n_{bond}}{n_{free}} \right) = [6 \cdot 10^{-4} - 10^{-2}] \text{ cm}^2\text{s}^{-1}$ depending on H concentration, as figured on Fig. 22.

$$D_H = D_0 \left(\frac{n_{bond}}{n_{free}} \right) \exp \left(\frac{1.95 \text{ eV} - 0.49 \text{ eV} = 1.46 \text{ eV}}{k_B T} \right) \text{ in } \text{cm}^2\text{s}^{-1}$$

These values are very similar to those of a-Si:H where $E_D = 1.5\text{eV}$ and $D_0 = 10^{-2} \text{ cm}^2\text{s}^{-1}$ [16], in good agreement with our assumption.

The resulting D_H will be used in the next paragraph for numerical modelling in order to compare the SIMS characterization of the implantation of a reference sample (implanted with $3.5 \cdot 10^{16} \text{ Hcm}^{-2}$) with our model of diffusion coefficient.

It is worth noting that our model does not consider the nucleation of platelets, which also act as a H trap. Indeed, the literature considers that there is no reverse formation of single H bonded to the Si matrix once forming H_2 to fill the platelet [5]. Thus, the H that fills the platelet is not supposed to participate to the diffusion anymore. As a reminder from the chapter 2 section 2.5, the zone of nucleation of platelets is about 200 nm around R_p . Nevertheless the zone of nucleation of platelets corresponds to the zone of highest concentration of H. For this concentration range, our model gives the lowest value of H diffusion coefficient. Therefore, our model considers that the H present in this zone will be less affected by diffusion. Thus, we consider that our model gives a good approximation for the out-diffusion of H from the lowest concentration of the implantation peak.

5.3. Comparison between numerical modelling and SIMS for $3.5 \cdot 10^{16} \text{ Hcm}^{-2}$ samples

The results of the modelling are compared with the SIMS analysis, considering the $3.5 \cdot 10^{16} \text{ Hcm}^{-2}$ samples (Fig. 23). As a reminder, we have chosen these samples as a reference, in order to allow 30s annealing at 600°C and 850°C without significant effect of temperature ramp and without splitting. Still, the comparison between our model and SIMS profiles of the implantation zone will bring arguments in order to validate our model of diffusion coefficient within the implanted material.

It is worth noting that for the modelling of the annealing at 600°C , only the elbows of the implantation peak are affected by the diffusion of H, whereas the maximum of the peak remains unchanged. It tends to show that the out-diffusion process is limited by the region with the lowest density of traps. On the other hand, the SIMS profile shows a clear decreasing of the overall peak, what can be explained by the formation of gaseous H_2 that fills the platelets and the micro-cracks.

For the annealing at 850°C , the simulated profile shows a decreasing in the region of peak maximum. In this case, the de-trapping process involved in the out-diffusion of H is sufficient to release H in the most defected part of the implantation zone.

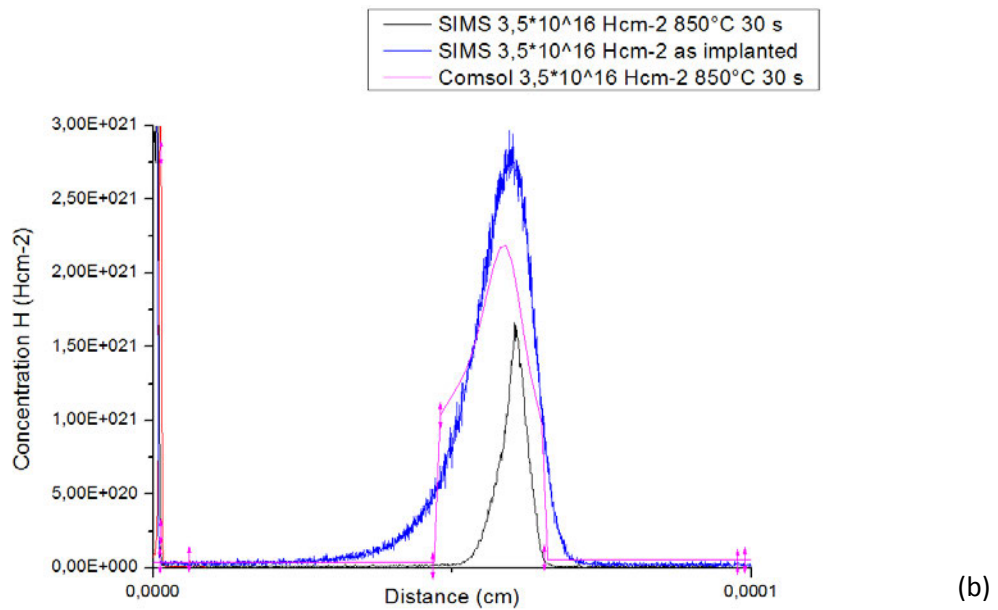
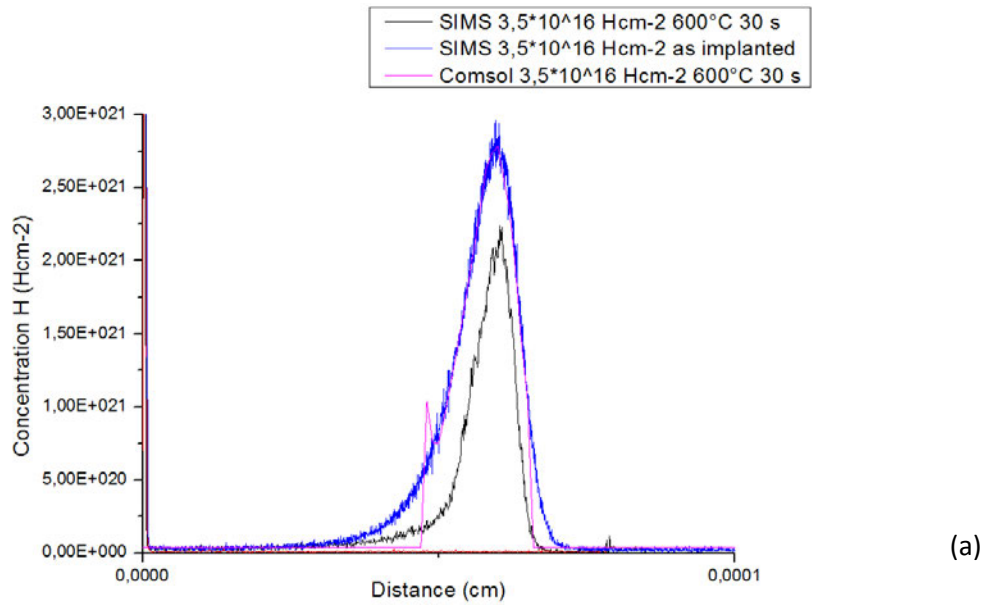


Figure 23: Comparison between the H concentration implantation zone of $3.5 \cdot 10^{16} \text{ Hcm}^{-2}$ obtained by SIMS characterization and numerical modelling, after 30 s annealing at 600°C (a) and 850°C (b).

NB: obviously, the signal of non-implanted sample is zero.

The Table 6 gives a summary of the calculation that can be done comparing the simulated profiles with the SIMS profiles. The out-diffused H is calculated from the difference between the as-implanted state and the modelled profiles after annealing. It gives a value of $7.3 \cdot 10^{15} \text{ Hcm}^{-2}$ after 600°C annealing, i.e. 19.1 % of the initial implanted dose, what is significant.

On the other hand, the comparison between the simulated profile and the SIMS analysis after annealing allows calculating the formation of gaseous H_2 . The value of 25.6 % of gaseous H_2 after the annealing at 600°C and 30 s can be compared with experimental observations considering mass spectrometry analysis as reported by Penot et al. [1, 6]. Indeed, these characterizations return a ratio

of 29 % of the initial implanted dose ($5.75 \cdot 10^{16} \text{ Hcm}^{-2}$ at 32 keV) released after a complete splitting annealing.

In case of an annealing at 850°C for 30 s, there is no comparison in the literature. Thus, it is hard to be conclusive about the profile of H after this annealing, especially for the zone of maximum concentration, where platelets nucleation occurs.

Table 6. Integral of the signal of H by SIMS for $3.5 \cdot 10^{16} \text{ Hcm}^{-2}$ samples within the implanted zone.

Annealing conditions (Temperature, duration)	Integral of H signal by SIMS (Hcm^{-2})	Integral of H signal by modelling (Hcm^{-2})	Out-diffused H (Hcm^{-2})	Formation of gaseous H_2 (Hcm^{-2})	Ratio of H in gaseous H_2 over the implantation dose (%)
As-implanted	$3.8 \cdot 10^{16}$	$3.8 \cdot 10^{16}$	-	-	-
600°C 30 s	$2.1 \cdot 10^{16}$	$3.1 \cdot 10^{16}$	$7.3 \cdot 10^{15}$	$9.8 \cdot 10^{15}$	25.6
850°C 30 s	$9.5 \cdot 10^{15}$	$2.8 \cdot 10^{16}$	$1.0 \cdot 10^{16}$	$1.9 \cdot 10^{15}$	48.4

6. Characterization of adhesion energy of bonding interface

6.1. Results

The bonding energy of the samples after thermal annealing is characterized by double cantilever beam test for samples implanted with $3.0 \cdot 10^{16} \text{ Hcm}^{-2}$, $4.0 \cdot 10^{16} \text{ Hcm}^{-2}$, $4.5 \cdot 10^{16} \text{ Hcm}^{-2}$ and non-implanted samples as a reference. As a reminder from the previous chapter, the measurement is realized by a blade insertion at the bonding interface, in anhydrous atmosphere (i.e. to avoid the water-assisted corrosion at the interface). The geometry of the samples is illustrated in Fig. 24.

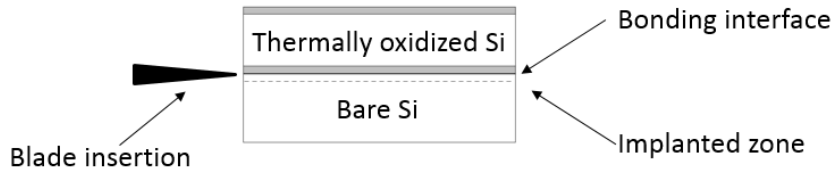
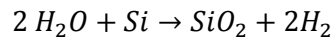


Figure 24: Schematic representation of the samples configuration for the characterization of the adhesion energy by blade insertion.

The results are presented on Fig. 25 and show the evolution of the adhesion energy during annealing at 850°C for various annealing times (from non-annealed state to 30 s of annealing). At this temperature, the following chemical reaction is considered as the driving force for the interface sealing [9]:



, where H_2O is the water that is trapped at the interface during the bonding step. It is accepted that this water diffuses through the native oxide layer to form additional SiO_2 layer. The first observation on Fig. 25 is the very abrupt change of adhesion energy between the non-annealed state and after 5s of annealing (corresponding roughly to the thermal ramp). The measured energy is coherent with what can be measured after 2 hours of annealing in literature [19]. It implies that sealing reaction occurs almost instantaneously at 850°C . Such a high bonding energy, superior to the toughness of Si ($5\text{J}/\text{cm}^2$), has already been measured for similar systems, and was proposed to be the consequence of additional relaxation mechanisms [19].

For longer annealing and for non-implanted samples, it can be observed that the opening occurs at the bulk-oxide interface instead of at the initial bonding interface, with a slightly lower bonding energy ($<6\text{J}/\text{m}^2$). Such a result is not reported in literature and suggests that the oxide interface is weaker than the bonding interface after the considered thermal reinforcement.

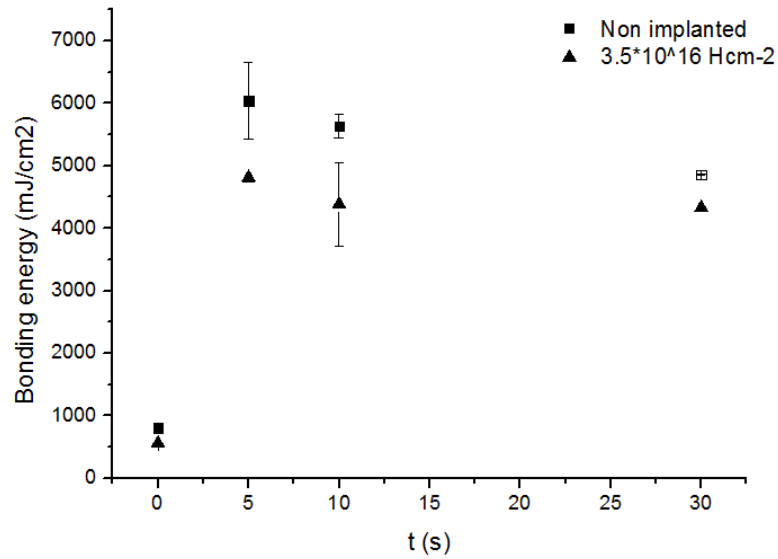


Figure 25. Comparison of bonding energy between $3.5 \cdot 10^{16} \text{ H cm}^{-2}$ and non-implanted samples, after annealing at 850°C , measured in anhydrous conditions. The empty square corresponds to an opening at the thermal oxide interface, whereas the full squared corresponds to an opening at the bonding interface.

It is worth noting that the bonding energy for implanted samples is lower than for non-implanted samples, as illustrated on Fig. 26. It is interesting to note that the opening occurs within the implantation zone for the $4.5 \cdot 10^{16} \text{ Hcm}^{-2}$ samples for 5 s and 10 s of annealing, whereas the opening occurs only at the bonding interface for the other samples. Thus, the formation of micro-cracks for $4.5 \cdot 10^{16} \text{ Hcm}^{-2}$ samples reduces the cohesion energy of the implanted zone below the cohesion energy of the bonding interface. For longer annealing than 10 s, the $4.5 \cdot 10^{16} \text{ Hcm}^{-2}$ samples spontaneously splits.

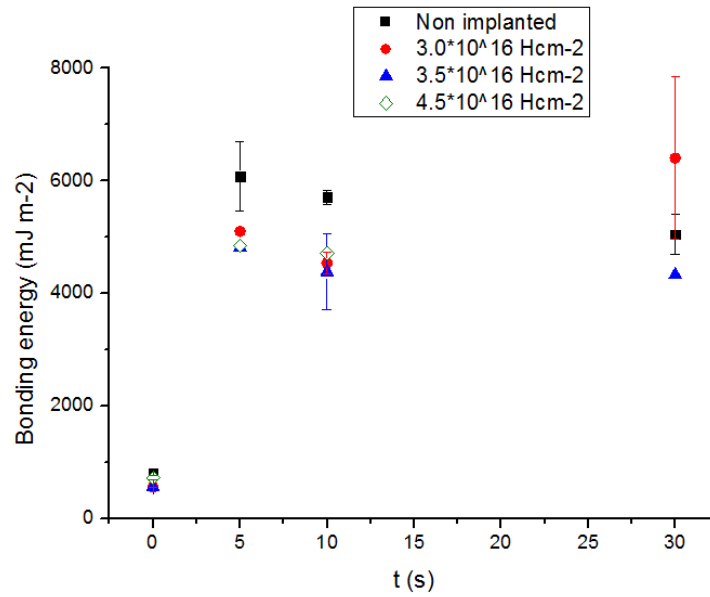


Figure 26: Bonding energy as a function of dose compared to non-implanted samples, after annealing at 850°C, measured in anhydrous conditions. The empty squares correspond to an opening occurring within the implantation zone for $4.5 \cdot 10^{16} \text{ Hcm}^{-2}$, whereas the full squared corresponds to an opening at the bonding interface.

It worth noting that the opening occurs systematically at the bonding interface for $3.0 \cdot 10^{16} \text{ Hcm}^{-2}$ and $3.5 \cdot 10^{16} \text{ Hcm}^{-2}$ samples. This aspect does not contradict the observation of transfer at the bulk-oxide interface, spontaneously observed for longer annealing time. Indeed, the measurement is realized at room temperature, i.e. without the thermal contribution. Thus, it appears that the bonding interface for $3.0 \cdot 10^{16} \text{ Hcm}^{-2}$ and $3.5 \cdot 10^{16} \text{ Hcm}^{-2}$ samples presents the lowest bonding energy.

On the other hand, it appears that there is a competition between the reinforcement of the bonding interface, a process that occurs within a few seconds only, and a weakening of the other interfaces (i.e. the oxide interface or the implanted zone). This aspect is coherent with the diffusion of H as previously characterized by SIMS. Indeed, H tends to migrate at the boundaries of the oxide layer. The most probable hypothesis is that the out-diffused H affects negatively the reinforcement of the bonding interface and can help to the detachment at the oxide interface, as discussed earlier.

Thus, we propose two hypothetic models of evolution of the bonding energy of the interfaces (bonding interface, thermal oxide interface and the implantation zone) as a function of time for a high temperature annealing (typically superior to 850°C). In case of a low dose implantation sample (e.g. inferior to $3.5 \cdot 10^{16} \text{ Hcm}^{-2}$), the thermal oxide interface is the weakest after a duration of typically a few tens of seconds, due to the migration of H to this interface, as illustrated on Fig. 27 (a). As a result, the interface can be split, creating the oxide transfer we have observed.

At the contrary, for a high implantation dose sample (i.e. with a dose superior to $4.5 \cdot 10^{16} \text{ Hcm}^{-2}$), damaging of the implantation zone is enough to allow the layer separation in this interface, creating the Smart Cut™ splitting (see on Fig. 27 (b)).

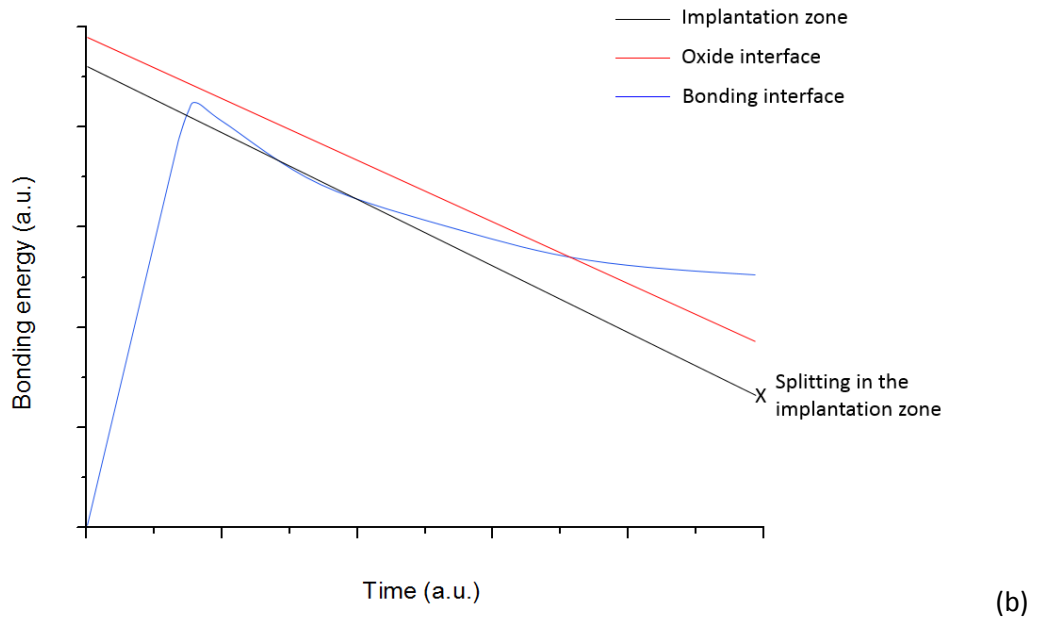
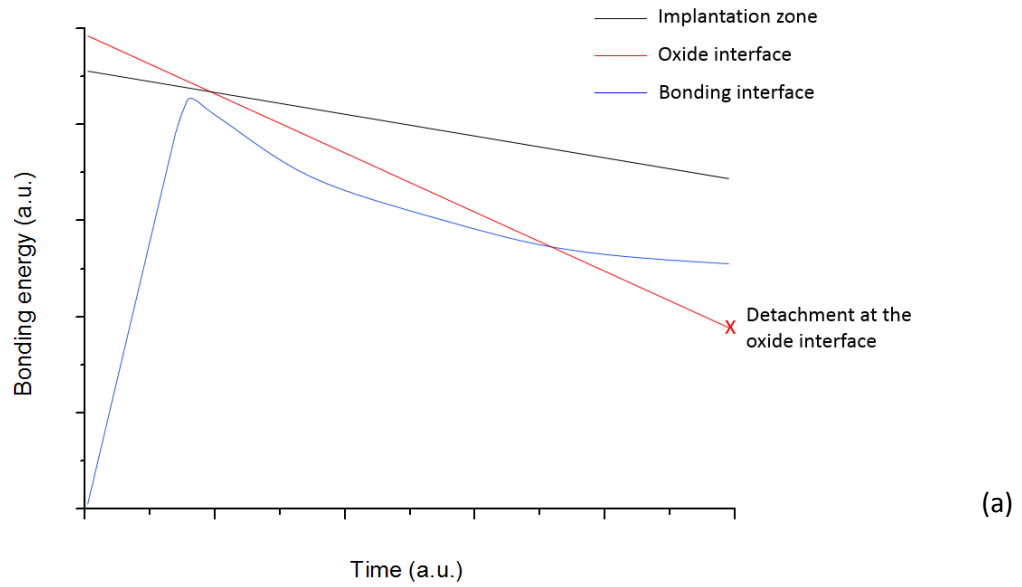


Figure 27: Proposition of model of the evolution of the bonding energy of the different interfaces for a sample implanted with a low dose (a), and a sample implanted with a sufficient dose to allow the splitting (b).

7. As-split surface roughness

7.1. Roughness as a function of temperature of Si splitting samples implanted with $5.0 \cdot 10^{16} \text{ Hcm}^{-2}$ by AFM characterization

Finally, the roughness of films after splitting is characterized by AFM for $5.0 \cdot 10^{16} \text{ Hcm}^{-2}$ samples and presented on Fig. 28. It can be observed that the roughness decreases almost linearly over a range of temperature from 500°C to 650°C. Such a reduction of roughness usually follows an increasing of the implantation dose [20], as a higher dose allows the nucleation of a higher density of platelets, of reduced dimensions. As expressed by the Freund's relation, already presented earlier in the chapter:

$$J_{min} = \frac{8}{3} \frac{\gamma}{k_B T}$$

, we know that increasing the annealing temperature leads to a reduction of the minimum dose needed for the splitting, J_{min} . It can be concluded that the increasing the annealing temperature over the considered temperature range is equivalent to an increasing of the implantation dose.

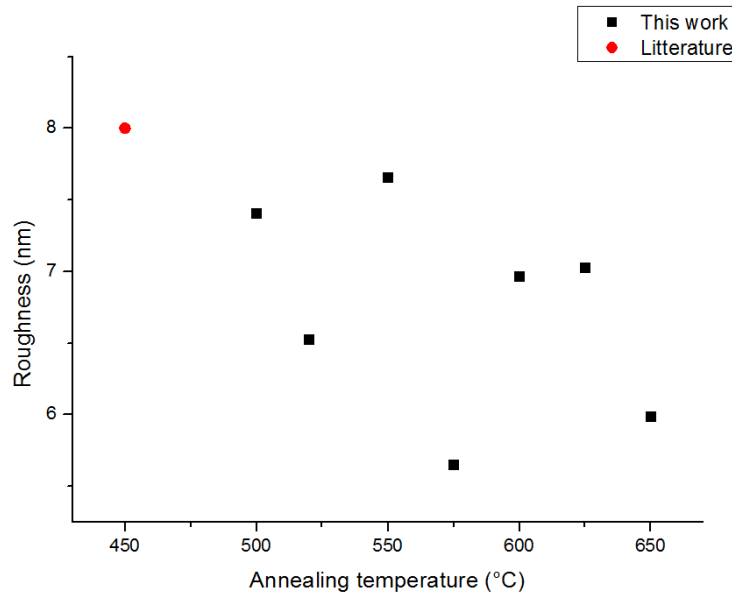


Figure 28: RMS roughness by AFM characterizations of $5.0 \cdot 10^{16} \text{ Hcm}^{-2}$ samples after splitting and comparison with literature [2].

This observation is coherent with the observation of the blisters earlier in this chapter. Thus, the effect of the higher temperature is an increase of the micro-cracks density, with a reduction of their size. As a result, there are less deviations of the splitting front propagation, what leads to a lower roughness.

Thus, we can postulate that the roughness of the as-split exfoliated layer continuously decreases with temperature. This postulate will be evaluated in the Chapter 5 with the laser-assisted splitting (i.e. for temperature superior to 900°C).

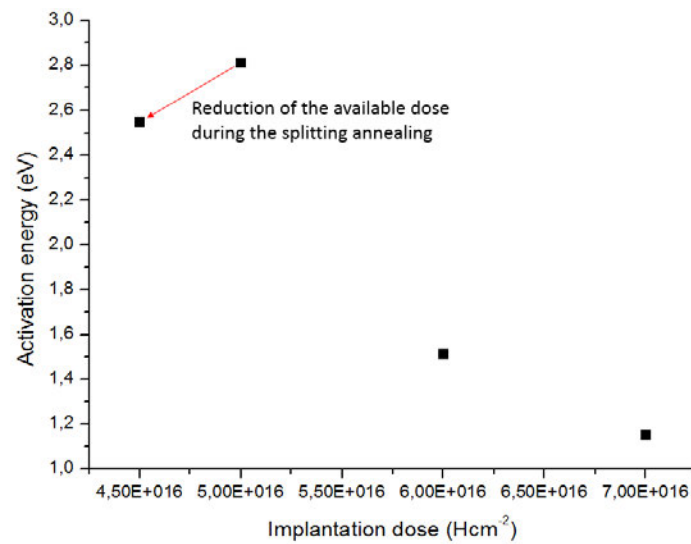
8. Model of splitting

8.1. Thermal budget calculation including the out-diffusion

The model that we propose relies on the various observations realized so far. Indeed, it appears that the evolution of the splitting kinetics for a same dose above 550°C-600°C (e.g. 550°C for $5.0 \cdot 10^{16} \text{ Hcm}^{-2}$) is affected by the reduction of the total dose of H available for the splitting, due to a phenomenon of out-diffusion. As a reminder, we have seen earlier that the out-diffusion of H slows down the splitting kinetics.

Thus, we will calculate the thermal budget of splitting σ_T with the contribution of out-diffusion. Therefore, we need first to calculate the out-diffusion during the thermal ramp followed by the splitting annealing. The temperature signal recorded by the thermocouple placed inside the sample is used applying our model of diffusion coefficient of H introduced earlier.

As a result, the evolution due to out-diffusion of H (for activation energy of splitting and pre-exponential factor as characterized in paragraph 2.2.2), can be used to determine the splitting kinetics of the $5.0 \cdot 10^{16} \text{ Hcm}^{-2}$ samples during the splitting annealing, as figured on Fig. 29.



(a)

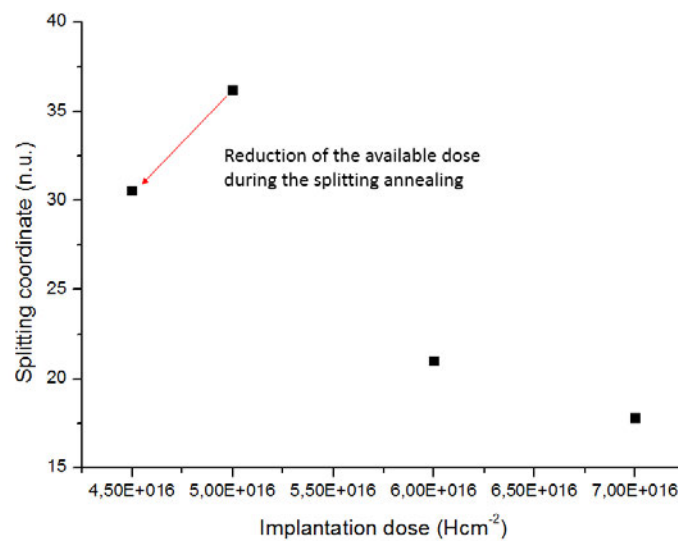


Figure 29: Evolution of the activation energy (a) and pre-exponential factor τ_0 (b) due to the loss of hydrogen during the thermal annealing, starting from an initial implanted dose of $5.0 \cdot 10^{16} \text{ Hcm}^{-2}$

The Fig. 30 gives the amount of H out-diffused during the splitting annealing for $5.0 \cdot 10^{16} \text{ Hcm}^{-2}$, considering the measured temperature during the splitting experiment. The time for the out-diffusion is considered as the time of splitting minus the time of thermal ramping as characterized earlier. The calculated out-diffusion is coherent with the measurement by SIMS $3.5 \cdot 10^{16} \text{ Hcm}^{-2}$ at 600°C after 30 s (see on Table 6).

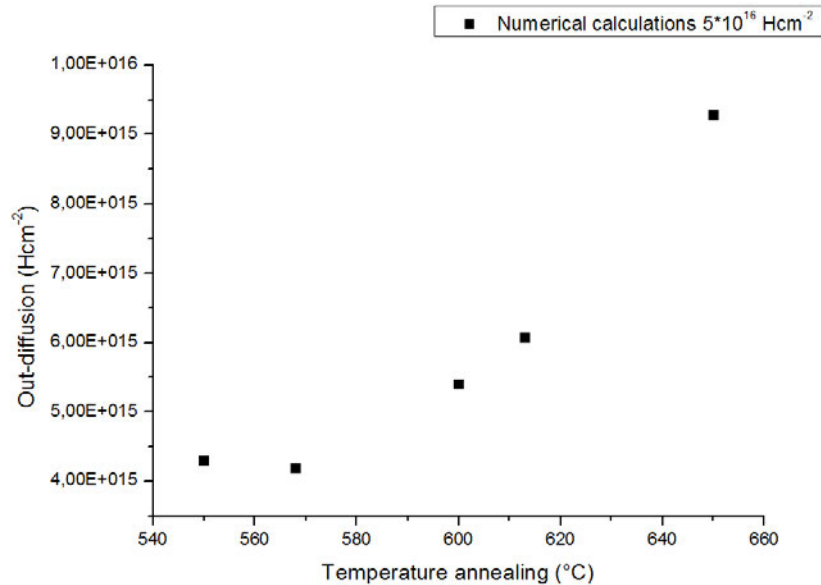


Figure 30: Amount of out-diffused H at the splitting, for $5.0 \cdot 10^{16} \text{ Hcm}^{-2}$ samples, by numerical modelling. The out-diffusion measured by SIMS for a $3.5 \cdot 10^{16} \text{ Hcm}^{-2}$ after an annealing of 30 s at 600°C is also plotted.

The Fig. 31 reports the normalized thermal budget values σ_T for $5.0 \cdot 10^{16} \text{ Hcm}^{-2}$ samples calculated with the two Arrhenius regimes proposed earlier (see Fig. 9). The third model relies on the calculation of the remaining H dose as a function of the annealing temperature. Thus, the modelled diffusion of H is used to calculate numerically the dose of H that is lost as a function of the annealing temperature. The normalized thermal budget function is then calculated considering the signal of the thermocouple.

The three hypotheses of Arrhenius regime are as following:

- Hypothesis 1: one single Arrhenius regime (as characterized for low temperature annealing)
- Hypothesis 2: diffusion of free H
- Hypothesis 3: the Arrhenius regime is affected by out-diffusion

It appears that the model considering the out-diffusion gives better approximation of the experimental data, even if the σ_T function returns values lower than 1 (i.e. the correspondence between the experimental conditions of splitting and a theoretical model), it seems that the out-diffusion is overestimated in the transition range between 550°C and 600°C . Indeed, a lower out-diffused dose during the annealing in this temperature range would return of σ_T closer to 1.

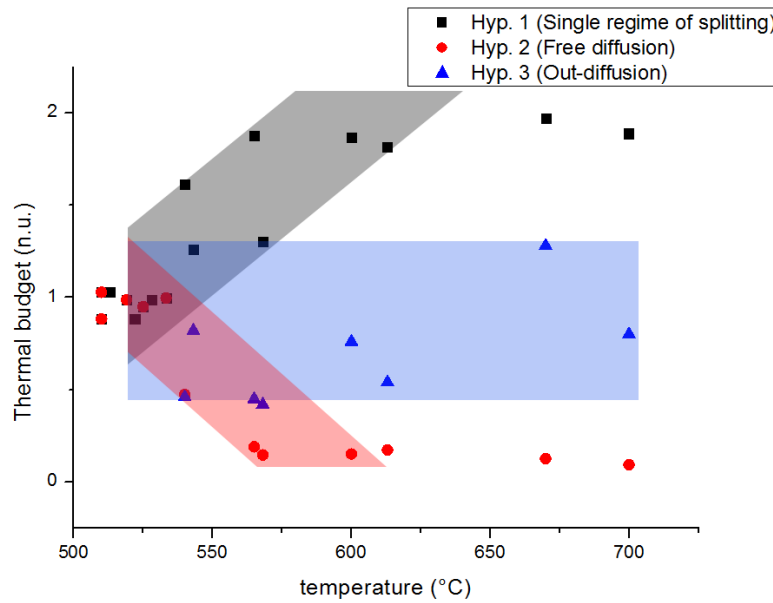


Figure 31: Calculation of the thermal budget (σ_T) with different hypothesis of splitting kinetics, including the hypothesis of out-diffusion of H.

As an intermediate conclusion on the kinetics of splitting, we propose that the splitting mechanics remains a function of the effective dose of H present within the implantation zone. The activation energy that is characterized at low temperature as a function of implantation dose gives a good approximation to determine the conditions of thermal annealing. The loss of H due to the out-diffusion process can be calculated as a function of the annealing conditions in order to determine the evolution of the effective dose of H during the annealing itself and its efficiency for splitting.

8.2. Prediction of the model for higher temperatures

We now propose to use our model of Arrhenius regime to evaluate if the splitting is possible for temperature going up to 1410°C (i.e. the melting point of Si). This will be a preparation step for the next chapter. Indeed, this chapter will present results of splitting by laser annealing (i.e. for temperature going up to melting point of Si). Therefore, we extrapolate the splitting time by taking the activation energy of splitting at low temperature and we calculate the out-diffusion of H using our model of diffusion during this splitting time. If the dose of out-diffused H during the corresponding annealing is small, the splitting is supposed to be possible.

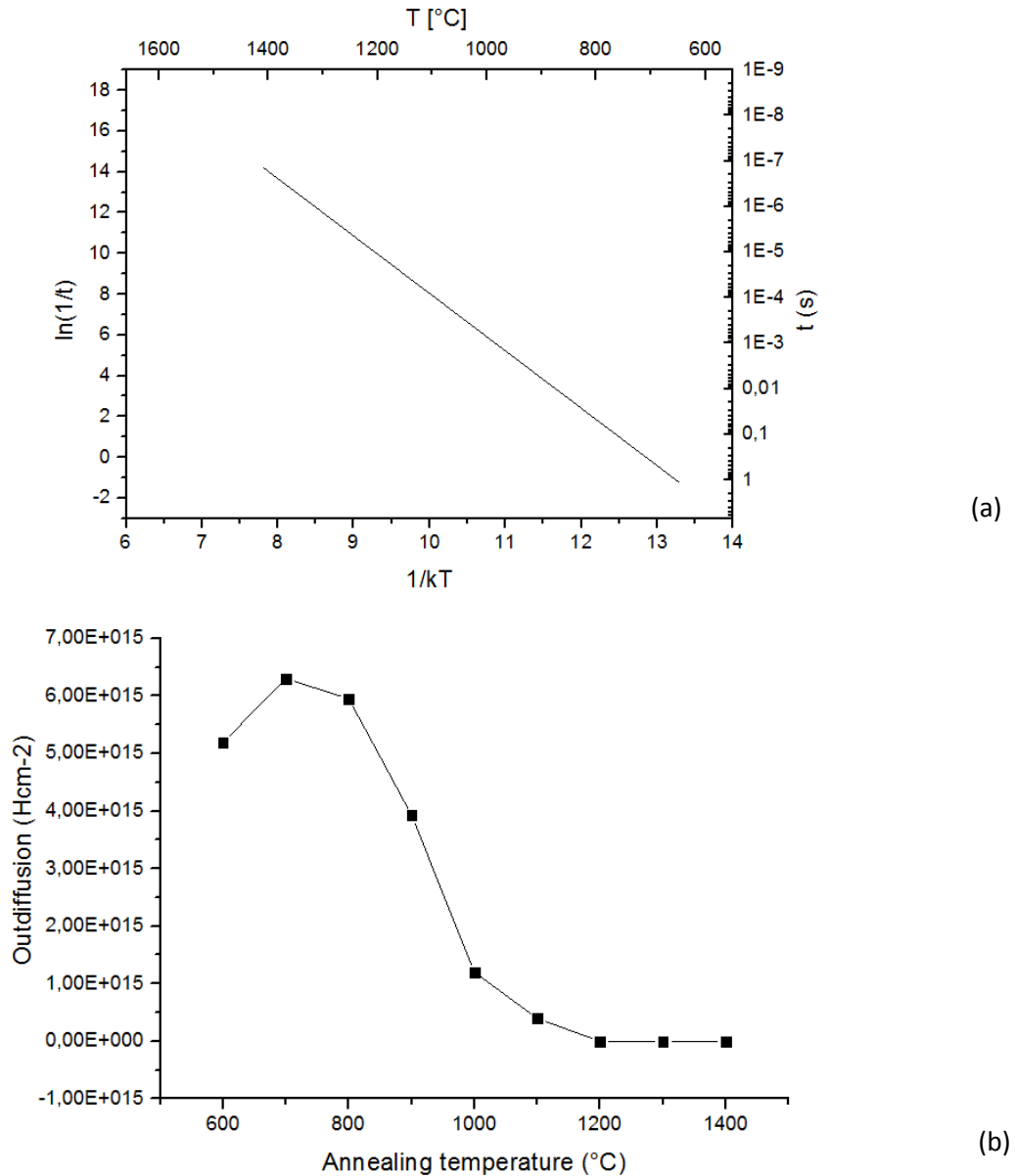


Figure 32: Prediction of the splitting time considering the splitting kinetics at low temperatures for splitting samples implanted with $5.0 \cdot 10^{16} \text{ Hcm}^{-2}$ (a), calculation of the out-diffusion of H during the corresponding splitting durations (b).

The Fig. 32 shows that the maximum of outdiffusion as calculated by our model occurs at 700 $^{\circ}\text{C}$ and then continuously decreases to zero. As a conclusion, the splitting should be possible at any temperature considering a sufficient implantation dose. This postulate will be experimented in the following chapters, by considering laser annealing and finally the liquid phase epitaxial growth, where the cristallization induces a very fast thermal ramping and potentially brings the implantation zone up to the melting point of silicon ($T = 1412^{\circ}\text{C}$).

8.3. Mechanisms leading to oxide layer transfer and detachment at the bonding interface

The mechanism of oxide layer splitting appears as being the result of several simultaneous processes. The out-diffusion of H is proved to be one of the driving forces of such a detachment, even the measured dose of H within the oxide is insufficient to satisfy the Freund's criterion.

Thus, it is not possible to conclude that the splitting at the oxide interface follows the splitting process based on growth of penny-shaped defects. On the other hand, it is well known that a high stress remains in thermal oxide at the interface between thermal oxide and silicon, due to the volume expansion from Si to SiO₂. The remaining stress is considered as equal to 500 MPa in case of thermal oxide formed at 950°C in O₂ atmosphere [21, 22]. Nevertheless, as the thermal expansion of Si is much higher ($\alpha_{\text{Si}} = 2.6 * 10^{-6} \text{K}^{-1}$) than the one of SiO₂ ($\alpha_{\text{SiO}_2} = 3.5 * 10^{-7} \text{K}^{-1}$), the thermal annealing will tend to compensate the remaining stress within the thermal oxide layer. Thus, a spalling effect induced by a stress field within the material, such as presented in the state of the art part for the SLiMCut process, can be a priori excluded [23]. It is worth noting that a thermal gradient inside the sample could also be an explanation of the oxide layer transfer. As a consequence, it is difficult to be conclusive on a precise physical mechanism leading to the oxide splitting. H is proved to concentrate at the oxide interfaces, as shown by SIMS analysis, and it is possible to postulate that this concentration reduces the cohesion energy of the bonding interface respectively the thermal oxide interface up to its spontaneous splitting.

9. Conclusion of the chapter

In this chapter, we have studied the splitting kinetics observed above 550°C-600°C, in order to understand the mechanisms that might affect the splitting possibility for higher temperature annealing. By introducing the calculation using the normalized thermal budget function, the hypothesis of out-diffusion of H as being the main factor in this transition has been validated. This diffusive process results from a de-trapping of H affects the splitting kinetics above 550°C and is indeed observed by SIMS characterization of the implanted zone as well as the buried oxide. Thereby, the hypothesis proposed in the literature and explaining a change of splitting regime at high temperature by the diffusion of free H can be definitively invalidated.

It is shown that the out-diffused H tends to aggregate at the oxide interfaces. It leads to mechanical weakening of these interfaces. This mechanism can lead to the layer separation at the bulk thermal oxide interface or at the bonding interface, for low implantation energy. The H is proved to play a role in this layer separation, even if the analysis of out-diffused dose of H summed with the H naturally present at the bonding interface, is not sufficient to satisfy the Freund's criterion of crack propagation. The characterization of the bonding energy with different annealing conditions shows that a rapid reinforcement of the bonding interface occurs within a few seconds. On the other hand, it is known in the literature that the high stress at the thermal oxide interface remains after the thermal oxidation. This stress combined with the out-diffusion of H within the oxide can explain the layer separation, under proper thermal conditions. As the splitting occurs in a plane of a few atomic layers only, the roughness of the newly created surfaces is much lower than the roughness of a "classical" splitting.

The roughness of as-split surface is proved to be reduced for a same implantation dose by the increase of annealing temperature. It is a consequence of a higher density of micro-cracks resulting from a higher contribution of the pressure within the micro-cracks.

A model for the diffusion coefficient of H inside the implantation zone is proposed, based on the decomposition of Si(100):H. The resulting activation energy for this diffusion coefficient returns a value of 1.46 eV. The numerical modeling of the evolution of H during the splitting annealing is in good agreement with the SIMS characterization of the H profiles of the implanted material after annealing. The SIMS characterization showed that the implanted H is still present within the implantation zone even for temperature annealing superior to 850°C. This observation was considered as unlikely in literature based on thermal annealing much longer than the theoretical duration of the splitting annealing at the corresponding temperature.

Thus, considering an ultrafast annealing system such as a laser-beam treatment or at high temperature LPE growth, the splitting should occur by following the same physical mechanisms of platelets nucleation, micro-cracks growth and coalescence up to the layer separation. The predictions of the model show that the kinetics of splitting should not be affected by the H out-diffusion at temperatures above 900°C.

References

- [1] **J. D. Penot**, Fragilisation et dynamique de rupture du silicium implanté, Thèse de l'Université de Grenoble, 2010.
- [2] **M. Bruel, B. Aspar, H. Moriceau, E. Jalaguier, C. Lagahe**, Single crystal layer delamination and transfer through hydrogen implantation, *Electroch. Soc. Proc.*, vol. 1, 1999.
- [3] **M. Nastasi, T. Höchebauer, J.-K. Lee, A. Misra, J. P. Hirth**, Nucleation and growth of platelets in hydrogen-ion-implanted silicon, *Appl. Phys. Lett.*, vol. 86, pp. 1-3, 2005.
- [4] **B. Aspar et al.**, The generic nature of the Smart-Cut™ process for thin film transfer, *J. of Electr. Mat.*, vol. 30, No. 7, pp. 834-840, 2001.
- [5] **J. Grisolia, F. Cristiano, G. Ben Assayad, A. Claverie**, Kinetic aspects of the growth of platelets and voids in H implanted Si, *Nucl. Instr. and Meth. in Phys. Res. B*, vol. 178, pp. 160-164, 2001.
- [6] **F.-X. Darras, N. Cherkashin, F. Cristiano, O. Kononchuk, L. Capello, A. Claverie**, Quantification of the number of Si interstitials formed by hydrogen implantation in silicon using boron marker layers, *Nucl. Instr. and Meth. in Phys. Res. B*, vol. 327, pp. 29-32, 2014.
- [7] **J.-D. Penot, D. Massy, F. Rieutord, F. Mazen, S. Reboh, F. Madeira, L. Capello, D. Landru, O. Kononchuk**, Development of microcracks in hydrogen-implanted silicon substrates, *J. of Appl. Phys.*, vol. 114, pp. 123513-1-6, 2013.
- [8] **L. B. Freund**, A lower bound on implant density to induce wafer splitting in forming compliant substrate structures, *Appl. Phys. Lett.*, vol. 70, pp. 3519-3521, 1997.
- [9] **C. Ventosa, C. Morales, L. Libralesso, F. Fournel, A. M. Papon, D. Lafond, H. Moriceau, J. D. Penot, F. Rieutord**, Mechanism of thermal silicon oxide direct wafer bonding, *Electr. and Sol.-St. Lett.*, vol. 12, no. 10, pp. 373-375, 2009.
- [10] **M. K. Weldon, Y. J. Chabal, D. R. Hamann, S. B. Christman, E. E. Chaban, and L. C. Feldman**, Physics and chemistry of silicon wafer bonding investigated by infrared absorption spectroscopy, *J. of Vac. Sc. & Tech. B*, vol. 14, pp. 3095-3106, 1996.
- [11] **S. Sasaki, T. Izumi, T. Hara**, Delamination of Si by high dose H-ion implantation through thin SiO₂ film (ESR characterization), *Mat. Sc. and Eng. B*, vol. 91-92, pp. 160-163, 2002.
- [12] **R. Boivin and B. Terreault**, Desorption and other effects of pulsed laser annealing of hydrogen implanted silicon, *J. of Appl. Phys.*, vol. 73, 1943-1951, 1993.
- [13] **O. Moutanabbir, B. Terreault, M. Chicoine, F. Schiettekatte**, The fluence effect in hydrogen-ion cleaving of silicon at the sub-100-nm scale, *Appl. Phys. A*, vol. 80, pp. 1455-1462, 2005.
- [14] **S. Personnic, K. K. Bourdelle, F. Letertre, A. Tauzin, N. Cherkashin, A. Claverie, R. Fortunier, and H. Klocker**, Impact of the transient formation of molecular hydrogen on the microcrack nucleation and evolution in H-implanted Si (001), *J. of Appl. Phys.*, vol. 103, pp. 023508-1-9, 2008.
- [15] **P. Pichler**, Intrinsic point defect, impurities and their diffusion in Silicon, Springer, 2004.
- [16] **A. Shah**, Thin-film solar cells, Ed. Arvind Shah, EPFL Press, 2010.
- [17] **D. J. Fisher**, Diffusion in Silicon 10 years of research, Ed. D. J. Fisher, Soitec Publications, 1998.
- [18] **N. Cherkashin, F.-X. Darras, P. Pochet, S. Reboh, N. Ratel-Ramond, A. Claverie**, Modelling of point defect complex formation and its application to H⁺ ion implanted silicon, *Act. Mat.*, vol. 99, pp. 187-195, 2015.
- [19] **F. Fournel, L. Continni, C. Morales, J. Da Fonseca, H. Moriceau et al.**, Measurement of bonding energy in an anhydrous nitrogen atmosphere and its application to silicon direct bonding technology, *J. of Appl. Phys.* vol. 111, pp. 104907-1-7, 2012.
- [20] **Y.J. Chabal, M.K. Weldon, Y. Caudano, B.B. Stefanov, K. Raghavachari**, Spectroscopic studies of H-decorated interstitials and vacancies in thin-film silicon exfoliation, *Phys. B*, No. 273-274, pp. 152-163, 1999.
- [21] **F. Maseeh, S. M. Gelston, S. D. Senturia**, Mechanical properties of microelectronics thin films: silicon dioxide (SiO₂), *VLSI Publ.*, no. 89-575, pp. 1-14, 1989.
- [22] **T.-C. Yang, K. C. Saraswa**, Effect of physical stress on the degradation of thin SiO₂ films under electrical stress, *IEEE Trans. on Electr. Dev.*, vol. 47, no. 4, pp. 746-754, 2010.

[23] **M. Reuter, W. Brendle, O. Tobail, J. H. Werner**, 50mm thin solar cells with 17.0% efficiency, *Sol. Energ. Mat. & Sol. Cells*, vol. 93, pp. 704-706, 2009.

Chapter 5. Application of laser annealing to Smart Cut™

In the previous chapter, we have seen that the diffusion coefficient of the bonded H in the implantation zone plays a determinant role for annealing in the temperature range of 550-700°C. It is now necessary to explore the behavior of splitting samples at much higher temperature, if possible up to the melting point of Si, as this temperature domain is potentially reached during deposition of molten Si upon an implanted substrate.

The strategy proposed in this chapter will be to realize the splitting annealing by laser beam, which allows a much faster thermal ramping and a good control on temperature. Thus, the splitting possibility and kinetics will be verified based on the results of modeling presented in the previous chapter.

Another motivation for this study relies on the industrial motivation to develop an alternative process for the production of heterostructures, such as SOS (Silicon on Sapphire) or SOG (Silicon on Glass). Indeed, the splitting annealing of large diameter wafers required for the classical approach of Smart Cut™ can lead to the damaging or breaking of the bonded structure. The possibility to realize the detachment and transfer of Si film on a foreign substrate will be demonstrated using a laser beam scanning the surface of the implanted Si by illuminating glass or sapphire substrate which is transparent to the chosen beam wavelength.

The chapter will start with description of preparation steps, such as the annealing by laser of an implanted material alone (i.e. without bonding with an acceptor wafer) and such as numerical modelling. These preparation steps aim to establish a design of experiment for the splitting annealing of implanted Si bonded with glass and sapphire.

After the characterization of the splitting kinetics in the proposed conditions of temperature, the properties of the obtained SOS and SOG films will be presented and discussed. Finally, the industrial potential of the process proposed here will be evaluated by the study of the best samples obtained during the study. Thus, films properties will be characterized on both structural aspects (roughness, thickness and homogeneity of transfer) and electrical properties (resistivity).

1. Effects of ns laser annealing of bulk implanted Si wafers

As a preliminary work, we propose to study the annealing of an implanted Si substrates without bonding with a stiffener wafer. This approach, very similar to that described in the previous chapter, allows to explore the possibility of splitting, as the blistering of an implanted sample after annealing is a necessary condition for the splitting of a bonded structure. Thus, we propose to treat an implanted wafer by zones, with a nanosecond (ns) laser working with a repetition of pulse (multi-pulse regime). The formation of blisters is analyzed afterwards by optical microscopy.

1.1. Description of the ns laser annealing setup

In this work commercially available laser anneal system based on ArF excimer laser was used to anneal implanted Si samples. The beam pulse frequency was chosen to be 100 Hz which is maximum frequency available with the setup. Pulse duration is fixed to be 20 ns FWHM (full width at half maximum). Nearly uniform top-hat shape of 500x500 μm^2 of the illumination spot was achieved by beam correction optics. A schematic representation of the system is given in Fig. 1. Multiple illumination conditions, e.g. varying laser flux from 0.5 $\text{J}\cdot\text{cm}^{-2}$ to 1.5 $\text{J}\cdot\text{cm}^{-2}$ or number of laser pulses could be tested utilizing different locations on just one single wafer.

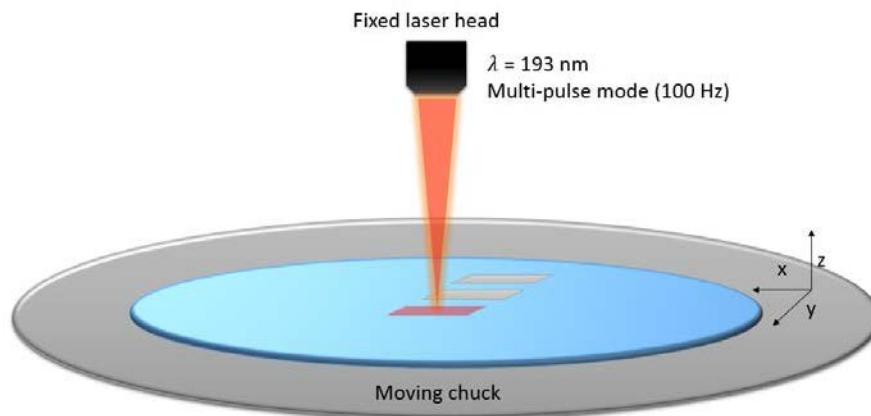


Figure 1: Schematic representation of the annealing of the sample by the ns-laser.

Additionally, the absorption length L defined by $\lambda/(4\pi k)$ gives a very low value of 4.4 nm at the laser wavelength of 193 nm (see on Fig. 2).

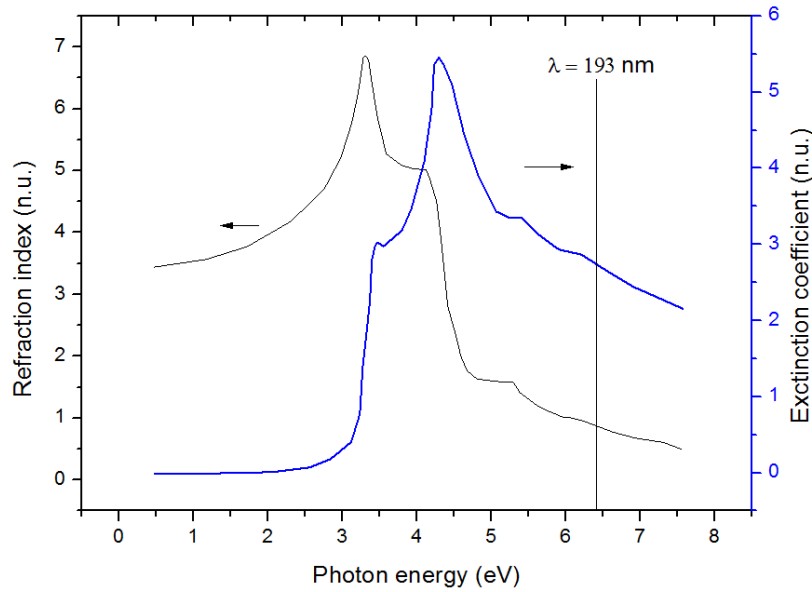


Figure 2: optical coefficient of Si as a function of the photon energy at 293K [1]. For the considered wavelength of 193 nm, $n = 0.87$ and $k = 3.48$.

1.2. Effect of multi-pulse annealing

Fig. 3 a) shows that no ablation occurs for single pulse annealing at a fluence of $1.0 \text{ J} \cdot \text{cm}^{-2}$ (i.e. with a power of $6 \cdot 10^7 \text{ W} \cdot \text{cm}^{-2}$). Indeed, it has been shown that ablation of the Si surface occurs for single pulse of ns laser annealing for power superior to $2.2 \cdot 10^{10} \text{ W} \cdot \text{cm}^{-2}$ [2]. Ablation process results from the generation of non-equilibrium electrons in a region near the surface during the laser beam absorption by Si [2].

On the other side, ablation starts to occur after 2000 pulses for a fluence of $1.0 \text{ J} \cdot \text{cm}^{-2}$ (see Fig. 3 b)). This phenomenon has been already observed and is called multi-pulse enhancement effect [3]. Nevertheless, the underlying physical mechanism is still unexplained [3].

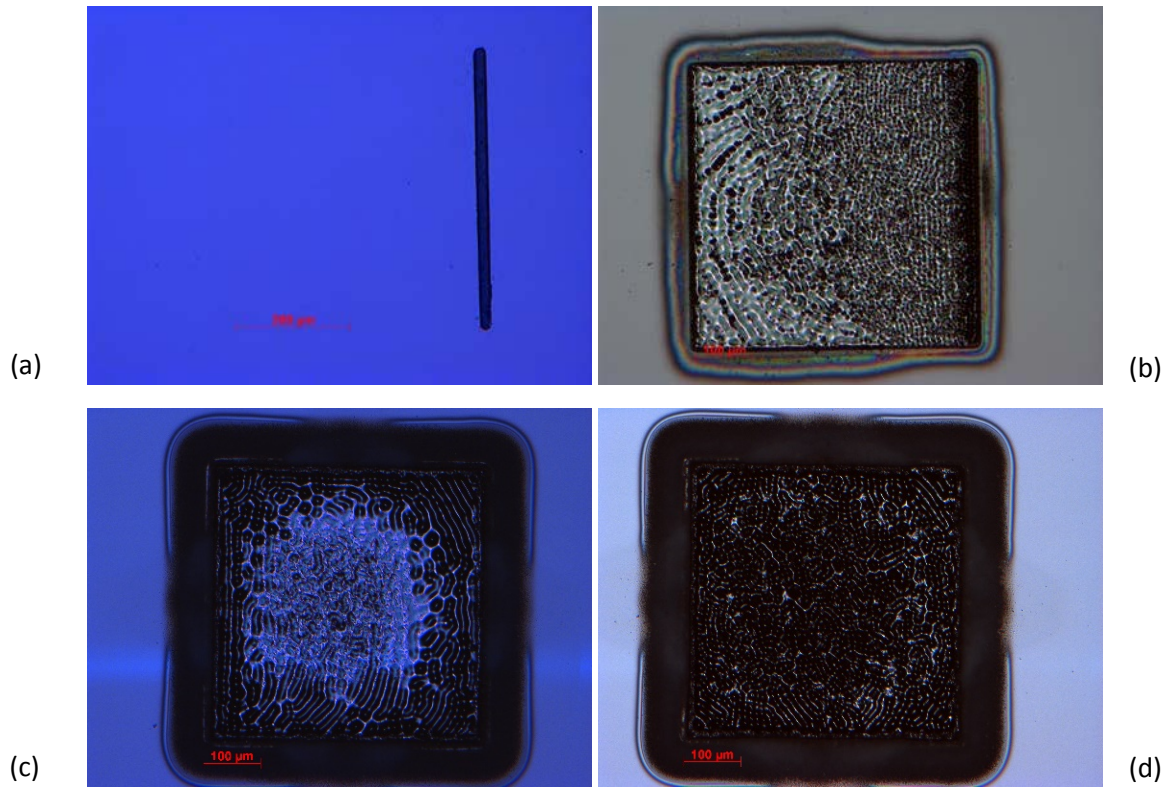


Figure 3: Single pulse at a fluence of $1.0 \text{ J} \cdot \text{cm}^{-2}$ (a) repetition of 2000 pulses at a fluence of $1.0 \text{ J} \cdot \text{cm}^{-2}$ (b), repetition of 6000 pulses at fluence of $1.0 \text{ J} \cdot \text{cm}^{-2}$, (c) repetition of 6000 pulses at a fluence of $1.1 \text{ J} \cdot \text{cm}^{-2}$. The sample is a non-implanted Si bulk.

The comparison between a repetition of 6000 pulses at fluence of $1.0 \text{ J} \cdot \text{cm}^{-2}$ and $1.1 \text{ J} \cdot \text{cm}^{-2}$ (Fig. 3 c) and d)) shows that the ablation effect increases with higher fluence. This effect was also reported in the literature [3].

It is worth noting that the ablation threshold is lower in case of an implanted sample, as shown on Fig. 4. A possible explanation is the lower thermal conductivity of implanted silicon that leads to concentrate the absorbed heat close to the laser absorption area, which is far less than the implantation depth as shown by numerical simulation.

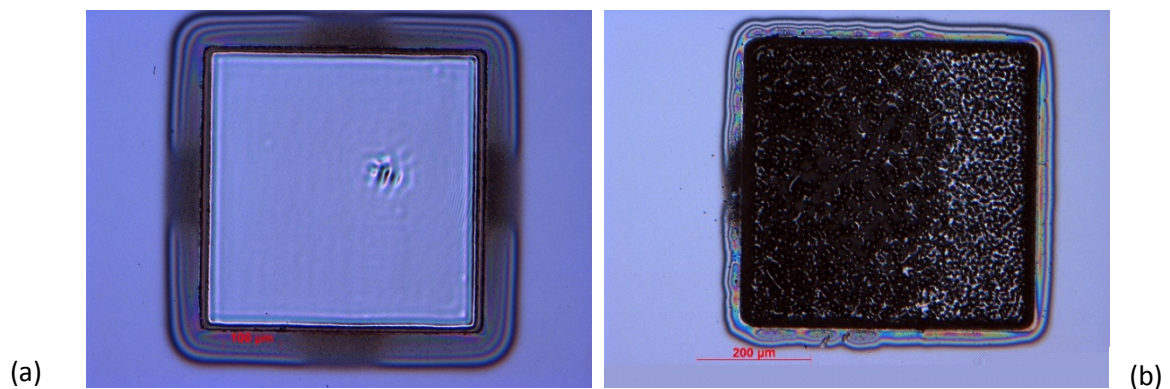


Figure 4: Comparison of non-implanted sample (a) and $1.0 \cdot 10^{17} \text{ Hcm}^{-2}$ implanted sample (b) for $0.9 \text{ J} \cdot \text{cm}^{-2}$ and a repetition of 6000 pulses.

1.3. Generation of blisters by multi-pulse ns laser annealing ($1.0 \cdot 10^{17} \text{ Hcm}^{-2}$)

Blistering can be observed for samples implanted with $1.0 \cdot 10^{17} \text{ Hcm}^{-2}$ with proper annealing conditions (i.e. fluence and number of pulses). This possibility of blistering of an implanted substrate with the laser annealing has been discussed in literature for a lower implantation energy, as mentioned in the second chapter [4].

In spite of the fact that the ablation threshold for the implanted sample is lower than the threshold of blisters formation, blisters can distinctively be observed by optical microscopy, as illustrated on Fig. 5. These blisters show a typical diameter of $20 \mu\text{m}$, which is large comparing to the blister size observed in the previous chapter for the same implantation dose, $1.0 \cdot 10^{17} \text{ Hcm}^{-2}$. However, it is still difficult to unambiguously classify blistering of the surface, due to the significant damage of the surface for both implanted and non-implanted samples.

Characterization of the annealed samples by mechanical profilometer shows that the surface reveals significant roughness with typical peak to valley heights of a few tens of microns. Such a high height suggests that the blisters explode during the pulse repetition, with a very strong deformation of the implantation zone and of the surface.

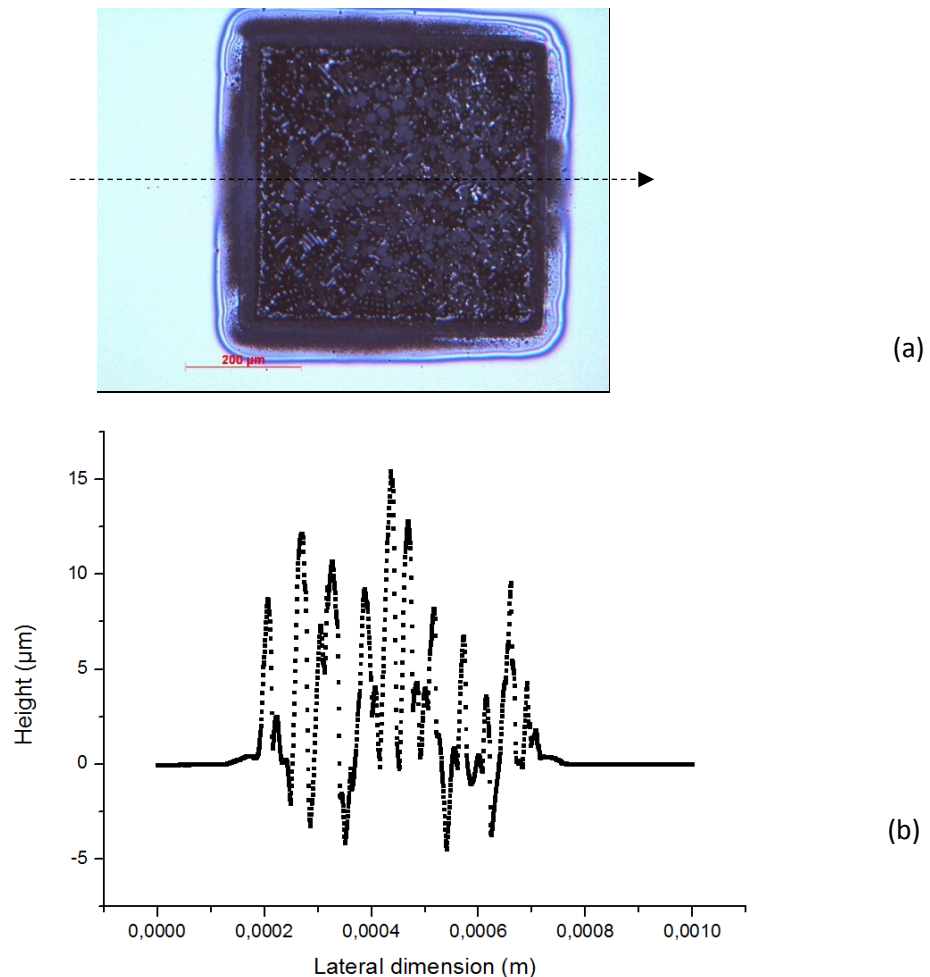


Figure 5: Optical microscopy images of a sample implanted with $1.0 \cdot 10^{17} \text{ Hcm}^{-2}$ after a repetition of 6000 pulses with a fluence of $1.0 \text{ J} \cdot \text{cm}^{-2}$ (a) height profile of the corresponding sample measured by mechanical profilometer (b).

The blisters generation as a function of the annealing conditions is summarized in the Fig. 6. Nevertheless, it is quite hard to establish a quantitative kinetics of blistering for such a high number of pulses. It is worth noting that for fluences superior to $1.4 \text{ J} \cdot \text{cm}^{-2}$ no blisters can be observed, probably due to ablation of the implanted zone itself before the formation of the blisters.

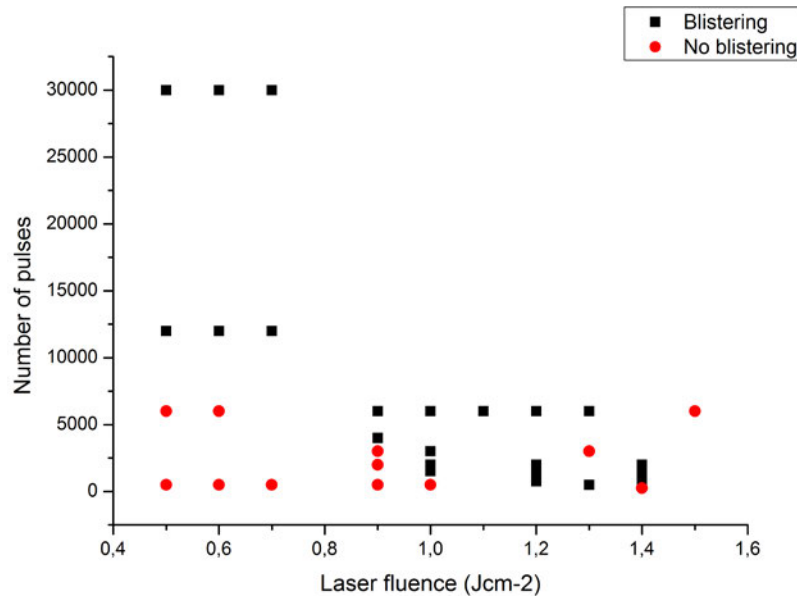


Figure 6: Conditions of blistering for $1.0 \cdot 10^{17} \text{ Hcm}^{-2}$ in terms of laser fluence and number of pulses.

In summary, these results show the possibility of splitting for the annealing temperatures above 1000°C by the observation of blisters on the implanted sample. Thus, it tends to prove that the H out-diffusion process is negligible or very limited due to the very short pulse duration. On the other hand, it demonstrates the cumulative effect of the splitting annealing. Finally, it appears that a longer laser pulses in ms range are required in order to reduce the laser fluence and the ablation effect during the multi-pulse annealing.

2. Kinetics of splitting by laser annealing (Implanted Si, SOS, SOG)

After establishing the possibility of local blistering by ns laser annealing, we will study annealing of full implanted wafers by continuous wave (CW) laser in ms time range. In order to provide the required stiffener layer, two types of transparent wafer are chosen to be bonded with the implanted surface of the donor wafer: sapphire of 100 mm diameter and glass of 200 mm diameter. Thus, after splitting, two types of structures are demonstrated: Silicon-On-Sapphire (SOS) and Silicon-On-Glass (SOG).

2.1. Numerical modelling of millisecond laser annealing of the bonded heterostructure

2.1.1. Constitutive equations

The numerical model considers a 2D system consisting of the laser wavelength transparent wafer (sapphire or glass) forming a contact with the Si wafer, as figured on Fig. 7.

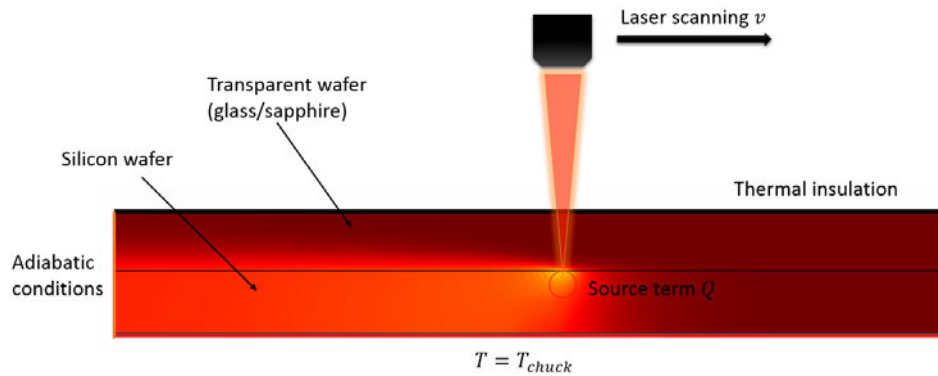


Figure 7: schematic representation of the modeling conditions of the annealing by ms laser.

The governing equation is the heat transfer equation:

$$\rho c_p \frac{\partial T}{\partial t} - \nabla(k \nabla T) = Q$$

with ρ being the density of the material, c_p the specific heat, k the thermal conductivity. For the sapphire, resp. glass part, the optical absorption is considered as null, as the material is transparent at this wavelength. For silicon, the source term Q of the laser beam is defined as following:

$$Q = (1 - R) I_0 e^{\left(-\frac{(x-vt)^2}{\sigma^2}\right)} f(y)$$

where I_0 is the incident beam power, v is the scanning speed of the laser upon the sample, σ is the width of the spot and t is the time [6]. The function $f(y)$ is the energy variation in depth, as defined by the Beer-Lambert law:

$$f(y) = \frac{1}{L} e^{-\frac{y}{L}}$$

with L being the absorption length of the material, defined by :

$$L = \frac{\lambda}{4\pi k}$$

where λ being the wavelength of the laser beam.

Finally, the source term is expressed as following:

$$Q = (1 - R) \frac{I_0}{L} e^{-(x-vt)^2/\sigma^2} e^{-\frac{y}{L}}$$

where R is the reflection at the surface of silicon.

Finally, it is worth noting that the model only considers thermal conduction as transfer mechanism. The other mechanisms are the radiation and the convection. Both can be neglected by simple estimations. Indeed, an incident power is in the order of $1 \cdot 10^9 \text{ W} \cdot \text{m}^{-2}$. The energy flux transferred by air convection is proportional to a ΔT between sample surface and the air temperature:

$$\kappa = h_{air} * \Delta T$$

, with h_{air} being the coefficient of convection of air varying between 10 and $100 \text{ W} \cdot \text{m}^{-2} \cdot \text{K}^{-1}$. Thus the energy flux is of order of magnitude of $10^5 \text{ W} \cdot \text{m}^{-2}$. The energy flux transferred by radiation follows the Stefan law:

$$\phi = \varepsilon \sigma (T_{surface}^4 - T_{atm}^4)$$

, where ε is the emissivity of silicon and σ is the Planck constant. Thus, considering the emissivity of silicon at 1200°C equals to 0.64, the ϕ could be estimated as $10^5 \text{ W} \cdot \text{m}^{-2}$. Both mechanisms are 6 orders of magnitude lower than the incoming power.

2.1.2. Bending of the bonded structure on the laser chuck

As the system is placed on a hot chuck in order to improve the optical absorption of Si, the sample structure follows a strong bending (see Fig. 8).

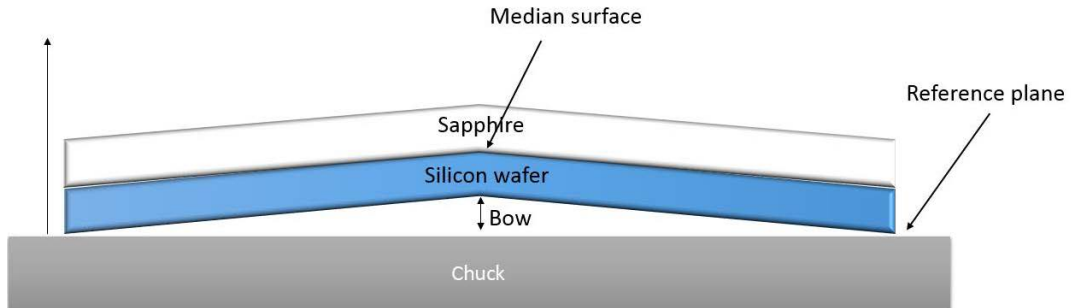


Figure 8: Schematic representation of the bow of the bonded structure composed of a wafer of sapphire (thickness of $700 \mu\text{m}$) and a wafer of Si. The deformation of the structure is due to the pre-heating of the chuck.

The resulting displacement b due to the difference of coefficient of thermal expansion α can be calculated analytically with the following formula [5]:

$$b = r \left(1 - \cos\left(\frac{R_w}{r}\right) \right)$$

All these parameters can be illustrated on the Fig. 9.

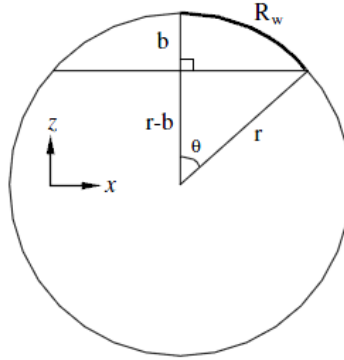


Figure 9: Schematic representation of the geometry used to calculate the wafer bow [5].

The different parameters are defined as following:

$$r = \frac{E_{sb}t_s^2(2t_s + 3t_b) + E_{Gb}t_G^2(2t_G - 3t_b)}{3[E_{sb}t_s^2(c - \alpha_s\Delta T) - E_{Gb}t_G^2(c - \alpha_G\Delta T)]}$$

$$c = \frac{(E_{sb}t_s\alpha_s + E_{Gb}t_G\alpha_G)\Delta T}{E_{sb}t_s + E_{Gb}t_G}$$

$$t_b = \frac{E_{Gb}t_G^2 - E_{sb}t_s^2}{2(E_{sb}t_sE_{Gb}t_G)}$$

where t is the thickness of the silicon wafer. The letter S refers to the silicon material, whereas G corresponds to the sapphire.

$$E_{sb} = \frac{E_S}{1 - \nu_S}$$

and

$$E_{Gb} = \frac{E_F}{1 - \nu_F}$$

where E and ν corresponds to the Young modulus, respectively the Poisson ration.

Thus, considering the properties of the respective materials, the bow is calculated for both sapphire and glass bonded structure, and summarized in Table 1.

Table 1.

	Si bonded with sapphire	Si bonded with glass
Temperature of chuck	150°C	325°C
Bow	2300 μm	500 μm

The bow could be measured in-situ by the laser equipment (the so-called z-map) for the case of the 200 mm Si bonded with glass, as plotted in Fig. 10. The bow on the chuck at 325°C is measured equal to 500 μm , which is a bit smaller than the theoretical model. It is worth noting that the z-map could not be measured in the case of Si bonded with sapphire due to the small diameter of the samples (100mm).

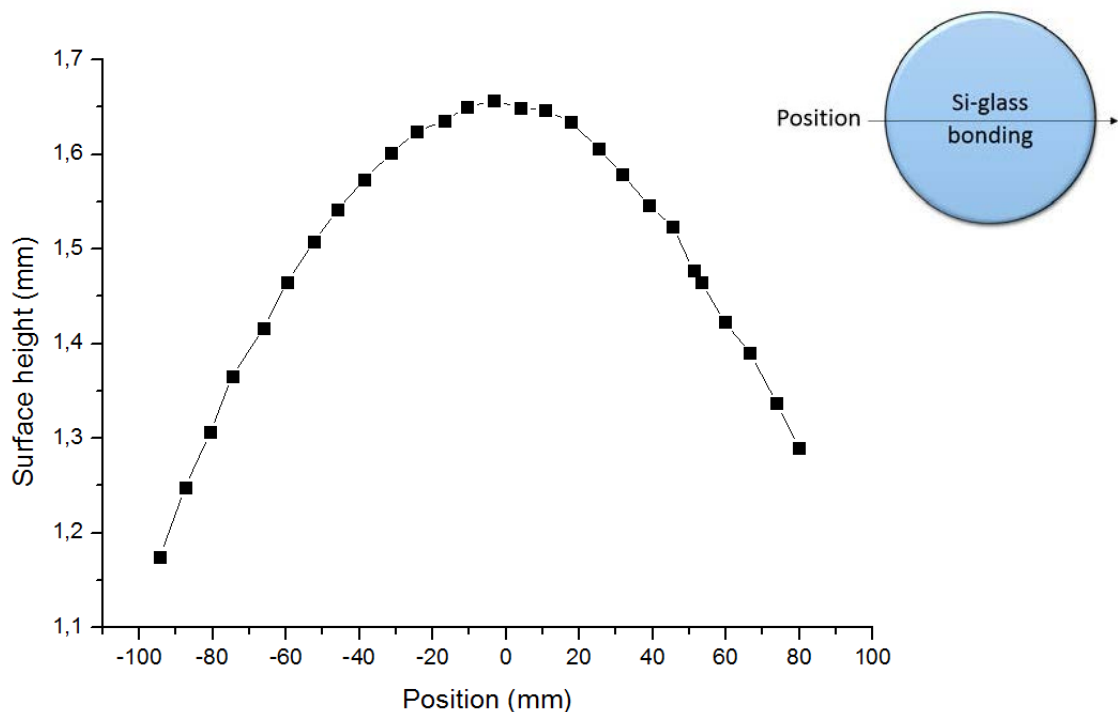


Figure 10: Height profile measured by the laser equipment in the middle of the Si bonded with the glass wafer (diameter of 200 mm).

2.1.3. Optical model

The structure of the samples is complex on the optical point of view as the layer of thermal oxide (400nm) at the interface between the sapphire/glass and the Si induces optical interferences. This requires the use of a multilayer interference model, based on the Maxwell equations establishing a continuity condition for the electric and magnetic field at the interface between two media. Thus, the multilayer structure can be represented by a transmission matrix which is the product of the matrix of each layer. An example of such a multilayer structure is given on Fig. 11. with a configuration of N th layer with n_N and d_N being the real part of the refraction index and the thickness of the N th layer, respectively.

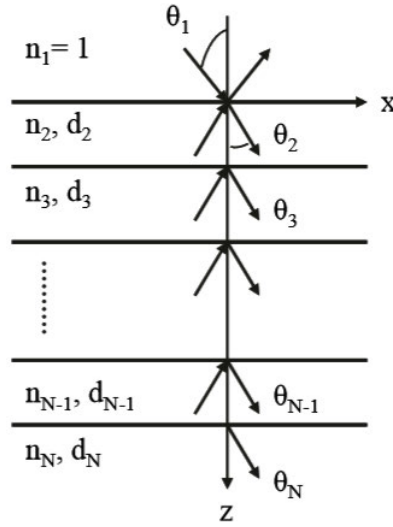


Figure 11: Schematic representation of the multilayer model [6].

For this structure, considering that the electric field E_j (in a layer j) is the sum of the optical waves from superior and inferior layers in z direction, we have for $j = 2, 3, \dots, N$:

$$E_j = (A_j * e^{i(z-z_{j-1})*v_{jz}} + B_j * e^{-i(z-z_{j-1})*v_{jz}}) * e^{(iv_x - i\omega t)}$$

with A_j and B_j being the amplitudes of the z_j waves from the layers j , ω the angular frequency and v_x and v_{jz} the parallel and perpendicular components of the wave vector. The resulting matrix can be converted in the coefficients R (reflection) and T (transmission) [6].

The Rad-Pro software allows to do this conversion, for different angle of incidence and different multilayer systems. The results in terms of reflectivity are plotted on Fig. 12, for systems composed of a wafer of sapphire (resp. of glass in Fig. 12 b)), a layer of 400 nm of SiO_2 and a wafer of Si.

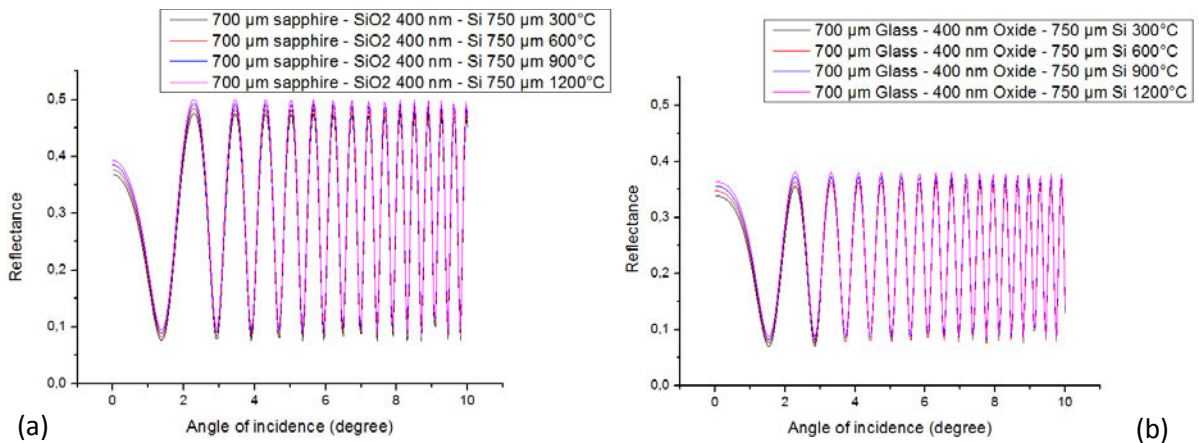


Figure 12: Reflectivity of the systems of Si bonded with sapphire (a) and Si bonded with glass (b).

It appears that the angle of incidence has a huge influence on the reflectance of the structure and so on the absorbed power. As a consequence, it can be deduced that the both initial and induced bow of the structure will affect the homogeneity of power as a function of the position over the sample.

Nevertheless, a vertical incidence angle will be considered for the numerical modelling, as an estimation. The results for an incident angle equal to zero are plotted in Fig. 13 as a function of temperature.

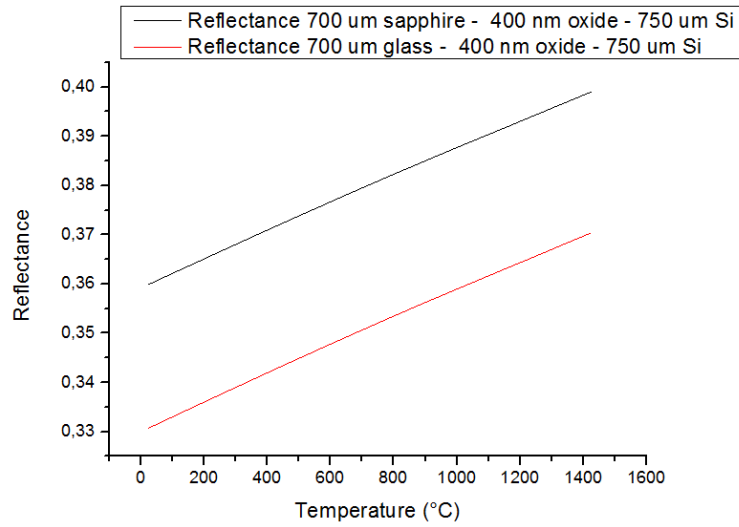


Figure 13: Calculation of the reflectance as a function of temperature for a system of glass/sapphire bonded with Si.

An example of annealing of the sample composed of Si bonded with glass is given in Fig. 14, for a fluence of 0.62 GWm^{-2} and a scanning speed of 150 mms^{-1} . The plotted temperature corresponds to a depth of $0.8 \text{ }\mu\text{m}$, i.e. the R_p of the implantation zone for the corresponding energy of 76 keV.

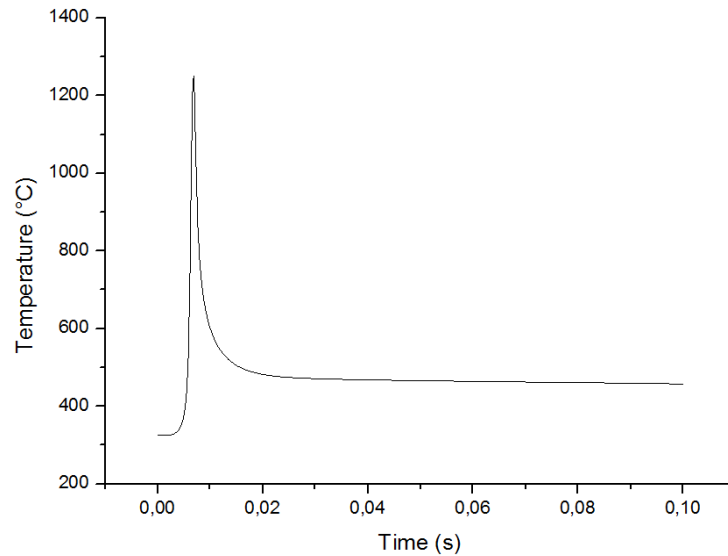


Figure 14: Numerical modelling of the temperature in the implanted zone of Si during the laser annealing with a fluence of 0.62 GWm^{-2} in the Si/glass bonded pair.

2.2 Application of the numerical modelling to the annealing of implanted structures

2.2.1 Comparison with pyrometer characterization

The temperature recorded by the pyrometer is defined by the following relation [6]:

$$T_c = \frac{0.014388}{\lambda \ln \left(\frac{3.74 * 10^{-16} S_f * \varepsilon}{\lambda^5 * R_p} \right) + 1}$$

where S_f is a calibration factor, normally obtained by determining the melting point of the material to anneal, R_p is the photocurrent, λ is the wavelength of the pyrometer and ε is the emissivity of the material.

It is worth noting that the usual procedure for the calibration of the pyrometer, which consists in determining the melting point of Si (1410°C) by progressively increasing the laser power, could not be achieved. Indeed, the diameter of the samples (100 mm or 200 mm) is lower than the 300 mm wafers usually treated with this equipment. The power ramp of the laser is not fast enough to reach the melting point of Si with 100 mm or 200 mm sample diameter. Thus, the temperature can only be estimated.

The temperature recorded in-situ by the pyrometer is compared to the numerical modelling, on Fig. 15. The temperature obtained by modelling gives a good fitting for temperature above 1200°C but progressively drifts for lower temperature. The explanation of this drift remains controversial for us. The optical model and the effect of the deformed sample surface during the laser scan should be studied more in depth.

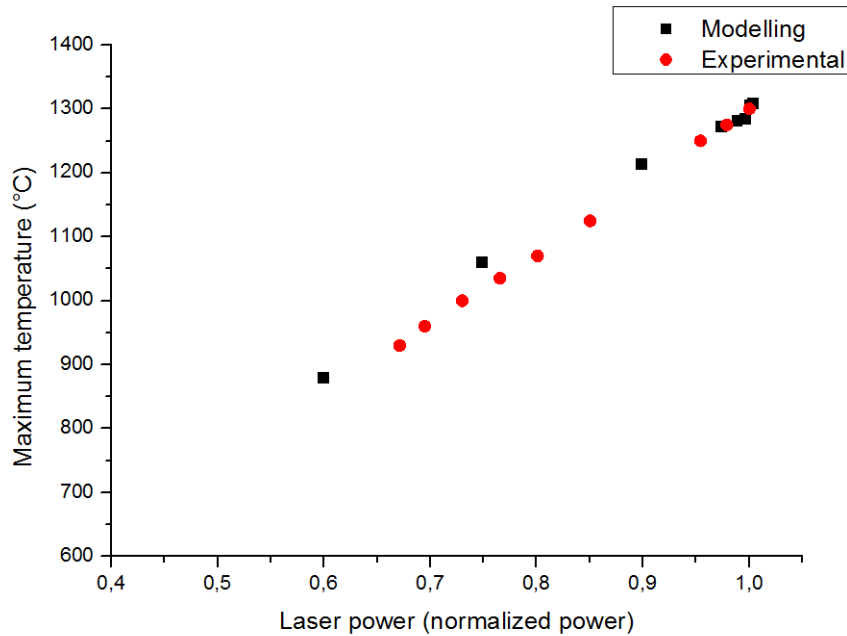


Figure 15: Comparison of the temperature obtained by numerical calculations and the temperature recorded by the pyrometer in-situ for the samples of sapphire bonded with Si. The reflectivity taken here for the numerical model corresponds to a vertical angle of incidence (i.e. $R=0.35$).

2.2.2 Modelling of the thermal stress within the structure

At this stage, it is necessary to analyse the stress generated within the bonded structure during the laser scan. The stress within the heated zone is modeled with the help of Comsol Multiphysics software, by considering the structure bonded at room temperature, i.e. an absence of stress at this temperature. The Fig. shows the maps of Von Mises stress within the structure for both SOS and SOG configuration.

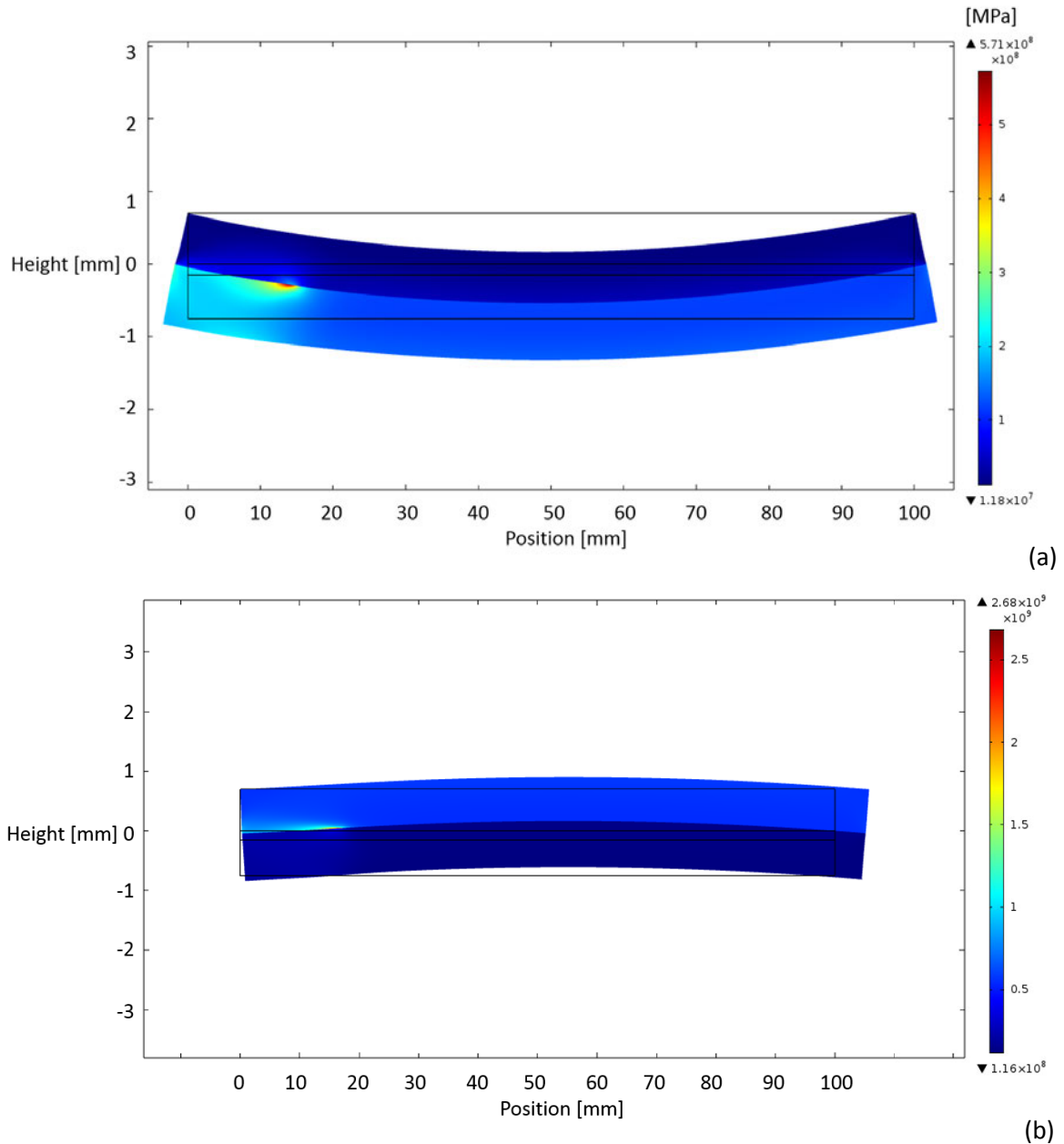


Figure 16: $0.62 \text{ GW} \cdot \text{m}^{-2}$ at 150 mms^{-1} for SOG structure. The maximum values of Von Mises stress are 571MPa in case of Si and in case of glass (a), $0.80 \text{ GW} \cdot \text{m}^{-2}$ at 150 mms^{-1} for SOS structure (b). The maximum values of Von Mises stress are 571MPa in case of Si and 2.68 GPa in case of sapphire.

It is worth noting that the Von Mises analysis of Fig. 16 (b) returns a value superior to the tensile strength of sapphire, which is a synonym of sample breaking. The values of Von Mises for different conditions of annealing are compared to the UTS for both sapphire and glass presented in Fig. 17 with

the mechanical properties of the respective material summarized in Table 2. It shows that the SOS structure is more likely to break during the laser annealing than the SOG structure. This numerical analysis will be profitably put into regard with the statistics of breaking of samples further in the chapter.

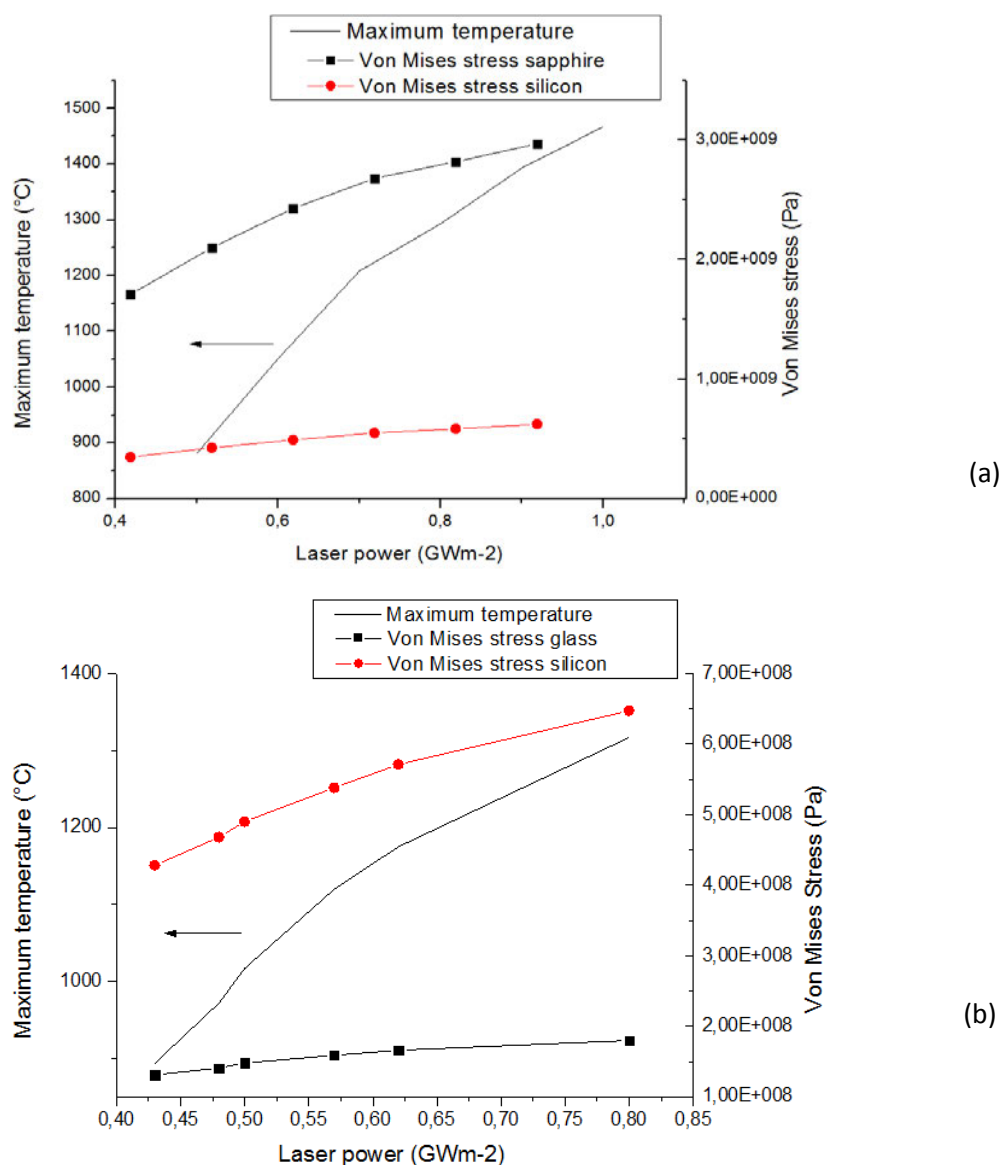


Figure 17: Dependence of calculated maximal Von Mises stress within the structure for Si bonded with sapphire (a) and Si bonded with glass (b).

Table 2. Mechanical properties of Si, sapphire and glass used for the study.

Material	Si	Sapphire [SI 18]	Corning Glass (from supplier)
Young modulus	179 GPa	335 GPa	73.6 GPa
Yield strength	7 GPa	1.9 GPa	280 MPa (borosilicate glass)
Melting temperature [°C]	1414°C	2050°C	1293°C (working point)

2.2.3 Modelling of out-diffusion during the laser annealing

The model of diffusion of implanted H developed in the previous chapter will be applied on the thermal modelling of the laser irradiation of the bonded system. Thus, the out-diffusion from the implantation zone during the annealing can be determined. The diffusion of bonded H we introduced in the chapter 4 (section 4.2) is used as the diffusion coefficient, i.e.:

$$D_H = D_0 \left(\frac{n_{bond}}{n_{free}} \right) \exp \left(\frac{1.46 \text{ eV}}{k_B T} \right)$$

The modelled implantation profiles as a function of different laser annealing conditions are plotted on Fig. 18.

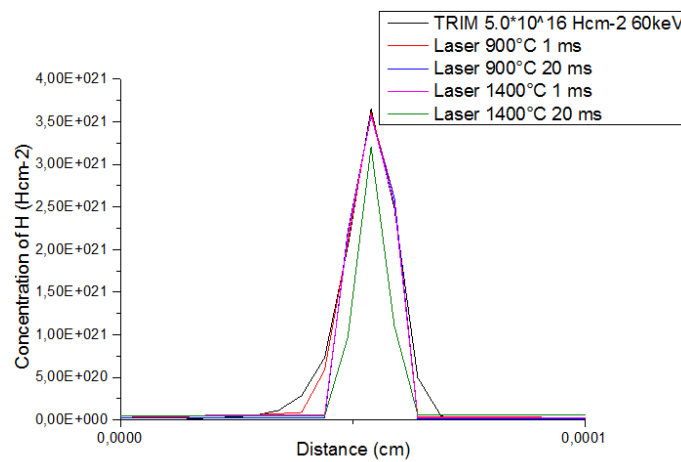


Figure 18: Numerical modelling of the evolution of the H concentration in the implanted Si under the annealing of the ms laser.

Table 3. Summary of the out-diffusion of H as a function of the laser annealing conditions of the study.

Laser annealing conditions	Remaining H [Hcm ⁻²]	Out-diffusion of H [Hcm ⁻²]	Theoretical minimal dose of splitting for the annealing temperature [Hcm ⁻²]
As-implanted	5.0*10 ¹⁶	0	-
900°C 1 ms	4.9*10 ¹⁶	9.8*10 ¹⁴	3.30*10 ¹⁶
900°C 20 ms	4.54*10 ¹⁶	4.61*10 ¹⁵	
1400°C 1 ms	4.67*10 ¹⁶	3.30*10 ¹⁵	2.31*10 ¹⁶
1400°C 20 ms	3.90*10 ¹⁶	1.10*10 ¹⁶	

Table 3 shows the calculated amount of implanted hydrogen outdiffused during laser ms annealing. It appears clearly that the amount of out-diffused H during the various annealing conditions should not affect the possibility of splitting, as the remaining dose after all the modelled annealing is still far superior to the minimum threshold dose required for splitting.

2.3 Design of experiment for the characterization of the splitting kinetics by laser annealing

In order to simplify the experimental plan in terms of time-temperature conditions to be explored, we propose to establish boundaries of splitting probability based on the results from the previous chapter. We have shown that Arrhenius law describing splitting kinetic at temperatures lower than 600°C is very likely to be maintained at higher temperature. Moreover, the numerical study of the laser beam annealing shows a very limited out-diffusion from the implantation zone.

Thus, we propose to extrapolate the splitting kinetics characterized for the different implantation doses considered in the previous chapter (section 2.2.2), as figured on the Fig. 19. Therefore, we can define a design of experiment by taking the two boundaries formed by the extrapolation of splitting kinetics of $5.0 \cdot 10^{16} \text{ Hcm}^{-2}$ and $1.0 \cdot 10^{17} \text{ Hcm}^{-2}$ samples determined in the chapter 4 (section 2.2.2), and considering the laser possibilities in terms of temperature and residence time. The results form a square, as represented on Fig. 19.

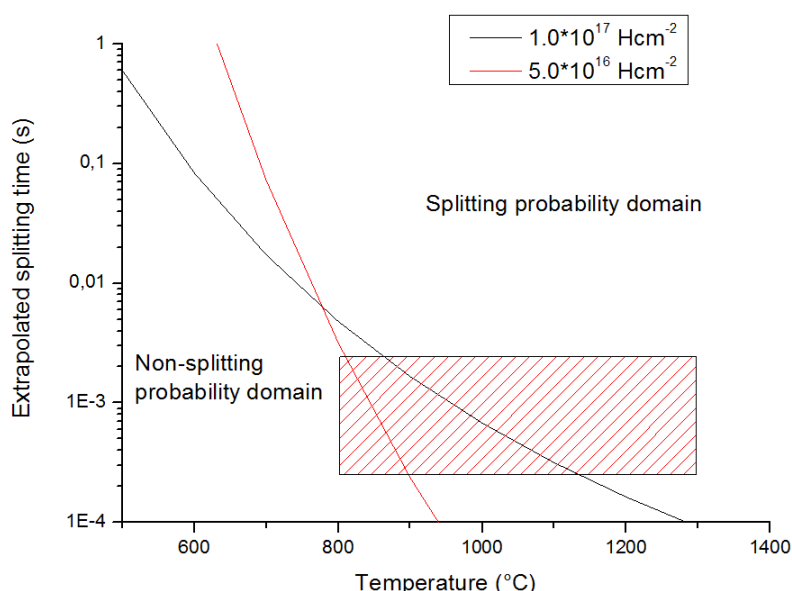


Figure 19: Representation of the splitting probability domain based on the results of the previous chapter. The hashed square corresponds to the design of experiments chosen for this study.

As the maximum time of residence of the laser is 0.5 ms, the annealing is proceeded by multiple laser scans, each scan being followed by a visual inspection, to detect the potential splitting occurrence.

It can be noticed that above 800°C, the splitting duration for $5.0 \cdot 10^{16} \text{ Hcm}^{-2}$ samples is shorter than the one for $1.0 \cdot 10^{17} \text{ Hcm}^{-2}$, which is opposite to the observations of splitting at lower temperature. This aspect will be investigated with the Silicon-On-Glass samples, with the two proposed doses ($5.0 \cdot 10^{16} \text{ Hcm}^{-2}$ and $1.0 \cdot 10^{17} \text{ Hcm}^{-2}$).

3. Experimental annealing of the Silicon-On-Sapphire samples

3.1 Experimental observations

It is worth noting that a high number of samples break during the annealing, as shown by the Fig. 20 representing the laser chamber after annealing.

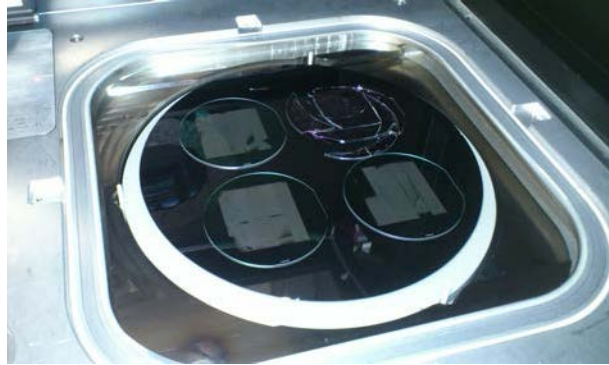


Figure 20: Picture of the laser chamber right after the annealing. The upper sample at the right side has been fractured during the annealing.

The Fig. 21 summarizes the conditions of samples breakage, for Si bonded with sapphire, as a function of the annealing conditions.

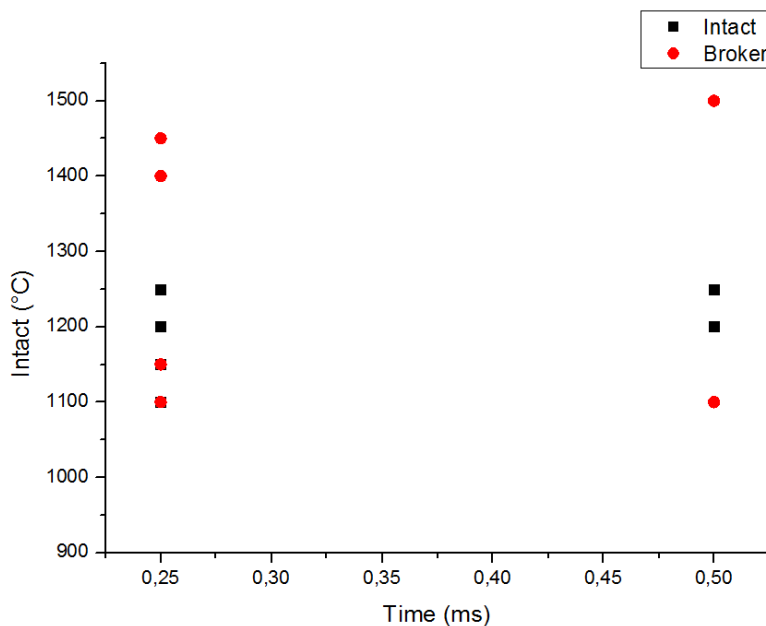


Figure 21: Summary of the fracture of samples of silicon bonded with sapphire during the laser annealing. Two annealing durations are tested, 0.25 ms and 0.5 ms.

The stress analysis presented in the previous paragraph is fully coherent with this experimental observation, in a sense that the von Mises stress is very close to the yield strength of sapphire. Furthermore, almost no fracture is observed in case of samples of silicon bonded with glass, as we will see later (also in good agreement with the stress analysis).

3.2 Blistering / non blistering domain determination ($4.0 \cdot 10^{16} \text{Hcm}^{-2}$, $5.0 \cdot 10^{16} \text{Hcm}^{-2}$, $1.0 \cdot 10^{17} \text{Hcm}^{-2}$, $1.2 \cdot 10^{17} \text{Hcm}^{-2}$)

Similarly than in the beginning of the chapter, we propose to focus first on the observation of blisters at the surface of the sample (see Fig. 22). These blisters are observed with many samples, and originate from a de-bonding of the structure, possibly helped by the sample breakage. Despite this mechanism is initially not expected as the samples are not supposed to de-bond, its observation provides indication on the possible kinetics of splitting.

The Fig. 22 a) shows the limit of the blistering zone, corresponding to the boundary of the scanned zone, for a $6.0 \cdot 10^{16} \text{Hcm}^{-2}$ sample, annealed at 1255°C for 0.25 ms. In this case, the observation is proceeded on the implanted silicon wafer after de-bonding. It is worth noting that the corresponding tops of the blisters can be observed on the sapphire, initially bonded with the same implanted silicon wafer.

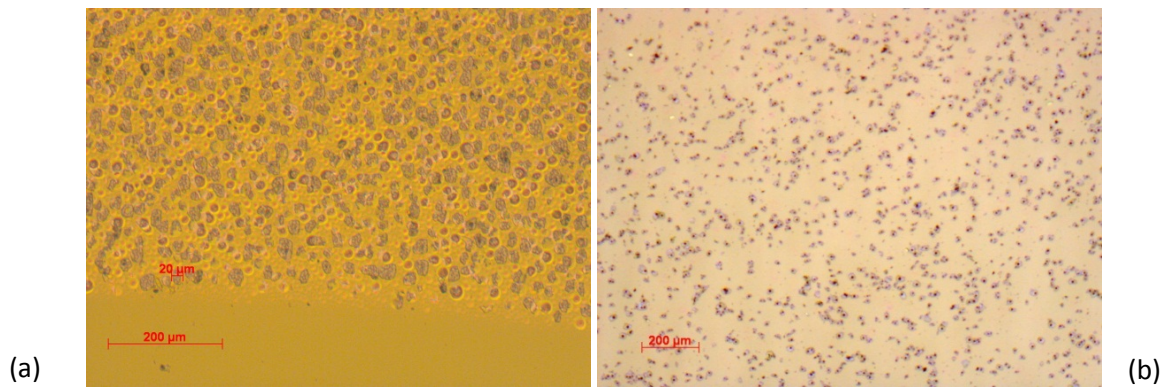


Figure 22: Images by optical microscopy of blisters on the silicon wafer implanted with a dose of $6.0 \cdot 10^{16} \text{Hcm}^{-2}$ after annealing at 1255°C for 0.25 ms (a), blister tops on the sapphire wafer initially bonded with the silicon wafer implanted with a dose of $6.0 \cdot 10^{16} \text{Hcm}^{-2}$ after annealing at 1250°C for 0.25 ms (b)

The Fig. 23 shows another unexpected effect observed on several samples with a partial debonding. It consists in an alternation of blisters bands, separated by non-blistered zones. The structure shows a progressively decreasing inter-distance between zones.

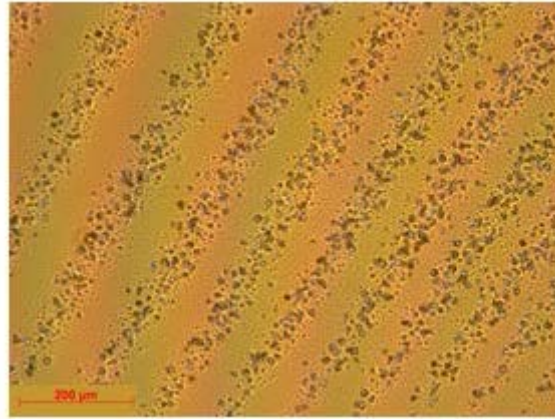


Figure 23: Image by optical microscopy of alternation of blisters on a $6.0 \cdot 10^{16} \text{ Hcm}^{-2}$ sample after annealing at 920°C for 0.5 ms.

This patterns can be explained by the evolution of reflectivity with the incident angle (calculated in Fig. 12). Nevertheless, the air blade resulting from the debonding of the sample also modifies the reflectivity of the system.

This effect can even be observed visually on some samples after partial debonding, the Fig. 24 gives an example of such debonding after the fracture of a part of the Si wafer. Thus, it can be postulated that the deposited laser power varies with the reflectance, bringing the implanted material to the blistering on limited areas.

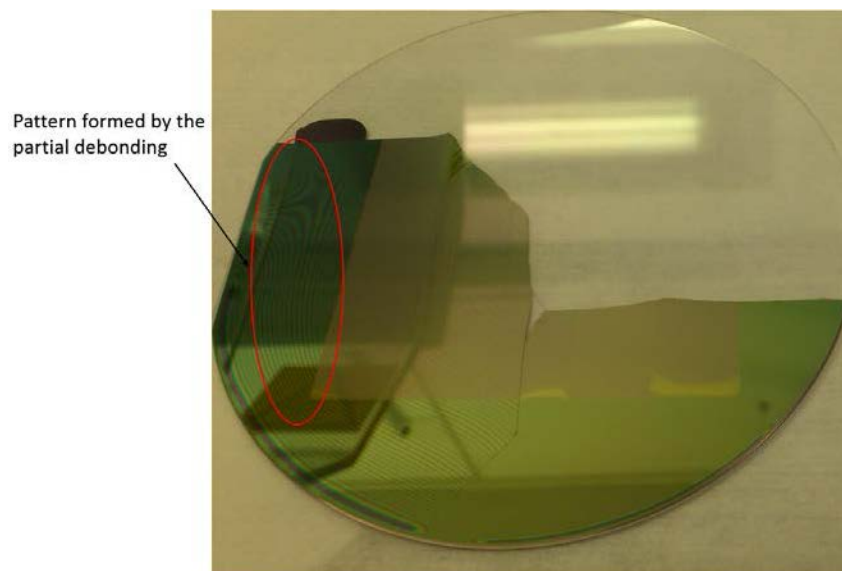
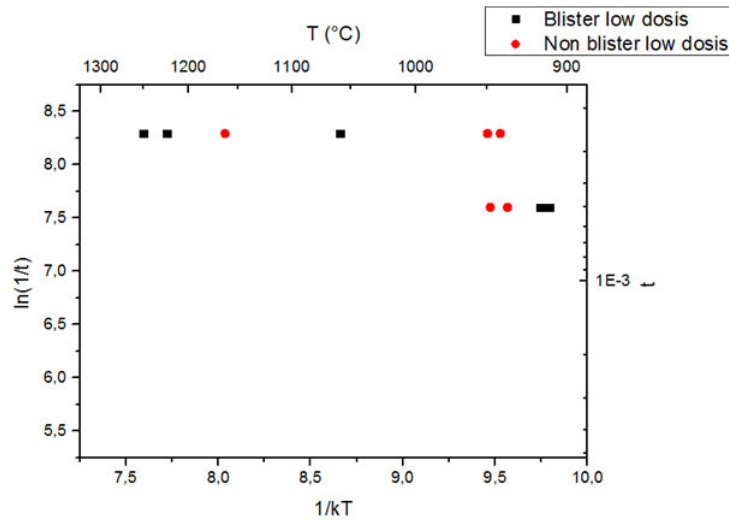
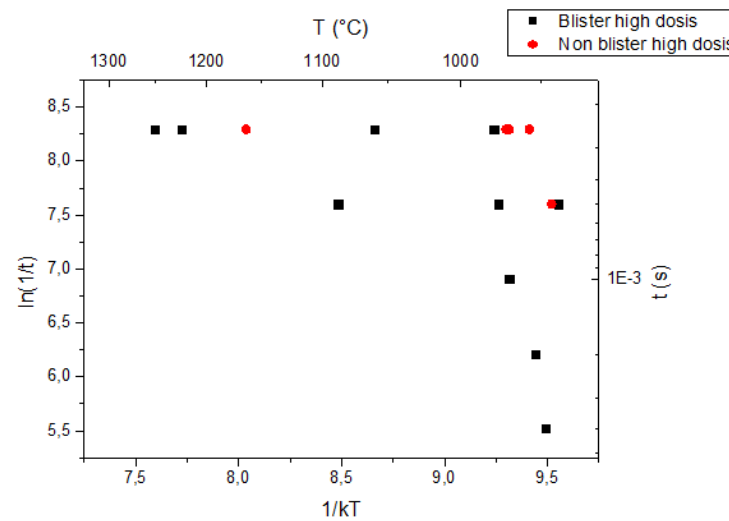


Figure 24: Optical patterns observed on a 100 mm sapphire bonded with Si after fracture of the Si wafer and partial debonding.

The results of blistering kinetics for SOS samples are summarized on Fig. 25. The “low dose” denomination corresponds to the results for $4.0 \cdot 10^{16} \text{ Hcm}^{-2}$, $5.0 \cdot 10^{16} \text{ Hcm}^{-2}$ and $6.0 \cdot 10^{16} \text{ Hcm}^{-2}$ samples, whereas the “high dose” denomination corresponds to the results for $1.0 \cdot 10^{17} \text{ Hcm}^{-2}$ and $1.2 \cdot 10^{17} \text{ Hcm}^{-2}$.



(a)



(b)

Figure 25: Results of blistering/non blistering for low dose samples ($4.0 \cdot 10^{16} \text{ Hcm}^{-2}$, $5.0 \cdot 10^{16} \text{ Hcm}^{-2}$ and $6.0 \cdot 10^{16} \text{ Hcm}^{-2}$) a). Results of blistering/non blistering for high dose samples ($1.0 \cdot 10^{17} \text{ Hcm}^{-2}$, $1.2 \cdot 10^{17} \text{ Hcm}^{-2}$) b).

It can be observed that the separation between the blistering and non-blistering conditions defines a trend which can be compared with the blistering characterization for temperature inferior to 600°C on Fig. 26. Thus, it is clear that the kinetics observed at low temperature on the heating plate gives a good approximation for the kinetics of blistering by laser annealing.

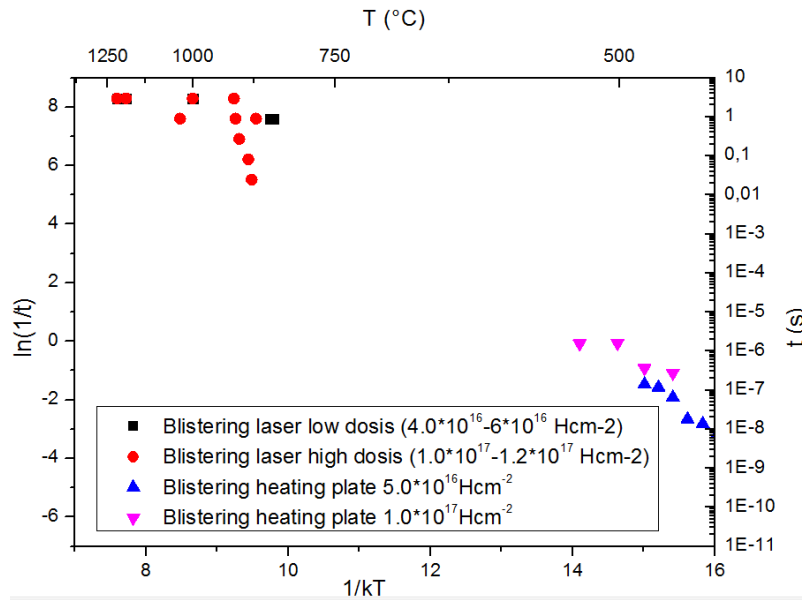


Figure 26: Comparison of the blistering kinetics for SOS samples obtained by laser annealing with Si blistering kinetics measured using a heating plate.

The Fig. 26 shows that the time for blistering is shorter for low dose samples than for high implantation dose. This observation is contradictory with literature [7] and with the characterization of blistering at lower temperature on the heating plate. Indeed, the defect growth leading to blistering (or to splitting) is supposed to be faster with higher dose implantation. On the other hand, the extrapolation of the splitting time in Fig. 19 shows that above 950°C, the splitting time is shorter for $5.0 \cdot 10^{16} \text{ Hcm}^{-2}$ than for $1.0 \cdot 10^{17} \text{ Hcm}^{-2}$ samples. Thus, the analysis of splitting with SOS and SOG will provide further elements of comprehension to conclude on the kinetics of splitting in this range of temperature.

3.3 Splitting/non-splitting domain determination SOS ($4.0 \cdot 10^{16} \text{ Hcm}^{-2}$, $5.0 \cdot 10^{16} \text{ Hcm}^{-2}$, $1.0 \cdot 10^{17} \text{ Hcm}^{-2}$, $1.2 \cdot 10^{17} \text{ Hcm}^{-2}$)

The results of splitting for the SOS structure are summarized on Fig. 27, with a comparison with the kinetics of splitting as characterized at low temperature. Similarly than for blistering, it appears that the splitting occurs faster for low dose samples. Additionally, it is worth noting that the kinetics of splitting by laser annealing follows the trend as defined below 600°C.

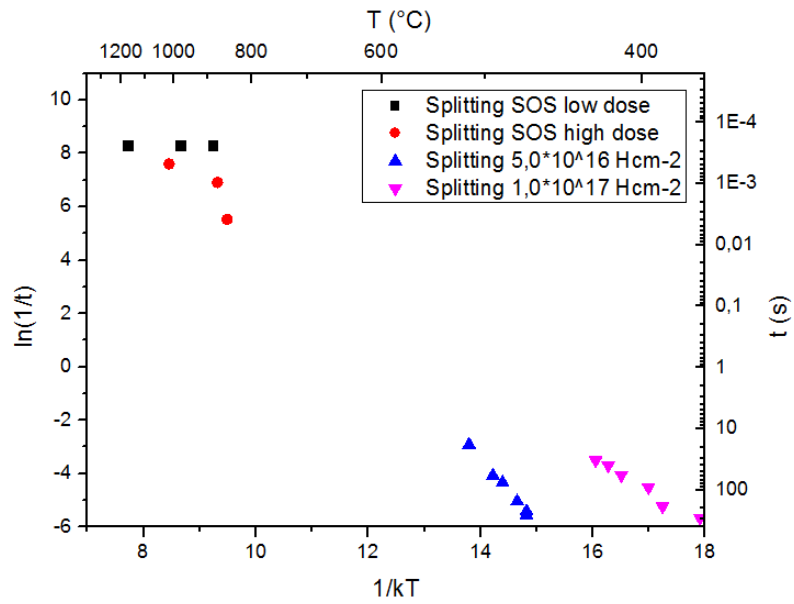


Figure 27: Summary of the kinetics of splitting for SOS samples ($4.0 \cdot 10^{16} \text{ Hcm}^{-2}$ to $1.2 \cdot 10^{17} \text{ Hcm}^{-2}$) and comparison with splitting kinetics for $5.0 \cdot 10^{16} \text{ Hcm}^{-2}$ and $1.0 \cdot 10^{17} \text{ Hcm}^{-2}$ samples at low temperature ($T < 600^\circ\text{C}$).

This observation will be compared with the following study presenting the results of splitting kinetics for SOG samples.

4. Splitting/non-splitting domain determination for SOG samples ($4.0 \cdot 10^{16} \text{ Hcm}^{-2}$, $5.0 \cdot 10^{16} \text{ Hcm}^{-2}$, $1.0 \cdot 10^{17} \text{ Hcm}^{-2}$, $1.2 \cdot 10^{17} \text{ Hcm}^{-2}$)

4.1. General observations

4.1.1. Inhomogeneity of annealing

It can be interestingly noticed that during the calibration of the laser using a reference sample implanted with a dose of $4.0 \cdot 10^{16} \text{ Hcm}^{-2}$, the annealed zones (the brown zones on Fig. 28) show inhomogeneous transfer. Thus, it appears that some stripes show zones of non-transfer in the middle of the sample (e.g. Fig. 28 c) and f)).

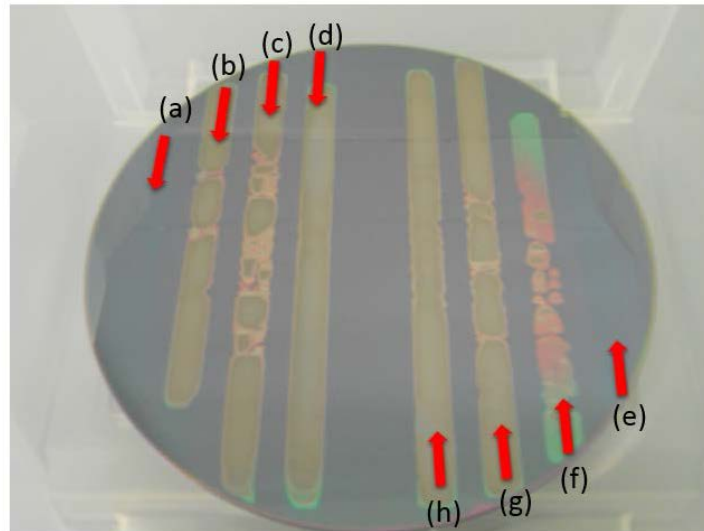


Figure 28: Picture of the wafer used for the calibration of the focus of the laser head. The sample is implanted with $4.0 \cdot 10^{16} \text{ Hcm}^{-2}$ at 76 keV. The height of the laser head is varied from 0.675 mm (a), 0.65 mm (b), 0.625 mm (c), 0.6 mm (d), on the left side where the scanning direction is from top to the bottom. On the right side, where the scanning direction is from the bottom to the top, the height of the laser head is varied from 0.575 mm (e), 0.55 mm (f), 0.525 mm (g), 0.5 mm (h).

This observation proves that despite the laser is supposed to have a parallel beam, there is an issue with the beam focus.

This observation is fully coherent with the acoustic microscopy image shown in Fig. 29, where the splitting occurs only at the border of the sample. It is worth noting that the diameter of the transferred zones of SOG increases continuously when getting closer to the border of the sample (Fig. 29 b)).

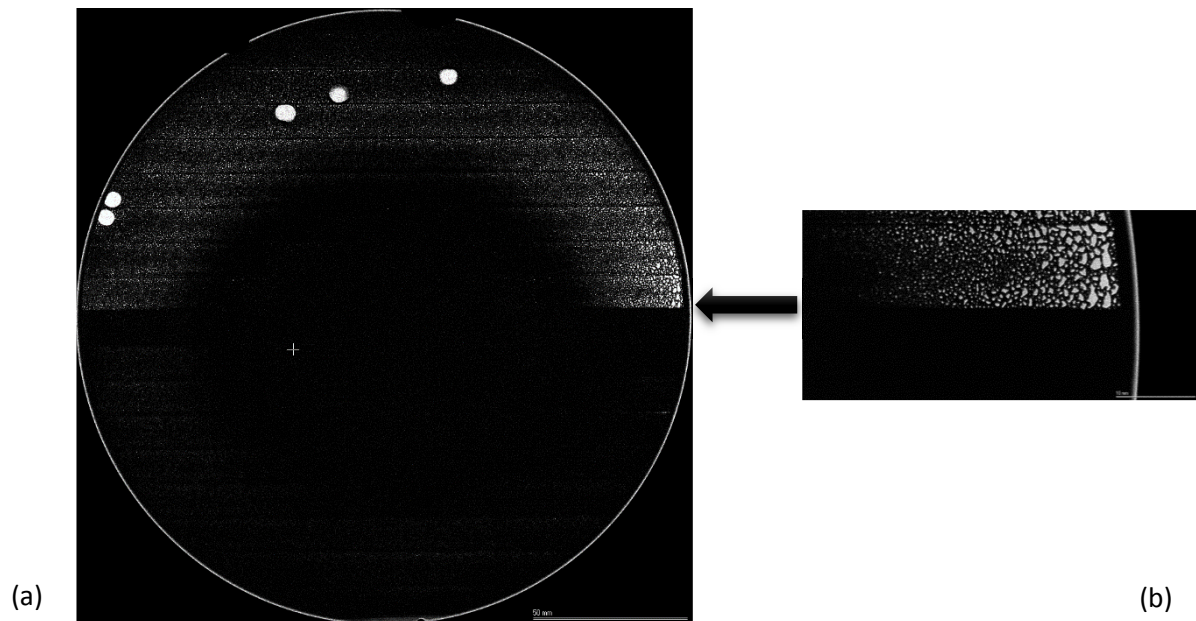


Figure 29: Image by SAM of the SOG $1.0 \cdot 10^{17} \text{ Hcm}^{-2}$ sample after laser annealing at 1000°C for 1 ms (a), detail of the edge (b) .

Both observations are coherent with the high bow of the bonded structure on the hot chuck of the laser annealing setup ($T = 300^\circ\text{C}$).

A thermal contribution due to the non-homogeneous initial temperature within the structure can explain this observation. Indeed, the concave-shape of the structure induces that the edges are slightly warmer than the bottom, being into contact with the hot chuck (see Fig. 8). Therefore, the optical absorption of silicon, increasing with temperature as expressed earlier, is supposed to be higher at the crown of the wafer. Additionally, the reflectivity variation being already mentioned also contributes to the non-homogeneity of the deposited power.

4.1.2. Fracture of samples of Glass bonded with Si

It is worth noting that most of silicon on glass samples were still intact after laser annealing (see Fig. 30). Only 1 SOG sample is broken (i.e. into several pieces) and 2 SOG samples have some cracks after laser annealing. On the contrary, very large number of si on sapphire samples were broken during laser treatment (see Fig. 21). Thus, it is clear that the integrity of SOG samples is more preserved than the one of SOS samples by laser annealing.

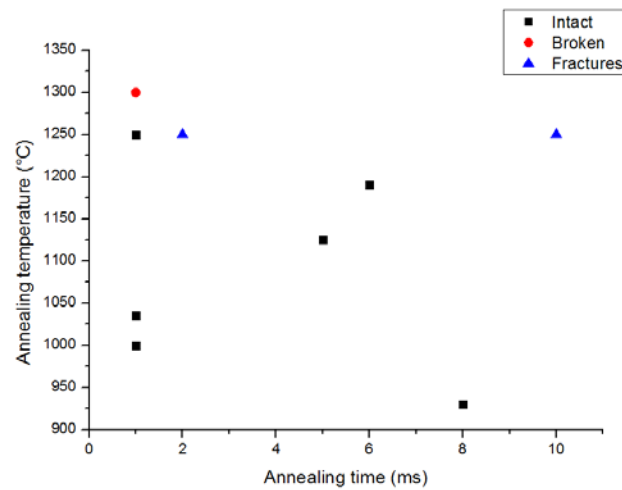


Figure 30: Summary of the fracture of samples of silicon bonded with sapphire during the laser annealing.

This observation is coherent with the numerical modelling of the induced stress within samples of SOS and SOG during the annealing, as presented in Fig. 17.

4.2 Characterization of splitting

The results of splitting for SOG structures are summarized on Fig. 31 for both $5.0 \cdot 10^{16} \text{Hcm}^{-2}$ and $1.0 \cdot 10^{17} \text{Hcm}^{-2}$ samples. It appears clearly that the kinetics of splitting is faster with $1.0 \cdot 10^{17} \text{Hcm}^{-2}$ dose of implantation, which is contradictory with the SOS results. On the other side, it is in agreement with the splitting time decreasing with the implantation dose, as characterized in chapter 4 and as presented in the literature.

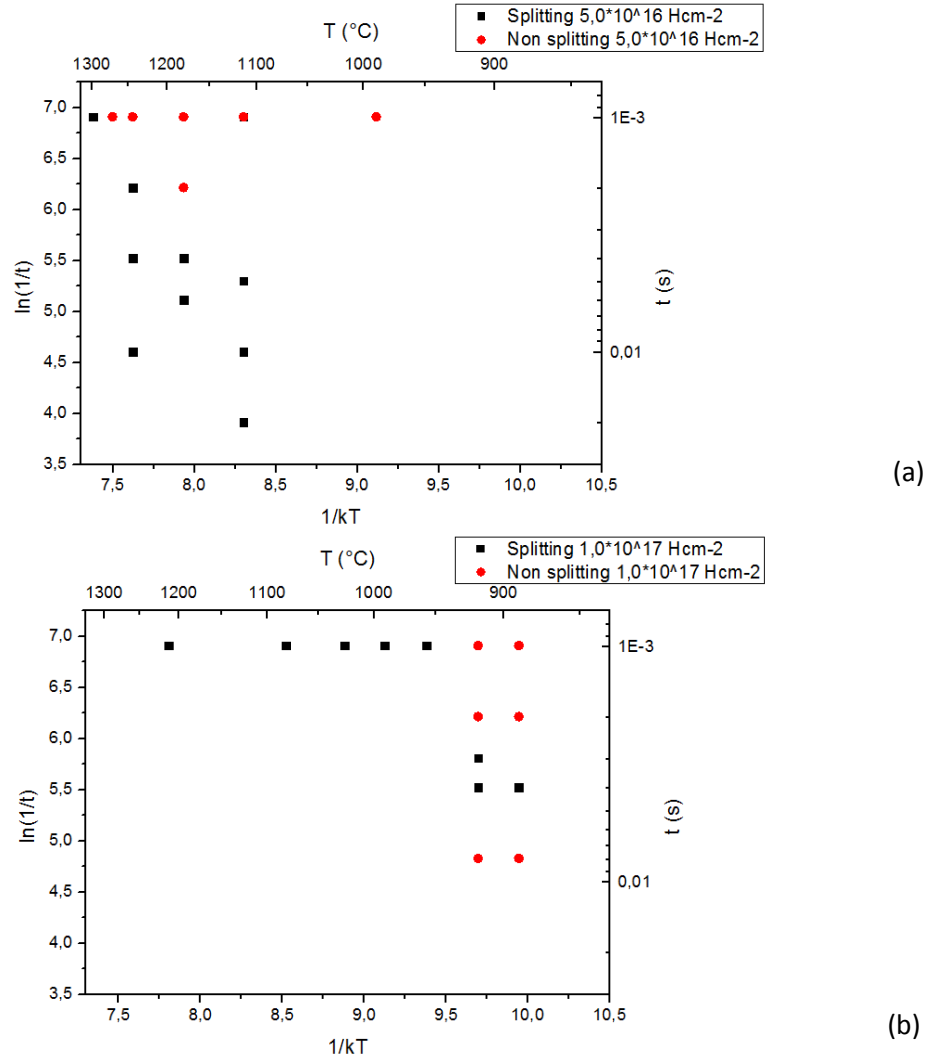


Figure 31: Results of splitting kinetics for SOG samples implanted with $5.0 \cdot 10^{16} \text{Hcm}^{-2}$ (a), and $1.0 \cdot 10^{17} \text{Hcm}^{-2}$ (b).

The Fig. 32 gives a summary of the splitting kinetics by laser annealing (for both SOS and SOG samples). Comparing results for SOS and SOG, it appears that kinetics are coherent for high dose of implantation, but not for low dose.

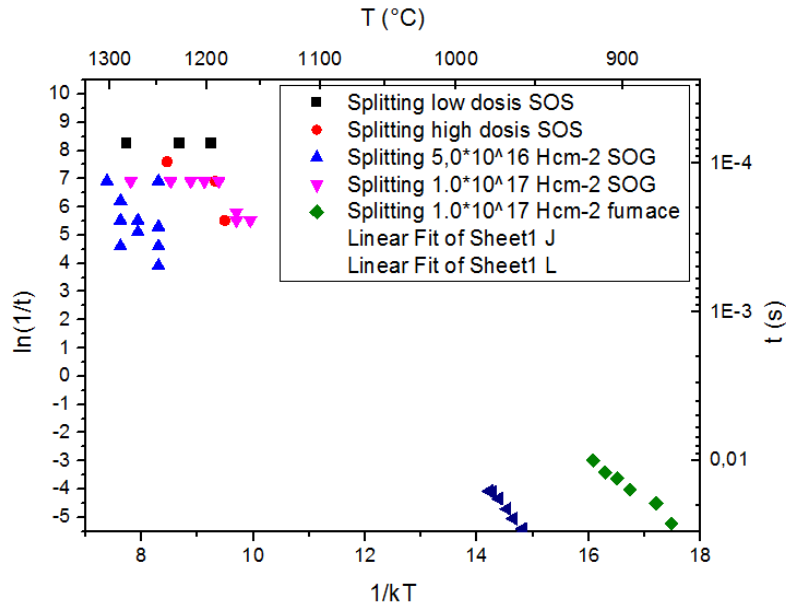


Figure 32: Summary of the kinetics of splitting for laser annealing and comparison with the kinetics obtained at low temperature for $5.0 \cdot 10^{16} \text{ Hcm}^{-2}$ and $1.0 \cdot 10^{17} \text{ Hcm}^{-2}$ samples.

As an intermediate conclusion, it appears clearly that the kinetics of splitting as defined in the previous chapter defines the trend of splitting time as a function of annealing temperature, as illustrated on the Arrhenius plot on Fig. 32. Nevertheless, we know now that the Arrhenius plot does not take into account the thermal ramp-up of the splitting annealing. Thus, in order to validate the splitting kinetics by laser annealing, the normalized thermal budget function will be calculated (similarly than in the chapter 4, section 2.2.3). Therefore, the temperature modelling of the laser annealing will be used to calculate the thermal budget.

Finally, we propose to establish the splitting model based on the SOG samples by laser annealing, as the number of characterization is higher than for SOS samples. The explanation of a faster splitting for lower implantation dose in case of SOS samples is not clear. An experimental error cannot be excluded as the cause of this observation.

4.3 Validation of the splitting model

4.3.1 Thermal budget calculations

As we have seen in the previous chapter, the splitting model developed is based on the effective diffusion of H within the implanted material in order to explain the change of activation energy of splitting above 550-600°C. Nevertheless, the numerical calculations of hydrogen diffusion during the laser annealing (fig x) realized at the beginning of this study tend to show that only a very small amount of H is out-diffused during the laser scanning. In this case, the splitting kinetics should follow single Arrhenius line. But, this would lead to an intersection of the curves for the low and high dose samples, what is contradictory with both theory and experimental observations made for glass on silicon samples.

Thus, we propose to calculate the normalized thermal budget of splitting σ_t , for the SOG samples using calculated temperature time dependence (Fig 14) calibrated by pyrometer measurements. As a reminder:

$$\sigma_T = \int \frac{1}{\tau(T(t))} dt$$

where τ is the characteristic time of splitting as defined by the Arrhenius law, expressed by:

$$\tau = \tau_0 * \exp\left(\frac{-E_a}{k_B T}\right)$$

with τ_0 being an fixed parameter.

The two hypothesis of splitting kinetics proposed in the previous chapter are considered again. The first hypothesis is a continuation of the splitting kinetics as defined at low temperature. The second hypothesis is a splitting kinetics defined by the diffusion of free H. We also propose another hypothesis with a splitting kinetics defined by the diffusion of bonded H. The different parameters used for the calculations are listed in Table 4.

We have seen that the activation energy of the diffusion of bonded H is a fixed parameter, determined by the dominant defects in the implantation zone. Thus, it is worth noting that the ratio of $H_{\text{bonded}}/H_{\text{free}}$ logically acts here as the fitting variable, as we have seen that this ratio depends on the H concentration (depending itself on the implantation dose). This ratio is found in the splitting coordinate coefficient, also mentioned in Table 4.

Table 4. Summary of the parameters used for the calculations of the thermal budget using the numerical modelling of the laser heating.

Dose of implantation [Hcm^{-2}] <i>Hypothesis</i>	Activation energy [eV]	Splitting coordinate coefficient	Ratio of $H_{\text{bonded}}/H_{\text{free}}$ (fitting parameter)
$5.0 \cdot 10^{16}$			
Hyp.1 Low temperature kinetics	2.82	36.2	-
Hyp.2 Diffusion of free H	0.49	17.8	-
Hyp.3 Diffusion of bonded H	1.46	17	2
$1.0 \cdot 10^{17}$			
Hyp.1 Low temperature kinetics	1.15	17.8	-
Hyp.2 Diffusion of free H	0.49	17.8	-
Hyp.3 Diffusion of bonded H	1.46	20	0.1

The results in terms of thermal budget are first presented for the $5.0 \cdot 10^{16} \text{ Hcm}^{-2}$ samples (see on Fig. 33). This results should be compared to the similar calculations for temperature range below 700C presented in Chapter 4, section 2.2.3. As a reminder, the normalized value of thermal budget equal to one signifies good agreement between proposed model and experimental results.

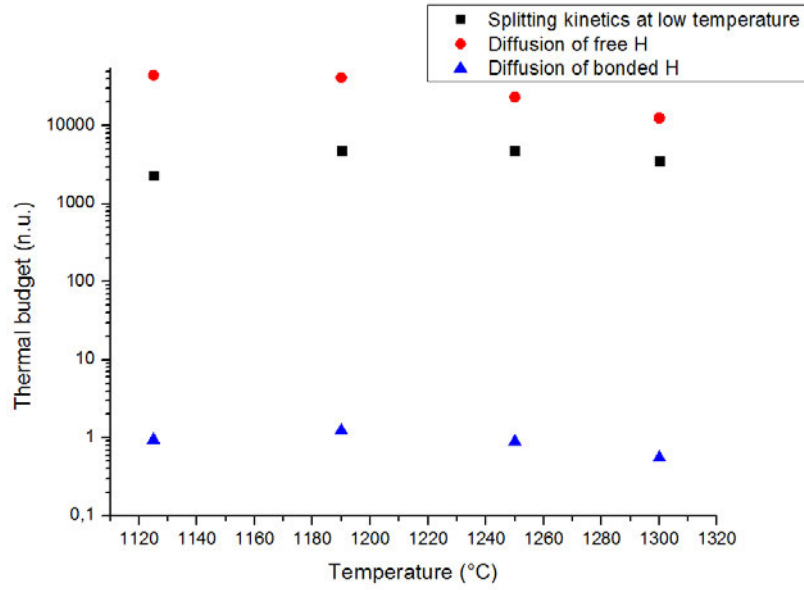


Figure 33: Plot of the thermal budget calculated for the $5.0 \cdot 10^{16} \text{ Hcm}^{-2}$ samples.

Here, it is clear that the good fit is obtained by taking the diffusion of bonded H (i.e. with an activation energy of 1.46 eV, very different from the splitting activation energy obtained at low temperature, 2.815eV).

Similarly, the best fit for the $1.0 \cdot 10^{17} \text{ Hcm}^{-2}$ samples is obtained with the same diffusion of bonded H (as illustrated on Fig. 34), but considering a different ratio of $H_{\text{bonded}}/H_{\text{free}}$. We will go back on this ratio later.

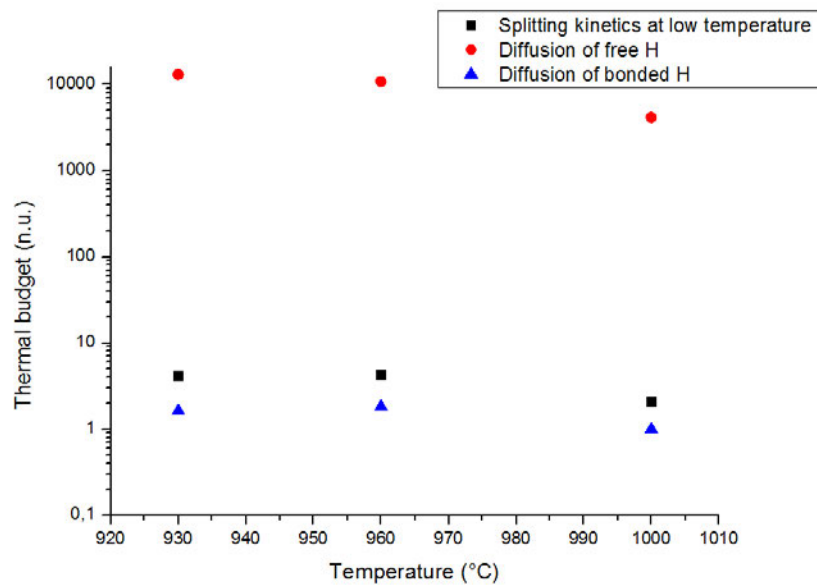


Figure 34: Plot of the thermal budget calculated for the $1.0 \cdot 10^{17} \text{ Hcm}^{-2}$ samples.

4.3.2 Unified model of splitting over the overall temperature range

Thus, combining the results obtained in the previous chapter below 700°C and the results by laser annealing of the SOG structure, it is possible to establish a complete picture of the splitting kinetics, see on Fig. 35. In the low temperature part (up to at least 700°C), the activation energy of splitting is defined by the implantation dose, with a possible evolution during annealing due to the out-diffusion of H. After a zone of transition, which is not explored in this study, the activation energy of splitting does not depend on implantation dose, but only on the effective diffusion coefficient of the bonded H.

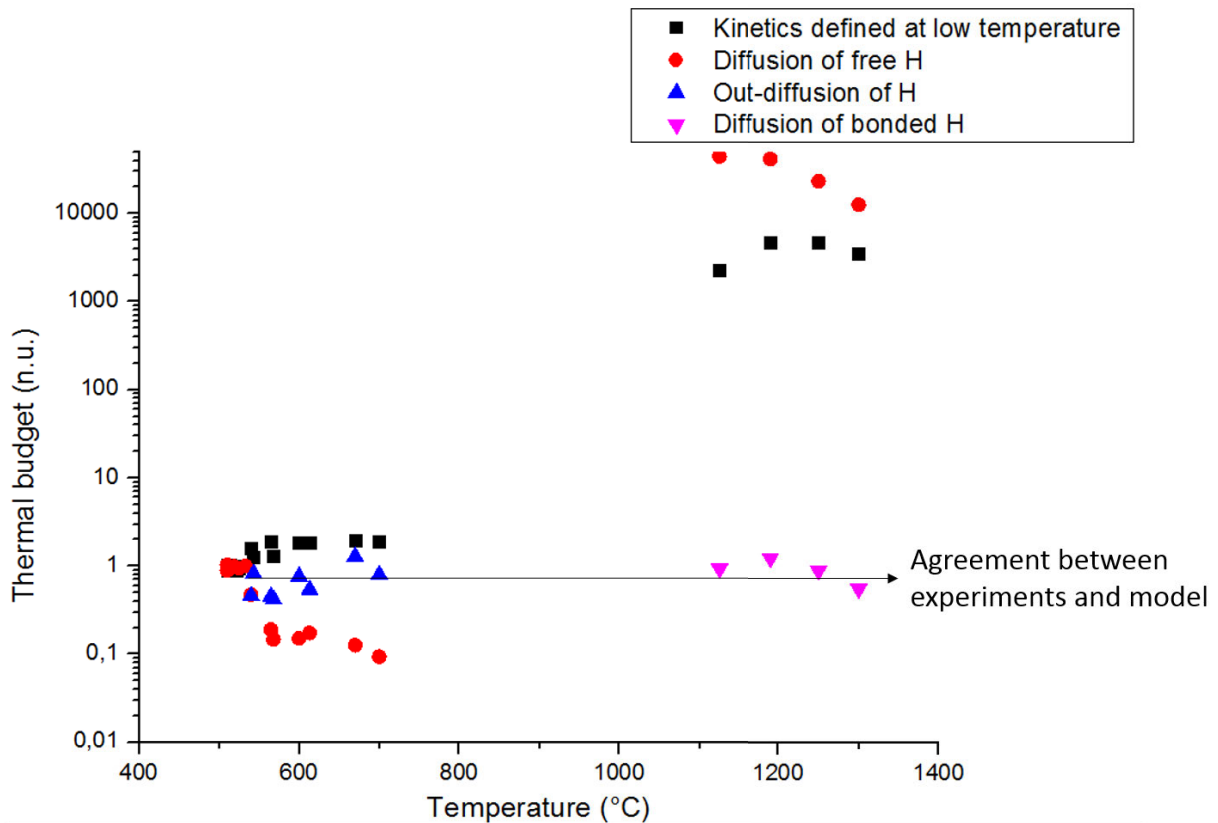


Figure 35: Summary of the calculations of thermal budget for $5.0 \cdot 10^{16} \text{ Hcm}^{-2}$ samples from low temperature domain (450°C) to very high temperature (up to 1300°C).

As an intermediate conclusion on splitting kinetics, it appears clearly that the splitting is indeed limited at very high temperature ($>900^\circ\text{C}$) by the diffusion coefficient proposed in the previous chapter (with an activation energy of 1.46eV), without any influence of the implantation dose. This transition occurs between the two temperature domains studied in this work (below 700°C and above 900°C). , This behavior is probably related to the temperature stability of hydrogen complexes defining bonded hydrogen diffusivity. However, literature data (7) suggest slightly lower temperature, in the 550C range.

5 Characterization of the films elaborated by laser-assisted Smart Cut™

This third part will be dedicated to the properties of the films of SOS and SOG obtained by laser annealing. Our objective is to compare the quality of the transferred Si films with the SOI films obtained by industrial Smart Cut™ process.

5.1.1 Best-in-class result

As this subchapter is dedicated to the properties of the films regarding their potential applications, we propose to begin the characterization by the best in class SOG sample. The Fig. 36 shows the 200 mm glass wafer, with the well-transferred SOG layer on the bottom part. This sample was initially implanted with $1.0 \cdot 10^{17} \text{ Hcm}^{-2}$ at 76 keV and annealed at 1000°C for 2 ms.

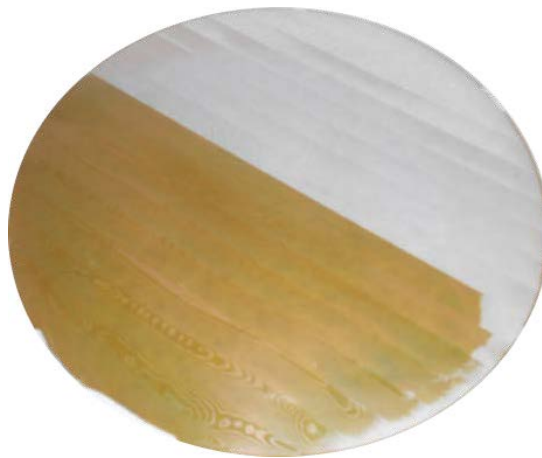


Figure 36: Picture of the best-in-class sample, obtained with implantation of $1.0 \cdot 10^{17} \text{ Hcm}^{-2}$ at 76 keV and a laser annealing at 1000°C for 2 ms.

A brief image analysis returns a transfer over of the glass wafer of 94.1 %, as illustrated on Fig. 37.

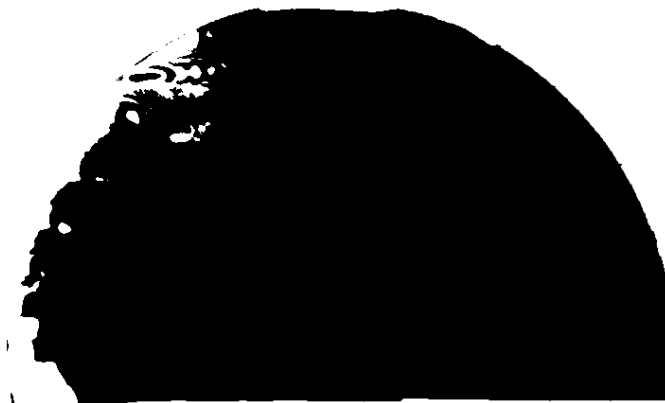


Figure 37: Image analysis of the transferred part of the best-in-class sample obtained with implantation of $1.0 \cdot 10^{17} \text{ Hcm}^{-2}$ at 76 keV and a laser annealing at 1000°C for 2 ms.

5.1.2 Analysis of the patterns formed by the transferred layers

The optical microscopy images of this marble effect are presented on Fig. 38. Different types of patterns can be observed, mainly under form of parallel bands with a width from 100 μm to a millimeter (Fig. 38 (a) and (b)). Additionally, dotted structure can be observed, as figured on Fig. 38 c) and (d)).

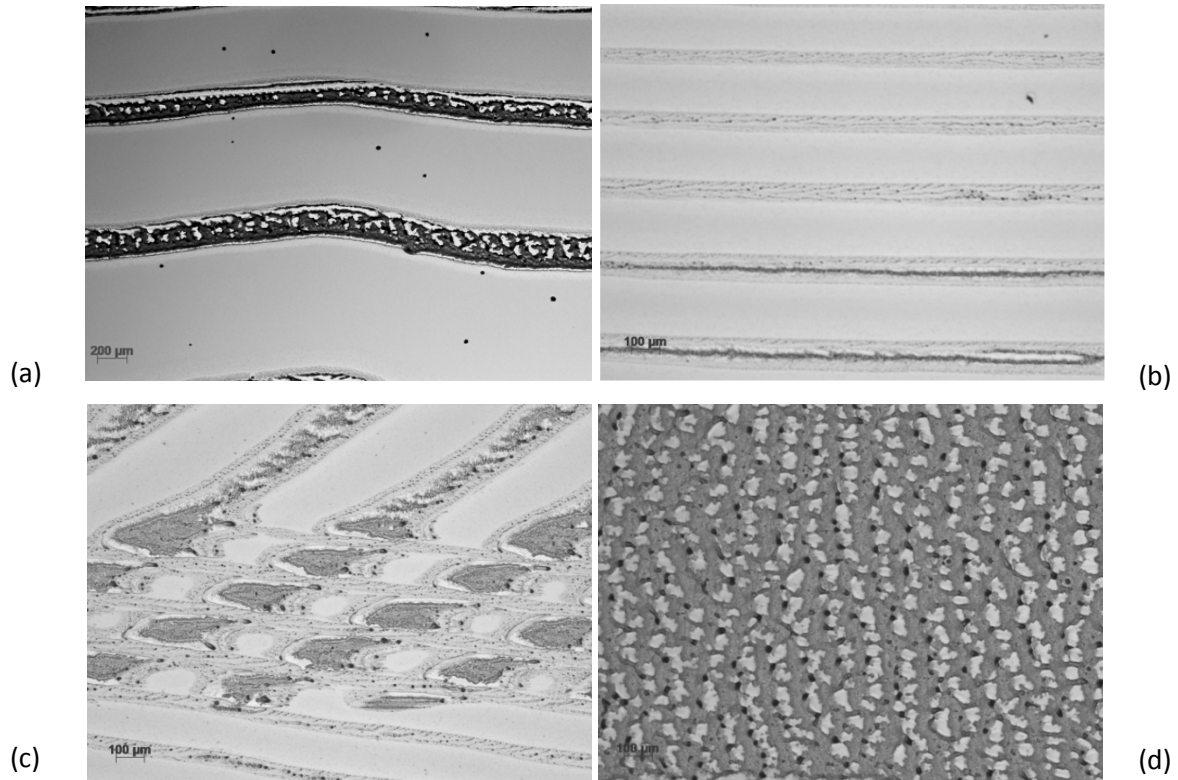


Figure 38: Images by optical microscope of patterns on sample implanted with $1.0 \cdot 10^{17} \text{ Hcm}^{-2}$ at 76 keV, after annealing at 1000°C and 2 ms.

It can be noticed that the observed wavy patterns remind optical patterns that could be obtained with samples after partial debonding of the Si and of the sapphire after the fracture of Si, already shown on Fig. 24. The variation of reflectivity can explain this non-homogeneous transfer as already mentioned. We will go back on the marbles model, after studying the residual stress present within the structure.

5.1.3 Bow of the structure after splitting

The SOG wafer, after laser-assisted splitting presents a persistent bow along both X and Y axis, as illustrated on Fig. 39. This bow is even bigger than the bow of the bonded structure (i.e. the silicon wafer bonded with the glass wafer) on the hot chuck of the laser annealing setup. It can be interestingly noticed that the deformation along the x-axis is symmetrical, whereas is it concentrated in the upper part (i.e. with the transferred Si film) along the y-axis. Thus, the deformation of the SOG sample is effectively caused by the Si layer transfer.

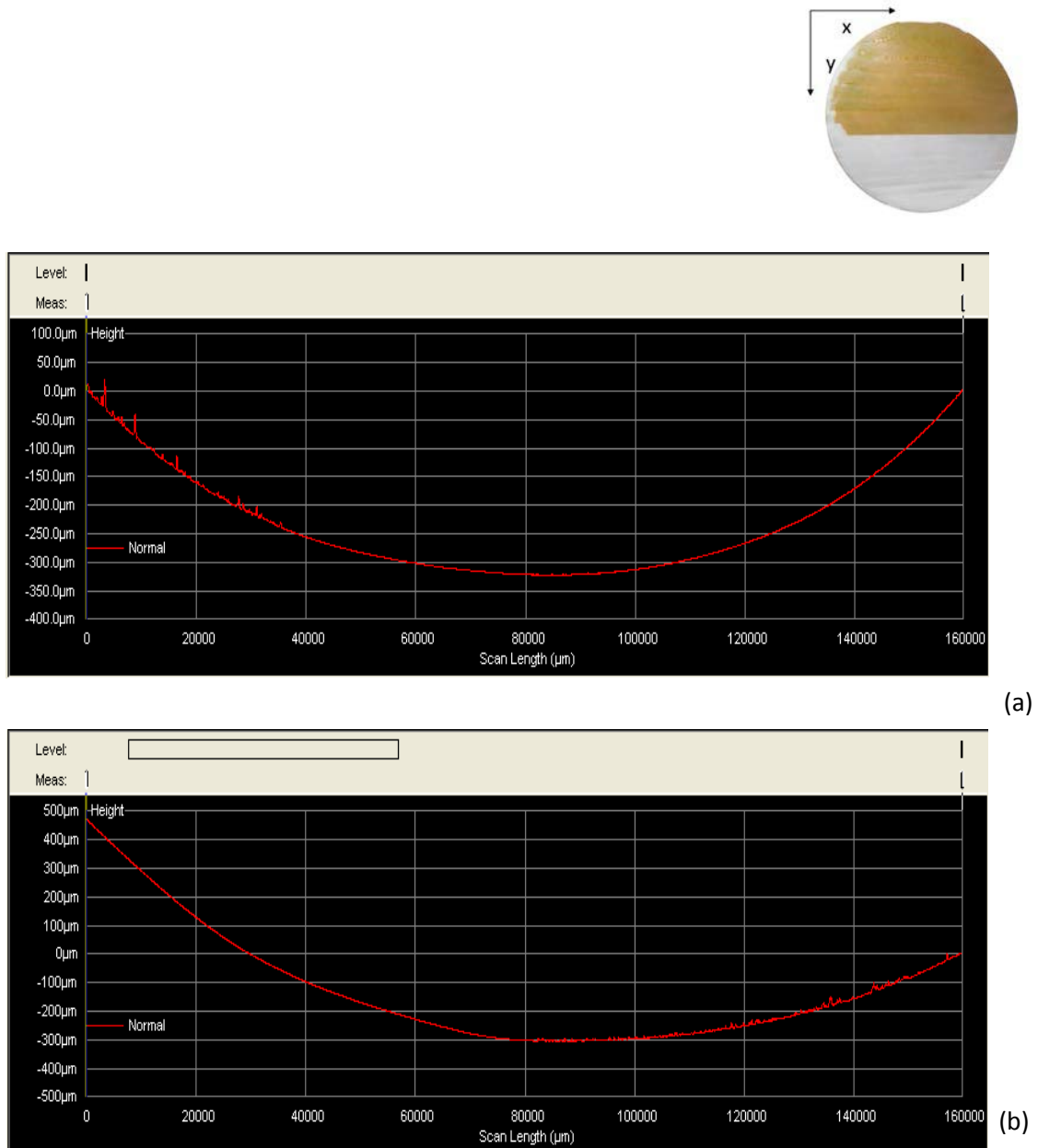


Figure 39: Deformation by mechanical profilometer of a sample implanted with $1.0 \cdot 10^{17} \text{ Hcm}^{-2}$ at 76 keV after laser beam annealing at 1000°C for 2 ms, in x-direction (a) and in y-direction (b).

As the working point, resp. softening point, of the glass used here is at 1293°C, resp. 971°C, a permanent deformation of the glass wafer during the annealing (proceeded here at 1000°C) and a subsequent freezing can be the explanation.

On the other hand, this bow can be compared with the deformation of the bonded structure during the scanning of the laser, as obtained by numerical calculations at the beginning of the chapter (and reminded on Fig. 40). During the laser scanning the silicon expands more than the glass causing the concave deformation of the structure. It can be proposed that the stress in Si layer is conserved during transfer on the glass substrate, as it is the case for the fabrication of strained-SOI [8]. The analysis of the eventual remaining stress in the transferred layer by Raman will bring additional information.

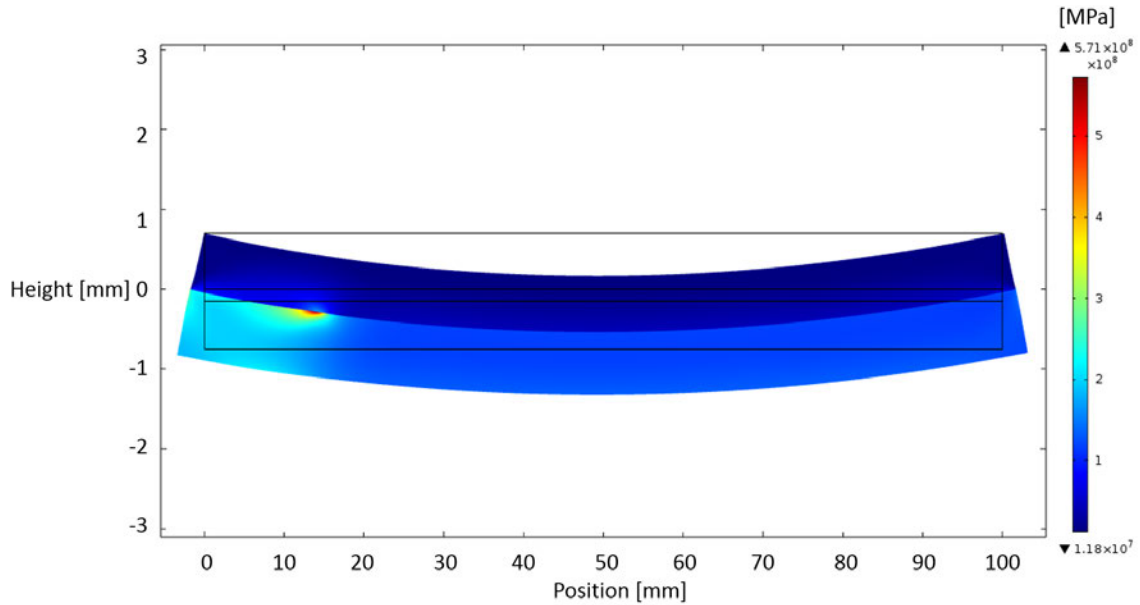


Figure 40: Deformation and stress distribution in a structure composed of Si bonded with glass.

5.1.4 Stress analysis by Raman

Raman analysis is used to compare the residual stress in the material between the well transferred zone and the zone of marbles. Three different types of zones are characterized, as summarized on Fig. 41, with different characteristic widths ($<2\text{ }\mu\text{m}$, $10\text{-}20\text{ }\mu\text{m}$, $>100\text{ }\mu\text{m}$).

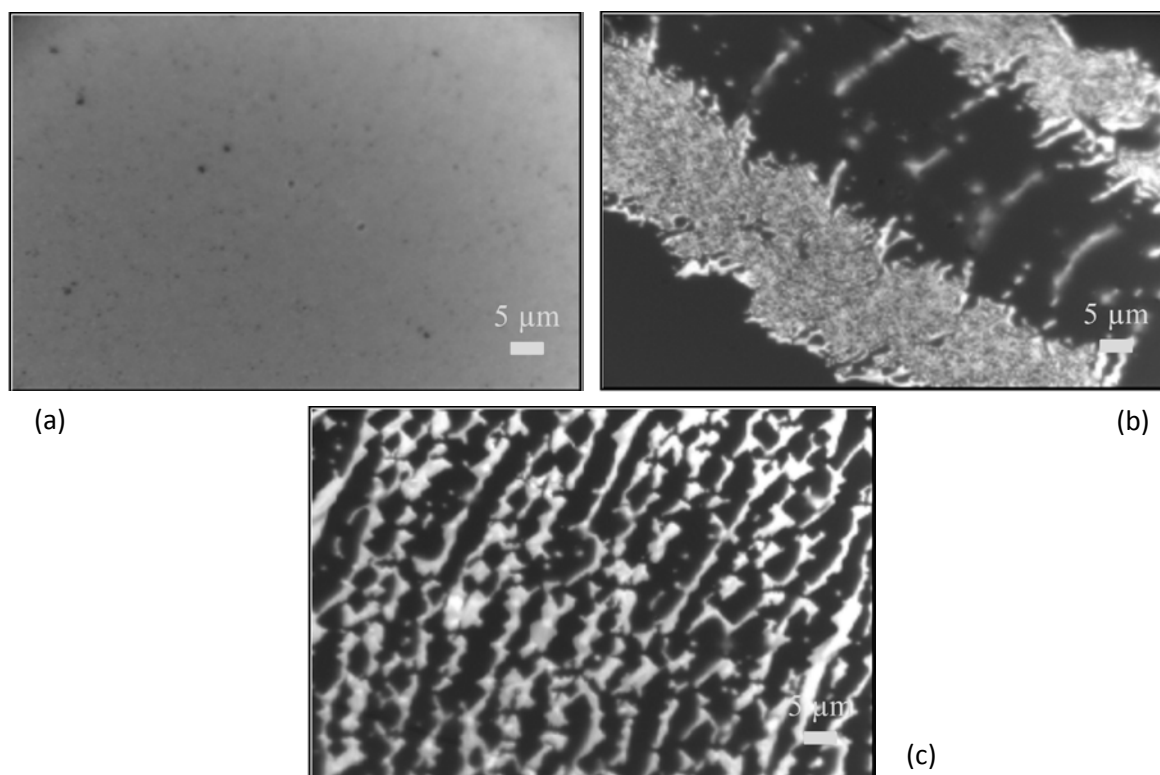


Figure 41: Images of the sample areas analyzed by Raman spectroscopy of the well-transferred SOG films (a), bands of $10\text{-}20\text{ }\mu\text{m}$ of width (b), dots/bands of $1\text{-}2\text{ }\mu\text{m}$ of width (c). The white areas correspond to the Si transferred onto the glass whereas the black areas correspond to the bare glass.

The Raman analysis allows to estimate the strain in a material, by determining the frequency shift of defined vibration modes, with a reference of the non-deformed material. In this case, the T2G mode is chosen. The Fig. 42 shows a Raman spectrum, with the reference of bulk Si and the signal for a sample of SOG after laser annealing. Postulating a biaxial stress in the (100) plane, there is a linear relation between the observed shift $\Delta\omega$ and the material stress. Additionally, the spectrum shows that the peak corresponding to the transferred film of SOG is enlarged compared to the reference peak, implying the presence of defects and structural modifications.

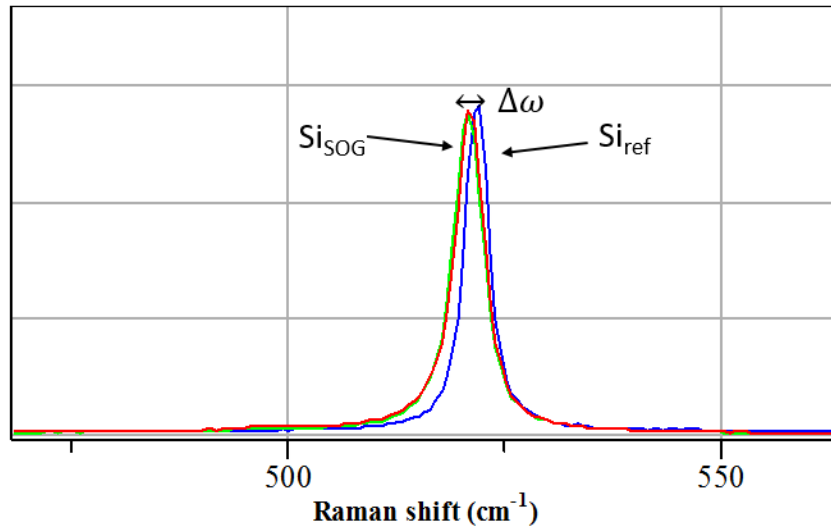


Figure 42: Raman spectrum showing the T2G mode of Si with the comparison between the reference Si and a SOG sample. The frequency shift allows to determine the deformation of the layer compared to a non-deformed Si.

The analysis is carried out for the different types of transferred areas presented in Fig. 41 and the calculated stress is plotted as a function of the lateral dimension of the SOG layers on Fig. 43.

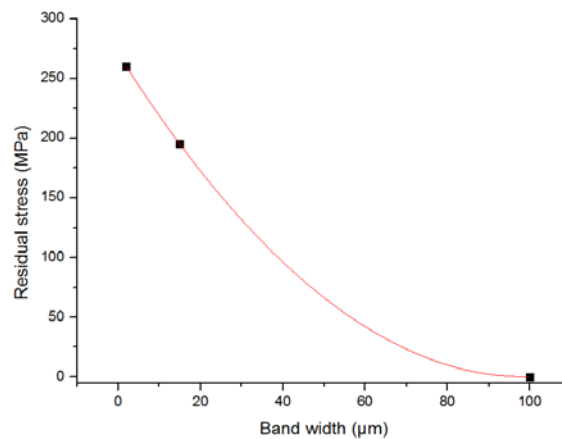


Figure 43: Residual stress in SOG films as a function of their characteristic width.

Thus, it appears that the laser-assisted Smart Cut™ modifies the structure of the transferred material. In case of the non-homogeneous transfer causing the marbles effect observed earlier, the residual stress seems to decrease with the transfer of larger lateral dimensions.

5.1.5 Model for the formation of marbles

As a summary on the formation of marbles, we propose the model illustrated on Fig. 44. The variation of reflectivity due to the deformation of the structure causes variations of power deposition in the implanted zone. As a result, the thermal budget of splitting is only fulfilled for particular area. The transfer of the Si occurs according to the fracture path as shown on Fig. 44 b).

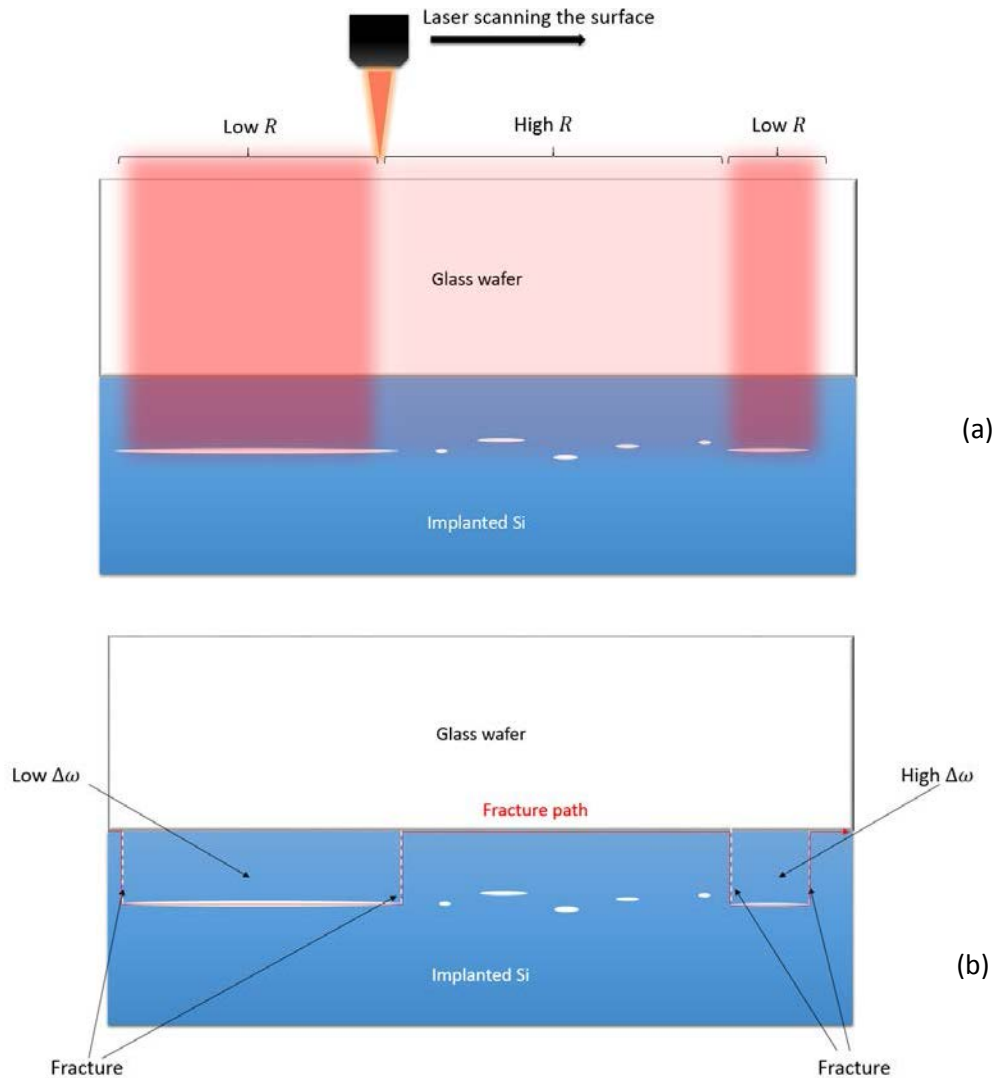


Figure 44: Schematic representation of the model of marbles formation. Formation of defects by laser annealing in the implanted zone (a), fracture path illustrating the formation of the non-transferred zones (b).

5.2 Roughness of SOS and SOG films by laser annealing and comparison with furnace annealing

5.2.1 Roughness of SOS films

The RMS roughness of SOS films is characterized by AFM and compared to the roughness of $5.0 \cdot 10^{16}$ Hcm⁻² SOI sample, obtained by conventional furnace annealing on Fig. 45. The roughness of the SOS films follows the trend observed in the previous chapter, i.e. it decreases with both splitting temperature and implantation dose. This observation confirms that the splitting mechanism is in many ways similar with the laser annealing.

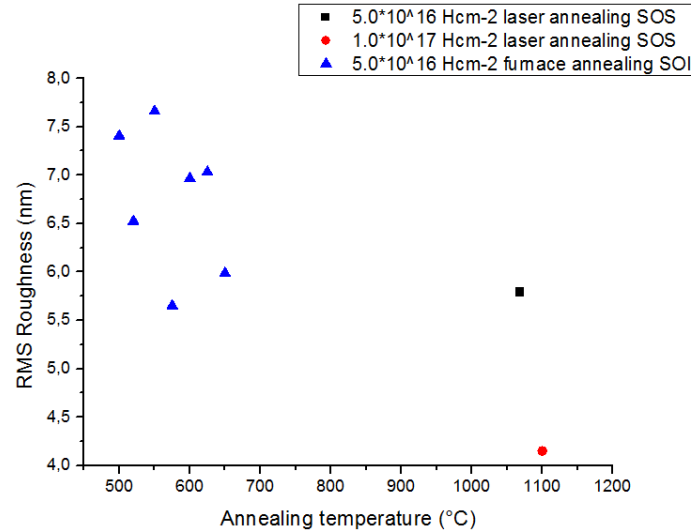


Figure 45: Comparison of the RMS roughness of SOS sample by laser annealing with SOI obtained with furnace annealing in regular Smart Cut™ conditions.

Two contributions can explain the lower roughness observed for SOS samples. First of all, the study of the previous chapter, i.e. the characterization of splitting for regular SOI structures, tends to show that the roughness decreases with the annealing temperature. Additionally, it can be postulated that the sapphire has a better stiffener effect, compared to the Si of the acceptor wafer in case of regular SOI structures. Indeed, the Young modulus of sapphire (E_{sapphire} 335 GPa) is higher than that of Si (E_{Si} = 179 GPa), which helps the lateral development of defects during the annealing, which leads at the end to a lower roughness. This effect was already mentioned in the work of Lagahe [7].

Due to the limited number of SOS samples, the characterization of the surface of SOG samples will bring additional information in order to complete the comparison between the annealing methods.

5.2.2 Surface analysis of the SOG films

The RMS roughness determined by AFM shows a higher roughness for SOG samples, compared to SOS samples, Fig. 46. It can be explained by the stiffener effect of the glass layer into contact with the implanted material being lower compared to sapphire, i.e. the Young modulus of sapphire is much higher than that of the Corning glass. Into addition, the softening point of glass occurs at $T=971^{\circ}\text{C}$ corresponding to a drastic reduction of the viscosity of glass from $10^{13.5}$ Pa*s at the strain point ($T=669^{\circ}\text{C}$) to $10^{6.6}$ Pa*s at the softening point.

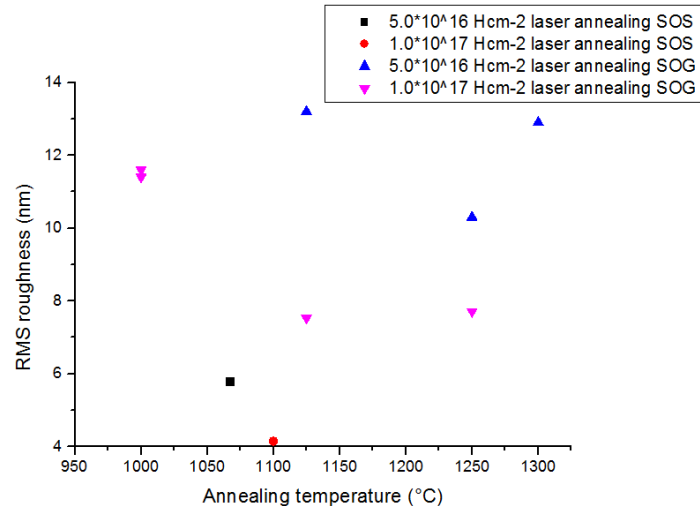


Figure 46: Comparison between the RMS roughness of SOS and SOG films by laser annealing.

The comparison with classical Smart Cut™ logically shows that the laser-assisted splitting with a glass stiffener returns a much higher roughness, as illustrated on Fig. 47.

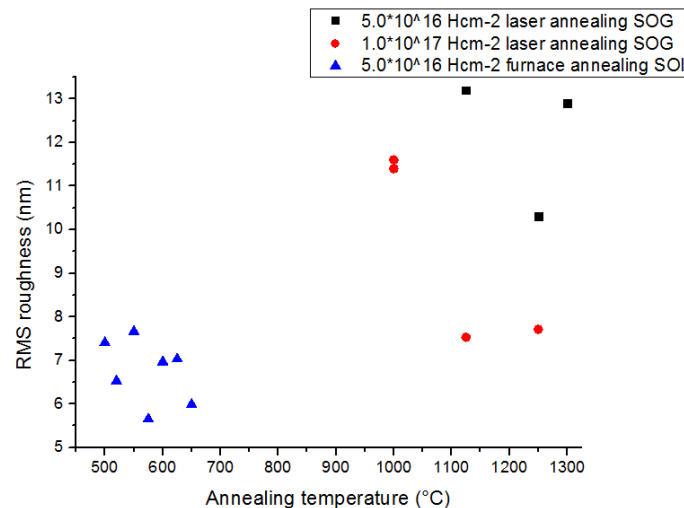
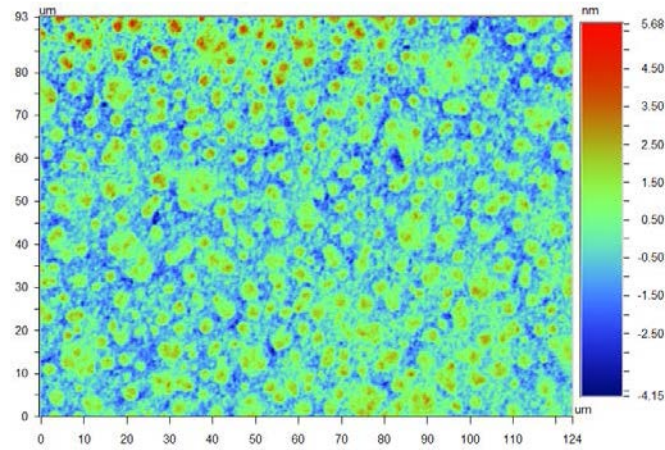


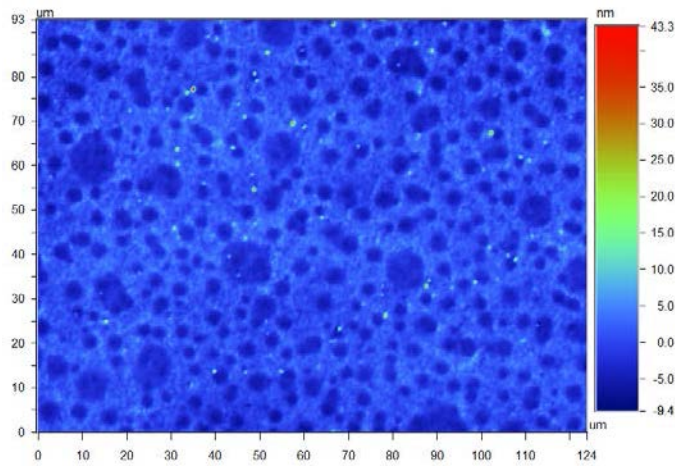
Figure 47: Comparison between the RMS roughness of SOI films obtained by conventional Smart Cut™ and SOG films obtained by laser-assisted splitting.

The surface topology of a $1.0 \cdot 10^{17}$ Hcm⁻² SOG sample obtained by optical profilometer shows that the profiles of micro-cracks can be clearly be recognized, on both transferred layer and donor wafer (see on Fig. 48 (a) and (b)).

This confirms the effect of the glass wafer whose stiffness is lower than sapphire or Si. Thus, the vertical development of the defects during the annealing is higher in case of glass.



(a)



(b)

Figure 48: As-splitted surface of SOG sample, initially implanted with $1.0 \cdot 10^{17} \text{ Hcm}^{-2}$ by optical profilometer (a), surface of the donor wafer initially implanted with $1.0 \cdot 10^{17} \text{ Hcm}^{-2}$ (b).

5.3 4-probe measurement (SOG)

Finally, we propose to pay attention on the electrical properties of the films of SOG, by the characterization of the resistivity of the layer of Si. Due to the high resistivity of the glass wafer, pseudo-mosfet measurement could not be carried out.

Nevertheless, this rough measurement tends to show that the resistivity of the films obtained by laser annealing are slightly higher than the films obtained by furnace annealing, as shown on Fig. 49. More noticeably can be observed that the resistivity increases a lot for the zone of marbles. This is coherent relation with the elevated residual stress within the silicon layer.

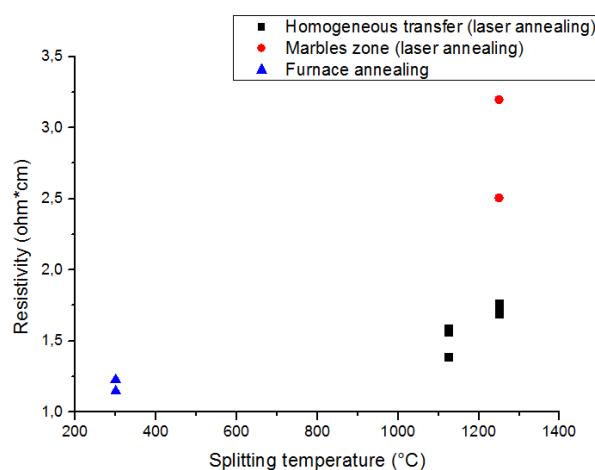


Figure 49: Comparison of the resistivity of SOG films obtained by laser annealing and SOI films obtained by regular Smart Cut™ measured by 4-probe measurement.

6 Conclusion of chapter

This chapter has followed a clear red line, in order to explore the possibility of splitting by laser annealing (i.e. at high temperature) with a reasonable experimental effort. The knowledge brought by the previous chapter has been used as a starting material for numerical modeling and, in a second time to build a unified model for the splitting kinetics at whole temperature range. Additionally, it is important to keep in mind the initial industrial motivations in developing an alternative process for the elaboration of heterostructure by Smart Cut™.

The first step has consisted in validating the possibility of blistering of an implanted material, without bonding with another wafer, using an ns laser equipment. The blistering has been indeed observed after a repetition of laser pulses. This acts as the first prerequisite for the splitting of an implanted and bonded structure, under equivalent annealing conditions. In particular, it tends to prove that despite the high temperature reached during the annealing by laser, the implanted H dose is not reduced sufficiently to avoid the splitting.

After this validation step, different numerical calculations have been used, in order to study the effect of ms laser annealing on the behavior of the implanted H and to optimize of the design of experiment (i.e. aiming to find proper splitting conditions with a limited number of samples).. Additionally, the different aspects such as the generated stress within the structure during the laser annealing, as well as the structure deformation have also been explored.

Based on the design of experiments, the annealing with an ms laser equipment has been carried out, on SOS structures of small size (100 mm of diameter). Despite an important number of samples breaking, both blistering and splitting are observed. The roughness of the SOS films are analyzed and are in good agreement with the trend observed in the previous chapter.

In addition the ms laser annealing is conducted on SOG samples of bigger diameter (200 mm). The splitting is demonstrated on large surface (more than 90% of the scanned surface) and the splitting kinetics trend can be clearly identified. Based on the numerical modelling of the laser annealing within the bonded structure, the thermal budget of splitting is calculated following different splitting model. It appears clearly that only a single regime rules the splitting in this temperature range (>900°C to melting point of Si). This regime is defined by the diffusion of bonded H in the implanted zone, as proposed in the previous chapter, i.e. with an activation energy of 1.46 eV. A pre-factor depending on the ratio of bonded / free H within the implanted dose explains the faster splitting for higher implantation dose. Thus, a unified model of splitting can be established over the whole temperature range.

Finally, this study has established for the first time the possibility of splitting in implanted Si by laser annealing. Marbles are observed for both SOG and SOS samples. The marbles are composed of an alternation of transferred and non-transferred zones, possibly with a remaining stress, as studied by Raman. This effect can be explained by the variation of reflectivity of the system, due to the bow of the structure on the hot chuck.

The roughness of the SOG samples appears to be higher than both for SOS and SOI films (i.e. obtained in regular annealing conditions). This observation is coherent with the lower stiffness of the glass acceptor wafer during the laser annealing.

References

- [1] **H. R. Philipp, E. A. Taft**, *Phys. Rev.* vol. 120, No. 1 pp. 37-38, 1960.
- [2] **S. H. Yoo, R. Greif, R. E. Russo**, Explosive change in crater properties during high power nanosecond laser ablation, *J. Appl. Phys.*, vol. 88, pp. 1638-1649, 2000.
- [3] **Z. Fu, B. Wu, Y. Gao, Y. Zhou, C. Yu**, Experimental study of infrared nanosecond laser ablation of silicon: the multi-pulse enhancement effect, *Appl. Surf. Sc.*, vol. 256, pp. 2093-2096, 2010.
- [4] **R. Boivin, B. Terreault**, Desorption and other effects of pulsed laser annealing of hydrogen implanted silicon, *J. Appl. Phys.*, vol. 73, pp. 1943-1951, 1993.
- [5] **M. J. Edwards, C. R. Bowen, D. W. E. Allsop, A. C. E. Dent**, Modelling wafer bow in silicon–polycrystalline CVD diamond substrates for GaN-based devices, *J. of Phys. D: Appl. Phys.*, vol. 43, pp. 1-9, 2010.
- [6] **A. Colin**, Etude des couplages radiatifs et thermiques et des modifications physico-chimiques engendrés par un recuit lasere milliseconde sur la grille polysilicium de la technologie CMOS 45 nm. Thèse de Doctorat de l'Université de Strasbourg. 2010.
- [7] **M. Bruel, B. Aspar, H. Moriceau, E. Jalaguier, C. Lagahe**, Single-crystal semiconductor layer delamination and transfer through hydrogen implantation, *Electrochem. Soc. Proc.*, vol. 1, 1999.
- [8] **H. Moriceau, F. Mazen, C. Braley, F. Rieutord, A. Tauzin, C. Deguet**, Smart Cut™ review of an attractive process for innovative substrate elaboration, *Nucl. Instr. and Meth. in Phys. Res. B*, vol. 277, pp. 84-92, 2012.

Chapter 6. Deposition of liquid Si on Si substrate.

This last experimental part will put into practice the results acquired and mentioned in the two last chapters. Our objective will be to explore the feasibility of the second process proposed in this thesis work, i.e. the fabrication of thin foil of single crystal Si by deposition of liquid Si upon implanted substrate (see Fig. 1).

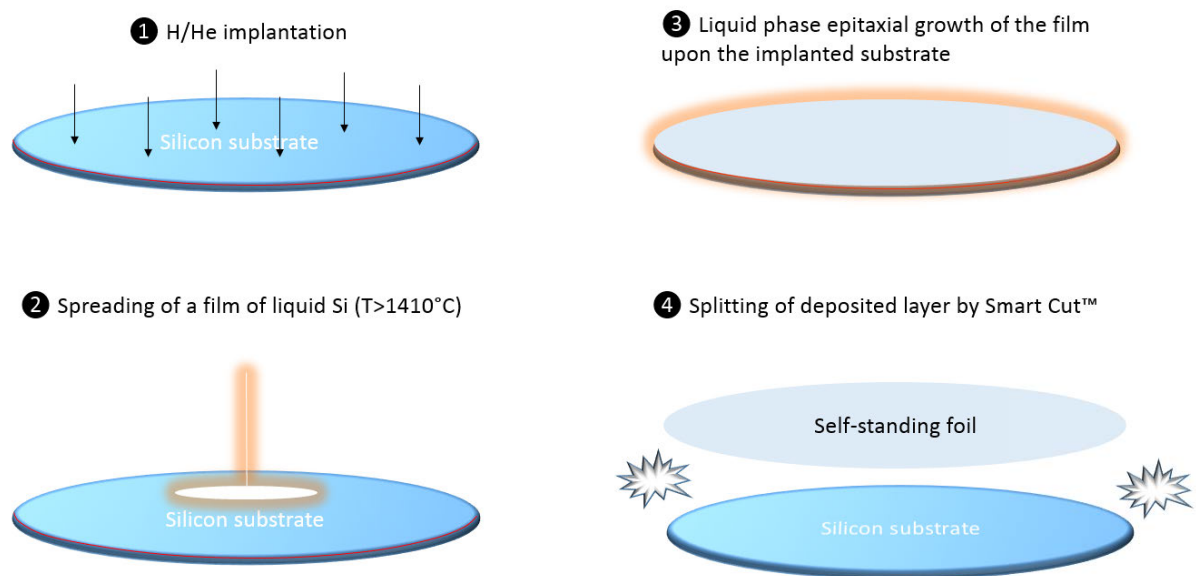


Figure 1: Schematic representation of the process of fabrication of thin foil of single crystal Si by deposition of liquid Si upon on implanted substrate.

As a short reminder, this process involves the spreading of a film of liquid silicon at temperature superior to $T_m = 1410^\circ\text{C}$ upon an implanted substrate, maintained at low temperature ($T < 300^\circ\text{C}$). Due to the huge thermal gradient in contact with the cold substrate, the solidification is supposed to occur fast enough to form a solid stiffener layer upon the implanted face of the substrate. The LPE growth in the proposed conditions will be presented after an introductive numerical study based on the main experimental observations. Finally, the films after solidification will be characterized for both microstructure and electronic properties.

1. Modelling of Si liquid crystallization

This preliminary study by numerical modelling aims to bring understanding on the feasibility of the process proposed in this chapter. This first step consists in studying the thermal aspects regarding the crystallization of the liquid film deposited on the substrate (implanted or non-implanted). The numerical model considers only the thermal aspect of the solidification. Nevertheless, it gives a sufficient approximation in regard of the solidification front displacement and of the thermal diffusion within the implanted material in contact with the film. For further studies, more complex models, such as Monte Carlo, would give a more reliable modelling taking into account the nucleation barriers and growth rates. Those parameters depend on numerous variables such as undercooling or liquid/solid interface roughness [1].

1.1 Model description

This study relies on the heat diffusion equation, already exposed in the chapter 5, section 2.1.1. We add here the contribution of the latent heat h_{sl} during the phase change. We consider here the method of equivalent specific heat. Thus, the latent heat release is included in the specific heat over a defined range of temperature, ΔT , around the melting point of silicon T_m (equal here to 10°C).

$$c_p(T) = \begin{cases} c_{ps} & T < T_m - \Delta T \\ \frac{h_{sl}}{2\Delta T} + \frac{c_{ps} + c_{pl}}{2} & T_m - \Delta T < T < T_m + \Delta T \\ c_{pl} & T > T_m + \Delta T \end{cases}$$

with c_{pl} and c_{ps} being the specific heat of liquid and solid phase, respectively. The Fig. 2 illustrates the variation of specific heat as a function of temperature.

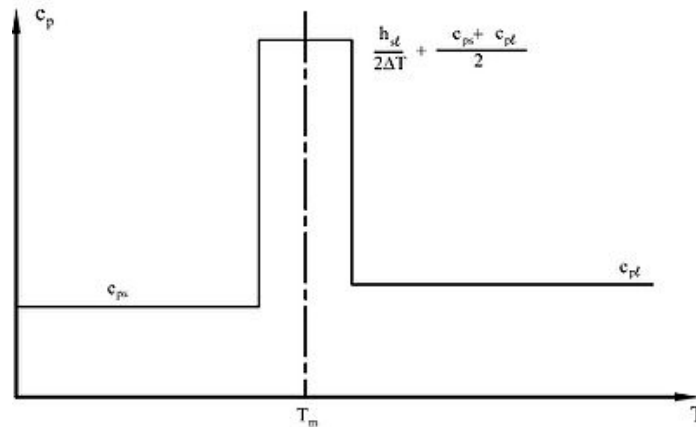


Figure 2: Equivalent specific heat protocol.

It is worth noting that our thermal model only aims to estimate the orders of magnitude for both solidification front advance and thermal profile during the crystallization.

1.2 Numerical study of solidification of the liquid silicon by Comsol Multiphysics®

This numerical modeling considers here a static system, i.e. after spreading of the liquid, composed of a layer of liquid Si of various thicknesses and shapes in contact with a substrate of Si, at room temperature.

1.2.1 Thermal profile during the solidification of a film of liquid Si

We propose two different configurations of liquid/solid systems based on the experimental observations that will be presented hereafter. The first calculation represents a layer shape, as illustrated on Fig. 3.

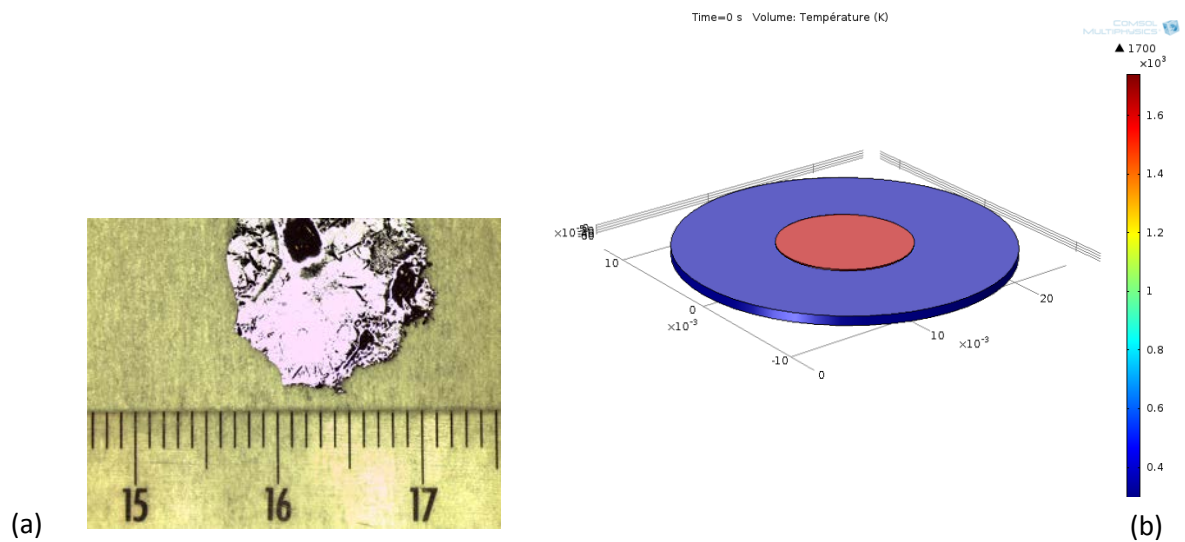


Figure 3: Image of a detached film of Si of a thickness of around 200 μm (a) illustration of the film of liquid Si at 1427°C spread over the cold Si substrate at room temperature. This schematic representation corresponds to the initial step, at $t = 0$ s (b).

This shape represents the most optimum shape of films. It consists of a 2D film of liquid Si, at 1427°C (i.e. 1700K) with a thickness of 50 μm , 100 μm and 200 μm . The width of the films is fixed to 2 cm, which is coherent with the experimental observations. The film is in contact with a substrate of 750 μm thick, at room temperature. Adiabatic conditions are imposed to the substrate surface with the exception of the part of the surface covered by the film. As a boundary conditions at the top film surface the radiation heat transfer is applied.

A radial symmetry criterion is applied to the system in order to reduce the calculation steps. Thus, the effective calculations are limited to a 2D system, composed of the corresponding thicknesses of film and substrate, and limited to the half of the system, as shown on Fig. 4.

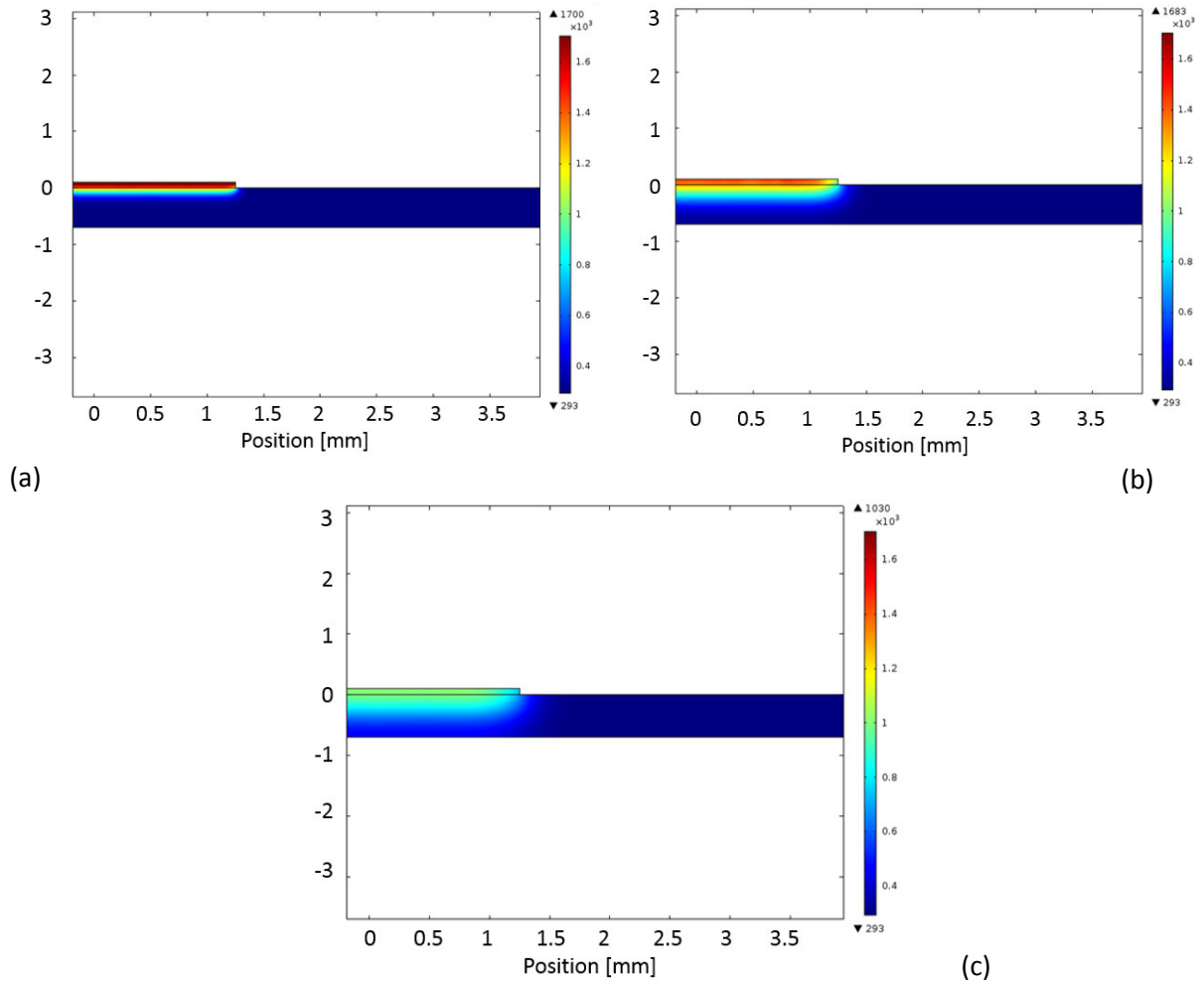


Figure 4: Modelling of the thermal profile during the solidification of a film of 100 μm of liquid Si in contact with a wafer of Si at RT, after 0.1 ms (a), 0.5 ms (b), 1 ms (c).

The results show that most of the latent heat releasing is evacuated by conduction in the substrate, and that the heat lost by radiation is very limited. Thus, the solidification is supposed to follow a columnar growth, due to a strong 1D gradient. Additionally, it appears that a very slight lateral diffusion occurs within the substrate near film edge as illustrated on Fig. 4 (c).

The displacement of the solidification front as a functions of time will be presented in section 1.2.3, based on a 1D approach with a finer mesh and a better spatial resolution.

1.2.2 Thermal profile of the solidification of droplet of liquid Si

Another type of experimental samples shows a droplet shape. The shape factor is basically a 2 mm height and a 2 mm diameter as illustrated on Fig.5 a). A Bezier polynomial is used to fit the corresponding shape to form the geometry of the numerical modelling, as figured on Fig. 5 (b).

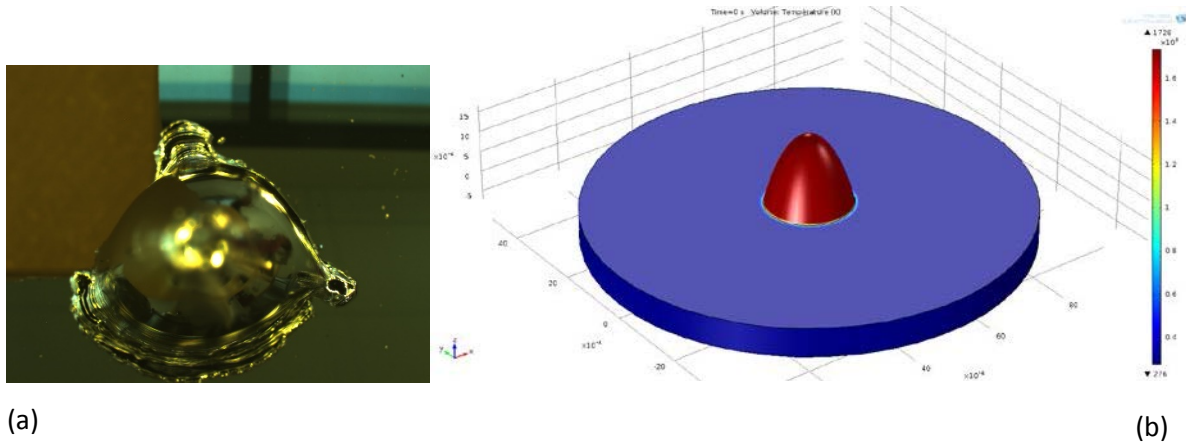


Figure 5: Image of a solidified Si droplet after deposition on a non-implanted rotating substrate (see details in chapter3) (a). The lateral size of the image is 5 mm. Schematic representation of the corresponding simulated shape by Comsol Modelling (b).

The Fig. 6 gives two temperature maps of such sample after 1 ms and 0.1 s after deposition. Thus, an area of about a 1 mm of width around the droplet can be identified as heated above 1000°C. It is worth noting that the lateral diffusion during the solidification of droplet is much higher than for the thin films presented in Fig. 4.

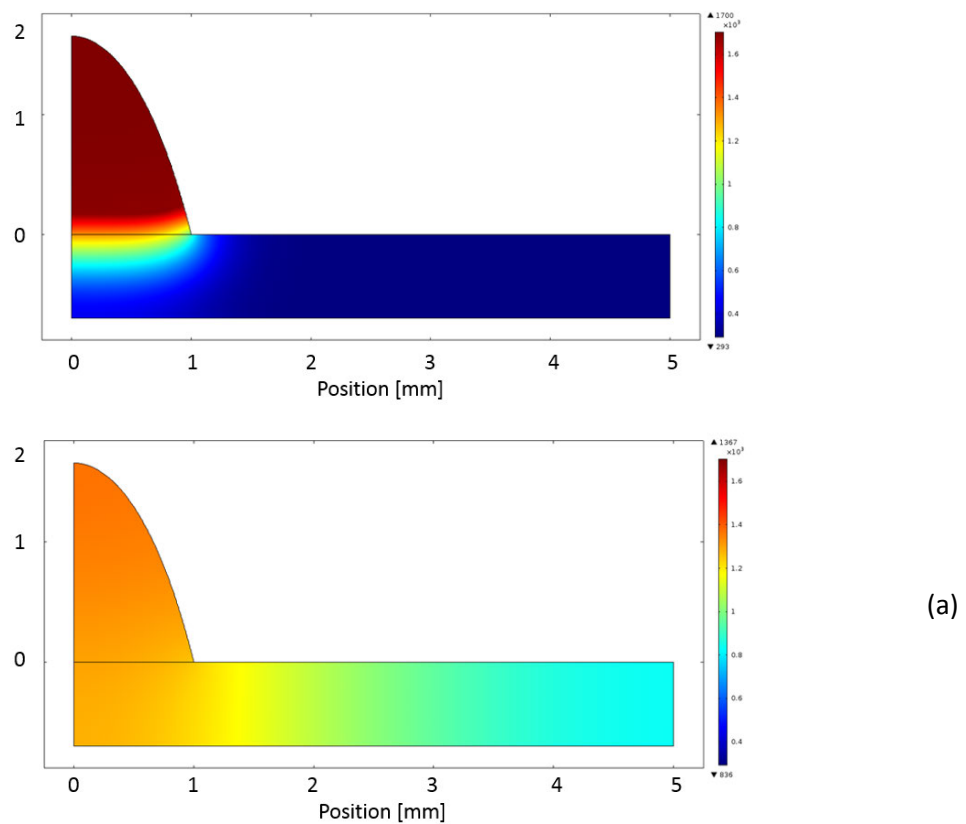


Figure 6: Modelling of the thermal profile during the solidification of droplet of 2 mm of height of liquid Si in contact with a wafer of Si at RT $t = 1$ ms (a), $t = 0.1$ s (b).

1.2.3 Numerical calculation of the temperature within the implanted zone during the solidification of liquid Si

The temperature signal is calculated at 1.5 μm depth (i.e. the R_p corresponding to 160 keV implantation energy), as illustrated on the TRIM calculation Fig. 7.

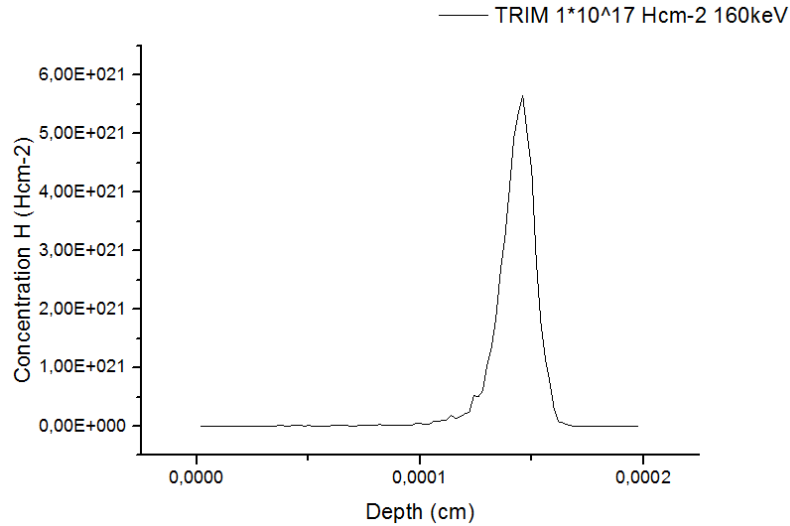


Figure 7: TRIM calculation of the implantation of a dose of $1 \cdot 10^{17} \text{ Hcm}^{-2}$ at 160keV.

The temperature within the implantation zone during the solidification is extracted using the 2D numerical calculations summarized above. In order to take the extreme case, the temperature is extracted at the middle of the film and the droplet, respectively. The results are plotted on Fig. 8.

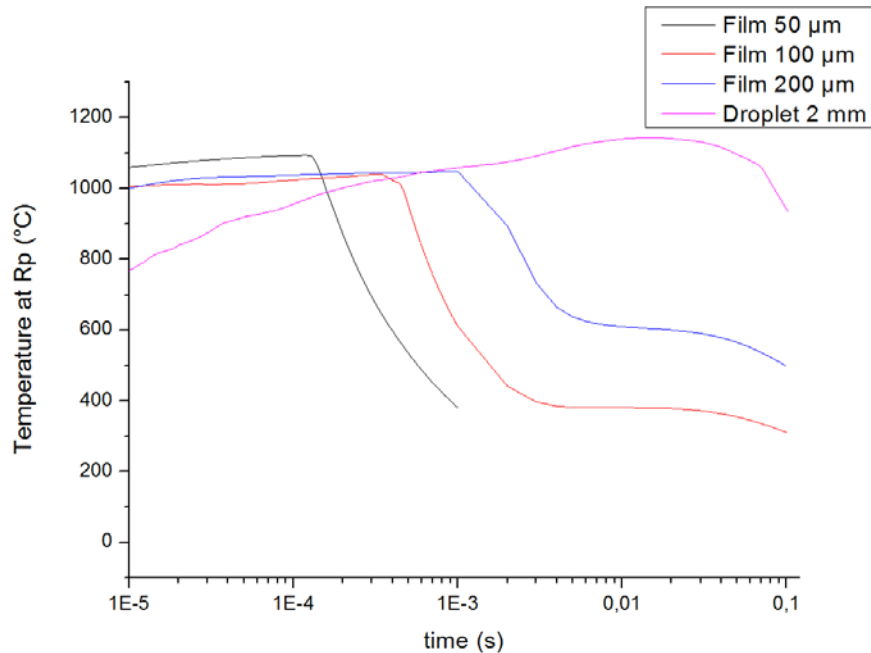


Figure 8: Numerical calculations of the temperature in the implantation zone of the substrate in contact with the deposited liquid Si for different conditions of geometry and thickness (films of 50 μm , 100 μm , 200 μm and droplet of 2 mm of thickness).

It can be observed that despite the low distance between the liquid Si and the implantation zone (i.e. 1.5 μm), the temperature does not go above 1100°C and 1150°C in the case of the film and the droplet, respectively. This observation is coherent with the large thermal diffusivity of Si.

Additionally, it is worth noting that the maximum temperature reached in the implantation is higher in case of 50 μm film thickness, compared to 100 μm and 200 μm film thickness. It can be explained by a faster release of the latent heat during the solidification due to the lower thickness of liquid Si.

1.2.4 Thermal budget of splitting

The temperature signal presented above can be used in order to evaluate the thermal budget and the possible occurrence of splitting within the implantation layer. Therefore, the model of splitting developed and validated earlier in this work is applied, considering the conditions of implantation (i.e. a dose of implantation of $1.0 \cdot 10^{17} \text{ Hcm}^{-2}$ at 160 keV). Similarly to the annealing by laser-beam in the previous chapter, the out-diffusion of H can be neglected due to the very high thermal ramping. Thus, the kinetics of splitting as determined for low temperature annealing is kept constant in case of annealing caused by the deposition of liquid Si. According to the characterizations presented in the chapter 5, the corresponding activation energy of splitting must be equal to 1.46 eV.

The calculations using these parameters are summarized on Fig. 9. It shows that the splitting conditions are not fulfilled (thermal budget less than 1) in case of films of 50 μm and 100 μm of liquid Si. On the other side, the splitting occurs during the steps of solidification and cooling of the system if the thickness of the film is above of 200 μm . This observation means that the growth of a stiffer layer in contact with the implantation wafer will always be satisfied in case of films of thickness below 200 μm .

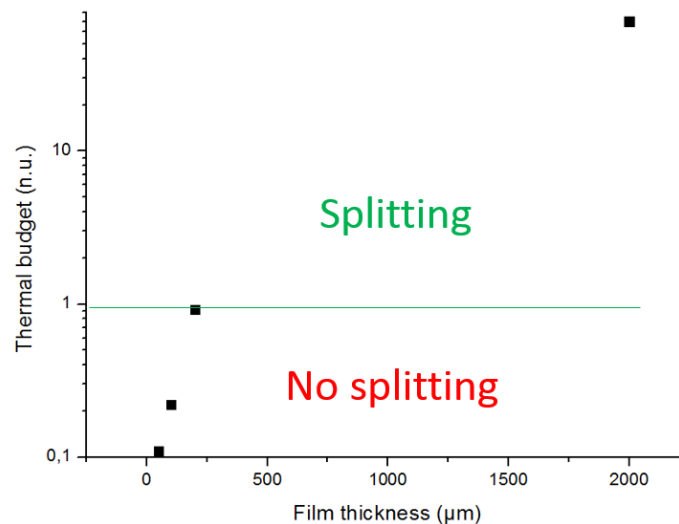


Figure 9: Calculation of the thermal budget of splitting using the numerical calculation of the solidification of liquid Si.

In case of films of higher thickness or in case of the droplets of liquid Si, it is necessary to calculate the advance of the solidification front and to compare it with the thermal budget of splitting. For this part, we will consider a 1D model, consisting of an assembly of liquid Si, initially at 1427°C (i.e. 1700 K), in contact with 750 μm of solid Si, initially at room temperature. This simple 1D model allows to a finer mesh resulting in a better spatial resolution.

Our objective is to confirm that the growth of the stiffener layer in contact with the implanted face is faster than the film separation. This is a necessary condition for the detachment of the continuous film. Indeed, we have seen in chapter 2, section 1.1 that a stiffener layer is required in contact with the implanted surface during the defect growth of the splitting annealing.

The solidification front position during the solidification is plotted in Fig. 10.

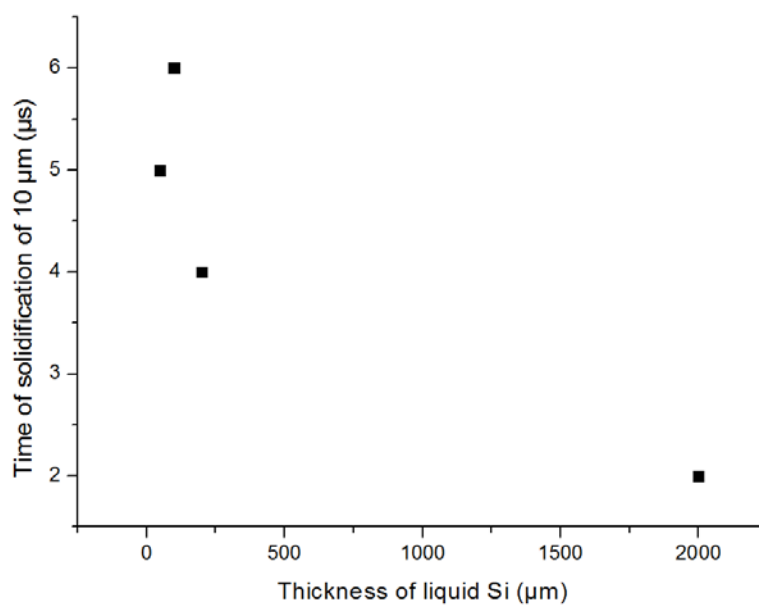


Figure 10: Numerical modelling of the time for the solidification of a stiffener layer (10 μm of solid Si) in contact with the implanted wafer.

The time for the solidification of a stiffener layer is about a few μs , which is far shorter than the time necessary for the splitting, with the corresponding thermal diffusion. Thus, it is possible to assess that the solidification of the film in contact with the implanted wafer will always allow the detachment by Smart Cut™.

It can be observed that the time required for the solidification of the stiffener layer starts to decrease above 100 μm of thickness of liquid Si, which can seem contradictory. A possible explanation is that a larger thickness of liquid Si, whose thermal conductivity is higher than that of solid Si, acts as a better thermal reservoir for the diffusion of the latent heat at the beginning of the solidification.

2 Liquid Si dropped on a rotating substrate (collaboration with Solarforce company)

Before presenting experimental results, we have to mention that great efforts were necessary to find and develop the deposition equipment. As a matter of fact, this very exploratory work was very challenging. Indeed, both high temperature of silicon melting and controlled atmosphere, are of high importance in this work but relatively hard to find in the current R&D facilities.

The first samples were realized with the generous help of Solarforce company in France. This study was planned to be a full design of experiment. Sadly, the company went to liquidation before the end of the work, and the complete experiments could not be finalized. Fortunately, another facility could be found thanks to the tremendous help of the SiMaP laboratory (France) and the experimental results will be presented in the second part.

2.1 General considerations

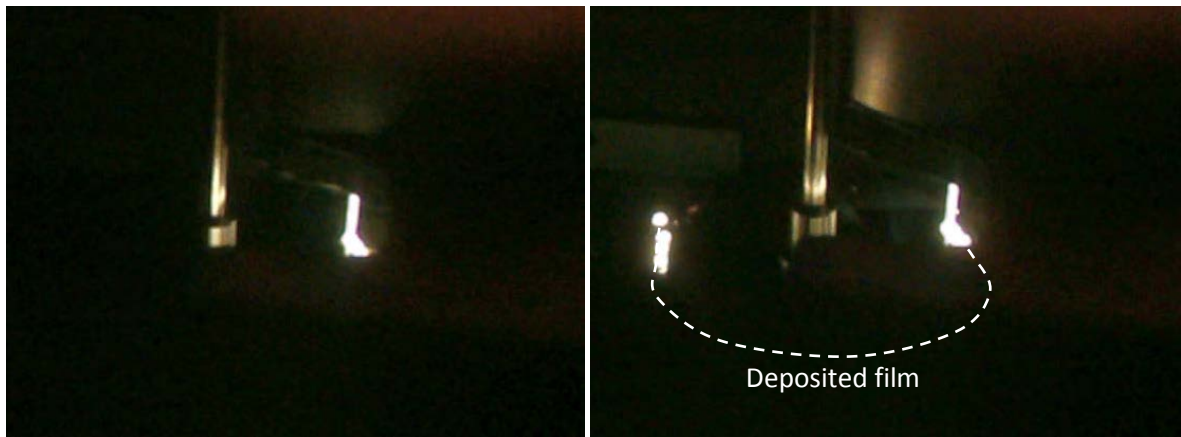
2.1.1 Deposition on a rotating substrate from a graphite crucible

We propose to begin this experimental part with illustrating the interior of the deposition chamber, as shown on Fig. 11. In spite of the fact that the different parts of the equipment are isolated from each other with a thermal insulator (graphite foam), the substrate and the area of deposition can be observed during all the experiment through a semitransparent window.



a)

b)



c)

d)

Figure 11: Snapshot of the video during the deposition on a rotating substrate: initiation of the deposition on the part of the chuck at $t < t_0$. The dashed lines define the contour of the substrate (a). Initiation of the rotation of the holder $t = t_0$ (b). During the rotation of the holder $t = t_0 + 0.3$ s (c). Right after the end of the rotation $t = t_0 + 0.5$ s (d).

2.1.2 Deposition rate of the silicon through orifice in the crucible

The deposition rate is characterized by measuring the emptying time of the crucible. Therefore, a test is done with 40 gr of Si powder. The time for the complete emptying is determined by a video observation, i.e. similar to as illustrated on Fig.11. A duration of 30 s is obtained, corresponding to a deposition rate of 1.33 g/s. This deposition rate will be taken as a reference in order to calculate the rotation speed of the substrate in the following part.

2.1.3 Spreading of the liquid film on the rotating substrate

In order to determine the rotation speed of the substrate, we consider that the liquid layer is spread with a semi-torus shape as illustrated on Fig. 12.

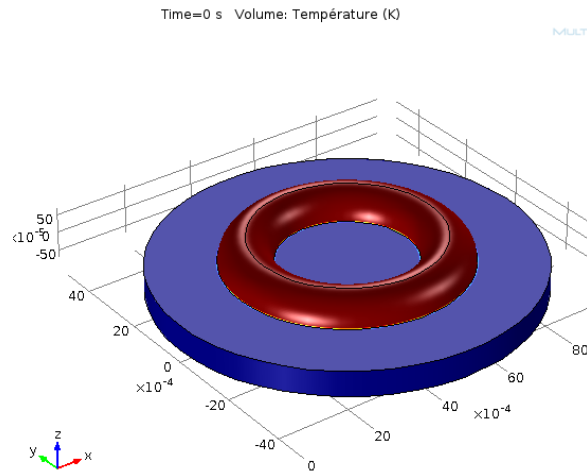


Figure 12: Illustration of the semi-torus shape as deposited upon the rotating substrate.

The volume of the corresponding structure is defined by the following relation:

$$V = \int_0^{2\pi} R \, d\theta \left(\int_0^{2\pi} \int_0^r r \, dr \, d\theta \right) = 2\pi^2 r^2 R$$

where r is the inner radius and R is the main radius of the semi-Torus. Thus, aiming for a inner radius of 1 mm and a semi-toruss radius wich is fixed at 3.75 cm, one obtains a rotation speed of 300 revolutions per minute, as summarized on Table 1.

Table 1. Main characteristics of the film of liquid Si deposited on a rotating substrate.

Inner radius [m]	Semi-torus radius [m]	Volume of semi-torus [m ³]	Mass of deposited Si [g]	Rotation speed [r*s ⁻¹]
1*10 ⁻³	3.75*10 ⁻²	3.7*10 ⁻⁷	8.61	5

2.2 Experimental observations

2.2.1 Film thickness characterization

The first type of samples consists in a film deposited on a non-implanted substrate. The adhesion between the substrate and the film is observed, which is the first necessary condition for the epitaxial growth. This observation confirms the convenience of the experimental protocol for both sample and chamber preparation (exposed in the chapter 3, section 3.3). The measured thickness is basically from 50 µm to 200 µm as figured on the Fig. 13, which corresponds to the first type of numerical calculations, exposed earlier. The characteristic mountain shape implies a relatively good spreading of the liquid, facilitated by the rotation of the substrate.

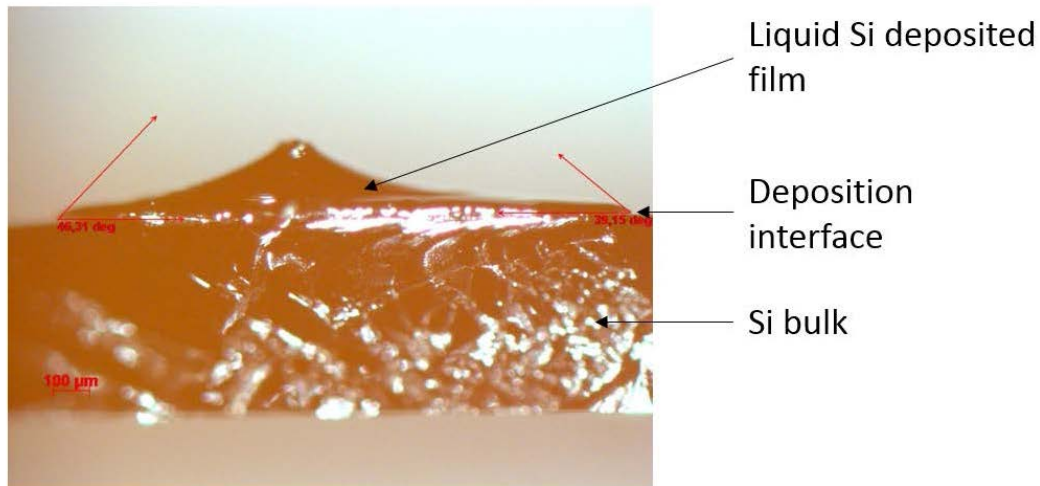


Figure 13: View by optical microscopy of the cross-section of the film deposited on the rotating substrate. Here the substrate is non-implanted and the film stands upon, without any splitting.

The second type of samples is obtained by the dropping of liquid silicon on top of an implanted substrate ($1.0 \cdot 10^{17} \text{ Hcm}^{-2}$ at 160 keV). In this case, the deposited films were found detached from the substrate, after chamber cooling. Considering the adhesion previously observed between the liquid and the non-implanted surface, we can conclude that the splitting indeed occurred by Smart Cut™.

The samples show a droplet shape, with a low spreading, as illustrated on Fig. 14 by optical microscopy. The droplet thickness is found to be between 1.5 mm and 2 mm, which is very similar to the orifice diameter (1.6 mm). At this stage, it is hard to conclude on why the spreading did not occur similarly than with non-implanted substrates.

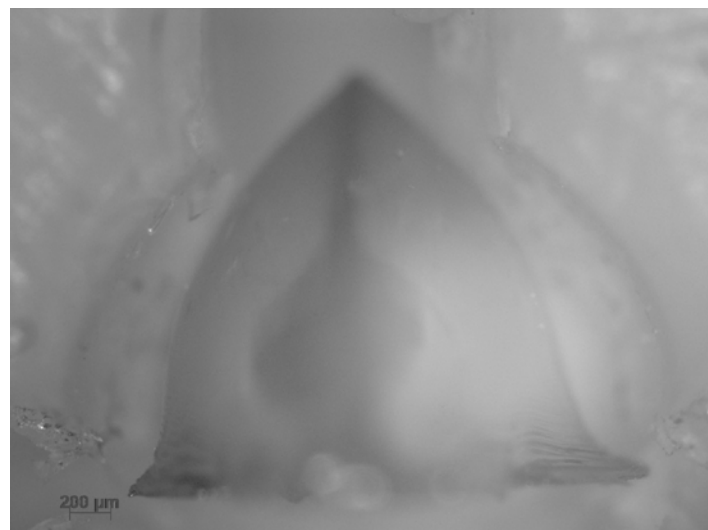


Figure 14: Optical microscopy view of the cross-section of the droplet deposited on the rotating substrate. The substrate is implanted in this case, and the deposited droplet is found detached by splitting.

The study of the impingement of liquid Si droplets on substrate of Nagashio et al. can be interestingly used in order to estimate the degree of undercooling of the droplet liquid when entering in contact with the substrate, as illustrated on Fig. 15 [2].

Thus, it is clear that there is no or a very low undercooling for the samples with a film shape (Fig. 13). On the other hand, the samples with a droplet shape (Fig. 14) indicates that the liquid is in a superheating state when touching the substrate surface.

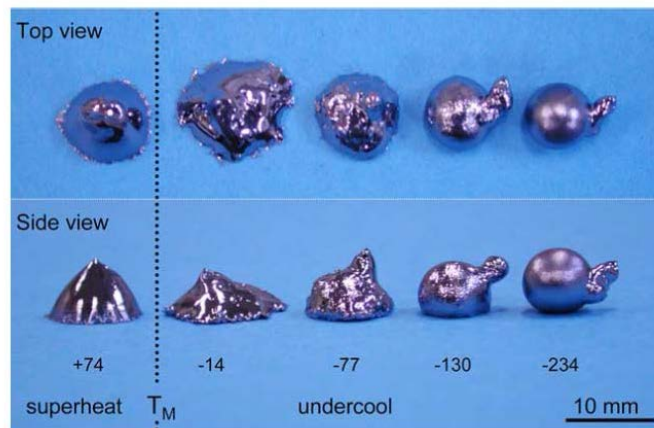


Figure 15: Macroscopic top/side views of samples dropped onto the silicon wafer at different initial undercoolings. The droplets were lined by initial undercoolings. Plus and minus indicates the superheating and undercooling, respectively [2].

Samples with fiber shape were also observed. This shape is coherent with the semi-torus considered to investigate the rotation speed of the equipment. The samples show an inner radius of around 200 μ m. The Fig. 16 gives an illustration of the cross-section of the fiber by optical microscopy.

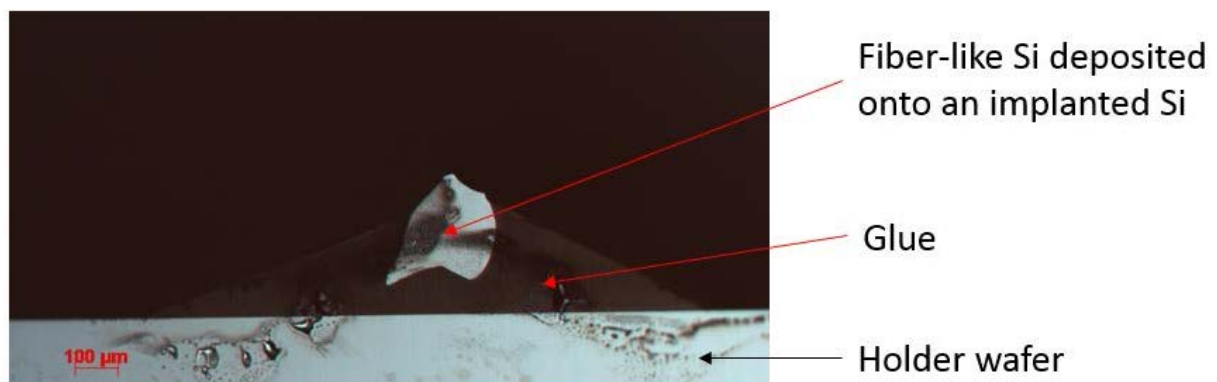


Figure 16: Optical microscopy image of the cross-section of a fiber-like shape structure deposited on the implanted substrate after detachment.

2.2.2 Generated stress in the substrate

It is worth noting that the non-implanted substrate was found broken at the vicinity of the deposited film. As can be observed on Fig. 17, the fracture follows the circular shape of the film. Into addition, the fracture is observed several seconds after the deposition, during the cooling. This breaking can be explained by the thermal stress generated by the cooling of the liquid film in contact with substrate, being initially at room temperature.

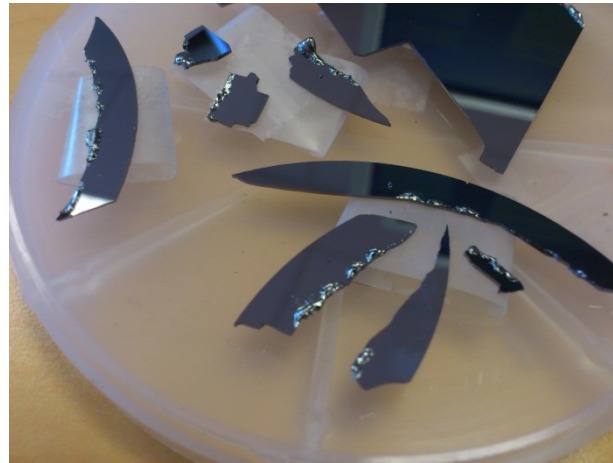


Figure 17: Substrate destroyed at the edge of the deposited Si layer

2.2.3 Thickness of the layer detached by Smart Cut™

The height profile of the donor wafer presented in Fig. 18 is characterized by mechanical profilometer, which gives a step of 1.5 μm , in good agreement with the R_p of implantation as calculated by TRIM modelling.

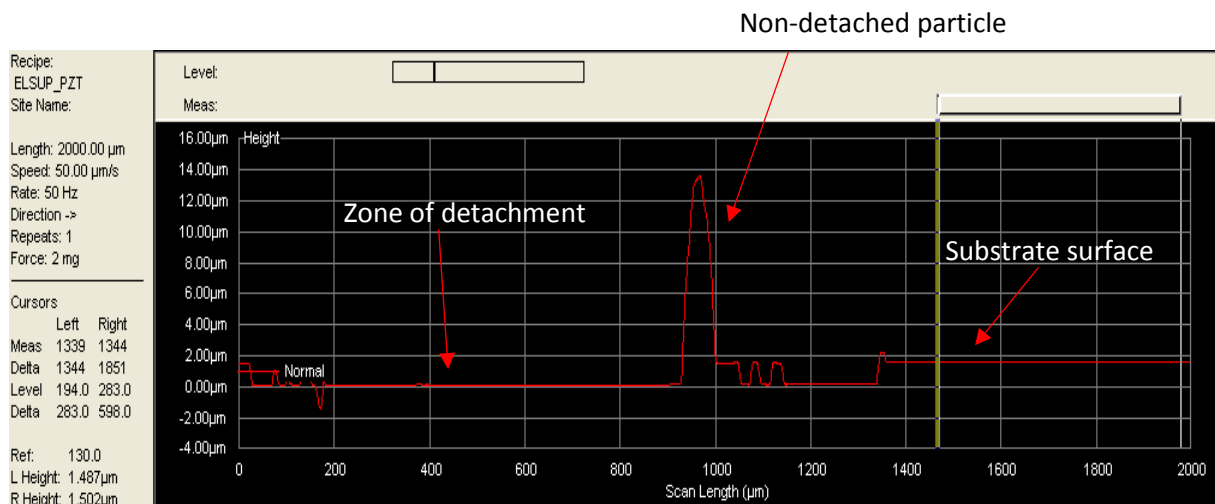


Figure 18: Height profile of the zone of detachment of the droplet measured by mechanical profilometer. The transferred thickness is 1.5 μm , which is coherent with the implantation depth.

This observation confirms that the detachment of the droplet consecutively to the deposition of liquid silicon upon the implanted substrate indeed occurs by Smart Cut™.

2.2.4 Characterization of the surface of the donor wafer by AFM

The surface of the donor wafer after detachment is very rough compared to the characterizations in the previous chapters. This roughness is confirmed by AFM characterization (see on Fig. 19). The surface presents a RMS roughness of 33.7 nm, to compare with typical 5-15 nm values of roughness obtained by laser-assisted splitting (see in chapter 5, section 5.2).

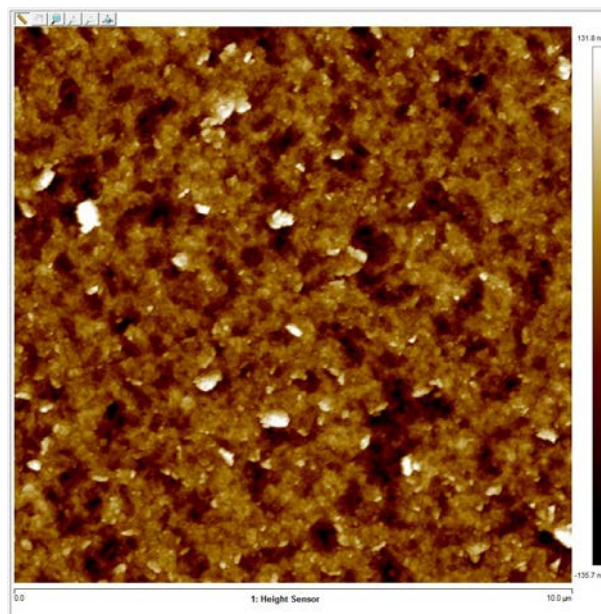


Figure 19: Roughness of the donor substrate initially implanted with $1.0 \cdot 10^{17} \text{ Hcm}^{-2}$ at 160keV, after detachment, characterized by AFM. The RMS roughness of the surface is equal to 33.7 nm.

The explanation can be a lower stiffness of the stiffener layer in contact with the implanted substrate (as proposed in the study of SOG compared to SOS by laser treatment). Indeed, the early stage of the defect nucleation occurs with a limited thickness of solidified silicon in contact with the implanted face.

2.2.5 Backside of the droplets detached by Smart Cut™

As can be observed by optical microscopy on Fig. 20, the backside of the droplets detached by Smart Cut™, shows circular rings, with an apparent high roughness. This is coherent with the roughness of the donor substrate, characterized in Fig. 19 by AFM. This ring structure can be explained by simultaneous solidification and spreading.

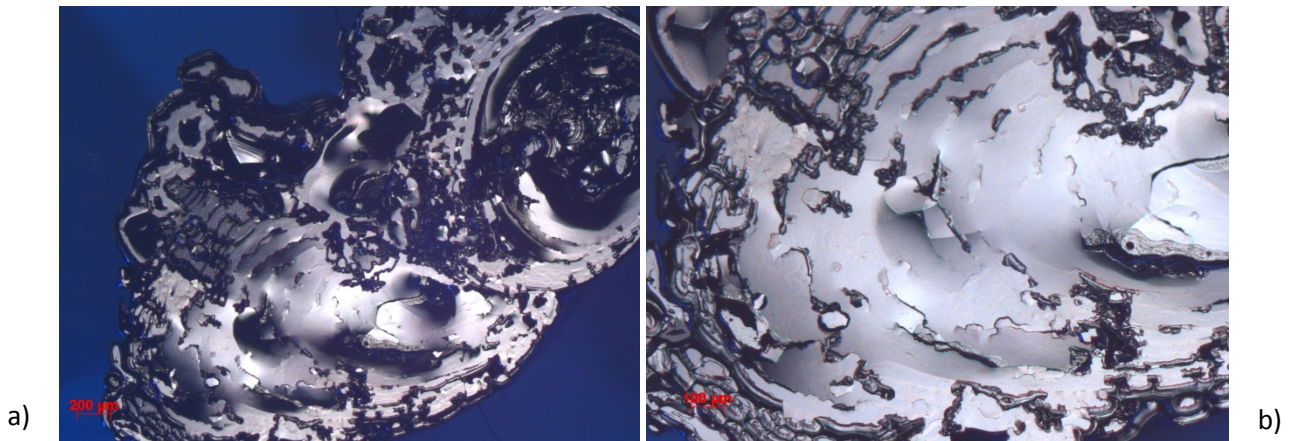


Figure 20: Images by optical microscope of the backside of the droplet, detached by splitting (a), detail of the central zone (b).

This observation confirms the challenge that represents the spreading of liquid silicon in contact with a cold substrate. These elements will be kept in mind, in order to design the dropping equipment of the last step of this study (section 7 of this chapter).

2.3 Film characterization

One of the main parameters which define quality of the detached films is their crystallographic orientation. A very efficient tool to study the local orientation of the films is EBSD technique. It allows to produce orientation maps of the whole transferred film as well as visualize areas close to the substrate – film interface. A complementary analysis will be done by HR-TEM at the close vicinity of this interface.

2.3.1 EBSD cartography of sample deposited onto a non-implanted substrate

The first analysis is presented on Fig. 21 and gives the EBSD contrast recorded at (100) conditions for the deposited film spread on a non-implanted sample. It clearly shows continuity between the substrate and the film, despite the interface with the substrate at the bottom of the film can be still observed (illustrated by the red arrow).

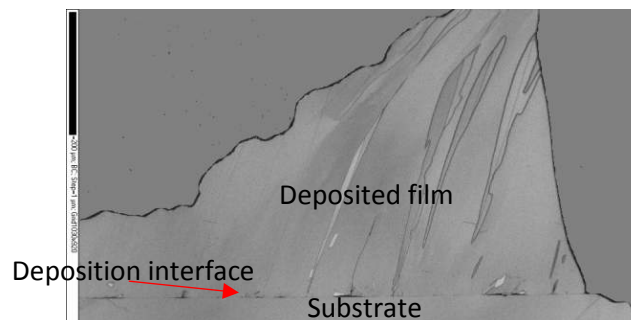


Figure 21: Image by EBSD band contrast of the film deposited on a non-implanted substrate of (100) orientation. The interface between the film and the substrate is identified by the red arrow.

Additional EBSD analysis illustrated on Fig. 22, shows that most of the film is single crystalline. Moreover the monocrystalline part of the film follows the (100) orientation of the substrate (a proper image processing shows that 88.9% of the film follows this substrate orientation). It tends to prove that the solidification of the liquid film indeed follows a liquid phase epitaxial growth, with the implanted surface acting as a seed substrate. It is worth noting that this very high ratio of monocrystalline film is far better than previous studies dealing with molten Si droplets impinging on a Si substrate ([2-3]). We will come back on these comparative elements in section 6.1.1.

It is now necessary to focus our attention on the microstructure and especially the morphology of the defects in the grown film. The few grains have a needle shape and are oriented along the growth direction, whereas the rest of the film is monocrystalline. That is, most of the growth occurred parallel to the surface with almost no nucleation elsewhere in the liquid. On the other hand, this 1D profile along the growth direction can be explained by a thermally controlled growth [2, 4]. On the other side, the profile of defects in the film is fully coherent with a very low undercooling of the melt before solidification [2].

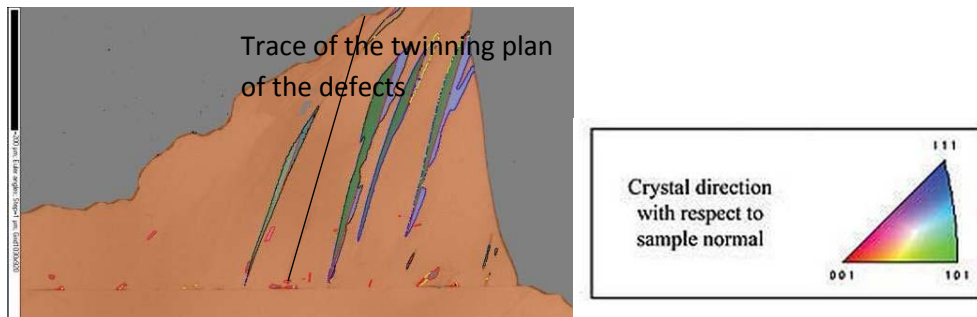


Figure 22: Image by EBSD of a film deposited on a non-implanted substrate of (100) orientation. The trace of the twinning plan is illustrated by the black line.

It is worth noting that no precipitates such as carbonated precipitates could be detected, despite the use of a graphite crucible that can be a source of carbon contamination [5].

The Euler's contrast of the EBSD cartography allows to determine the relation between the grains and the rest of the film, as illustrated on Fig. 23, where only the grain boundaries remain. It appears that most of grains show twins by the middle and have a $\Sigma 9$ or $\Sigma 27$ relation with the rest of the film. The presence of these grains might be explained by a multi-twinning effect, those grains resulting from a grain with a $\Sigma 3$ relation somewhere else in the film.

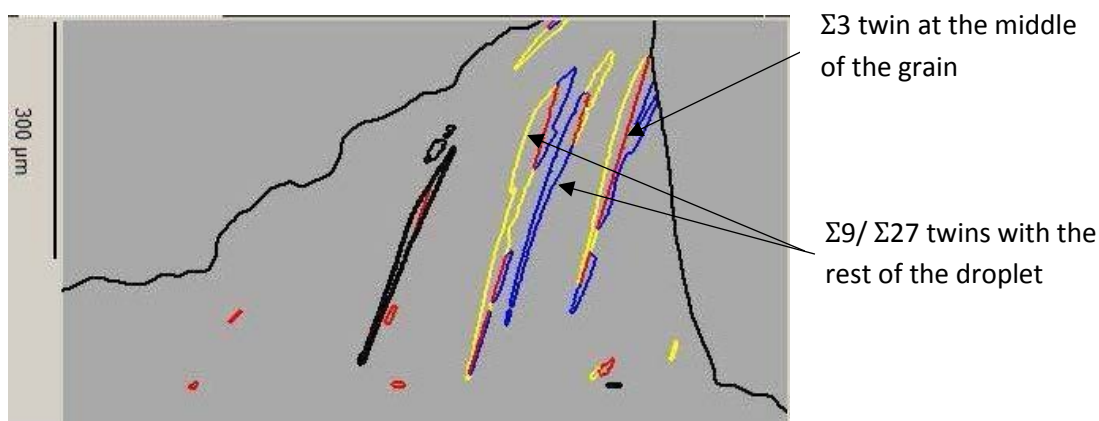


Figure 23: Euler's contrast of the EBSD image of the film deposited on a non-implanted substrate of (100) orientation, after image processing. The red grains correspond to $\Sigma 3$ twin, the yellow grains correspond to $\Sigma 9$ and the blue grains to $\Sigma 27$.

2.3.2 HR-TEM imaging at the interface between the substrate and the droplet

A more detailed imaging of the interface between the substrate and the solidified film is given in Fig. 24. It appears clearly that the crystalline network is maintained during the solidification of the spread of liquid, confirming the epitaxial growth. The Fig. 24 interestingly shows the formation of a twin at the interface.

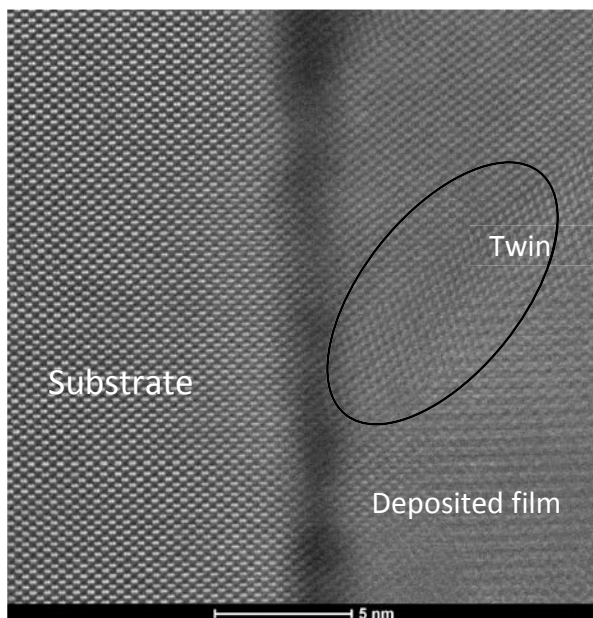


Figure 24: HR-TEM image of the interface of the film deposited on a non-implanted substrate.

2.3.3 Deposition onto an implanted substrate

The Fig. 25 shows the cross-section of a film deposited on an implanted substrate after detachment by splitting. The detached droplet is glued on a (100) holder, before polishing the bonded system.

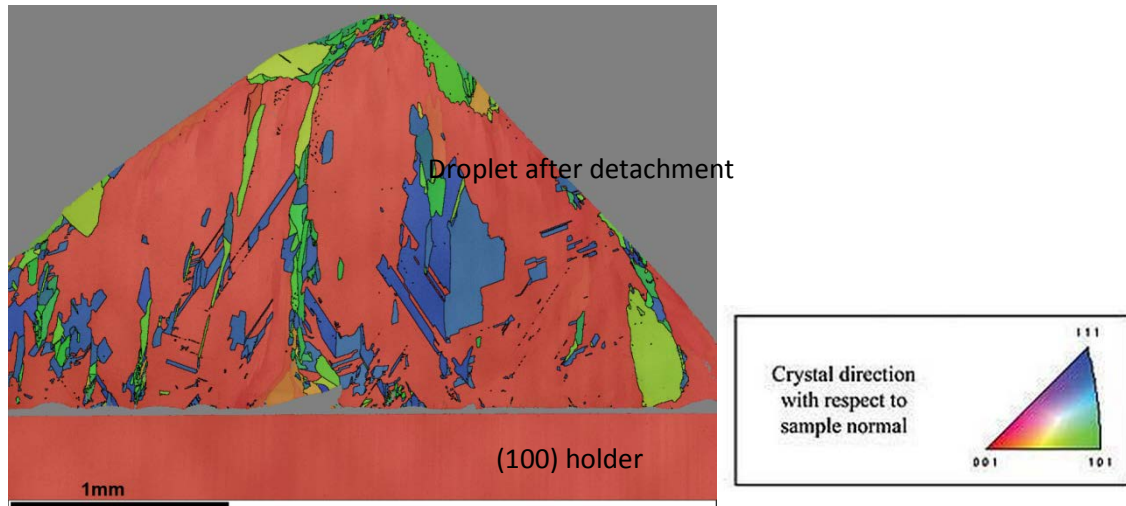


Figure 25: EBSD cartography of the cross-section of a detached droplet after deposition of liquid Si on an implanted substrate. The droplet is glued (gray layer) onto a (100) holder, placed below.

It appears clearly that the solidified droplet presents a larger amount of grains compared to sample deposited on a non-implanted substrate. An image processing shows that 67.7% of the droplet follows the same crystalline orientation. In order to verify that the solidification follows an epitaxial growth, the bottom part of the droplet will be analyzed by EBSD.

2.3.4 Interface between the implanted substrate

The Fig. 26 gives the detail of the bottom of the droplet by SEM. The interface between the droplet and upper part of the implanted substrate being detached can be clearly identified. The thickness of this layer is equal to $1.35\ \mu\text{m}$, what is coherent with the TRIM calculation presented earlier (with a R_p of implantation equal to $1.5\ \mu\text{m}$).

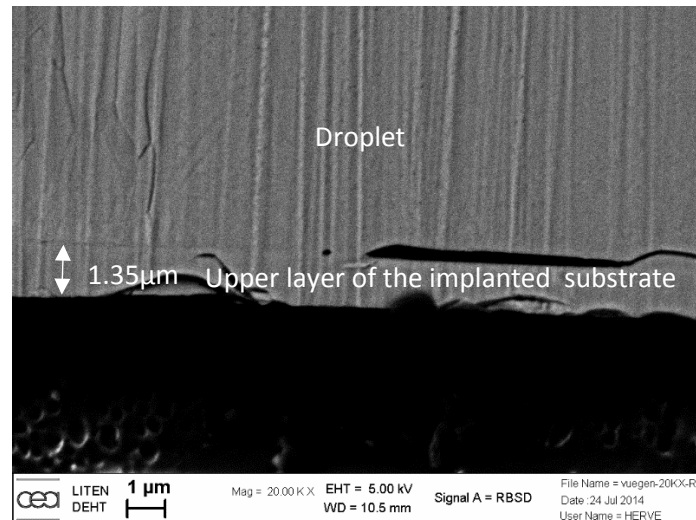


Figure 26: Detail of the bottom of the droplet after detachment by splitting by SEM imaging.

The Fig. 27 shows an EBSD cartography of this same area, showing that the overall orientation of the droplet is indeed defined by the detached layer of the substrate.

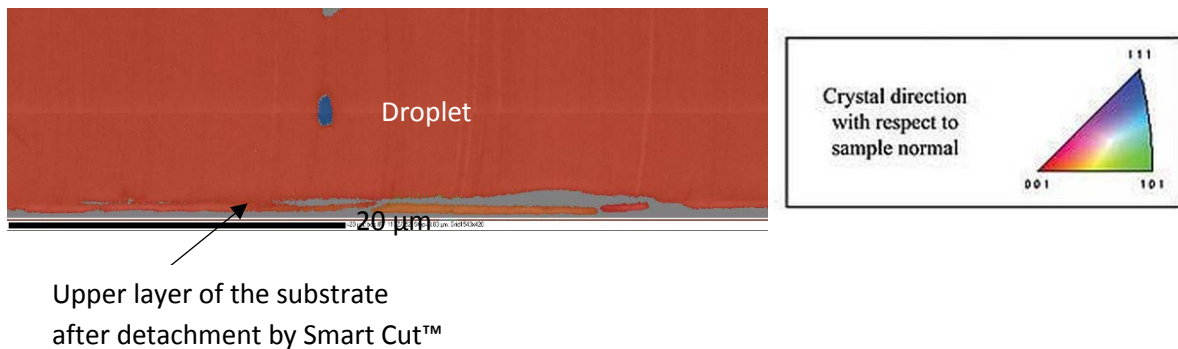


Figure 27: Detail of the bottom of the droplet after detachment by splitting by EBSD cartography. The gray zone corresponds to the glue.

From these observations, it is possible to assess that the droplet observed here is indeed detached by Smart Cut™ from the substrate by splitting in the implanted zone.

2.3.5 Grains study in the droplet after detachment by Smart Cut™

The Euler's contrast of the cross-section of a droplet deposited onto an implanted substrate is given in Fig. 28. Long defects along the growth direction (with a twin at the middle) can be similarly observed, as indicated by the black arrow. On the other side, a lot of small defects do not present a symmetry with the substrate or the matrix crystal, as figured by the absence of twins at the grain boundaries. These defects are concentrated at the top of the droplet, or close to non-contact areas between the droplet and the substrate. This can be explained by a nucleation occurring in the liquid.

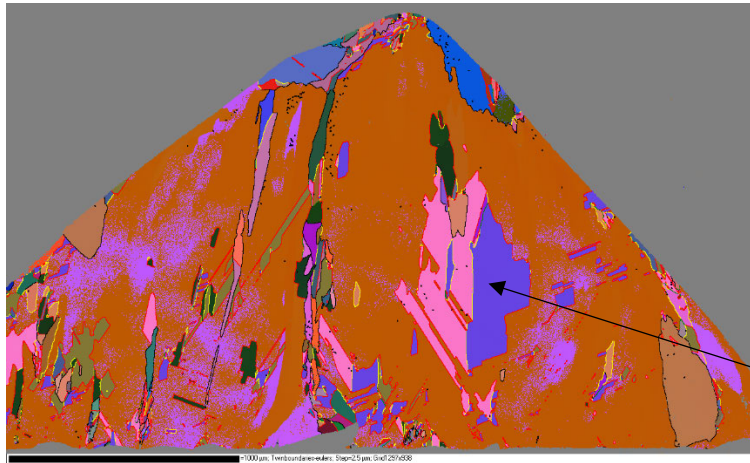


Figure 28: EBSD cartography with Euler contrast of the cross-section of a detached droplet after deposition of liquid Si on an implanted substrate. The red grains correspond to $\Sigma 3$ twin, the yellow grains correspond to $\Sigma 9$ and the blue grains to $\Sigma 27$.

3 Deposition of liquid Si by use of a self-aligned crucible (collaboration with SiMaP laboratory)

The equipment considered in this part is located in SiMaP and is figured on Fig. 29. It consists in releasing a load of liquid Si onto an inclined sample (with different inclination angles).

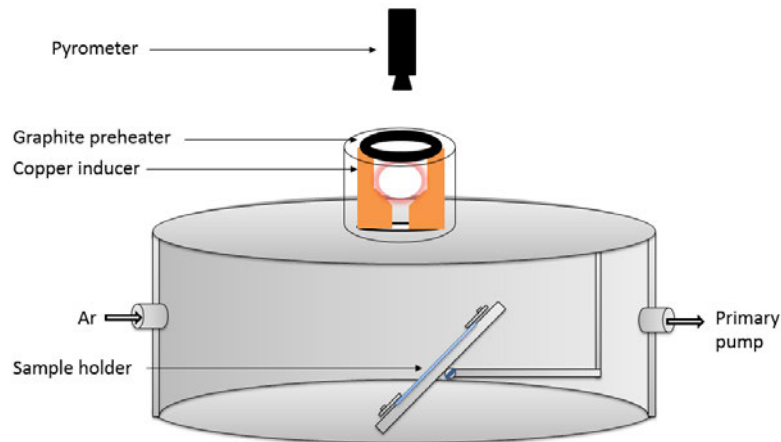


Figure 29: Schematic representation of the liquid Si deposition chamber, using a self-crucible of liquid Si as the source.

3.1 Preliminary observations

3.1.1 Spreading of the liquid on the substrate

The first observation concerns the good spreading of the liquid upon the inclined substrate. The Fig. 30 shows two different samples, presenting a mean width of around 2 cm, comparable to the diameter of crucible orifice of the equipment. Additionally, the thickness is measured as thin as 200 μm for parts as large as several cm^2 . The characterization for both width and thickness is summarized on Fig. 31.

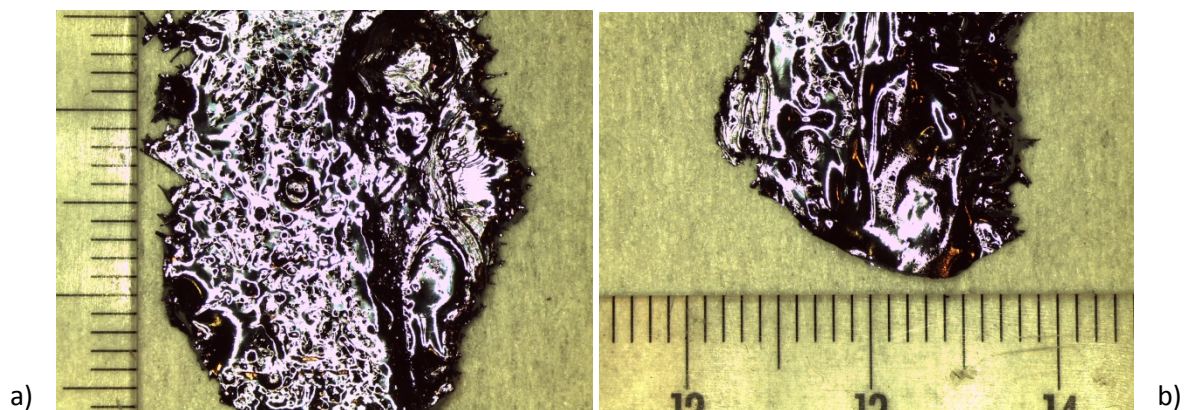


Fig. 30: Image of the spread liquid after deposition onto a non-implanted sample inclined at 45°(a), and inclined at 30° (b).

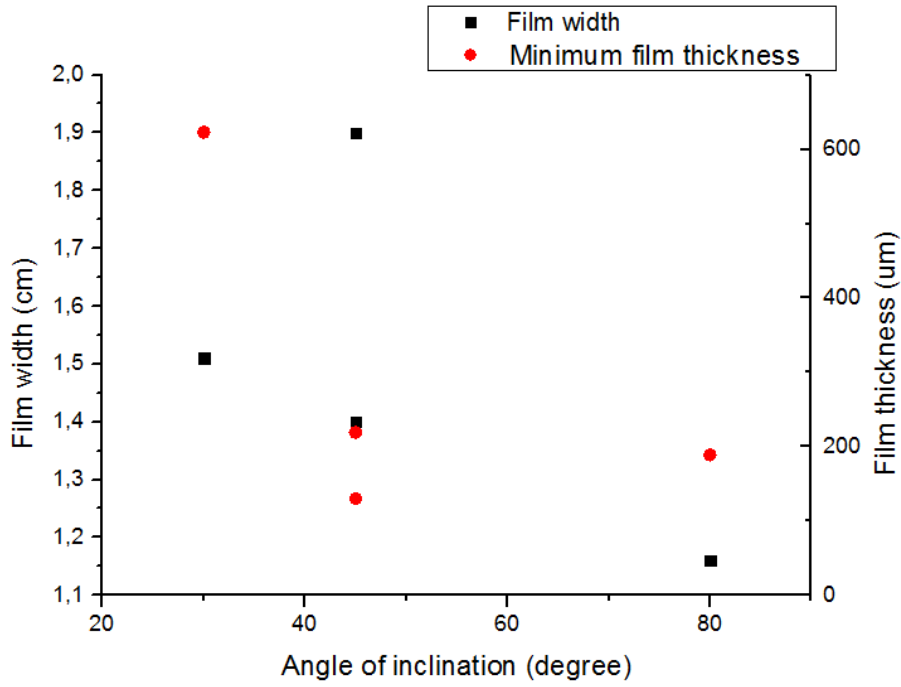


Figure 31: Characterization of films grown by self-aligned crucible deposited in SiMaP.

Thus, the system seems to reach a steady state corresponding to a flow upon an inclined plane during the liquid spread. The velocity distribution in the liquid is described by the Navier-Stokes equation as following:

$$\vec{v} = \frac{\rho g \sin \alpha}{2\eta} (2h - y)y\vec{e}_x$$

where ρ and η are resp. the density and viscosity of liquid Si, α is the angle of inclination and h is the thickness of the liquid film. Fig. 32 gives an illustration of the system.

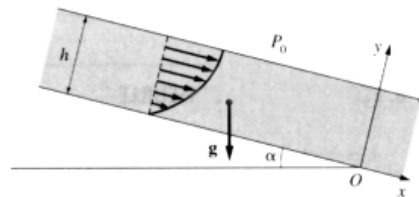


Figure 32: Illustration of the inclined plane with a flow in stationary regime.

Therefore, integrating this distribution on x over the width of the film, the flow rate can be determined. The results are summarized in the table 2 and show a large dispersion of values, in terms of flow rate. This dispersion can be explained by the instability of the flow rate of the crucible, indeed observed experimentally.

Table 2. Summary of the flow rate of liquid Si upon the inclined substrate.

Angle of inclination [degree]	Mean thickness [μm]	Film width [cm]	Flow rate [g/s]
30	623	1.51	104.7
45	130	1.4	1.6
80	189	1.16	4.7

3.1.2 Adhesion between the substrate and the deposited films

It is worth noting that for almost all samples, no adhesion between the liquid film and the substrate is observed (i.e. the film of Si is not attached to the substrate, even with the non-implanted sample). Several chamber parameters have been varied in order to reduce the contamination of the chamber, without effect. The 3 experimental conditions are summarized in the Table 3. As a reminder, the preparation of the sample surface is kept constant. Indeed, this surface preparation has been effective for the deposition on a rotating substrate. The procedure consists in an oxide removal by HF acid, a rinsing with ethanol and IPA and an Ar drying. Finally, the control of the temperature of liquid Si is realized by varying the power of the induction.

Table 3. Summary of the deposition conditions with the self-aligned crucible.

Experimental configuration	Chamber preparation	Chamber atmosphere during deposition	Temperature of Si liquid before cast [$^{\circ}\text{C}$]	Angle of inclination (degree)
				<i>Green : adhesion</i>
				<i>Red : no adhesion</i>
1	IPA cleaning, primary vacuum	P _{atm} of Ar	1450	0 ; 80
2	IPA cleaning, primary vacuum	Overpressure of Ar (no valve)	1450	45
3	IPA cleaning, primary vacuum	Overpressure of Ar (with valve)	1410	30 ; 45 ; 0
<i>Rotating substrate (previous results)</i>	<i>IPA cleaning, no vacuum</i>	<i>Overpressure of Ar (no valve)</i>	<i>1450</i>	<i>0</i>

Thus, it appears that the parameters that we have varied do not improve the possibility of adhesion with the substrate surface. Paradoxically, the only adhesion between the liquid film and the substrate

occurs with an atmosphere pressure of Ar, configuration 1 in the Table 3 (i.e. less optimized conditions than an overpressure of Ar).

We will come back on the experimental conditions in a comparative study at the end of the chapter.

3.1.3 Formation of SiO₂ layer at the vicinity of the solidified films

A crown of a bluish thin layer is observed at the vicinity of the solidified films for almost all the samples. This thin film is very probably a thermally-formed SiO₂ layer, as the layer vanishes after a few seconds with a HF acid droplet (see on Fig. 33).

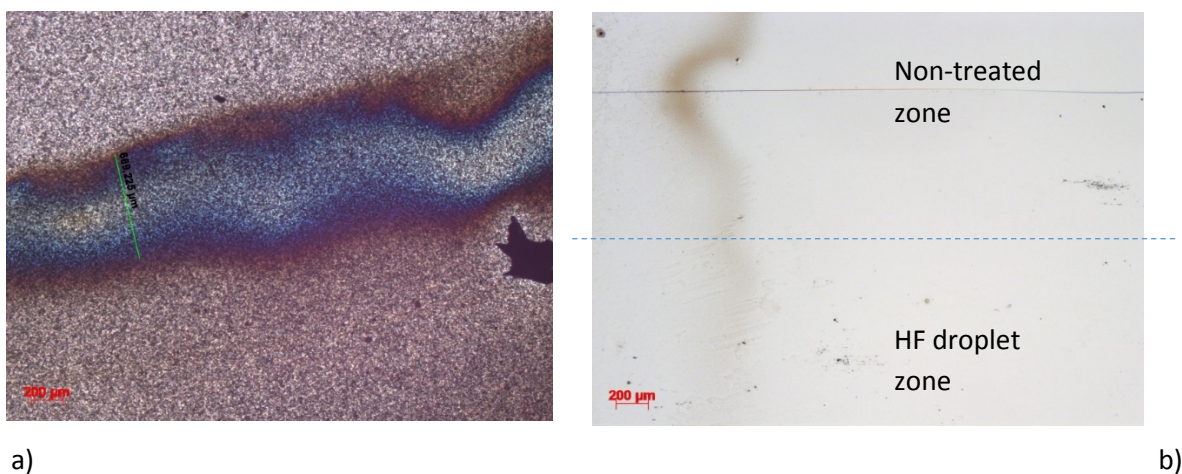


Figure 33: Images of the droplet border after deposition onto a horizontal non-implanted substrate (a), after deposition onto a non-implanted substrate inclined at 80° (b).

The oxide formation is a proof of the presence of contaminants, such as O₂, H₂O or organic impurities. These impurities can be most probably at the surface of the sample or in the chamber atmosphere. A contamination from the liquid Si can be a priori excluded, as the liquid Si acts as an impurities trap instead of a source of.

According to a color chart in Fig. 34 a), it is possible to estimate the oxide thickness at around 100 nm. Nevertheless, the growth of such a thickness of SiO₂ would require at least several minutes at the estimated temperature at the vicinity of the droplet (i.e. 1200 °C, confer the modelling part) (see on Fig. 34 b) [7]). Additionally, this kinetics would be observed in wet oxygen conditions, what is not the case in our chamber. Thus, the presence of this oxide crown remains ambiguous.

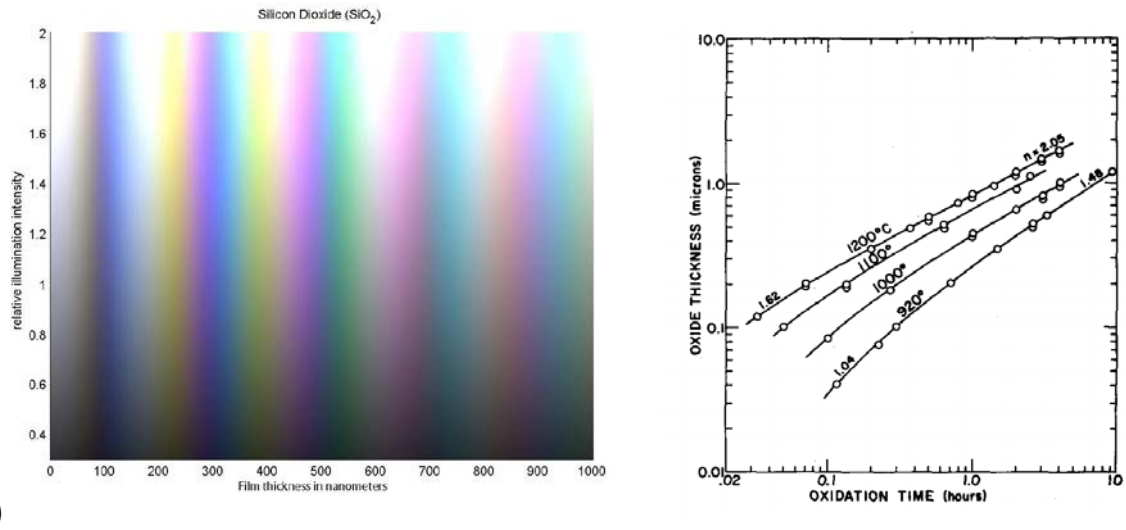


Figure 34: Chart of oxide thickness color [6] (a), kinetics of oxidation of silicon in wet oxygen [7] (b).

3.1.4 Blistering analysis

Blisters are observed for all the implanted substrates, below and at the vicinity of the droplet impact. Their growth results from the thermal diffusion during the droplet solidification and cooling. The Fig. 35 shows two optical microscope images of the contact zone below the droplet. The squared shape of the exfoliated part can be interestingly noticed, for both low and high dose of implantation. The orientation of the edges of exfoliated areas is along $\langle 110 \rangle$ directions, with the (001) wafer considered here, as already observed in the chapter 4, section 2.1.

The density of blisters is emphasized here compared to the blistering by laser annealing in chapter 5, section 3.2. This can be explained by the longer annealing time during the LPE compared to the laser annealing (chapter 5, Fig. 22 a)).

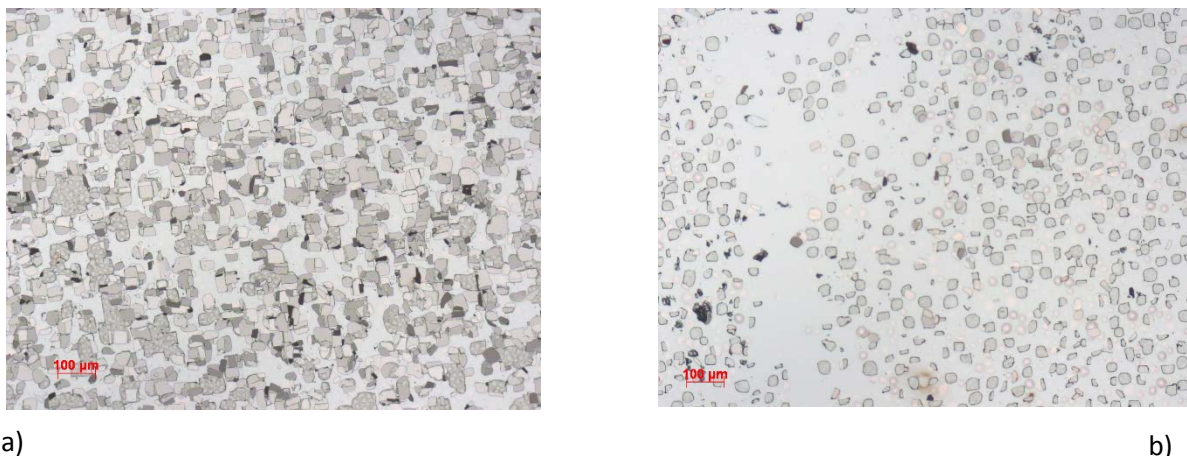


Figure 35: Optical microscope image of the surface blisters on the implanted substrate $1.0 \times 10^{17} \text{ Hcm}^{-2}$, 160 keV placed below the liquid droplet of Si (a) similar observation with an implanted substrate $5.0 \times 10^{16} \text{ Hcm}^{-2}$, 160 keV (b).

The mean diameter of blisters is about $48\text{ }\mu\text{m}$ for $1.0 \cdot 10^{17}\text{ Hcm}^{-2}$ at 160 keV samples, compared to $25\text{ }\mu\text{m}$ in case of implantation with $5.0 \cdot 10^{16}\text{ Hcm}^{-2}$ at 160 keV.

3.2 EBSD cartography of sample deposited on an implanted substrate

EBSD analysis has been carried out for a complete set of samples and we propose to focus on the two most interesting ones, both films being deposited on a substrate after implantation at $1.0 \cdot 10^{17}\text{ Hcm}^{-2}$ and 160keV. The first sample is presented on Fig. 36 and is deposited in an atmospheric pressure of Ar. No sign of adhesion between the substrate and the film can be found. Nevertheless, it appears that a few domains show the crystal orientation of the substrate (001), over 10% of the film cross-section. This surprising result can be explained by the strong blistering and film exfoliation, at the zone of contact between the substrate and the liquid film, as seen on Fig. 36. Thus, the explanation of these (001) domains would be the detachment of small exfoliated domains from the substrate to act as small seeds during the solidification of the liquid film.

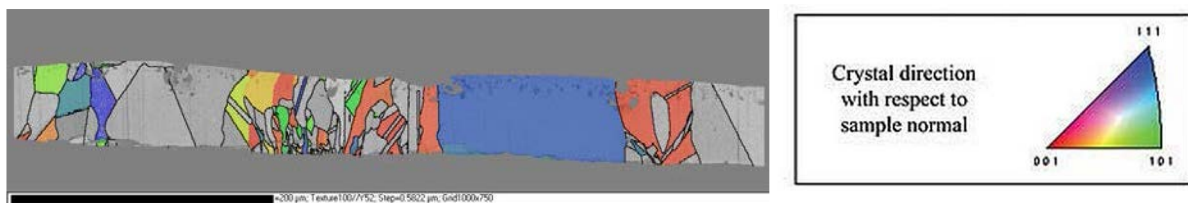


Figure 36: EBSD cartography of the cross-section of a detached droplet after deposition of liquid Si onto a substrate implanted with $1.0 \cdot 10^{17}\text{ Hcm}^{-2}$ and 160keV substrate in a deposition chamber with Ar at P_{atm} .

The EBSD cartography presented in the Fig. 37 shows similar observation but with a higher amount of domains presenting the crystal orientation of the substrate (i.e. 26% of the cross-section). This result can be explained by the different atmosphere of deposition chamber (i.e. over-pressure of Ar in this configuration).

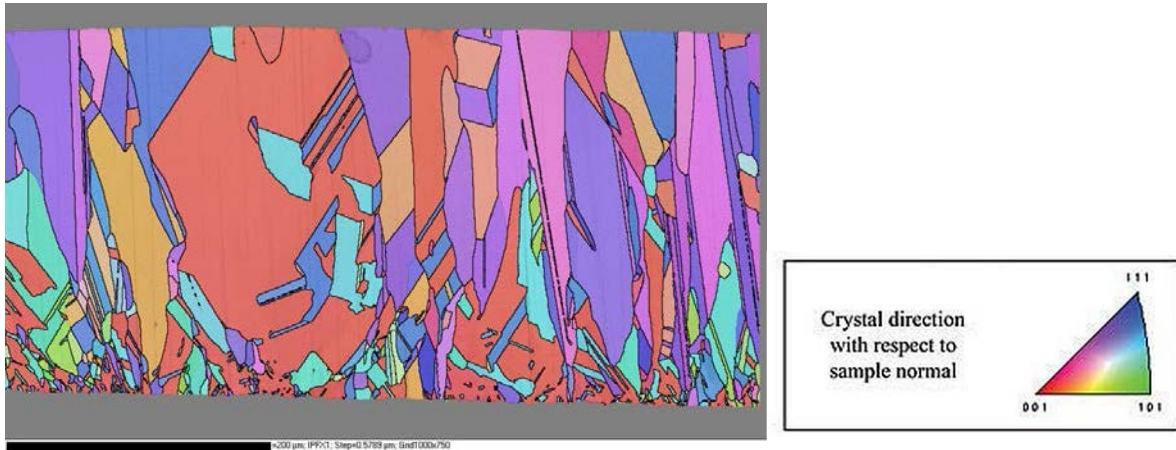


Figure 37: EBSD cartography of the cross-section of a detached droplet after deposition of liquid Si onto a substrate implanted with $1.0 \cdot 10^{17} \text{ Hcm}^{-2}$ and 160keV substrate with the deposition chamber in overpressure of Ar.

As an intermediate conclusion, this study of deposition on an inclined-substrate has shown the possibility of a good spreading on an implanted substrate. However, the sought-after epitaxial growth is lower than for the preliminary results, considering the efforts to reduce the contaminations inside the deposition chamber. Therefore, we have considered a last deposition equipment, offering the possibility to put the deposition chamber under a secondary vacuum (i.e. up to 10^{-5} mbar).

4 Deposition of liquid Si by electromagnetic levitation (collaboration with SiMaP laboratory)

The last equipment considered in this work also relies on the self-crucible principle, but with a higher level of confinement of the levitated droplet. Thus, the droplet of liquid Si is in levitation, without any contact with the copper inducers. Additionally, the chamber is equipped with a turbo-molecular pump and an ionic pump, which allows to reduce the presence of contaminants inside the chamber. In order to reduce the heating of the sample by the radiation of the molten droplet into levitation, the substrate holder is put away from the deposition trajectory during the thermal ramp, as illustrated on Fig. 38.

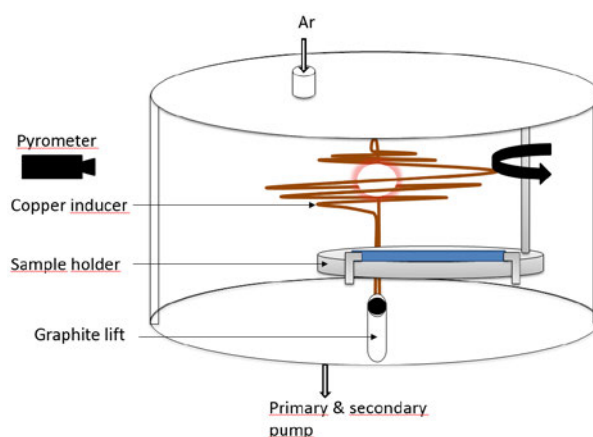


Figure 38: Schematic representation of the deposition chamber by electromagnetic levitation.

4.1 Summary of the experimental conditions

The table 4 summarizes the conditions of deposition. Thus, different conditions of temperature and of chamber atmosphere during the deposition are considered. The adhesion between the liquid film and the substrate is observed for the majority of the samples. It is worth noting that no adhesion is observed for the lowest initial temperatures of liquid. Additionally, it appears that the vacuum during the deposition (limited to $2 \cdot 10^{-4}$ mbar to avoid the evaporation of the liquid Si droplet into levitation) helps the adhesion. Nevertheless, the role of each single parameter (i.e. temperature of droplet and chamber atmosphere), is difficult to distinguish.

Table 4. Summary of the deposition conditions with the self-aligned crucible.

Experimental configuration	Chamber preparation	Chamber atmosphere during deposition	Temperature of Si liquid before cast [°C]
1	IPA cleaning, secondary vacuum	P_{atm} of Ar	1420 ; 1465 ; 1580
2	IPA cleaning, secondary vacuum	Vacuum ($2 \cdot 10^{-4}$ mbar)	1530 ; 1540 ; 1560

4.2 General observations of the deposited films

The films obtained by electromagnetic levitation present comparable thickness than the films presented in the previous part. The Fig. 39 gives two SEM characterizations of a film deposited on a non-implanted substrate and deposited on an implanted substrate after detachment, with a thickness between 150 μm and 200 μm .

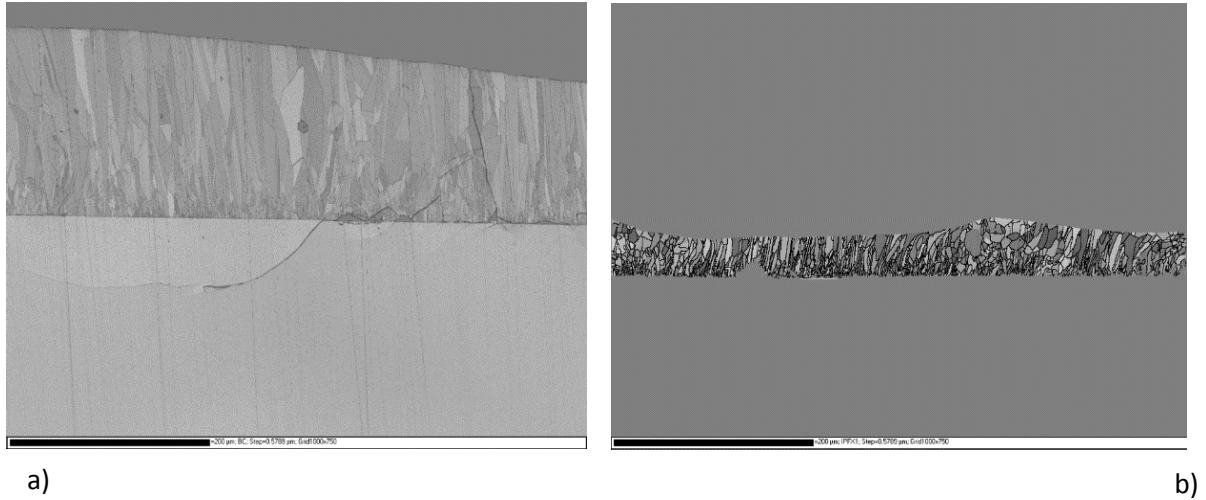


Figure 39: SEM images of the cross-section of a film deposited onto a non-implanted substrate (a), deposited onto an implanted with $5.0 \cdot 10^{16} \text{ Hcm}^{-2}$ at 160 keV (b).

4.3 Detachment by Smart Cut™

Contrary to the samples by self-aligned crucible, zones of detachment by splitting can be observed (see Fig. 40). It is interesting to notice that a thin layer of SiO_2 is again observed at the crown of the detached film. Thus, in spite of the better control on the chamber atmosphere brought by this third deposition equipment, the source of contamination is apparently not avoided. Nonetheless, the observation of detachment zones proves the occurrence of both adhesion and detachment by Smart Cut™. We will go back on the possible sources of contamination in section 6.1.1.

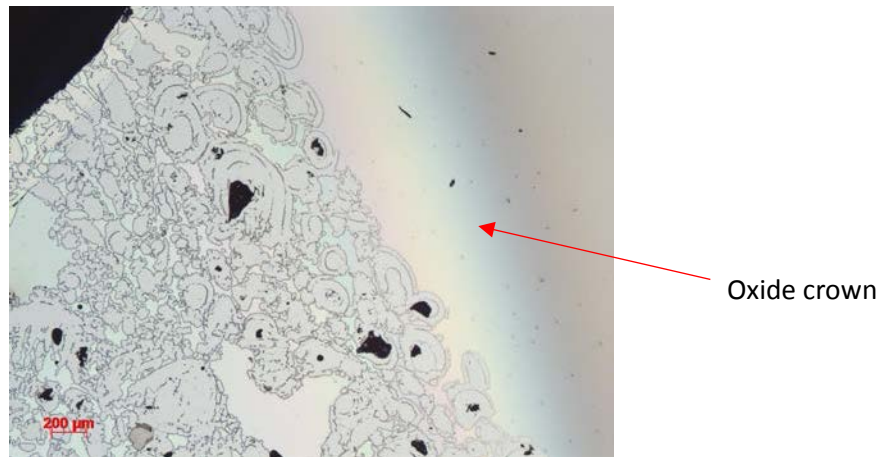


Figure 40: Optical microscope image of the zone of detachment of the deposited film. The film is deposited from a liquid initially at 1560 °C in vacuum ($6 \cdot 10^{-4}$ mbar).

4.4 EBSD characterizations

This final part of EBSD characterizations will present cartographies of samples deposited in vacuum. It will show the complexity to establish an exhaustive comprehension of the role of the different parameters in the epitaxial growth.

4.4.1 EBSD cartography of samples deposited on a non-implanted substrate

The two samples presented here are deposited in very close conditions for both temperature and chamber atmosphere (secondary vacuum). Nevertheless, as the comparison between Fig.41 and Fig.42 highlights, the microstructures are completely different. Almost no epitaxial domains exists in the Fig. 41, whereas 56% of the film follows the substrate orientation in Fig. 42.

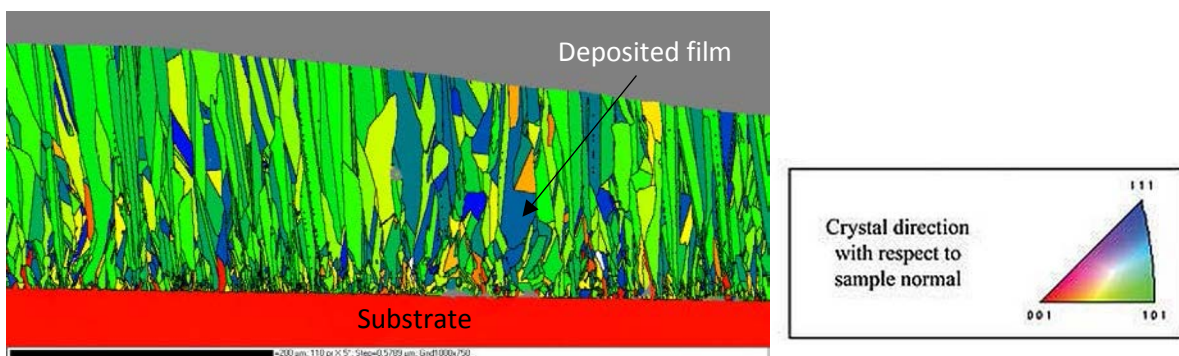


Figure 41: EBSD cartography of a film deposited onto a non-implanted substrate from a liquid initially at 1540 °C, in vacuum ($2 \cdot 10^{-4}$ mbar).

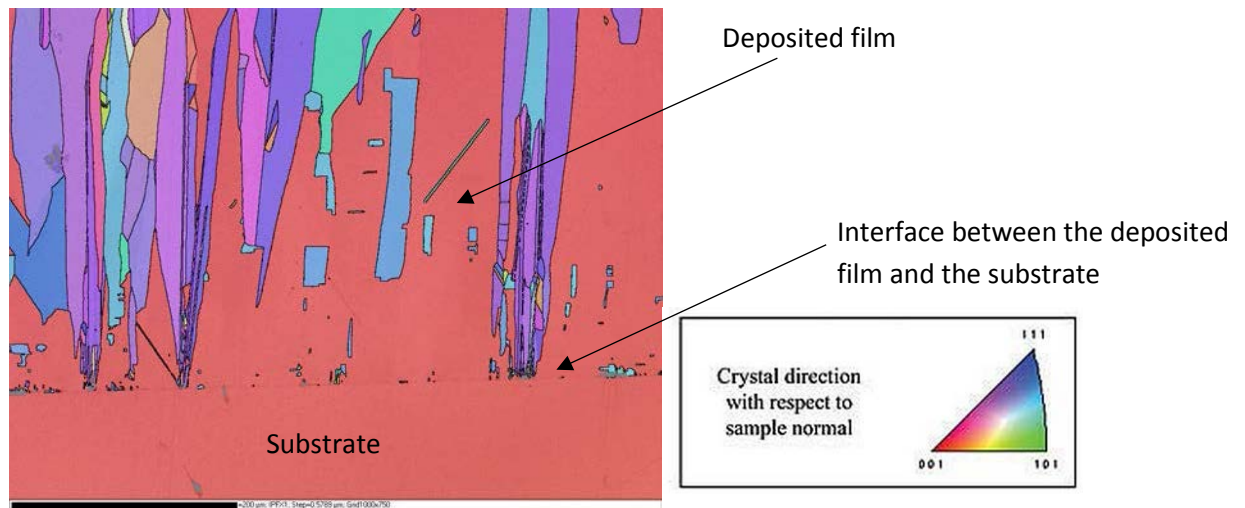


Figure 42: EBSD cartography of a film deposited onto a non-implanted substrate from a liquid initially at 1530 °C, in vacuum ($6 \cdot 10^{-4}$ mbar).

From the comparison between the Fig. 41 and Fig. 42, it is possible to exclude any role of the vacuum. Indeed, a better epitaxial growth is observed, with a higher pressure ($6 \cdot 10^{-4}$ mbar for the sample in Fig. 42, as compared to $2 \cdot 10^{-4}$ mbar for the sample in Fig. 41). In order to bring further comprehension to this observation, HAADF characterization at the interface between the film and the substrate will be presented a bit later in the chapter (section 6.1.1).

4.4.2 EBSD cartography of a sample deposited on an implanted substrate

The Fig. 43 presents an EBSD cartography, of a film detached by Smart Cut™ from the substrate. The epitaxial domains are again almost absent (covering less than 2% of the film cross-section). The bottom of the film presents some small domains apparently originating from the detachment of the upper layer of the implanted substrate.

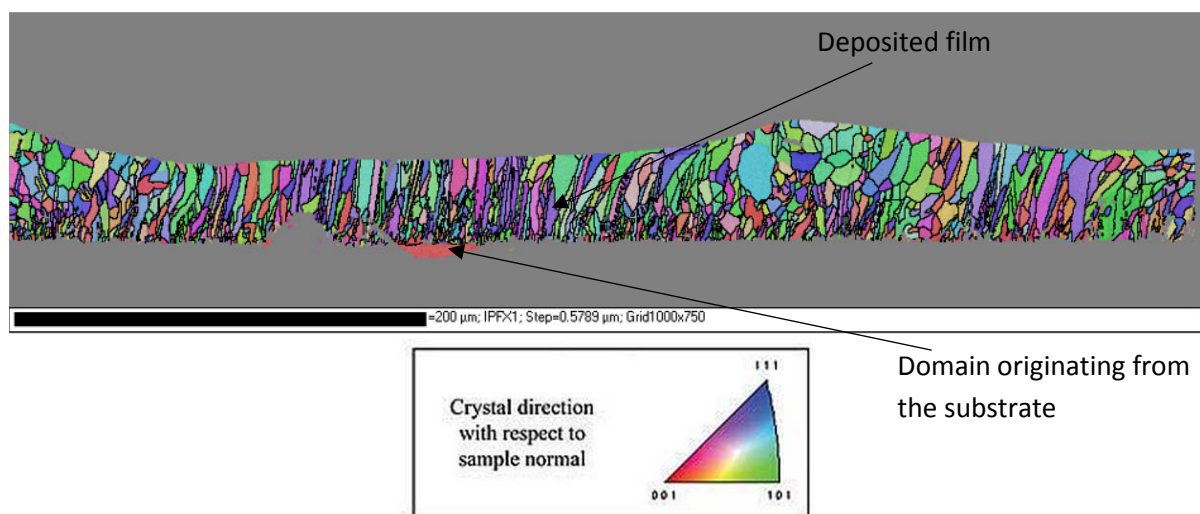


Figure 43: EBSD analysis of a film deposited on an implanted substrate ($5 \cdot 10^{16}$ Hcm⁻² at 160keV) from a liquid initially at 1530 °C, in vacuum ($6 \cdot 10^{-4}$ mbar).

4.5 High Angle Annular Dark Field (HAADF) analysis at the interface between the film and the substrate

In order to understand the absence of epitaxial growth, HAADF analysis is realized for some samples at the interface between the deposited film and the substrate. The samples analyzed here are deposited films on non-implanted substrate. Indeed, these samples are supposed to bring optimal conditions for the epitaxial growth, as we have seen at the beginning of the chapter (section 2.3).

From the TEM image presented in Fig. 44 (b), the contrast between the perfect single crystal of the substrate and the disordered film is clearly identified.

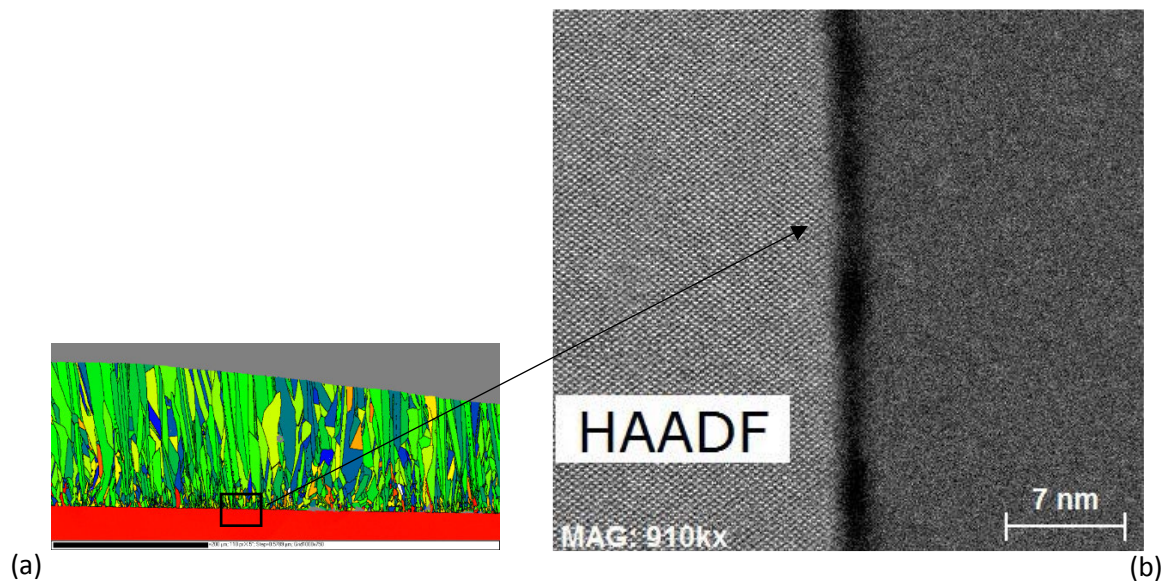


Figure 44: EBSD analysis of a film deposited on a non-implanted substrate from a liquid initially at 1540°C in vacuum ($2 \cdot 10^{-4}$ mbar) (a), HAADF analysis of the same sample at the interface between the substrate and the film (b).

The analysis of the elements present at the interface (fig. 45), clearly shows a strong concentration of O at the interface. This high concentration shows the presence of a layer of SiO_2 , possibly formed by the presence of water at the surface of the substrate. Interestingly, Cl can be also detected at the interface. As the surface preparation does not include any Cl-based chemicals, it can be explained by the lubricants of the vacuum pumps.

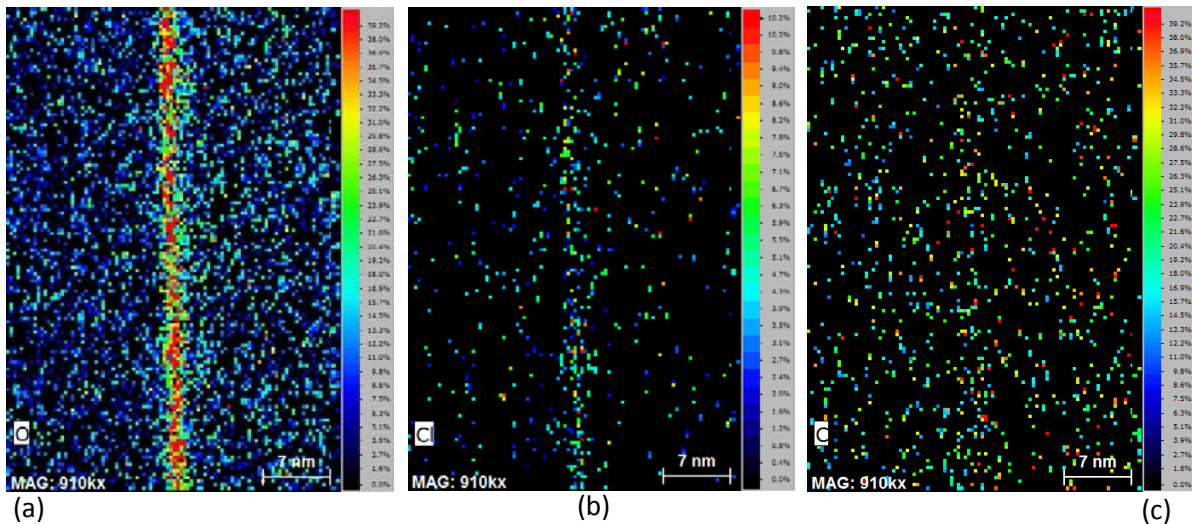


Figure 45: Concentration of O (a), concentration of Cl (b), concentration of C (c).

5 Photoluminescence analysis

The Fig. 46 shows different photoluminescence spectra, unfortunately limited to the samples realized by self-aligned crucible (i.e. with a low epitaxial growth).

The bulk Si substrate acts here as the reference. The main part of the photoluminescence signal consists in band-to-band recombination, i.e. the recombination involved into the photovoltaic conversion. At the opposite, the two samples obtained with liquid deposition on a non-implanted/implanted substrate by self-crucible deposition do not show such band to band recombination. Different peaks are observed for both types of samples in the 1500-1600 nm range corresponding to dislocations.

Thus, this analysis confirms the low crystalline quality of the samples proposed here, even if another analysis should be lead on the samples deposited from a graphite crucible (the samples presented at the beginning of the study).

Another study of photoluminescence would be useful to evaluate the properties of the samples deposited with a graphite crucible (i.e. with a high epitaxial growth).

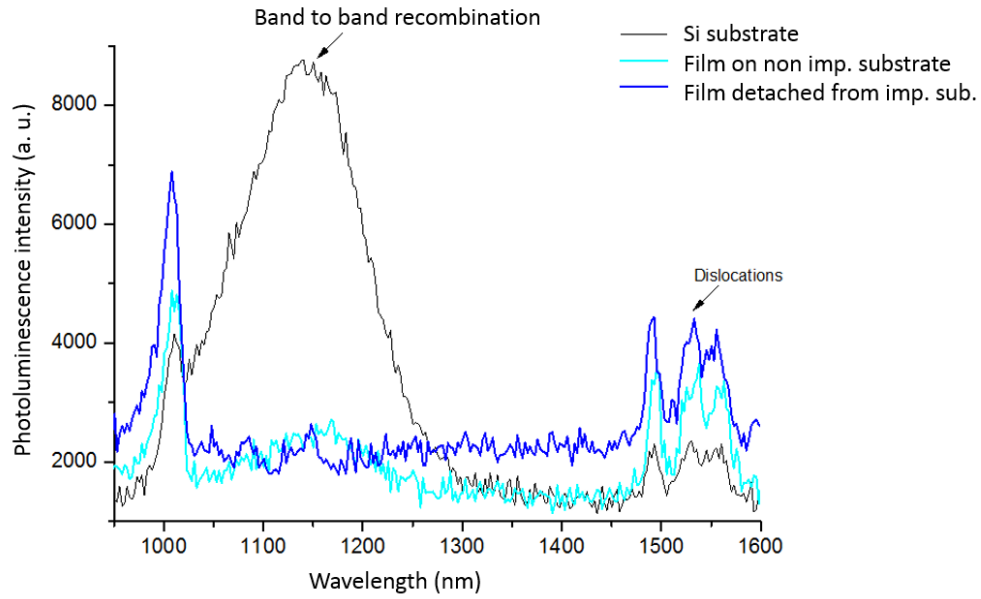


Figure 46: Photoluminescence spectrum of the reference bulk substrate, of a film deposited on a non-implanted substrate (in a deposition chamber at $2 \cdot 10^{-4}$ mbar by levitation, shown in Fig. 44) and of a film detached from the implanted substrate (in a deposition chamber with Ar at P_{atm} by self-aligned crucible, shown in Fig. 36).

6 Comparative study between the graphite and the self-aligned crucible

6.1.1 Summary of the experimental conditions

The summary of all deposition conditions is established in Table 5. As already mentioned, the best results in terms of epitaxial growth are paradoxically obtained with the less optimized chamber conditions (i.e. the chamber of the preliminary essays). On the other hand, a part from those preliminary results, the best epitaxial growth is obtained in high vacuum chamber. Thus, it appears that the chamber atmosphere is a key factor, but of the second order.

Table 5. General summary of the deposition conditions

Exper. config.	Chamber preparation	Chamber atm. during deposit.	Temp. of subst. [°C]	Temp. of liquid Si [°C]	Config. of subst. [degree]	Epitaxial growth [%]
Rotating substrate	IPA cleaning, no vacuum	Overpressure of Ar (no valve)	200	1450	0	89% (non-imp.) 68% (imp.)
Self-aligned crucible	IPA cleaning, primary vacuum	P _{atm} of Ar	~RT	1450	0 ; 80	10% (imp.)
	IPA cleaning, primary vacuum	Overpressure of Ar (no valve)	~RT	1450	45	26% (imp.)
	IPA cleaning, primary vacuum	Overpressure of Ar (with valve)	~RT	1410	30 ; 45 ; 0	-
Electrom. levitation	IPA cleaning, secondary vacuum	P _{atm} of Ar	~RT	1420 ; 1465 ; 1580	0	-
	IPA cleaning, secondary vacuum	Vacuum (2*10 ⁻⁴ mbar)	~RT	1530 ; 1540 ; 1560	0	56% (non-imp.) 2% (imp.)

The contamination of the liquid Si must also vary as a function of the deposition. Nevertheless, the highest level of contamination is supposed to be with the first deposition equipment, where the graphite crucible is a source of carbon contamination. On the other side, the self-aligned crucible as well as the electromagnetic levitation normally avoids the contact between the liquid and any surface contaminants. On this point again, the best results are obtained with the supposedly less optimized conditions.

The last parameter playing a role in the epitaxial growth is the substrate surface. As the cleaning method is the same for all the samples, they are supposed to enter the chamber with the same surface state. Nevertheless, after the cleaning step, one or two monolayers of water can be absorbed at the surface of Si [8]. Additionally, the cleaning step of the substrate can also leave water at the substrate surface, even if the Ar drying after the chemical treatment (HF then ethanol) is supposed to remove it.

However, the substrates are kept at 200 °C during an hour of thermal ramp of the crucible in case of the deposition on a rotating substrate. Thus, the surface water can desorb during this hour of annealing. On the other side, the surface is kept close to the room temperature for all the other samples.

As a conclusion, the monolayers of water are proposed to disturb the epitaxial growth. Into addition, we propose that the SiO₂ films observed at the vicinity of the deposited droplets originate from this absorbed water.

In case of an annealing of the substrate surface at low temperature (200°C), the water can be desorbed what facilitates the epitaxial growth.

7 Roadmap for future developments

The combination of the different deposition equipment has proved that it is possible to achieve an epitaxial growth on an implanted Si wafer. A liquid Si flow can be spread onto an inclined substrate to form a low thickness film (possibly inferior to 100 μm) over a large width (possibly up to several cm). The solidification of the deposited layer can be followed by a splitting when depositing the liquid Si onto an implanted substrate. Thus, the next studies should focus on two pillars: to improve the quality of the epitaxial layer and to develop new equipment in order to spread a film over an entire wafer.

The quality of the epitaxial growth depends strongly on the surface state of the substrate. The deposition of the chamber should be maintained at a temperature sufficient to desorb the wafer from the substrate surface. On the other hand, the initial preoccupation regarding the implanted material is still valid. Indeed, the implanted substrate has to be kept below 300 $^{\circ}\text{C}$ to preserve the possibility of detachment after the deposition step. Further analysis should be focused on the surface state of the substrate before deposition.

The new equipment should allow to have a stable liquid flow, in order to have homogeneous properties of the film in terms of thickness, over a large surface. The source of liquid Si can be made of a graphite crucible or of a self-aligned crucible. The orifice

diameter can be quite large (e.g. 1 cm) as the very good property of spreading of the liquid Si allows to reach the required thickness. The substrate can be advantageously placed on a sliding holder, as illustrated on the Fig. 47. A key aspect to investigate will be the dynamics of separation of the solidified film on one defined area, simultaneously to the continuation of spreading over another area. The substrate holder includes a heating system in order to preheat the substrate at 200 $^{\circ}\text{C}$ -300 $^{\circ}\text{C}$, in order to remove any trace of water at the surface substrate.

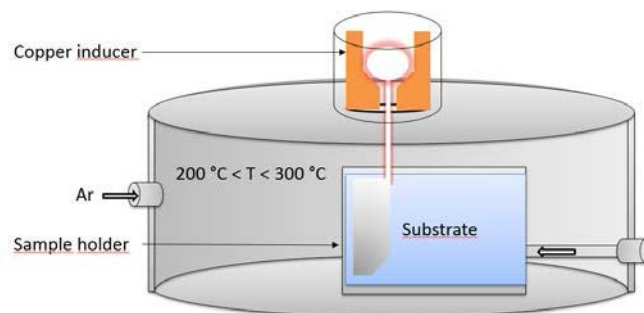


Fig. 47: Schematic of a proposition of design of equipment for a further study. The substrate holder can be slid continuously to facilitate the spreading of a thin film of liquid Si.

The properties of the films in terms of doping level, dislocations as well as the electrical properties will have to be studied in depth, for liquid sources of different types of Si grade and conditions of deposition.

Finally, as the thin silicon foil is very brittle because of the properties of the surface and edges [9], the handling of such foils will have to be studied, in terms of probability of breakage as a function of the thickness.

8 Conclusion of the chapter

In this chapter, we have incrementally explored several aspects regarding the main topic of this thesis, whose objective is to produce thin wafers of Si by epitaxial growth. This process implies a good spreading of the liquid upon an implanted substrate, in order to reach a low thickness (inferior to 100 μm) over the largest area possible. The substrate surface state is a key aspect to allow a directed epitaxial growth of the film. Finally, the splitting step due to a defect growth within the implantation zone of the substrate during the solidification of the liquid film requires an adequate thermal budget. Indeed, the growth of the micro-cracks necessary for the splitting involves the presence of a stiffener layer in contact with the implanted face, which role must be fulfilled but the solidified film after deposition onto the implanted surface of the substrate.

The preliminary results have shown the accuracy of the solidification modelling for the thermal budget brought into the implantation as well as for the solidification kinetics of the liquid film. Thus, the detachment by Smart Cut™ of the deposited droplets in contact with the superficial layer of the implanted wafer is observed. The comprehension of the Smart Cut™ brought by the two previous chapters has been profitably used in order to predict the separation kinetics into competition with the development of a stiffener layer by the solidification of the liquid film in contact. The observation of a separation by Smart Cut™ proves the growth of such a layer sufficiently soon in the process of defect growth. On the other hand, the very high roughness of the detached zone tends to show that the early stage of defects development occurs without a stiff enough solid layer being in contact with the implanted substrate.

The epitaxial growth of the liquid film upon this superficial layer acting as a seed is demonstrated. As predicted, the surface state of the substrate appears as the key conditions for the epitaxial growth. For several depositions, the substrate surface did not allow a proper epitaxial or even just the adhesion with the liquid film. Thus, it is worth noting that the cleaning step is necessary but not sufficient. Indeed, in spite of the use of inert atmosphere for the deposition chamber, such as Ar at P_{atm} or in overpressure, the presence of thermal SiO_2 can be observed at the vicinity of the deposited film. It proves the presence of oxygen, most probably resulting from the thermal desorption of absorbed monolayers of water at the substrate surface. This water can simply be removed by an annealing at low temperature (typically 200 °C) as observed during the preliminary study. Paradoxically, the necessity to preserve the implanted species of the substrate from any annealing before the deposition, has led to avoid as much as possible any side-effect annealing during the step of design of experiment. Thus, many samples present a low degree of epitaxial growth despite the efforts put on the other aspects of the deposition step or of the deposition chamber.

For the best in class films, the degree of epitaxial growth can reach up to 90%, which is far better than the previous studies of LPE in the literature under similar conditions [2, 3]. The presence of twinning and multi-twinning can be explained by the cooling of the film on the initially cold substrate, in case of deposition on non-implanted substrate. The epitaxial growth of the deposited film is lower in case of a deposition onto an implanted substrate. It can be supposed that the faster cooling in case of deposition on a non-implanted substrate helps a directed crystallization, with a lower amount of germination within the rest of the liquid phase. Regrettably, this observation is difficult to explain more exhaustively based on this single study. Further works will be necessary to bring further explanations and we have proposed a strategy for these next studies.

References

- [1] **K. M. Beatty, K. A. Jackson**, Monte Carlo modelling of silicon crystal growth, *J. of Cryst. Grow.*, vol. 211, pp. 13-17, 2000. SO 01
- [2] **K. Nagashio, H. Murata, K. Kuribayashi**, Spreading and solidification behavior of molten Si droplets impinging on substrates, *Act. Mat.*, vol. 52, 2004. DR 14
- [3] **Z. Wang, K. Kutsukake, H. Kodama, N. Usami, K. Fujiwara, Y. Nose, K. Nakajima**, Influence of growth temperature and cooling rate on the growth of Si epitaxial layer by dropping-type liquid phase epitaxy from the pure Si melt, *J. of Cryst. Grow.*, vol. 310, pp. 5248-5251, 2008. SO 04
- [4] **K. Nagashio and K. Kuribayashi**, Growth mechanism of Si from undercooled melts, *Sp. Utiliz. Res.*, vol. 21, pp. 9-12, 2005. SO 08
- [5] **O. Dezellus, S. Jacques, F. Hodaj, N. Eustathopoulos**, Wetting and infiltration of carbon by liquid silicon, *J. of Mat. Sc.*, Proceedings of the IV international conference/high temperature capillarity, vol. 40, pp. 2307-2311, 2005. DR 10
- [6] http://www.cleanroom.byu.edu/color_chart.phtml
- [7] **B. E. Deal, A. S. Grove**, General relationship for the thermal oxidation of silicon, *J. of Appl. Phys.*, vol. 36, no. 12, 1965. SI 23
- [8] **M. K. Weldon, Y. J. Chabal, D. R. Hamann, S. B. Christman, E. E. Chaban, L. C. Feldman**, Physics and chemistry of silicon wafer bonding investigated by infrared absorption spectroscopy, *J. of Vac. Sc. & Tech. B*, vol. 14, pp. 3095-3106, 1996. BO 03
- [9] **F. Ayazi, K. Najafi**, High aspect-ratio combined poly and single-crystal silicon (HARPSS) MEMS technology, *J. of Micromech. Syst.*, vol. 9, no. 3, 2000. TW 07

Conclusion of the thesis

This thesis has fulfilled the initial objectives motivated by an industrial and scientific context in both microelectronics and photovoltaics, two application fields where Soitec is involved. The two processes introduced in this thesis (i.e. the Smart Cut™ of implanted Si by laser annealing and the fabrication of Si foils by LPE on implanted Si) have been demonstrated and investigated. Additionally, the thesis redline of the kinetics of Smart Cut™ under high temperature annealing has been characterized. In summary, this work has paved the way for further research in order to define process windows for the two processes.

Kinetics of Smart Cut™ at high temperature

This work has started by a precise characterization of the annealing system, in order to calculate the thermal budget of splitting with the required accuracy. Thus, it has appeared that for temperatures superior to 550°C-600°C, the classical representation of the splitting kinetics under form of an Arrhenius plot brings artifacts. Therefore, we have proposed to calculate the thermal budget of splitting, with different hypothesis of kinetics of splitting, including those from the literature (i.e. a kinetics of splitting defined by the diffusion of free H). It has appeared that the best fit for the kinetics of splitting is obtained by calculating the dose of H evolving during the splitting annealing itself. Indeed, we have experimentally observed an out-diffusion of H during the annealing by SIMS. Thus, considering that the out-diffused hydrogen does not participate in the growth of the defects involved in the layer separation, the splitting kinetics is slowed down. We have proposed a model for the diffusion coefficient of the H trapped at the defects in the implantation zone.

Another consequence of the H out-diffusion is to induce non-expected layer separation, at the bonding interface or at the thermal oxide interface. This particular transfer of the thermal oxide is only observed for low implantation doses and for temperatures superior to 850°C.

Finally, numerical calculations have been carried out in order to validate the possibility of splitting for regular implantation dose (i.e. superior to $5.0 \cdot 10^{16} \text{ Hcm}^{-2}$) over wide range of annealing temperatures. Thus, these calculations show that the H loss is not sufficient to prevent splitting in the whole considered temperature range.

Smart Cut™ assisted by laser beam annealing

This study has demonstrated the possibility of splitting for annealing temperatures up to 1300°C, confirming the prediction of our splitting model. We could obtain films of Si on sapphire (SOS) and Si on glass (SOG) by scanning laser beam across the implanted Si surface by illuminating through the sapphire or glass wafer bonded with silicon. The best annealing conditions returned a layer transfer over more than 90% of the annealed surface, for samples of a diameter of 200 mm. This achievement proves the industrial potential of this approach.

The calculation of the thermal budget of splitting has shown that the activation energy of splitting for temperature in the range 900-1300°C is defined by the diffusion coefficient of trapped H that we have introduced earlier.

Fabrication of Si foils by LPE onto an implanted substrate

This study has relied on three different deposition equipment, mainly for practical issues. Nevertheless, the possibility of detaching by Smart Cut™ a layer of Si after solidification onto an implanted substrate has been demonstrated, in good agreement with preliminary modelling. The best samples show an epitaxial growth over more than 90% of the deposited film, which is far better than previous studies considering dropping-type LPE. Considering an equipment of deposition of liquid Si by self-crucible, films as thin as 100 µm could be obtained over surface of several cm². These results are very encouraging regarding the possibility of forming films of an optimal thickness for PV applications (i.e. 50 µm of thickness).

The conditions of the deposition chamber appear as the critical for the epitaxial growth quality. Thus, the best samples were obtained by preheating the substrate at a moderated temperature (200°C). Different characterizations have shown the presence of oxide at the interface between the film and the substrate, or at the crown of the deposited film, for samples deposited onto a substrate at room temperature. This oxide formation is explained by the presence of water at the surface of the substrate.

Finally, we have proposed a design of equipment that would be the most suitable for further studies, aiming to fabricate films of thickness inferior to 100 µm, over larger surface.

About the thesis strategy

The redline of the thesis, i.e. the kinetics of splitting at high temperature, has been an efficient tool to organize these 3 years of work. Once validating the splitting model and the possibility of layer separation for annealing temperature going up to the melting point of Si, the attention could be focused on the remaining investigation aspects, i.e. the laser-beam annealing of a bonded structure, the deposition of thin layers of liquid Si and their epitaxial growth.

Conferences, publications and patents

Poster presented in a conference

GDR Pulse “*Processus ULtimes d’épitaxie de SEMiconducteurs*”, Aix-en-Provence, France, July 2013.

Papers presented in a conference

ACEEES *Academy for Co-creative Education of Environment and Energy Science*, Los Angeles, USA, December 2013.

EUROSOI-ULIS *Ultimate Integration on Silicon*, Bologna, Italy, January 2015.

Scientific publications

R. Meyer, O. Kononchuck, H. Moriceau, M. Lemiti, M. Bruel, Study of high-temperature Smart Cut™: application to Silicon-On-Sapphire films and to thin foils of single crystal silicon, *Sol. St. Electron.*, vol. 115, Part B, pp. 225-231, January 2016.

R. Meyer, O. Kononchuck, H. Moriceau, M. Lemiti, M. Bruel, Physical model for the Smart Cut™ process at elevated temperature (900°C to 1300°C): application to laser annealing of hydrogen implanted silicon bonded with glass, aiming to be submitted in *Phys. Rev. B*.

Patent

R. Meyer, Fibre de matériau cristallin et procédé de fabrication associé, deposited in June 2015 (Patent number: FR1556184).

Résumé de thèse

1. Description du sujet de la thèse

1.1. Vues et motivations personnelles

La quantité de main-d'œuvre nécessaire à la production industrielle a connu une baisse continue depuis la deuxième révolution industrielle. Ainsi, en vertu principe de Fourastié, le coût unitaire des produits industriels a connu la même baisse [1]. Ceci, additionné d'une concurrence exacerbée par la place grandissante du libre-échange depuis la chute du bloc communiste et la constitution de grands ensembles continentaux, a fortement comprimé les marges des acteurs industriels. La stratégie mise en place par ces derniers pour préserver leurs profits a consisté à élargir l'assise productive vers des pays à bas-coûts, ainsi qu'à diversifier très fortement les gammes de produits, d'où l'accélération des cycles d'innovation, que l'on peut observer depuis.

L'industrie microélectronique est probablement l'industrie la plus emblématique de cette réalité. La loi de Moore illustre parfaitement la nécessité sous-jacente d'augmenter de façon exponentielle la puissance de calculs des processeurs pour préserver la rentabilité des grands acteurs du secteur. En parallèle, une importante diversification sectorielle a été effectuée au début des années 2010 avec l'émergence de l'internet des objets. Ces dispositifs reposent sur une autre logique que la loi de Moore, consistant à compenser leur faible valeur ajoutée par un nombre exponentiel d'unités vendues.

L'industrie du photovoltaïque (PV) est face à un autre contexte industriel, dans la mesure où la plupart des acteurs traditionnels, principalement européens et américains, a disparu du fait du développement planifié de capacités industrielles en Chine. Le futur d'une industrie européenne se fera probablement par le développement de nouvelles fonctionnalités, telle que la flexibilité des panneaux ou le développement du stockage d'énergie.

Tout ceci ne doit pas faire oublier que de nouveaux enjeux tels que la rareté de certaines matières premières, autant que la nécessité de la réduction des émissions industrielles vont faire peser une contrainte supplémentaire sur ces deux industries, gourmandes sur ces deux aspects. Ainsi, des procédés nouveaux, frugaux en ressources et en énergie, vont être nécessaires pour garantir la pérennité industrielle. Cette thèse s'inscrit dans cet effort de développer des approches alternatives.

1.2. Le procédé Smart Cut™ et ses variantes possibles

Le procédé Smart Cut™ s'est inscrit dès le départ dans cette optique, dans la mesure où il permet de réaliser des couches semi-conductrices (silicium sur isolant ou SOI), en économisant la matière première. Il repose sur l'implantation ionique d'ions légers (H, He) dans un substrat dit donneur, avant d'effectuer un collage direct avec un autre substrat, dit accepteur. Un recuit thermique va ensuite permettre d'effectuer un report de couche du substrat donneur sur le substrat accepteur, par la génération de défauts ponctuels (platelets puis microfissures) [2]. Le substrat donneur peut ensuite être recyclé pour un autre cycle de transfert. Les principales du procédé sont illustrées en Fig. 1.

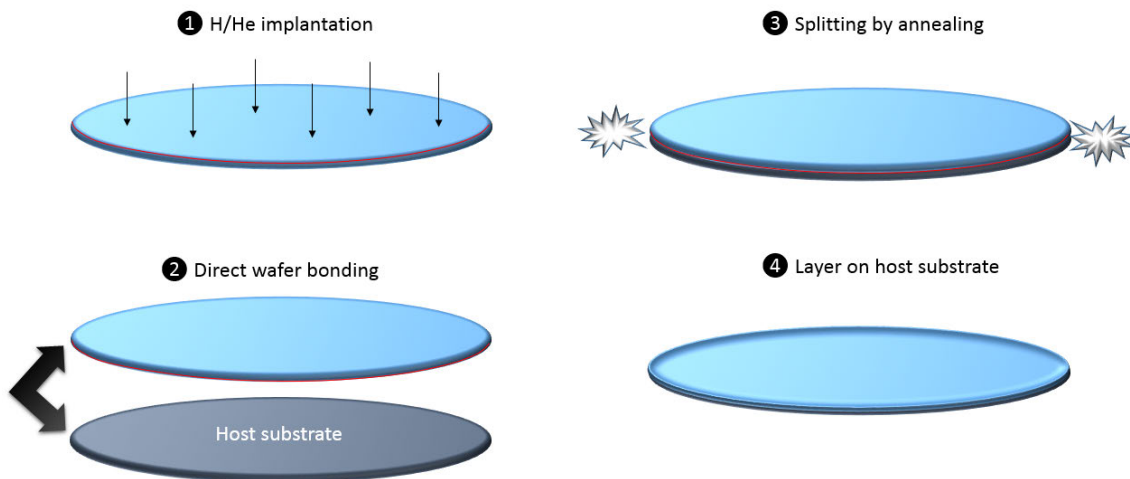


Figure 1 : Principales étapes du procédé Smart Cut™.

Ce procédé peut être appliqué à une grande diversité de matériaux, tels que matériaux III-V et utiliser des substrats accepteurs de différents types (verre, polymères) [3, 4].

Si ce procédé est versatile en termes de matériaux considérés, une difficulté demeure lorsqu'il s'agit de coller ensemble deux matériaux dans les coefficients d'expansion thermique (CTE) sont très différents. Dans ce dernier cas, le recuit de séparation peut conduire à une déformation ou même à une casse des plaques [4]. C'est la principale motivation à la première variante du procédé proposée dans cette thèse, et qui consiste à effectuer le recuit non pas en pleine plaque, mais de façon localisée en utilisant un laser.

1.3.Smart Cut™ assisté par laser pour la réalisation d'hétérostructures

L'approche consiste donc à implanter un substrat donneur de la même façon que précédemment, et à effectuer un collage direct avec un substrat accepteur, qui sera transparent à la longueur d'onde du laser considéré. Le recuit de séparation s'effectue donc progressivement par le balayage de la surface du matériau implanté, en passant à travers le donneur. Le procédé est décrit en Fig. 2.

Il est à noter que le recuit dans cette configuration s'effectue à bien plus haute température que lors d'un Smart Cut™ tel qu'il est utilisé à l'échelle industrielle (c'est-à-dire sous 600°C [2]). Cela permet de réduire de plusieurs ordres de grandeur le temps de recuit, et donc la diffusion thermique dans le matériau.

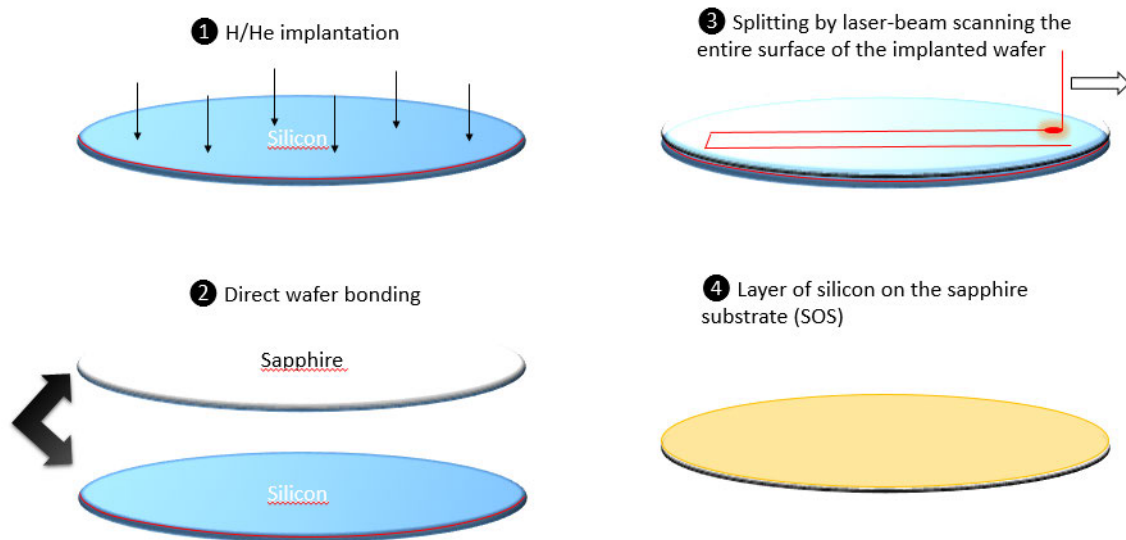


Figure 2 : Les principales du procédé Smart Cut™ assisté par laser, ici dans le cas d'un report d'une couche de Si sur un substrat en saphir. NB: la couleur jaune du film correspond effectivement à une couche de Si sur saphir (SOS) avec une épaisseur inférieure au micron.

Ce procédé a déjà été implémenté dans le cas d'un transfert de niobate de lithium (NbLiO_3) sur Si [5]. Il sera ici étudié dans le cas d'un transfert de Si sur verre et sur saphir. Les enjeux en termes de compréhension portent sur la cinétique de séparation dans les conditions du recuit laser, ainsi que sur les propriétés des films qu'il est possible d'obtenir avec cette approche.

1.4. Elaboration de feuilles de Si par épitaxie en phase liquide sur substrat implanté et détachement par Smart Cut™

Le second procédé introduit dans cette thèse propose d'adresser la problématique de réaliser des wafers fins ($< 200 \mu\text{m}$), principalement pour des applications PV. Le principe consiste à déposer en phase liquide du Si liquide (c'est-à-dire à des températures $> 1410^\circ\text{C}$) sur un substrat implanté de Si monocristallin. Ainsi, la croissance épitaxiale est facilitée, en vue d'obtenir des bonnes propriétés cristallines du film déposé. D'autre part, le dépôt sur un substrat implanté permet de détacher le film par Smart Cut™. Le procédé est décrit en Fig. 3.

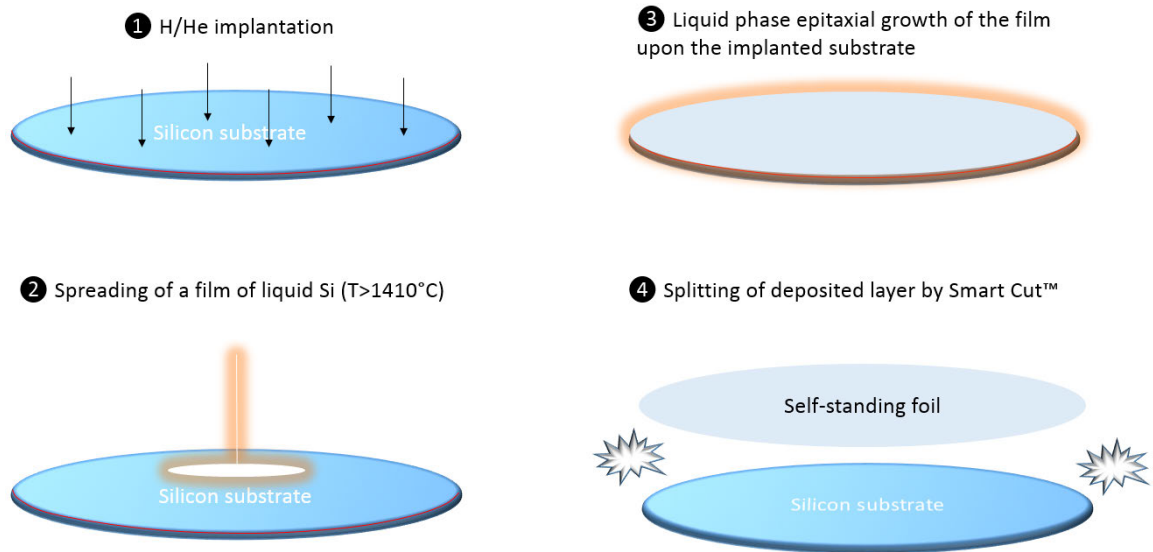


Figure 3 : Description du procédé d'élaboration de feuilles de Si par épitaxie en phase liquide sur substrat implanté.

L'avantage de l'approche est d'être kerf-less, c'est-à-dire sans étape de découpage qui génère d'importantes pertes en termes de matières premières.

Les enjeux de cette approche portent sur la compréhension de la croissance épitaxiale, d'un film de Si fondu, sur un substrat qui se doit de rester à une température faible ($< 300^{\circ}\text{C}$) afin de ne pas perdre la capacité de détachement ultérieure liée à l'implantation du substrat. D'autre part, la cinétique de détachement par Smart Cut™ devra être caractérisée dans la gamme de température correspondant au procédé (i.e. potentiellement jusqu'à la température de fusion du Si, 1410°C).

1.5.A propos de la stratégie de thèse

Le tronc commun des travaux de cette thèse reposent sur la compréhension de la réponse du substrat implanté pendant des recuits à très haute température (900°C - 1300°C). Le plan d'expérience va donc porter sur l'étude de Smart Cut™ en partant des températures couvertes dans la littérature pour aller vers les températures plus élevées (jusqu'à 700°C).

L'étude du procédé de Smart Cut™ assisté par laser va permettre d'établir un modèle de compréhension jusqu'à des températures de recuit de 1300°C .

Enfin, le dépôt de Si liquide sur substrat implanté va être investigué par différents équipements d'épitaxie en phase liquide.

Bibliographie

- [1] **E. Cohen**, La prospérité du vice, Une introduction (inquiète) à l'économie, Albin Michel, 2009.
- [2] **M. Bruel, B. Aspar, H. Moriceau, E. Jalaguier, C. Lagahe**, Single crystal layer delamination and transfer through hydrogen implantation, *Electroch. Soc. Proc.*, vol. 1, 1999.
- [3] **I. Radu, I. Szafraniak, R. Scholz, M. Alexe, U. Gösele**, Low-temperature layer splitting of (100) GaAs by He+H coimplantation and direct wafer bonding, *Appl. Phys. Lett.*, vol. 82, No. 15, 2003.
- [4] **K. Bourdelle**, Engineered substrates for advanced CMOS technology nodes and More-than-Moore applications, in Functional nanomaterials and devices for electronics, sensors and energy harvesting, editors : Alexei Nazarov, Francis Balestra, Valeriya Kilchytska, Denis Flandre, pp. 12-20, 2014.
- [5] **D. Klingera, J. Auleytnera, D. Zymierskaa, L. Nowickib**, Nanostructure of near-surface Si layers formed by implantation and pulsed laser annealing, *J. of All. And Comp.*, vol. 362, pp. 282-286, 2004.

Cinétique de Smart Cut™ à haute température.

2. Etat de l'art du Smart Cut™

2.1.Principales étapes du Smart Cut™

Le procédé, décrit en Fig. 1, commence par une oxydation (thermique ou par dépôt en phase vapeur) du substrat donneur (wafer A) avant une étape d'implantation ionique d'ions légers (H et/ou He). L'énergie d'implantation est d'ordinaire inférieure à 200 keV et définit la profondeur moyenne de la zone d'implantation (R_p), et donc l'épaisseur du film transféré (généralement comprise entre 10 nm et 1.5 μ m) [2, 3]. Un collage direct est ensuite effectué avec un substrat accepteur (wafer B). Enfin, un recuit thermique est effectué (à des températures généralement comprises entre 450°C et 600°C). Pendant cette étape, différents objets se forment dans la zone d'implantation (platelets puis microfissures) jusqu'à la fracture horizontale de la zone. La partie supérieure du wafer implanté se détache et celui-ci peut être recyclé pour un autre cycle.

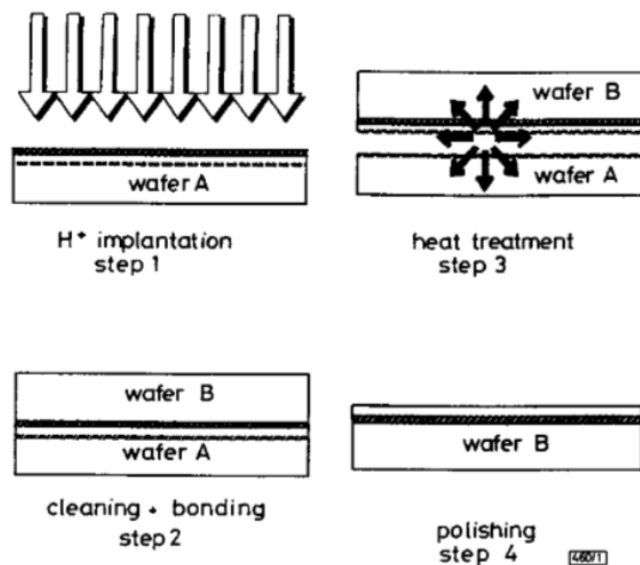


Figure 1: Principe du Smart Cut™ tel que décrit par M. Bruel dans la première publication révélant le procédé [1].

2.2.Evolution dans la zone implantée du substrat donneur

L'implantation ionique consiste à introduire des espèces capables de former des espèces gazeuses dans le matériau implanté. La distribution suit une gaussienne, comme illustré en Fig. 2. L'implantation d'espèces ioniques conduit à déformer la matrice cristalline et à générer une importante quantité de défauts (tels que lacunes et interstitiels).

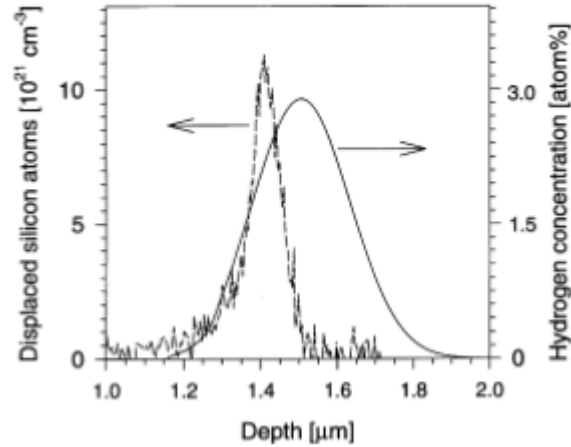


Figure 2: Distribution de l'hydrogène implanté (par Elastic Recoil Detection Analysis, ERDA) et la distribution des défauts générés par l'implantation en fonction de la profondeur d'implantation (par Rutherford Back-Scattering, RBS) pour un substrat de Si implanté $5.0 \cdot 10^{16} \text{ Hcm}^{-2}$ à 175 keV [4].

Il a été observé que l'H forment une variété de défauts dans la zone implantée, comme illustré sur la Fig. 3 par Raman. La répartition de ces défauts varie avec la dose d'implantation et il est important de constater que pour des doses d'implantation telles qu'utilisées pour le Smart Cut™ en conditions industrielles, les défauts de type Si:H représentent la plus grosse concentration. Par ailleurs, l'analyse montre que la concentration de ces défauts diminue durant le recuit de séparation, quand d'autres types de défauts (tels que $V_n H_m$) reste stable ou augmente [5].

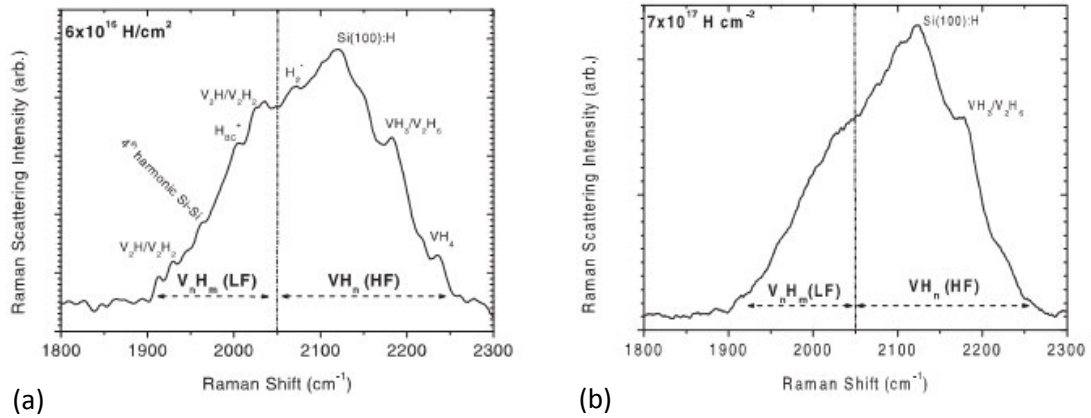


Figure 3: Spectres Raman pour des substrats implanté à une énergie de 10 keV et des doses d'implantation de $6.0 \cdot 10^{16} \text{ Hcm}^{-2}$ (a), and $7.0 \cdot 10^{16} \text{ Hcm}^{-2}$ (b) [5].

Durant le recuit thermique de la zone implantée, des objets nanométriques apparaissent progressivement, les platelets, avec un phénomène de croissance compétitive, c'est-à-dire que les objets les plus gros croissent au détriment des objets les plus petits. Ces objets de formes lenticulaires sont formés à partir de défauts de type $V_n H_m$ et alimentés par une inter-diffusion de H, qui une fois introduit dans le platelet, forme de l' H_2 [6].

Freund a établi un modèle de type Griffith (c'est-à-dire de minimisation d'énergie de surface) pour expliquer la croissance des platelets. Il définit donc une dose minimale d'implantation I_{min} pour alimenter la croissance du platelet et donc fracturer le matériau environnant [7] :

$$I_{min} = \frac{8}{3} \frac{\gamma}{k_B T}$$

avec γ l'énergie de surface du matériau.

Ultérieurement dans le recuit apparaissent des défauts microscopiques, les microfissures, dont la croissance est alimentée par une diffusion d'H depuis les platelets [8]. Ces défauts vont connaître un phénomène de croissance compétitive puis de coalescence jusqu'à la fracturation complète du matériau.

2.3. Cinétique de séparation (splitting)

Il a été observé que la cinétique de séparation suit un régime d'Arrhenius, dont l'énergie d'activation dépend de la dose d'implantation [9], comme illustré sur la Fig. 4. Un point controversé de cette caractérisation porte sur le régime à haute température (<500°C). En effet, il avait été observé un changement de régime, indépendamment de la dose d'implantation, avec une énergie d'activation de splitting convergeant vers 0.5 eV. Ce changement était expliqué par la diffusion de l'H libre dans le Si, considérant qu'au-dessus de ces températures, les défauts hydrogénés devaient se décomposer, laissant l'H de diffuser dans les platelets puis les microfissures.

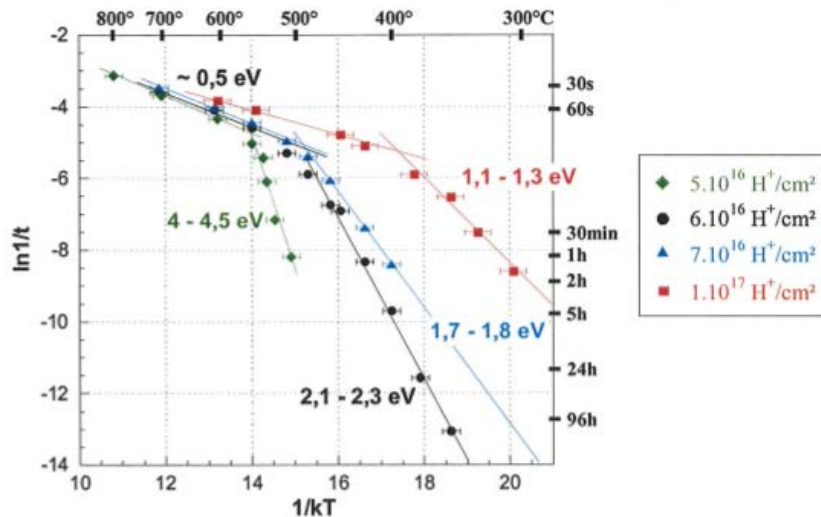


Figure 4: Cinétiques de splitting en fonction de la dose d'implantation d'H [9].

Dans ce travail de thèse, nous allons commencer par reprendre cette caractérisation avant d'étudier les cinétiques dans la gamme de température où la compréhension est controversée (500°C-700°C).

2.4. Protocole expérimental

Nous avons créé un équipement de recuit spécialement pour cette étude, afin d'offrir un bon contrôle de la température de recuit et des montées en température rapide (60°C/s). Il consiste en un système coulissant de deux plaques en acier, déjà montée à la température souhaitée, entre lesquelles l'échantillon de splitting est inséré (voir Fig. 5 (a)).

D'autre part, les échantillons de splitting sont préparés de façon à pouvoir y introduire un thermocouple comme illustré en Fig. 5 (b). Ainsi le recuit de splitting peut être caractérisé précisément, et notamment $T(t)$, c'est-à-dire la température dans l'échantillon en fonction du temps qui nous servira pour calculer les budgets thermiques de splitting.

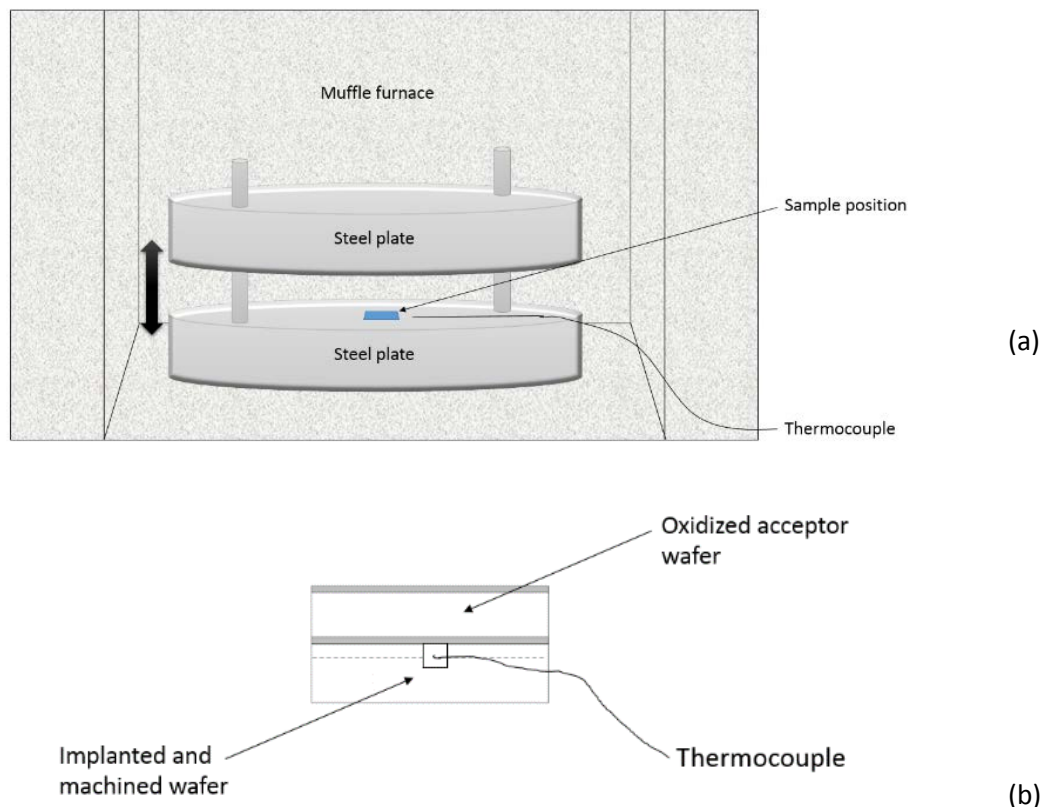


Figure 5: Représentation du four développé pour l'étude de splitting (a), architecture de l'échantillon de splitting présentant un espace pour y introduire un thermocouple (b).

2.5. Caractérisation de cinétiques de splitting

En utilisant le dispositif expérimental, nous avons pu caractériser les temps de splitting en fonction de la température pour différentes doses d'implantation ($4.5 \cdot 10^{16} \text{ Hcm}^{-2}$ à $1 \cdot 10^{17} \text{ Hcm}^{-2}$) (voir Fig. 6). Il apparaît que le changement de cinétique tel qu'observé dans la littérature n'est pas présent, mais un affaissement des courbes peut néanmoins être relevé. L'analyse des temps de montée en température des échantillons, caractérisées par notre dispositif montrent cependant que les temps de splitting sont comparables. Ainsi, il n'est pas possible d'utiliser la représentation d'Arrhenius dans les hautes températures.

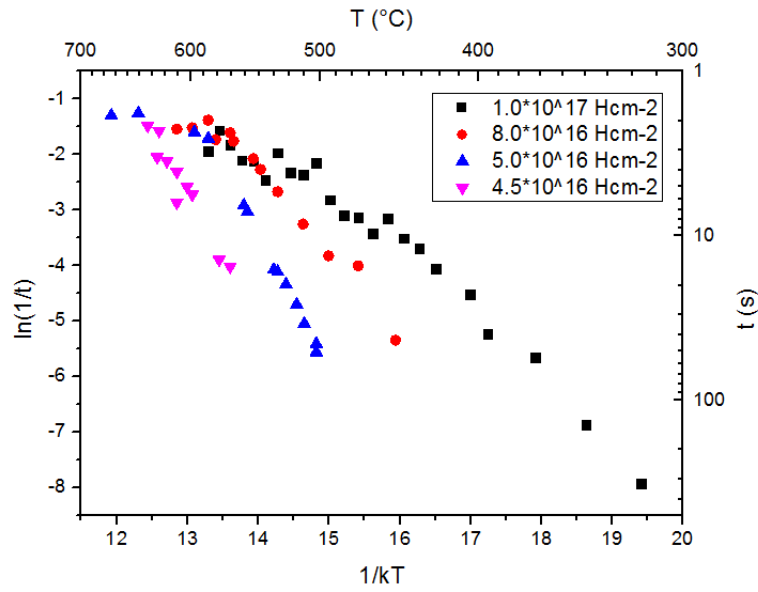


Figure 6: Temps de splitting τ en fonction de la température.

Afin de surmonter l'artefact de la représentation d'Arrhenius, nous introduisons ici la fonction de budget thermique, σ_T , définie comme suit :

$$\sigma_T = \int \frac{1}{\tau(T(t))} dt$$

avec τ le temps de splitting, qui peut être défini selon différents régimes d'Arrhenius d'énergie d'activation E_a :

$$\tau = \tau_0 * \exp\left(\frac{-E_a}{k_B T(t)}\right)$$

où $T(t)$ est le signal de température en fonction du temps tel qu'enregistré par le thermocouple inséré dans l'échantillon de splitting. Ainsi, il est possible d'investiguer différentes hypothèses de cinétique de splitting, l'hypothèse correcte étant celle qui retourne un budget thermique égal à 1 à l'issue du recuit de splitting.

La première hypothèse de régime d'Arrhenius est celle de la littérature, c'est-à-dire la diffusion d'H libre, avec une énergie d'activation de 0.5 eV. La seconde hypothèse est que la cinétique observée à faible température (<500°C) est maintenue à plus haute température (ce qui correspond pour les échantillons implantés à $5.0 \cdot 10^{16}$ Hcm⁻² à une énergie d'activation de 2.8 eV).

La figure 7 montre que les deux hypothèses divergent de la valeur 1 à partir de 550°C, il est donc possible d'affirmer que ni l'une ni l'autre ne sont correctes. Il est donc nécessaire d'introduire une nouvelle hypothèse.

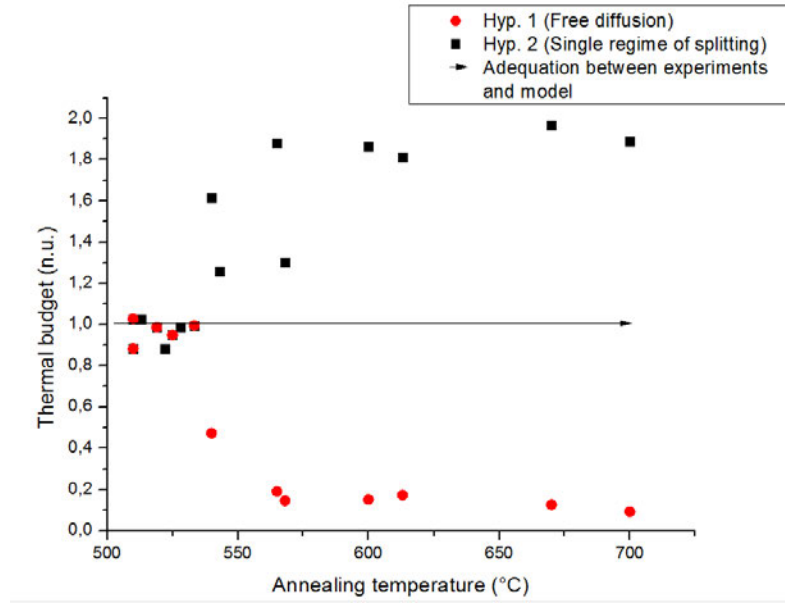


Figure 7: Calcul du budget thermique en utilisant le signal de température du thermocouple, pour des échantillons de splitting implantés avec $5.0 \cdot 10^{16} \text{ Hcm}^{-2}$.

2.6. Contribution de l'exodiffusion d'H

Nous posons donc l'hypothèse que les dérives progressives observées en Fig. 5, bien qu'étant soumise à l'artefact de la représentation d'Arrhenius, illustre un processus progressif qui vient affecter la cinétique de splitting au-dessus de 550°C . Ce processus repose sur le fait qu'une partie l'H exo-diffuse hors de la zone d'implantation et ne participe donc pas à la croissance des objets (platelets et microfissures). La quantité d'H disponible pour le splitting étant plus faible, le temps de splitting est allongé (i.e. selon la tendance illustrée sur la Fig. 6).

L'approche proposée est donc également liée à la diffusion de l'H dans le matériau implanté, mais en considérant que l'H reste piégé dans les défauts hydrogénés et en particulier dans les Si:H. Ainsi, le coefficient de diffusion de l'H est défini par le dé-piégeage du complexe Si:H, selon :

$$D_H = D_0 \left(\frac{n_{\text{bond}}}{n_{\text{free}}} \right) \exp \left(\frac{E_B - E_a}{k_B T} \right) \quad [10]$$

avec E_B l'énergie de liaison dans Si:H qui est estimé égal à celui dans le Si amorphe (a-Si:H) à 1.95 eV [11], et E_a l'énergie de diffusion de l'H libre. Ainsi l'énergie d'activation du dé-piégeage est de 1.46 eV.

$\left(\frac{n_{\text{bond}}}{n_{\text{free}}} \right)$ est le ratio entre l'H piégé dans les Si:H et l'H libre et est déterminé en s'appuyant sur des calculs ab-initio d'une autre étude [12].

Ainsi, en utilisant ce coefficient de diffusion, la dose perdue par exodiffusion durant le recuit de splitting peut être simulée (par Comsol Multiphysics), voir Fig. 8.

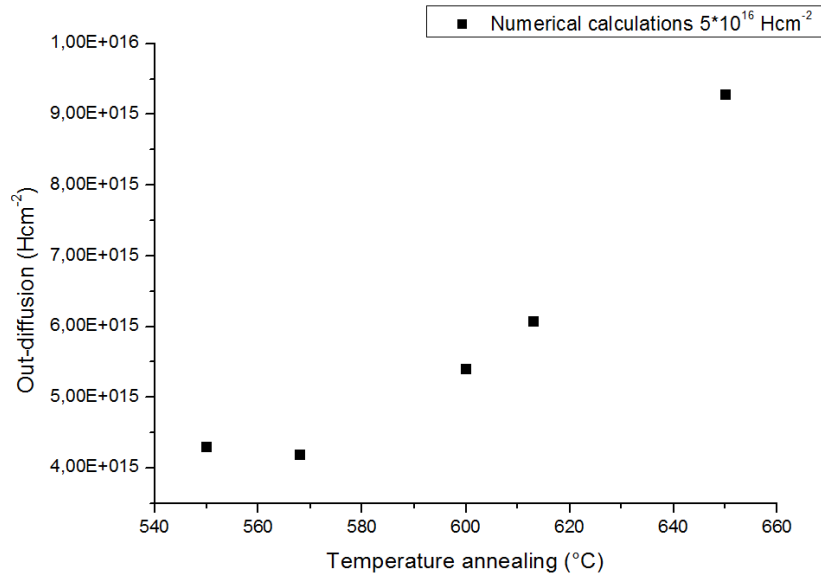


Figure 8: Exodiffusion d'H pour un échantillon implanté avec $5.0 \cdot 10^{16} \text{ Hcm}^{-2}$ en fonction de la température de recuit, obtenu par simulations.

En appliquant maintenant cette perte d'H en fonction du recuit, il est possible de déterminer l'évolution d'énergie de splitting de l'échantillon durant le recuit (Fig. 9).

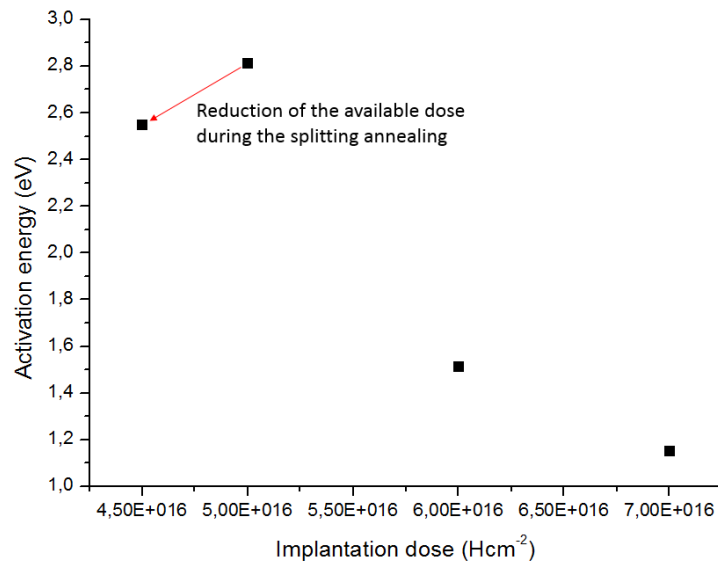


Figure 9 : Evolution de l'énergie d'activation en fonction de la dose d'implantation (extraite depuis la Fig. 6 à basse température). L'effet de la perte d'H durant le recuit est illustré par la flèche.

Ainsi, la fonction de budget thermique σ_T peut être calculée en utilisant l'énergie d'activation qui varie en fonction du recuit. Le résultat est illustré sur la Fig. 10, reprenant les deux premières hypothèses de splitting, précédemment invalidée, et la troisième hypothèse tenant compte de l'exodiffusion d'H.

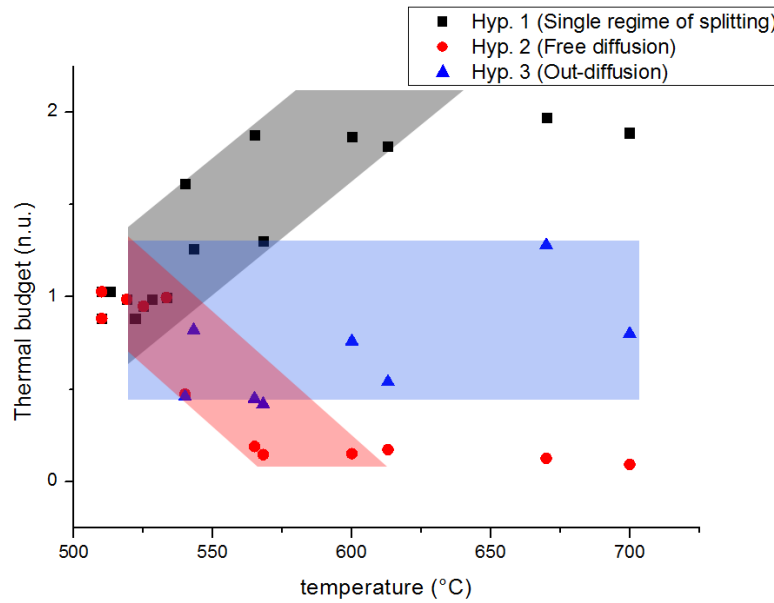


Figure 10: Calcul du budget thermique en utilisant le signal de température du thermocouple, pour des échantillons de splitting implantés avec $5.0 \cdot 10^{16} \text{ Hcm}^{-2}$, en considérant la troisième hypothèse de réduction de la dose d'H par exo-diffusion (Hyp. 3).

Il apparaît que la troisième hypothèse propose un bon fit pour les températures 550-700°C, considérant les incertitudes de mesure. Nous en déduisons donc que la cinétique de splitting pour des températures de recuit supérieures à 550°C est principalement influencée par le phénomène d'exodiffusion d'H.

2.7. Extrapolation du modèle pour des températures entre 700°C et 1400°C

Afin d'évaluer les possibilités de splitting à plus haute température que considérée dans cette première étude, nous calculons l'exo-diffusion d'H pour des recuits théoriques, extrapolés à partir de l'étude (Fig. 11).

Il apparaît que le maximum de dose perdue par exo-diffusion se situe pour une température de recuit de 700°C et que la dose est rapidement très faible passé 1000°C. Ainsi, il est possible d'affirmer que le splitting est toujours possible dans cette gamme de température (la dose perdue n'est jamais suffisamment importante pour empêcher le splitting).

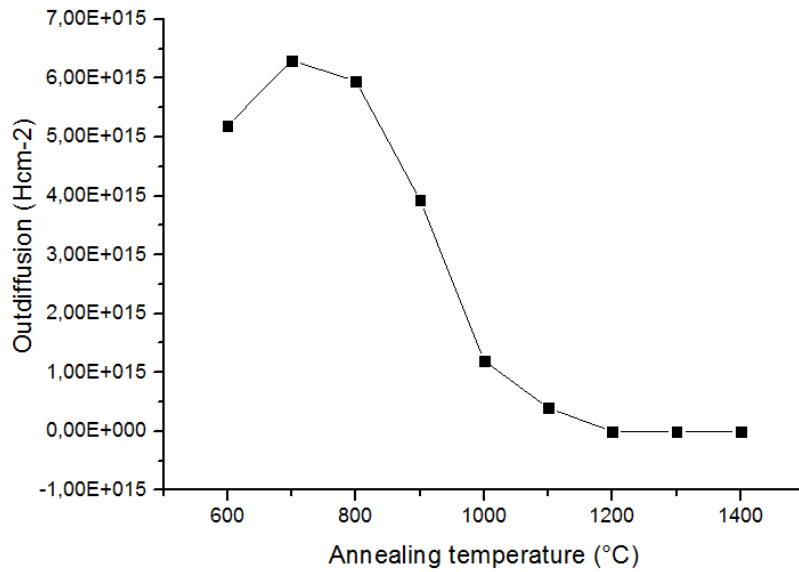


Figure 11: Simulation de la dose d'H perdue par exo-diffusion en fonction pour des températures de recuit allant jusqu'à 1400°C pour un échantillon implanté avec $5.0 \cdot 10^{16} \text{ Hcm}^{-2}$.

2.8. Conclusion du chapitre

Nous avons apporté une compréhension aux mécanismes influençant la cinétique de splitting pour une gamme de température de 500-700°C, où la littérature apportait une hypothèse controversée. De ces résultats, il est possible d'affirmer que le splitting d'un matériau implanté, impliqué dans le Smart Cut™ est possible pour des températures supérieures (en théorie jusqu'à la fusion du Si à 1410°C).

Cette étude nous a donc servi à préparer l'étude de Smart Cut™ assisté par laser ainsi que l'étude d'épitaxie en phase liquide sur substrat implanté.

Bibliographie

- [1] **M. Bruel**, Silicon on insulator material technology, *Electr. Letters*, vol. 31, p. 1201, 1995.
- [2] **J. D. Penot**, Fragilisation et dynamique de rupture du silicium implanté, Thèse de l'Université de Grenoble, 2010.
- [3] **P. E. Acosta-Alba, O. Kononchuk, G. Riou, C. Moulin, C. Bertrand-Giuliani, A. Claverie**, Multi-Scale Thickness and Roughness Characterization of Thin Silicon-On-Insulator Films, *ECS J. of Sol. State Sc. And Techn.*, vol. 2, No. 9, pp. 357-361, 2013.
- [4] **T. Höchbauer, A. Misra, R. Verda, Y. Zheng, S. S. Lau, J. W. Mayer, M. Nastasi**, The influence of ion-implantation damage on hydrogen-induced ion-cut, *Nucl. Instr. and Met. In Phys. Res. B*, No. 175-177, pp. 169-175, 2001.
- [5] **O. Moutanabbir, B. Terreault, M. Chicoine, F. Schiettekatte**, The fluence effect in hydrogen-ion cleaving of silicon at the sub-100-nm scale, *Appl. Phys. A*, vol. 80, pp. 1455-1462, 2005.
- [6] **J. Grisolia, F. Cristiano, G. Ben Assayad, A. Claverie**, Kinetic aspects of the growth of platelets and voids in H implanted Si, *Nucl. Instr. and Meth. in Phys. Res. B*, vol. 178, pp. 160-164, 2001.
- [7] **L. B. Freund**, A lower bound on implant density to induce wafer splitting in forming compliant substrate structures, *Appl. Phys. Lett.*, vol. 70, pp. 3519-3521, 1997.
- [8] **J.-D. Penot, D. Massy, F. Rieutord, F. Mazen, S. Reboh, F. Madeira, L. Capello, D. Landru, O. Kononchuk**, Development of microcracks in hydrogen-implanted silicon substrates, *J. of Appl. Phys.*, vol. 114, pp. 123513-1-6, 2013.
- [9] **M. Bruel, B. Aspar, H. Moriceau, E. Jalaguier, C. Lagahe**, Single crystal layer delamination and transfer through hydrogen implantation, *Electroch. Soc. Proc.*, vol. 1, 1999.
- [10] **P. Pichler**, Intrinsic point defect, impurities and their diffusion in Silicon, Springer, 2004.
- [11] **A. Shah**, Thin-film solar cells, Ed. Arvind Shah, EPFL Press, 2010.
- [12] **N. Cherkashin, F.-X. Darras, P. Pochet, S. Reboh, N. Ratel, A. Claverie**, Semi-analytic model of the precipitation of hydrogen atoms, silicon interstitials and vacancies in form of their complexes at room temperature in H+ implanted Si., to be published.

Smart Cut™ assisté par laser pour la fabrication d'hétérostructures

3.1. Etat de l'art

3.1.1. Applications des hétérostructures planaires

Une hétérostructure planaire se définit par un empilement de matériaux en couche, de types différents. Les hétérostructures sont utilisées dans la microélectronique ainsi que dans le PV. Dans ce dernier cas, on considère des cellules solaires à hétérojonctions dont l'absorption lumineuse est optimisée en combinant un ensemble de matériaux ayant chacun une bonne absorption dans une partie spécifique du spectre lumineux. Les différentes couches sont alors en règle générale composées de matériaux III-V [1].

En microélectronique, l'utilisation des hétérostructures est motivée par la combinaison des propriétés spécifiques d'une couche (par exemple, haute mobilité, tunabilité) avec les propriétés d'une seconde (haute résistivité électrique, bonne conduction thermique etc.). A part le SOI, qui est une hétérostructure, des couches de matériaux III-V ou de Ge peuvent être transférées sur Si pour la fabrication de NMOS ou PMOS [2]. Un autre type d'hétérostructure qui va nous intéresser est composé d'une couche de Si transférée sur un substrat transparent (tel que verre, Si on Glass ou SOG, et saphir, Si on Sapphire ou SOS). Par exemple, le SOS est utilisé pour des applications en radiofréquence, du fait de la haute résistivité du saphir qui évite la formation d'harmoniques parasites [2].

3.1.2. Méthodes de fabrication des hétérostructures

La méthode la plus ancienne pour la fabrication d'hétérostructures est l'hétéroépitaxie, consistant à croître un matériau sur l'autre, servant de substrat de croissance. Dans cette configuration, le choix est relativement limité (Si, GaAs, InP, 6H-SiC, saphir étant les plus couramment rencontrés) [3]. En plus de ce choix limité, le désaccord de maille peut engendrer la formation de dislocations, affectant les propriétés électroniques. D'autre part, la différence de coefficients d'expansion thermique peut engendrer de la contrainte résiduelle dans le film ou même affecter l'intégrité de la couche déposée. Enfin, des réactions chimiques peuvent être engendrées à l'interface entre deux couches, conduisant à la formation d'une troisième couche, non-désirée.

Une autre approche consiste à faire un collage direct des deux matériaux ensemble, et à amincir un des deux substrats jusqu'à atteindre l'épaisseur souhaitée. Cette approche appelée bonding and etch-back. Ce procédé, bien que permettant d'obtenir des films de très bonne qualité, est coûteuse dans la mesure où un substrat est perdu à chaque opération, et lente sur le plan industriel [4].

Le Smart Cut™ est bien entendu une approche possible, le SOI étant une hétérostructure. D'autres matériaux peuvent également être utilisés, comme le GaAs, implanté et transféré sur Si avec un recuit thermique en pleine plaque [5]. La principale limite de cette approche réside dans la différence de coefficients thermiques entre le substrat donneur et le substrat accepteur, qui peut conduire à la dégradation ou à la casse des plaques durant le recuit de splitting.

3.2. Fabrication d'hétérostructures par Smart Cut™ assisté par laser

Cette limite du Smart Cut™ constitue notre motivation à utiliser une autre approche pour la fabrication d'hétérostructures. Elle consiste à effectuer le recuit de splitting, non pas en pleine plaque dans un four, mais localement et progressivement avec un laser. Le matériau implanté à transférer est alors collé avec un matériau transparent à la longueur d'onde du laser considéré. Le transfert de film se fait en scannant la surface du matériau implanté en passant à travers le matériau transparent.

Cette approche a déjà été validée pour le transfert de niobate de lithium (NbLiO_3) sur Si [6]. Ainsi, le substrat de NbLiO_3 est implanté (co-implantation He et H) avant d'être collé avec un substrat de Si. Le recuit de splitting est effectué avec un laser CO_2 (longueur d'onde $10.6 \mu\text{m}$) qui permet une bonne absorption dans le NbLiO_3 et une bonne transmission dans le Si.

Nous proposons donc ici d'appliquer ce procédé sur pour la fabrication de Si sur verre (SOG), avec en considérant des substrats de 200 mm de verre Eagle (de Corning) collé avec des substrats de Si implantés avec des doses de $5.0 \cdot 10^{16} \text{ Hcm}^{-2}$ et $1.0 \cdot 10^{17} \text{ Hcm}^{-2}$ avec une énergie de 76 keV. Ces substrats ont été au préalable oxydés thermiquement pour faciliter le collage direct (400 nm de SiO_2 thermique). Le laser utilisé ici est un laser à diodes, émettant à 808 nm en continu. Le scan des surfaces s'effectue en passant à travers le substrat de verre, tel qu'illustré en Fig. 1. Les vitesses de scan permettent d'avoir des temps de résidence entre 0.25 ms et 1 ms.

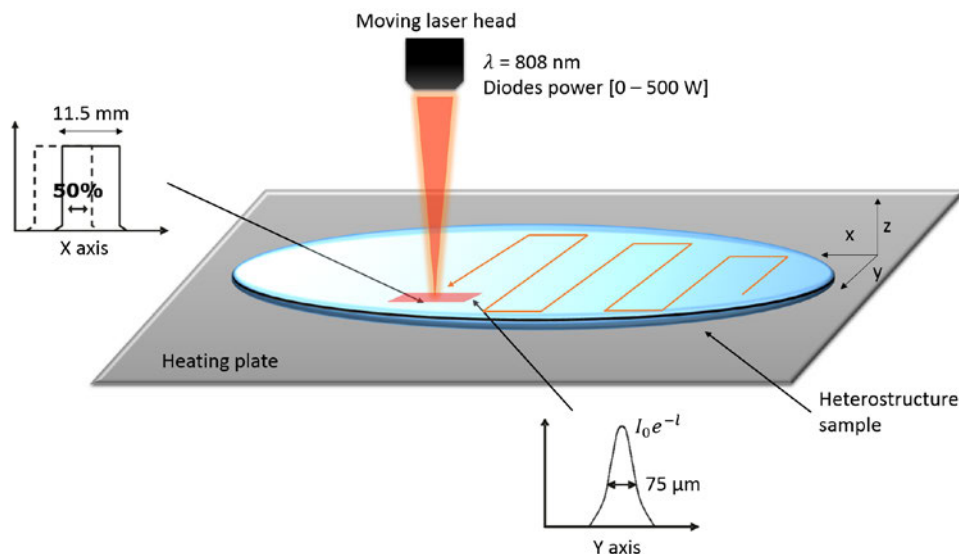


Figure 1: Représentation schématique du recuit laser des échantillons de Si implantés, collés avec des substrats de verre.

3.3. Simulation numérique du recuit laser

Afin de pouvoir étudier précisément la réponse du substrat implanté au passage du laser, celui-ci est simulé numériquement. La modélisation porte donc sur un système en 2D, avec dans la partie supérieure le wafer en verre, transparent à l'irradiation laser et dans la partie inférieure, le substrat de Si (voir Fig. 2).

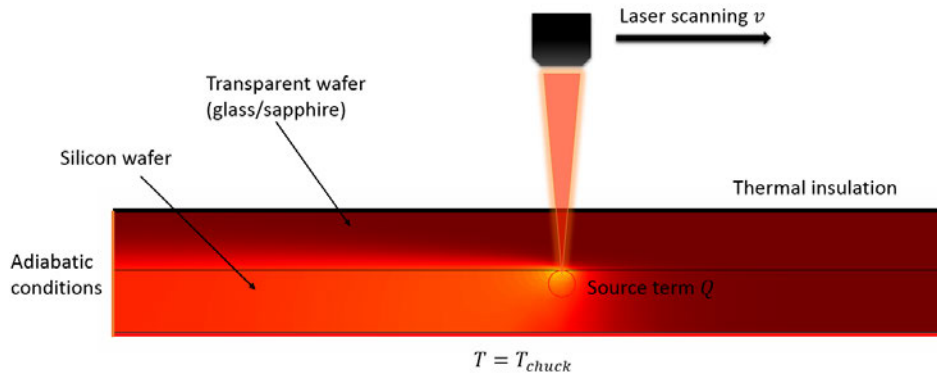


Figure 2: représentation schématique du système considéré pour la simulation du recuit laser.

L'équation de référence utilisée pour la simulation est l'équation de la chaleur :

$$\rho c_p \frac{\partial T}{\partial t} - \nabla(k \nabla T) = Q$$

avec ρ la densité, c_p la chaleur spécifique et k la conductivité thermique du matériaux. Considérant que l'absorption est nulle dans le saphir, le terme source du Si, Q , est défini:

$$Q = I_0 e^{-\frac{(x-vt)^2}{\sigma^2}} f(y)$$

où I_0 est la puissance incidente du laser, v est la vitesse de balayage du laser, σ la largeur du spot laser (75 μm) [7]. La fonction $f(y)$ défini la variation d'énergie en fonction de la profondeur dans le Si, d'après la loi de Beer-Lambert :

$$f(y) = e^{-\frac{y}{L}}$$

avec L la longueur d'absorption dans le matériau défini par :

$$L = \frac{\lambda}{4\pi k}$$

où λ est la longueur d'onde du laser.

Ainsi le terme source est défini par :

$$Q = (1 - R) \frac{I_0}{L} e^{-(x-vt)^2/\sigma^2} e^{-\frac{y}{L}}$$

avec R le coefficient de réflexion à la surface du Si, déterminé par une matrice de transfert optique, en utilisant le logiciel Rad-Pro.

Un exemple de signal de température est donné en Fig. 3, pour une puissance de 0.62 GWm^{-2} et un temps de résidence de 0.5 ms. La température est enregistrée pour une position à une profondeur de 0.8 μm , correspondant au R_p de la zone d'implantation pour l'énergie d'implantation de 76 keV des échantillons.

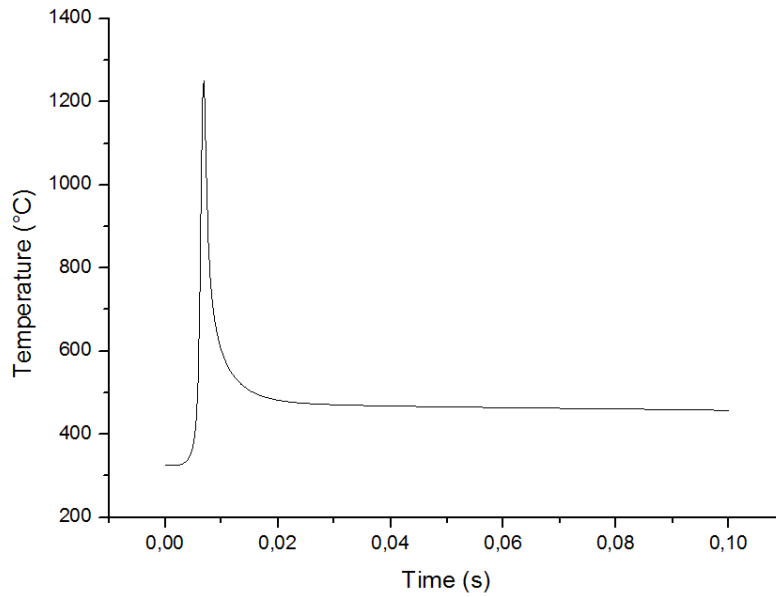


Figure 3: Simulation de la température dans la zone d'implantation durant le passage du laser, pour une puissance de 0.62 GWm^{-2} .

3.4. Conditions de splitting par recuit laser

Le sommaire des conditions de splitting est représenté en Fig. 4. Il est d'abord à noter que les régimes observés à basse température pour le transfert de SOI pour les deux doses considérées ici ($5.0 \cdot 10^{16} \text{ Hcm}^{-2}$ et $1.0 \cdot 10^{17} \text{ Hcm}^{-2}$) se sont pas suivies dans le cas du splitting laser. Si cela avait été le cas, le splitting laser pour les échantillons de $5.0 \cdot 10^{16} \text{ Hcm}^{-2}$ serait plus rapide que pour les échantillons de $1.0 \cdot 10^{17} \text{ Hcm}^{-2}$, ce qui n'aurait pas de sens d'un point de vue scientifique.

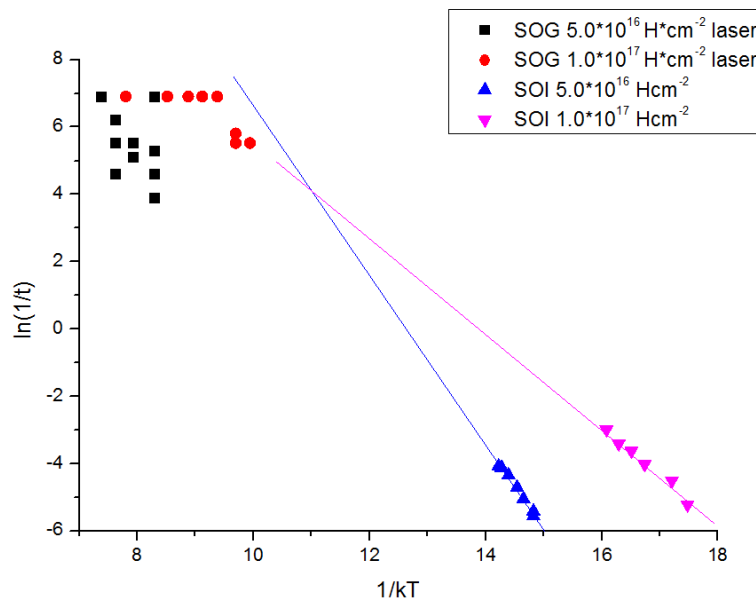


Figure 4: Conditions de splitting pour les échantillons de SOG ($5.0 \cdot 10^{16} \text{ Hcm}^{-2}$ et $1.0 \cdot 10^{17} \text{ Hcm}^{-2}$) avec le recuit laser et comparaison avec le splitting d'échantillons de SOI ($5.0 \cdot 10^{16} \text{ Hcm}^{-2}$ et $1.0 \cdot 10^{17} \text{ Hcm}^{-2}$), effectué avec un recuit en four.

3.5. Cinétiques de splitting pour des températures > 900°C

Afin d'étudier la cinétique de splitting, et pour les mêmes raisons qu'exposées dans le chapitre précédent, nous allons utiliser la fonction de budget thermique de splitting σ_T :

$$\sigma_T = \int \frac{1}{\tau(T(t))} dt$$

avec τ le temps de splitting, qui peut être défini selon différents régimes d'Arrhenius d'énergie d'activation E_a :

$$\tau = \tau_0 * \exp\left(\frac{-E_a}{k_B T(t)}\right)$$

où $T(t)$ est le signal de température en fonction du temps obtenu par simulation.

Nous proposons de reprendre les deux hypothèses (hypothèse 1 et hypothèse 2) du chapitre précédent, c'est-à-dire la continuation de la cinétique définie à basse température (hypothèse 1) et une cinétique définie par la diffusion de l'H libre (hypothèse 2). A ces deux hypothèses, nous rajoutons une troisième hypothèse qui définit la cinétique de splitting comme étant limitée par la diffusion de l'H piégé dans les complexes hydrogénés (hypothèse 3). Les trois hypothèses sont listées dans le tableau 1.

Table 1. Sommaire des paramètres de calculs de budget thermique, en utilisant le signal de température obtenu par simulations.

Dose d'implantation [Hcm ⁻²] <i>Hypothèse</i>	Energie d'activation [eV]	Ordonnée à l'origine de splitting [s.u.]	Ratio de H _{bonded} /H _{free}
5.0*10¹⁶			
<i>Cinétique basse température</i>	2.82	36.2	-
<i>Diffusion de l'H libre</i>	0.49	17.8	-
<i>Diffusion de H piégé</i>	1.46	17	2
1.0*10¹⁷			
<i>Cinétique basse température</i>	1.15	17.8	-
<i>Diffusion de l'H libre</i>	0.49	17.8	-
<i>Diffusion de H piégé</i>	1.46	20	0.1

Les résultats en termes de budgets thermiques sont représentés en Fig. 5 (a) et (b). Il apparaît extrêmement clairement que l'hypothèse 3 correspond à la cinétique de splitting pour cette gamme de température (> 900°C). En effet, cette hypothèse retourne une valeur de budget thermique égale à 1 (ou très proche), quand les autres

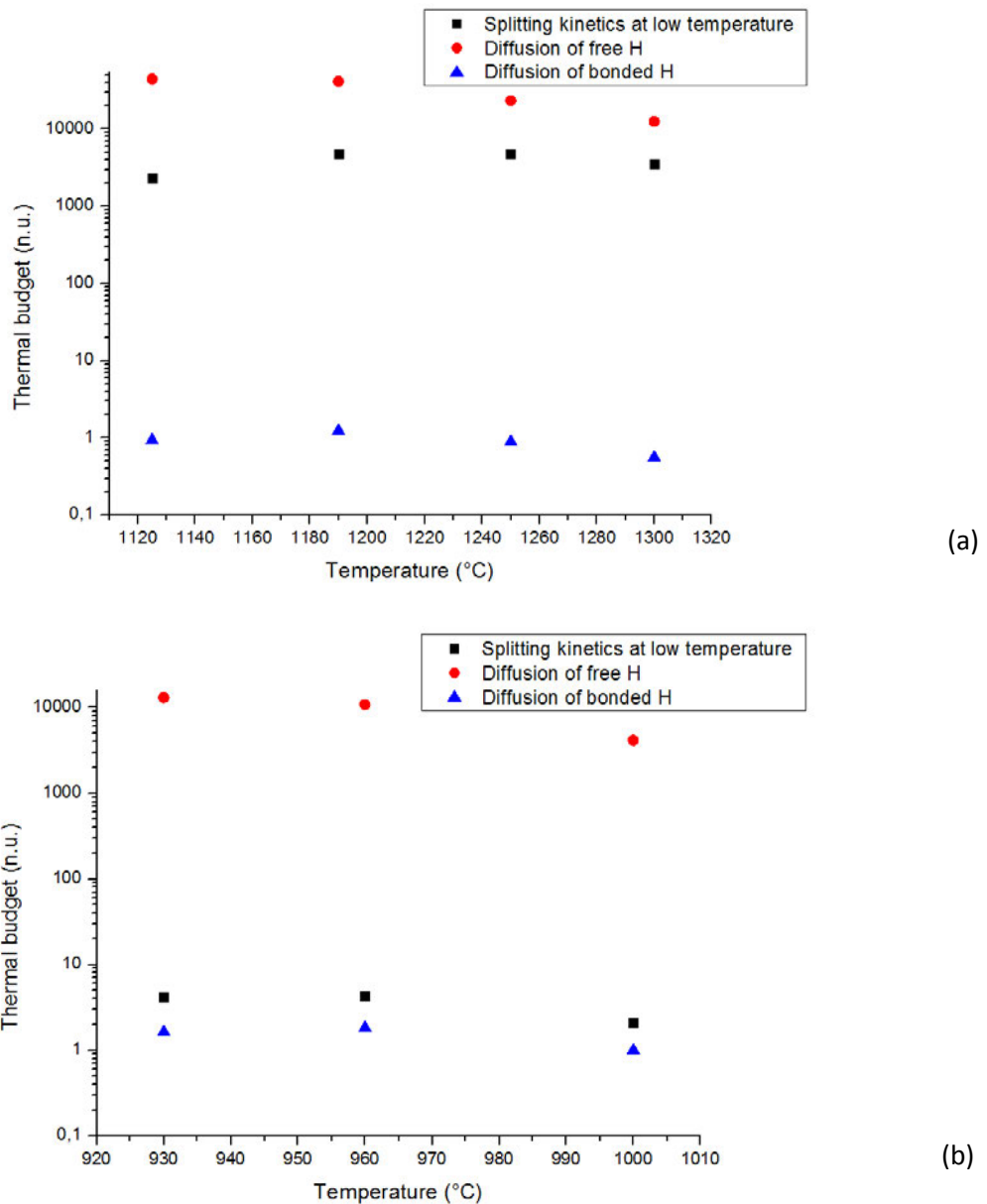


Figure 5: Calcul du budget thermique en utilisant le signal de température obtenu par simulation pour les échantillons de SOG implanté à $5.0 \times 10^{16} \text{ Hcm}^{-2}$ (a), 1.0×10^{17} (b).

3.6. Modèle unifié de splitting (450°C à 1300°C)

Nous sommes donc en mesure d'établir un modèle de splitting unifié, portant sur une gamme de température bien plus étendue que ce que la littérature rapporte (voir Fig. 6). Ainsi jusqu'à au moins 700°C, la cinétique de splitting dépend de la dose d'implantation, et de son évolution durant le recuit du fait de l'exo-diffusion d'H. A partir d'au plus 900°C (pour les échantillons implantés avec $1.0 \times 10^{17} \text{ Hcm}^{-2}$) et d'au plus 1000°C (pour les échantillons implantés avec $5.0 \times 10^{16} \text{ Hcm}^{-2}$), la cinétique est définie par la diffusion de l'H piégé

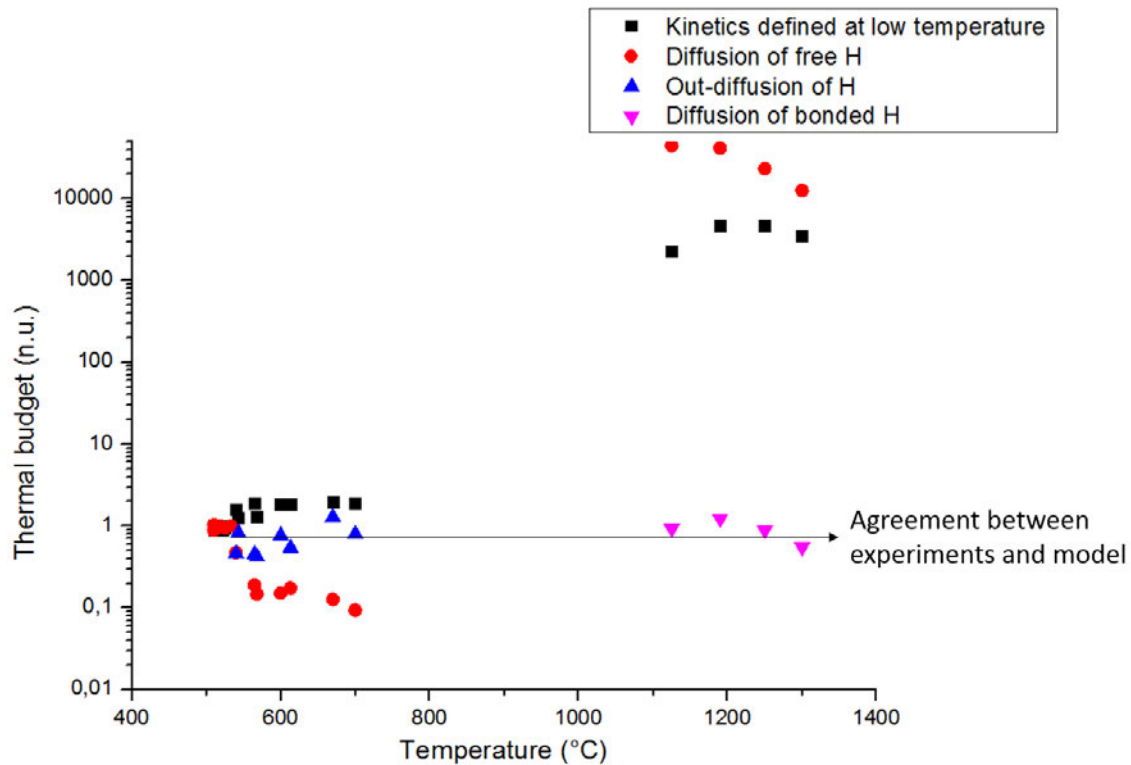


Figure 6: Calcul des budgets thermiques pour un échantillon implanté avec $5.0 \cdot 10^{16} \text{ Hcm}^{-2}$ depuis un domaine de basses températures (450°C) jusqu'à un domaine à très haute température (jusqu'à 1300°C).

3.7.Caractérisation des films de SOG obtenus par Smart Cut™

L'échantillon pour lequel le transfert s'est fait de la façon la plus homogène est un échantillon implanté avec $1.0 \cdot 10^{17} \text{ Hcm}^{-2}$ et recuit à 1000°C pendant 2 ms est représenté en Fig. 7 (a). Un traitement d'image de la moitié bien transférée montre que le transfert s'effectue sur 94 % de la surface du substrat de verre (voir Fig. 7 (b)).

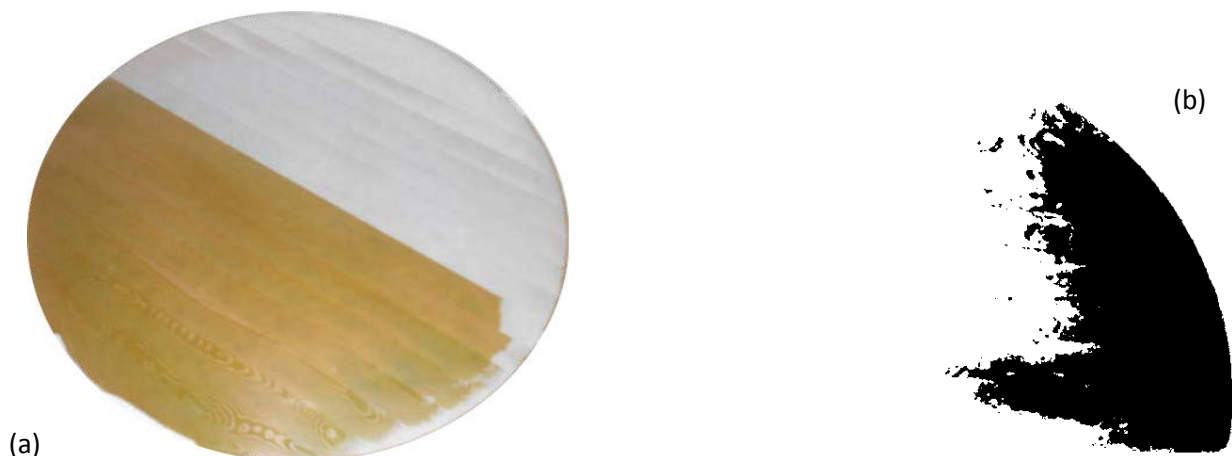


Figure 7: Image de l'échantillon présentant le meilleur taux de transfert, implanté à $1.0 \cdot 10^{17} \text{ Hcm}^{-2}$ et recuit à 930°C de 2 ms (a), image de la moitié bien transférée après traitement d'image (b).

3.8.Conclusion du chapitre

Dans ce chapitre nous avons montré pour la première fois la possibilité de splitting par laser dans du Si implanté. Nous avons obtenu des échantillons présentant un taux important de transfert (plus de 90 % de la surface) sur des wafers de grand diamètre (200 mm).

Par ailleurs, nous avons pu établir un modèle de cinétique de splitting portant sur des températures allant de 450°C jusqu'à 1300°C. Il s'avère que pour des températures supérieures à 900°C, la cinétique de splitting est définie par la diffusion de l'H piégé dans les complexes hydrogénés de type (Si:H).

Bibliographie

- [1] **F. Dimroth et al**, Wafer bonded four-junction GaInP/GaAs//GaInAsP/GaInAs concentrator solar cells with 44.7% efficiency, *Progr. In Photov.: Res. and Appl.* vol. 20, pp. 277-282, 2014.
- [2] **M. R. Oliver**, Chemical-mechanical planarization of semiconductor materials, Material Sciences, Springer, pp.5- 15, 2004.
- [3] **J. E. Ayers**, Heteroepitaxy of semiconductors. Theory, growth and characterization. CRC Press. Taylor Francis Group. pp. 1-15, 2007
- [4] **K. K. Bourdelle**, Engineered Substrates for Advanced CMOS Technology Nodes and More-Than-Moore Applications. in Functional Nanomaterials and Devices for Electronics, Sensors and Energy Harvesting. Engineering Materials, *Springer*, pp. 3-5, 2014. SC 47
- [5] **I. Radu, I. Szafraniak, R. Scholz, M. Alexe, U. Gösele**, Low-temperature layer splitting of (100) GaAs by He+H coimplantation and direct wafer bonding, *Appl. Phys. Lett.*, vol. 82, No. 15, 2003.
- [6] **Y.-B. Park, B. Min, K. J. Vahala, H. A. Atwate**, Integration of single-crystal LiNbO₃ thin film on silicon by laser irradiation and ion implantation-induced layer transfer, *Adv. Mat.*, vol. 18, pp. 1533-1536, 2006.
- [7] **A. Colin**, Etude des couplages radiatifs et thermiques et des modifications physico-chimiques engendrés par un recuit laser milliseconde sur la grille polysilicium de la technologie CMOS 45 nm. Thèse de Doctorat de l'Université de Strasbourg. 2010.

Épitaxie en phase liquide de Si sur substrat implanté

4.1. État de l'art de la fabrication de wafers fins de Si

L'amincissement de l'épaisseur des wafers de Si utilisés en tant que couche active des cellules solaires est un des leviers de réduction de coût par Watt crête (W_p) utilisé par l'industrie PV. En parallèle du perfectionnement de l'étape de sciage de wafers, d'autres approches innovantes ont été explorées, s'affranchissant du sciage : les approches « kerf-less ».

Le concept commun à ces approches repose sur la constitution d'une couche de séparation dans un substrat de Si. Celui peut être utilisé comme un donneur, par analogie à l'approche Smart Cut™. Une première approche, appelée SLiM-Cut (Stress-induced Lift-off) consiste à déposer un film métallique, p. ex. Al ou Ag, à la surface du donneur en Si. Du fait de la différence de coefficient d'expansion thermique, un champ de contrainte est généré par le recuit de la structure, de façon à former une fracture à une profondeur de $\sim 50 \mu\text{m}$ dans le donneur [1]. Le film ainsi détaché présente une épaisseur optimale pour l'absorption lumineuse, une fois réalisé sous forme de couche active. Une autre approche consiste à implanter à très haute énergie (MeV) de l'H dans le substrat, avant d'effectuer un recuit de séparation, similaire à celui du Smart Cut™ [2].

Une autre approche consiste à faire une couche de séparation dans le substrat, et à effectuer une croissance cristalline à la surface de celui-ci. Une première approche consiste à porosifier la surface du substrat par attaque chimique avant de faire un dépôt par voie chimique vapeur (CVD) [1]. Après dépôt, un recuit est effectué, de manière à détacher le film par coalescence des pores.

Une dernière approche consiste à effectuer une implantation ionique, avec des énergies d'implantation rencontrées dans le Smart Cut™ ($< 200 \text{ keV}$), avant de réaliser un dépôt par CVD. Le détachement du film s'effectue enfin par un recuit de séparation, analogue à celui effectué dans un procédé Smart Cut™ [3].

4.2. Procédé d'élaboration de wafers fins par épitaxie en phase liquide sur substrat implanté

Nous introduisons une approche nouvelle consistant à déposer par épitaxie en phase liquide du Si (à une température $> 1410^\circ\text{C}$) sur un substrat donneur de Si, après implantation ionique (voir en Fig. 1). Le procédé est motivé par la très faible viscosité du Si en phase liquide (inférieure à celle de l'eau), afin de former des films d'une épaisseur inférieure à $200 \mu\text{m}$. D'autre part, la diffusion de chaleur dans le substrat implanté pendant la solidification du film liquide est mise à profit pour activer thermiquement la séparation dans la zone implantée par Smart Cut™. Ainsi, il est proposé que le wafer fin ainsi se détache de lui-même durant la solidification/refroidissement.

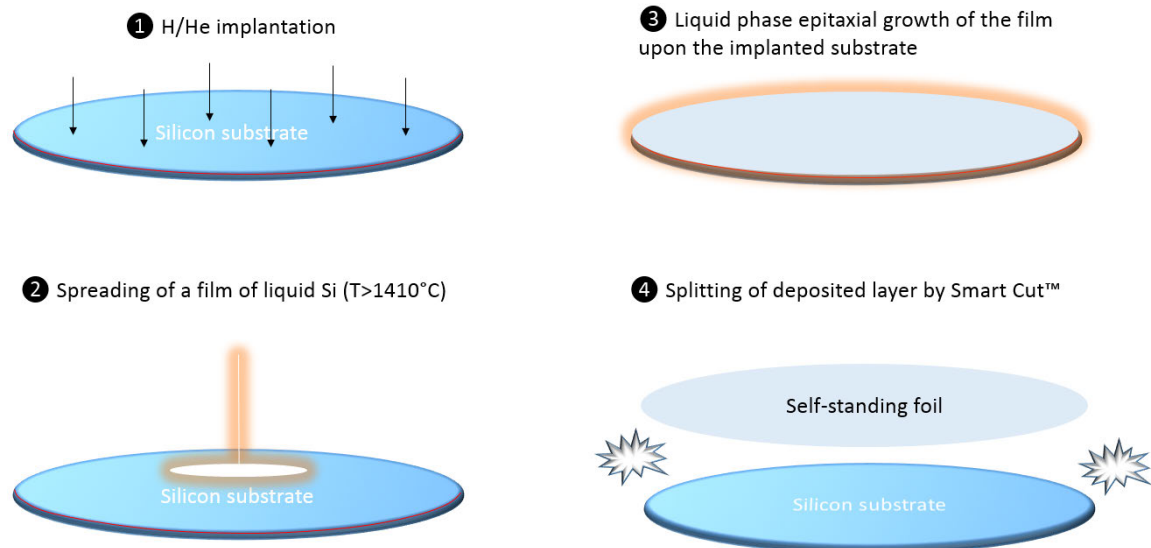


Figure 1 : Description schématique du procédé d'élaboration de wafers fins de Si par épitaxie en phase liquide sur substrat implanté.

4.3. Simulations de la solidification d'un film liquide de Si sur un substrat de Si

Afin d'évaluer les aspects thermiques du procédé, le système d'un film liquide déposé sur un substrat de Si est simulé, en utilisant la méthode des chaleurs spécifiques équivalentes pour la transformation de phase. Ainsi, le rejet de chaleur latente, h_{sl} , du fait du changement de phase est intégré dans la chaleur spécifique, c_p , sur une gamme de température située autour du point de solidification (T_m), tel qu'illustré en Fig. 2.

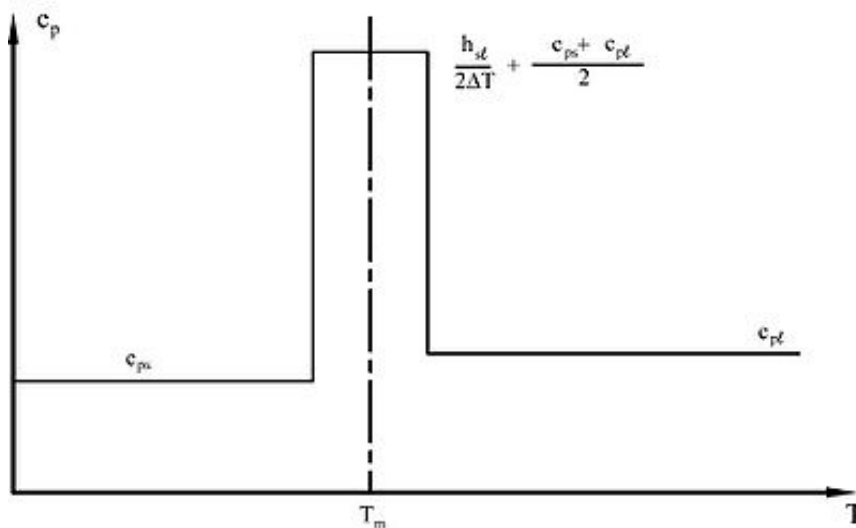


Figure 2 : Méthode des chaleurs spécifiques équivalentes.

Un exemple de système simulé, en cohérence avec des échantillons obtenus expérimentalement (Fig. 3 (a)) est illustré en Fig. 3 (b), avec un film de $200\ \mu\text{m}$ de Si liquide à 1427°C reposant sur un substrat de Si à température ambiante.

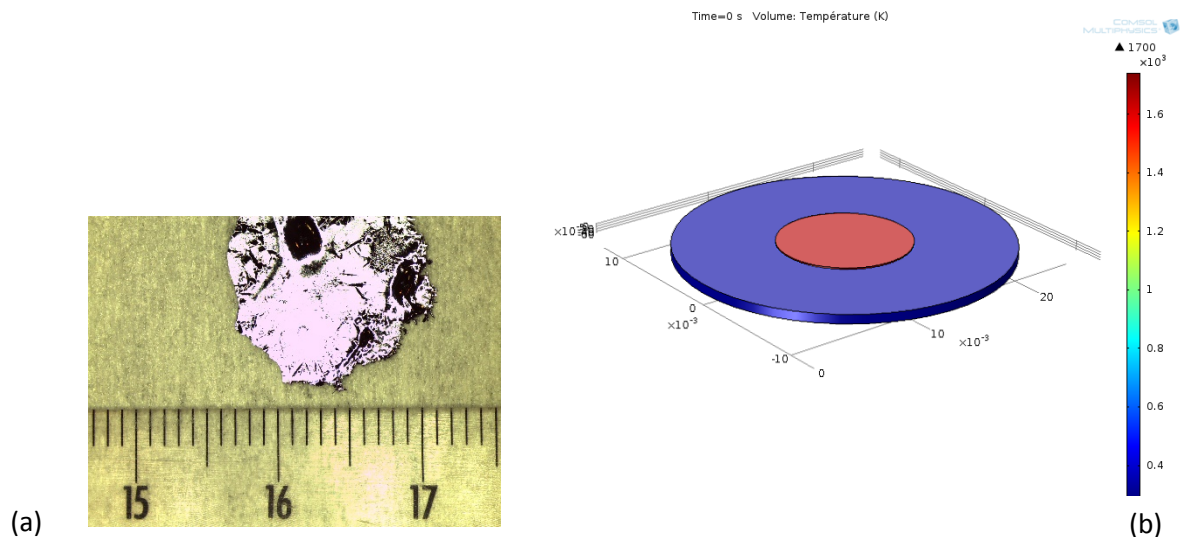


Figure 3 : Image d'un film détaché de Si obtenu expérimentalement, avec une épaisseur d'environ 200 μm (a), représentation schématique du système équivalent utilisé dans la simulation de solidification, avec un film de 200 μm de Si à 1427°C déposé sur un substrat à température ambiante, à $t = 0$ s (b).

Les résultats obtenus en termes de températures dans la zone implantée, correspondant à une profondeur de 1.5 μm , c'est-à-dire à l'énergie d'implantation de 160 keV, utilisée expérimentalement, sont représentés en Fig. 4. Différentes épaisseurs de films liquides sont simulées, de 50 μm jusqu'à 2 mm, correspondant à l'éventail d'épaisseurs obtenues expérimentalement.

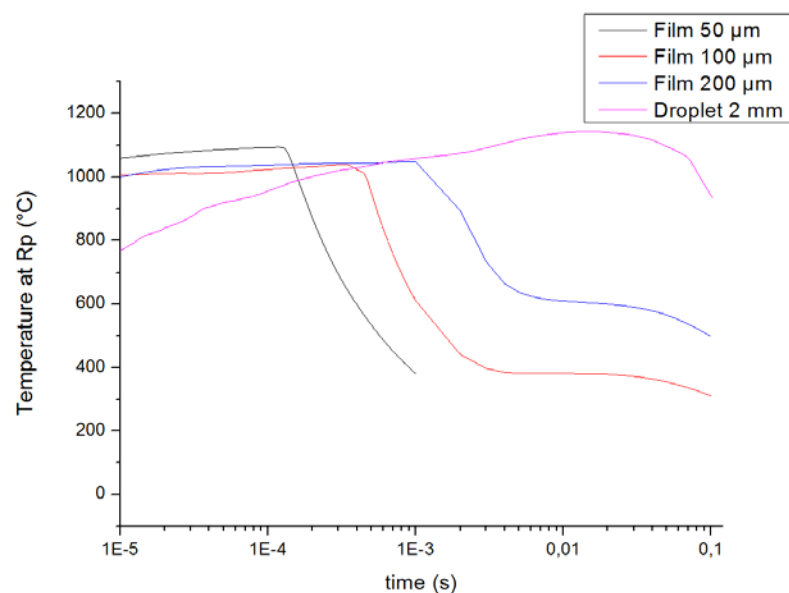


Figure 4 : signal de température obtenu par simulation pour un système de Si liquide déposé sur un substrat à température ambiante pour différentes épaisseurs de 50 μm jusqu'à 2000 μm .

Il est intéressant d'observer qu'en dépit de la grande proximité entre le film liquide à 1427°C avec la zone d'implantation, celle-ci ne s'échauffe pas au-delà de 1100°C, ce qui s'explique par la très bonne conductivité thermique du Si.

Les résultats obtenus en Fig. 4 sont utilisés pour calculer le budget thermique, en termes de splitting, en s'appuyant sur le modèle de splitting établi dans le chapitre précédent (c'est-à-dire avec une énergie d'activation de 1.46 eV). Les résultats sont illustrés en Fig. 5 et montrent que le budget thermique de splitting est atteint à partir d'une épaisseur de film de Si liquide de 200 µm.

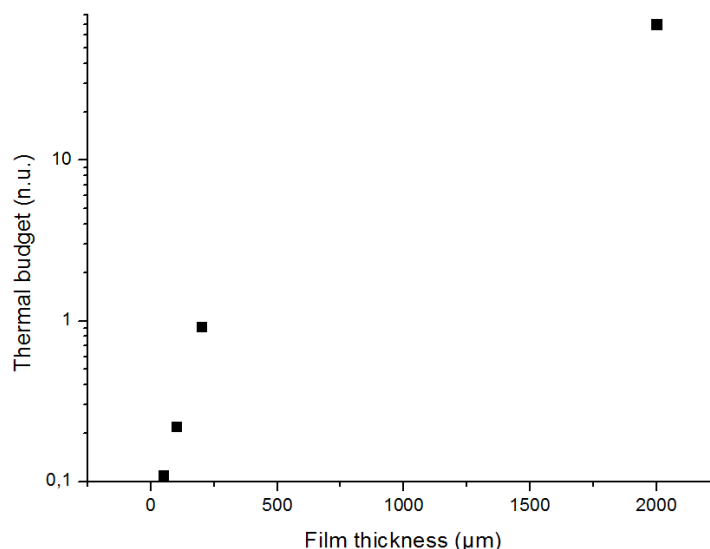


Figure 5 : Calculs du budget thermique de splitting en utilisant le signal de température simulé en Fig. pour la solidification de Si liquide à la surface d'un substrat de Si implanté à 160 keV et $1.0 \cdot 10^{17} \text{ Hcm}^{-2}$.

Ainsi, l'étude de simulations montre que le procédé proposé ici est cohérent, tant sur le fait que la zone d'implantation n'est pas refondue durant la solidification du film de Si liquide, que sur le fait que la solidification d'un film de Si liquide inférieur à 200 µm est plus lente que le splitting de la zone implantée. Ainsi, il est possible d'affirmer que le film solidifié peut jouer le rôle de wafer accepteur en contact avec le substrat donneur, nécessaire pour le Smart Cut™.

4.4. Dépôt en utilisant un creuset de fusion en graphite

Le premier équipement de dépôt utilise un creuset en graphite pour la fusion du Si, le contrôle du dépôt de liquide se faisant par injection d'Ar dans le creuset. Le substrat est placé sur un support en rotation, afin de faciliter l'étalement du liquide. Enfin, un pyromètre bi-canal est utilisé pour contrôler la température dans le creuset. Une illustration est donnée en Fig. 6. Il est à noter que la chambre de dépôt est maintenue à une température de 200°C.

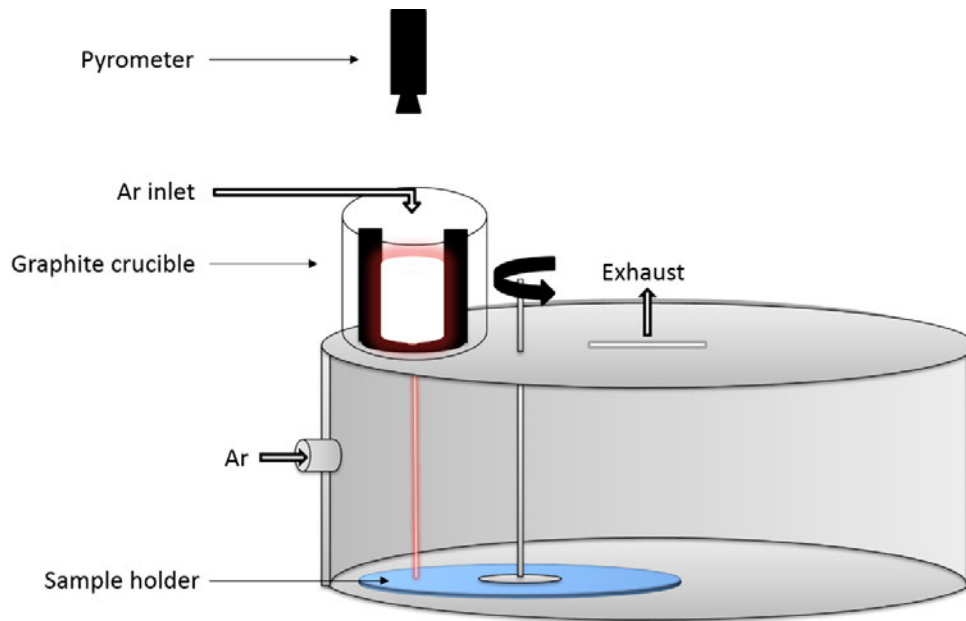


Figure 6 : Représentation schématique de l'équipement de LPE utilisant un creuset en graphite comme source de Si liquide.

4.4.1. Dépôt sur un substrat non-implanté

La Fig. 7 montre une cartographie de diffraction d'électrons rétrodiffusés (EBSD) de la tranche d'un dépôt de Si sur un substrat non-implanté. Il est important de noter que près de 90 % du film reprend l'orientation du substrat, prouvant que la croissance se fait de façon épitaxiale, le substrat agissant comme un germe à la cristallisation. Le ratio obtenu de croissance épitaxiale est très supérieur à ce que la littérature rapporte pour des dépôts en utilisant des équipements similaires [4-6].

D'autre part, la morphologie du film, et des grains formés, selon une géométrie 1D obtenue laisse à penser que la croissance se fait par une croissance contrôlée en température [4, 6]. La trace d'un plan de maillage est illustrée en Fig. 7. On peut poser l'hypothèse que l'apparition de macles s'est effectuée durant le refroidissement du film.

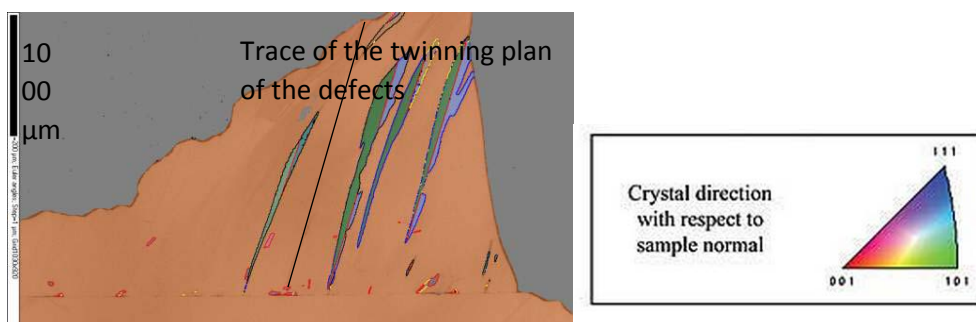


Figure 7 : Cartographie EBSD de la tranche du film déposé sur un substrat non-implanté. Le plan de maillage est illustré par la ligne noire.

4.5. Dépôt sur un substrat implanté

La Fig. 8 montre une cartographie de la tranche d'un film déposé sur un substrat implanté, après détachement par Smart Cut™.

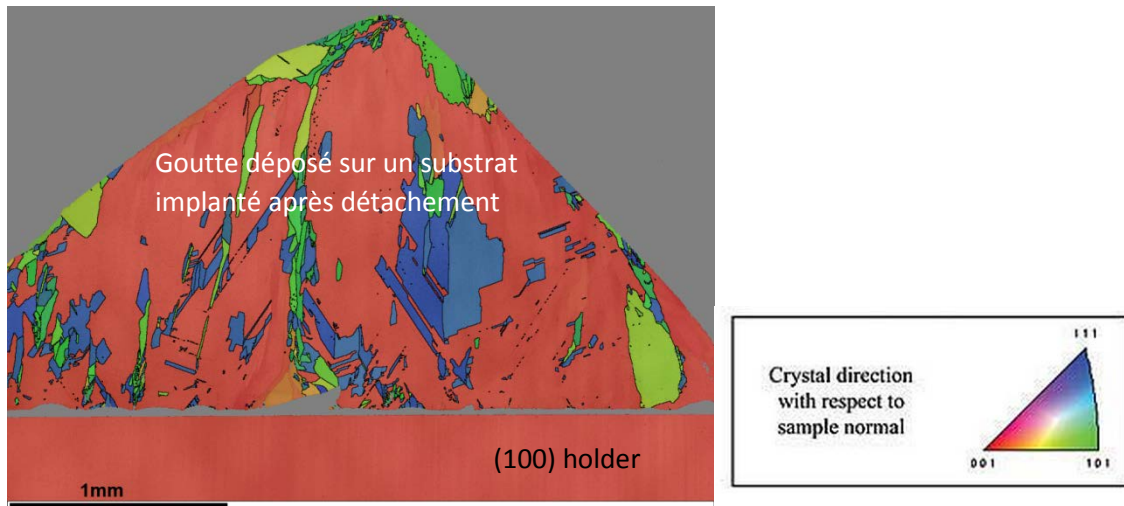


Figure 8 : Cartographie EBSD de la tranche d'un film déposé sur un substrat implanté à $1.0 \cdot 10^{17} \text{ Hcm}^{-2}$ après détachement par Smart Cut™.

Il apparaît nettement que la goutte ainsi solidifiée montre un niveau de grains beaucoup plus important que dans le cas d'un dépôt sur un substrat non-implanté. Toutefois, le niveau de croissance épitaxiale est toujours de 68 %, qui reste très supérieur à ce que la littérature rapporte.

La Fig. 9 montre le détail de la partie inférieure de la goutte après détachement. Elle montre qu'une couche d'environ $1.5 \mu\text{m}$, correspondant à la partie superficielle du substrat implanté détachée par Smart Cut™, peut être clairement identifiée. Cela démontre que le détachement s'effectue bien par Smart Cut™, et que le substrat implanté définit effectivement l'orientation cristalline du film durant sa solidification.

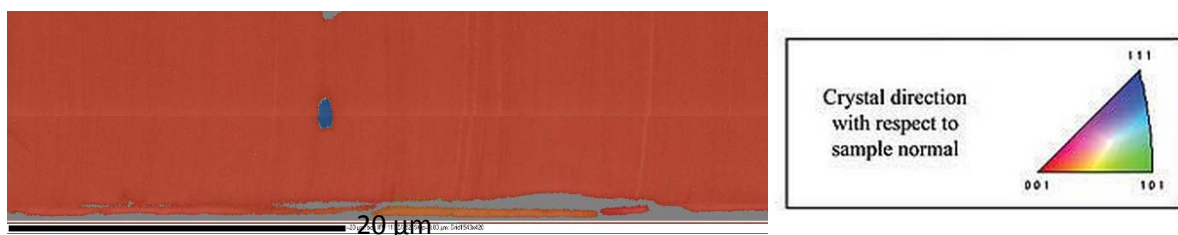


Figure 9 : Détail de la partie inférieure de la goutte détachée par Smart Cut™ par cartographie EBSD.

4.6. Dépôt en utilisant un auto-creuset

Le second équipement de dépôt utilise un auto-creuset de Si généré par des inducteurs en cuivre. L'échantillon est placé dans la trajectoire du jet de Si liquide, contrôlée par l'induction, et peut être incliné. Le contrôle de température est effectuée par un pyromètre bi-canal, comme précédemment. La Fig. 10 donne une illustration de l'équipement. Il est important de noter que la chambre de dépôt est maintenue à température ambiante.

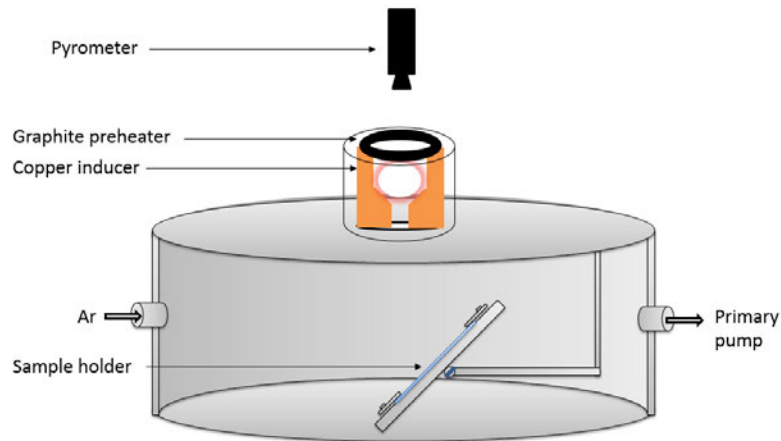


Figure 10 : Représentation schématique de l'équipement de dépôt de Si liquide par utilisation d'un auto-creuset.

La Fig. 11 donne une cartographie d'un film obtenu par dépôt sur un substrat implanté à $1.0 \cdot 10^{17}$ Hcm⁻² après détachement. Un grand nombre de grains orientés selon 1D sont observés et seulement 26 % du film reprend l'orientation du substrat, montrant que le couplage entre le substrat et le film liquide est moins grand que dans le cas de l'équipement précédent.

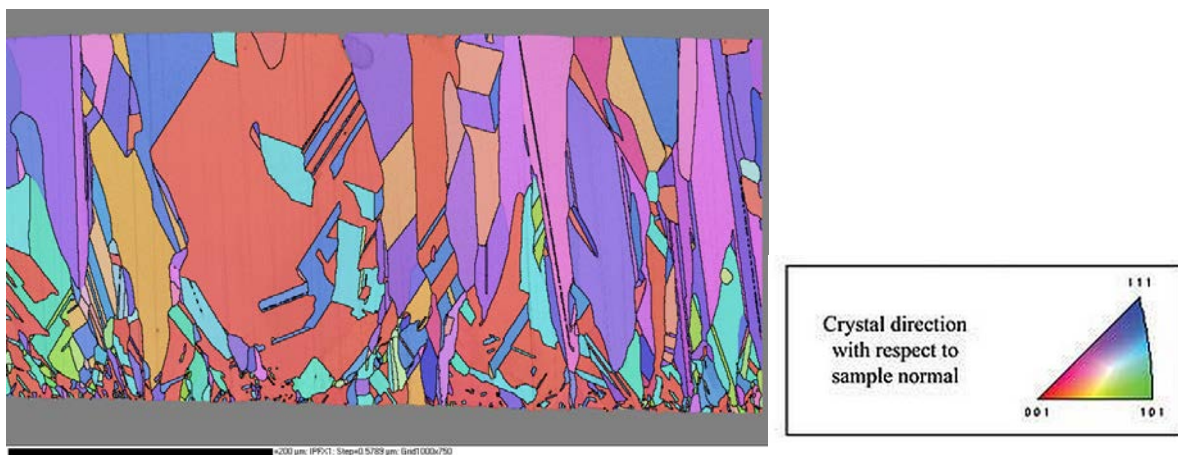


Figure 11 : Cartographie EBSD de la tranche d'un film déposé sur un substrat implanté à $1.0 \cdot 10^{17}$ Hcm⁻² en utilisant un auto-creuset.

Une analyse de composition à l'interface entre le substrat et le film déposé est effectuée par imagerie en grand angle et champ sombre (HAADF) et montre une concentration importante d'O à l'interface (voir Fig. 12). Cette concentration d'O est mise en relation avec la présence d'eau à la surface du

substrat, eau qui est évaporée dans le premier équipement (du fait de la chambre de dépôt placée à 200°C) ce qui n'est pas le cas dans l'équipement de dépôt par auto-creuset, où la chambre de dépôt est située à température ambiante.

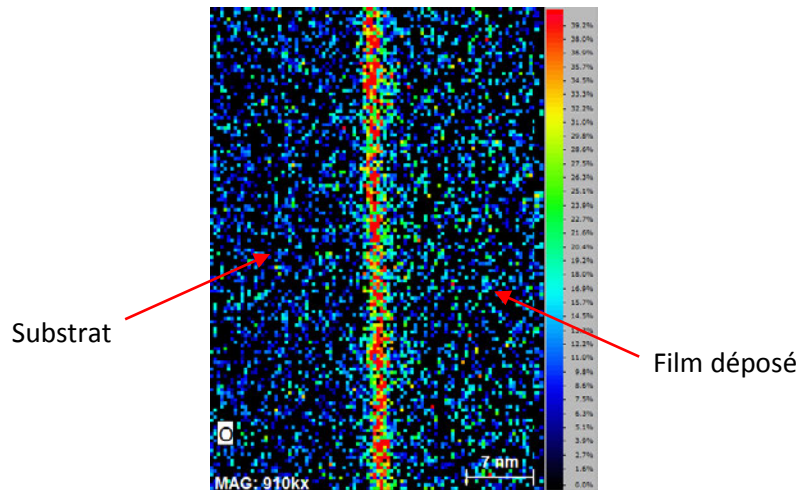


Figure 12 : Concentration d'O à l'interface entre le substrat et le film déposé par HAADF.

4.7. Conclusion et perspectives

Il apparaît donc que le procédé permet effectivement de croître par croissance épitaxiale des films d'épaisseurs inférieures à 200 μm par dépôt sur un substrat implanté, et de détacher le film après solidification par Smart Cut™. La présence d'eau à l'interface du substrat réduit la possibilité de croissance épitaxiale. Il est donc nécessaire de placer le substrat dans une enceinte chauffée, 200°C étant une température suffisante pour permettre une croissance épitaxiale sur 90 % du film déposé.

Pour des études ultérieures, il serait intéressant de développer un nouvel équipement, tel que décrit en Fig. 13. La chambre de dépôt peut ainsi être chauffée entre 200°C et 300°C. Le substrat est placé sur un support incliné et coulissant sous la coulée de Si. L'alimentation s'effectue par un auto-creuset donc le contrôle de coulée s'effectue par l'induction.

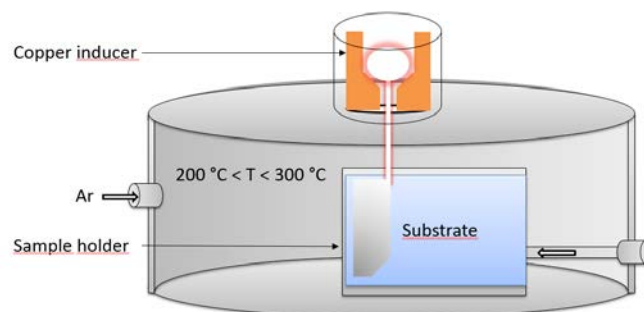


Fig. 13: Proposition d'architecture d'équipement pour des études ultérieures.

Bibliographie

- [1] **F. Dross et al**, Crystalline thin-foil silicon solar cells: where crystalline quality meets thin-film processing, *Prog. In Photov.: Res. And Appl.*, vol. 20, pp. 770-784, 2012.
- [2] **S. Amtablian**, Du transfert de films minces de silicium monocristallin vers un procédé cellule à faible budget thermique, Thèse de doctorat de l'Insa de Lyon, 2008.
- [3] **A. Beaumont**, Adaptation du procédé de fragilisation par faisceau d'ions pour la réalisation de couches minces de silicium monocristallin application au photovoltaïque, Thèse de doctorat de l'Insa de Lyon, 2003.
- [4] **K. Nagashio, H. Murata, K. Kuribayashi**, Spreading and solidification behavior of molten Si droplets impinging on substrates, *Act. Mat.*, vol. 52, 2004.
- [5] **Z. Wang, K. Kutsukake, H. Kodama, N. Usami, K. Fujiwara, Y. Nose, K. Nakajima**, Influence of growth temperature and cooling rate on the growth of Si epitaxial layer by dropping-type liquid phase epitaxy from the pure Si melt, *J. of Cryst. Grow.*, vol. 310, pp. 5248-5251, 2008.
- [6] **K. Nagashio and K. Kuribayashi**, Growth mechanism of Si from undercooled melts, *Sp. Utiliz. Res.*, vol. 21, pp. 9-12, 2005.

Conclusion de la thèse

La thèse porte sur l'étude de la cinétique de Smart Cut™ dans du silicium après implantation hydrogène, pour des températures de recuit comprises entre 500°C et 1300°C. Ainsi, la cinétique de séparation de couches (splitting) est caractérisée en considérant des recuits dans un four à moufle ainsi que des recuits laser. Sur la base de cette caractérisation, un modèle physique, basé sur le comportement de l'hydrogène implanté durant le recuit, est proposé. Le modèle s'appuie sur des caractérisations SIMS de l'évolution de la concentration d'hydrogène durant le recuit, ainsi que sur des simulations numériques. Le modèle propose une explication aux propriétés des films obtenus en fonction des conditions de recuit et mesurées par microscopie optique, AFM ainsi que par des mesures des énergies d'interfaces.

Sur la base du modèle de splitting obtenu, deux procédés de fabrication de films de silicium sont proposés pour l'élaboration de matériaux de silicium sur saphir et verre par recuit laser ainsi que pour l'élaboration de feuilles de silicium monocristallin par épitaxie en phase liquide sur substrat silicium implanté.

L'étude de premier procédé prouve pour la première fois la possibilité d'appliquer le procédé Smart Cut™ sur des substrats de silicium implanté. Les films ainsi obtenus présentent des grandes surfaces de transfert (wafer de 200 mm), ce qui présente un grand intérêt industriel. L'étude propose différentes caractérisations des films obtenus (AFM, profilométrie optique, mesure 4 pointe).

Le deuxième procédé est démontré en utilisant des bancs d'épitaxie en phase liquide de silicium (température supérieure à 1410°C) afin d'effectuer des dépôts sur des substrats de silicium implantés. Les films obtenus montrent un grand degré de croissance épitaxiale (jusqu'à 90% du film déposé mesuré par EBSD) et présentent une épaisseur aussi faible que 100 µm. D'autre part, le détachement par Smart Cut™ des films ainsi déposés est démontré. Les films obtenus par ce procédé sont caractérisés par HR-TEM ainsi que par photoluminescence.

THESE DE L'UNIVERSITE DE LYON OPEREE AU SEIN DE L'INSA LYON

NOM : MEYER

DATE de SOUTENANCE : 20/04/2016

Prénoms: Raphaël Germain Augustin

TITRE: The Advanced Developments of the Smart Cut™ Technology: Fabrication of Thin Wafers & Silicon-On-Something Hetero-structures.

NATURE : Doctorat

Ecole doctorale : Matériaux de Lyon

Spécialité : Matériaux

RESUME :

La thèse porte sur l'étude de la cinétique de Smart Cut™ dans du silicium après implantation hydrogène, pour des températures de recuit comprises entre 500°C et 1300°C. Ainsi, la cinétique de séparation de couches (splitting) est caractérisée en considérant des recuits dans un four à moufle ainsi que des recuits laser. Sur la base de cette caractérisation, un modèle physique, basé sur le comportement de l'hydrogène implanté durant le recuit, est proposé. Le modèle s'appuie sur des caractérisations SIMS de l'évolution de la concentration d'hydrogène durant le recuit, ainsi que sur des simulations numériques. Le modèle propose une explication aux propriétés des films obtenus en fonction des conditions de recuit et mesurées par microscopie optique, AFM ainsi que par des mesures des énergies d'interfaces. Sur la base du modèle de splitting obtenu, deux procédés de fabrication de films de silicium sont proposés pour l'élaboration de matériaux de silicium sur saphir et verre par recuit laser ainsi que pour l'élaboration de feuilles de silicium monocristallin par épitaxie en phase liquide sur substrat silicium implanté. L'étude de premier procédé prouve pour la première fois la possibilité d'appliquer le procédé Smart Cut™ sur des substrats de silicium implanté. Les films ainsi obtenus présentent des grandes surfaces de transfert (wafer de 200 mm), ce qui présente un grand intérêt industriel. L'étude propose différentes caractérisations des films obtenus (AFM, profilométrie optique, mesure 4 pointe). Le deuxième procédé est démontré en utilisant des bancs d'épitaxie en phase liquide de silicium (température supérieure à 1410°C) afin d'effectuer des dépôts sur des substrats de silicium implantés. Les films obtenus montrent un grand degré de croissance épitaxiale (jusqu'à 90% du film déposé mesuré par EBSD) et présentent une épaisseur aussi faible que 100 µm. D'autre part, le détachement par Smart

MOTS-CLÉS :

Smart Cut™, silicium, implantation, silicium sur saphir, silicium sur verre, laser épitaxie en phase liquide, wafer fins, EBSD, SIMS.

Laboratoire (s) de recherche :

-Institut des Nanotechnologies de Lyon (INL)
-Université Grenoble Alpes, CEA, Leti, SSURF
-Soitec

Directeur de thèse: Mustapha Lemit

Président de jury :

Composition du jury :

Claverie, Alain	Professeur/CNRS	Rapporteur
Tournié, Eric	Professeur/Université Montpellier	Rapporteur
Bruel, Michel	Directeur/Aplinov	Examineur
Bremond, Georges	Professeur/Insa Lyon	Examineur
Zaidat, Kader	Maître de conférence/Grenoble INP	Examineur
Lemit, Mustapha	Professeur/Insa Lyon	Directeur de thèse
Moriceau, Hubert	Docteur/CEA	Co-encadrant
Kononchuk, Oleg	Docteur/Soitec	Co-encadrant
Rieutord, François	Directeur de recherche/CEA	Invité